Imperial College London

Department of Materials
London Centre for Nanotechnology
Imperial College London

The nanoscale behaviour of disordered proteins confined within biomimetic nuclear pore complexes

Bernice Akpinar

Supervisors: Bart Hoogenboom(UCL) and Joshua Edel(ICL)

January 30, 2020

Thesis submitted for the degree of
Doctor of Philosophy

Declaration of originality

I declare that the work presented in this thesis is my own. Where information has been obtained from other sources and presented, I confirm that it has been properly cited.

Bernice Akpinar (September 2019)

Copyright declaration

The copyright of this thesis rests with the author. Unless otherwise indicated, its contents are licensed under a Creative Commons Attribution-NonCommercial-ShareAlike 4.0 International (CC BY-NC-SA 4.0). Under this licence, you may copy and redistribute the material in any medium or format. You may also create and distribute modified versions of the work provided you distribute your contributions under the same license as the original. This is on the condition that: you credit the author and do not use it, or any derivative works, for a commercial purpose. When reusing or sharing this work, ensure you make the licence terms clear to others by naming the licence and linking to the licence text. Where a work has been adapted, you should indicate that the work has been changed and describe those changes. Please seek permission from the copyright holder for uses of this work that are not included in this licence or permitted under UK Copyright Law.

Imperial College London PhD regulations 2019

Abstract

The nuclear pore complex (NPC) forms a nanochannel for selective transport into and out of the cells nucleus. Notably, the transport selectivity of the NPC critically depends on an assembly of intrinsically disordered proteins with multiple phenylalanine-glycine repeats (referred to as FG nups), grafted to the inner walls of the NPC. The focus of this work is to probe the biophysical nature of this indispensable nanochannel by using mimetic systems that emulate key properties of the NPC.

Using a DNA origami scaffold, it has been possible to study the configurations adopted by purified FG-nups confined to a nanopore geometry that mimics the NPC central channel. In this thesis, atomic force microscopy (AFM) has been used extensively to compare different flavours of FG-nups and to monitor their stochastic behaviour as they form transient condensates that occlude the pore's central lumen. Rearrangements of these entanglements were observed on the timescale of seconds, suggesting that reordering occurs at little energetic cost. This supports the idea that the FG nups are sufficiently 'sticky' or 'cohesive' to form dense condensates that seal the NPC's transport barrier yet are sufficiently dynamic at the molecular scale to facilitate the transport of larger molecules. Furthermore, the dynamics of two different FG-nup (the more cohesive Nup100 and the less cohesive Nsp1) was quantified using autocorrelation analysis and compared to analogous data acquired on native NPCs. As predicted Nup100 condensates were found to be longer lived than those formed by its less cohesive counterpart Nsp1. By contrast, no fluctuations above the background noise were observed in native NPCs. A possible explanation being due to the presence of soluble transport receptor proteins and molecules caught in transport that trap the FG-nups in given morphologies.

To further probe this hypothesis additional components of the transport system have been added to the mimetic nuclear pore complexes and their binding has been visualised with single molecule resolution, both by AFM and by total internal reflection fluorescence microscopy (TIRFM). Importinβ was seen to bind to both Nup100 and Nsp1 whereby a systematic increase in the number of nucleoporins led to greater binding.

Acknowledgements

The completion of this work would not have been possible without the guidance and support from a number of individuals both personally and academically. Firstly I would like to thank my two supervisors Prof.Bart Hoogenboom and Prof.Joshua Edel for their advice and constructive input over the duration of my PhD research. Also to our collaborators Prof.Patrick Lusk and Prof.Chenxiang Lin for taking me under their wing during my 3 month placement at Yale; a time that proved invaluable in making this project a success.

My thanks are extended all those who helped train me in various techniques that were integral to this project; Dr.Alice Pyne and Dr.Richard Thorogate for AFM training along with Dr.Patrick Ellis Fisher and Dr.Qi Shen for all things DNA origami related. I would also like to thank Dr.George Stanley with whom I have worked closely alongside and without whom such rigorous data analysis would not have been possible. Members of Joshua and Bart's research groups at Imperial and UCL respectively whose input has contributed to this work; Dr.Binoy Paulose, Ren Ren, Joe Beton, Dr.Adrian Hodel, Luke Davies, Dr.Kwasi Kwakwa and Roxana Mironska along with everyone else who has made for such a supportive working environment. I am also grateful for the mentorship provided by the Advanced Characterisation of Materials Centre for Doctoral Training, for the ancillary courses and support they provided over these 4 years. Lastly I would like to acknowledge the Engineering and Physical Sciences Research Council for providing the funding for this work.

Throughout my PhD I have received unwavering support from my friends and family, especially my mum and sister. I would like to say a special thanks to my husband Lawrence Sly for his positivity and encouragement that has helped me so much along the way. Lastly to my late father Isaac Akpinar, for always believing in me, I dedicate this work to you.

List of publications directly related to the work presented in this thesis

1. P. D. Ellis Fisher[#], Q. Shen[#], **B. Akpinar**, L. K. Davis, K. K. H. Chung, D. Baddeley, A. Saric, T. J. Melia, B. W. Hoogenboom, C. Lin, and C. P. Lusk "A programmable DNA origami platform for organizing intrinsically disordered nucleoporins within nanopore confinement", *ACS Nano*, vol. 12, no. 2, pp 1508-1518, 2018.

2. G. J. Stanley[#], **B. Akpinar**[#], Q. Shen, P. D. Ellis Fisher, C. Lin, C. P. Lusk and B. W. Hoogenboom, "Quantification of biomolecular dynamics inside real and synthetic nuclear pore complexes using time-resolved atomic force microscopy", *ACS Nano*, vol. 13, no 7, pp 7949-7956, 2019.

3. **B. Akpinar**, P. J. Haynes, N. A. W. Bell, K. Brunner, A. L. B. Pyne, B. W. Hoogenboom, "PEGylated surfaces for the study of DNA-protein interactions by atomic force microscopy", *Nanoscale*, vol. 11, pp 20072-20080, 2019.

List of other publications

1. R. Ren, Y. Zhang, B. P. Nadappuram, **B. Akpinar**, D. Klenerman, A. P. Ivanov, J. B. Edel, and Y. Korchev "Nanopore extended field-effect transistor for selective single-molecule biosensing", *Nature Communications*, vol. 68, pp 42-51, 2017.

[#] These authors contributed equally to this work.

Contents

List of Figures **9**

List of acronyms and abbreviations **14**

1 Introduction **16**

1.1 A molecular gatekeeper: the nuclear pore complex 17

1.1.1 The central transport barrier 19

1.1.2 Nuclear transport receptors 21

1.1.3 Proposed mechanisms for nucleocytoplasmic transport 24

1.1.4 Probing the transport barrier of intact NPCs 24

1.2 Building synthetic nuclear pore complexes 27

1.2.1 Modification of solid state nanopores 27

1.2.2 Designing nanopores using DNA 29

1.3 Concluding Remarks 32

2 Materials and methods **35**

2.1 Building NuPODs 35

2.1.1 DNA origami scaffold 35
2.1.2 Modified Nucleoporins for scaffold attachment 36
2.1.3 Hybridisation of FG-nups to DNA origami 37
2.1.4 Cleavage of MBP tags 40
2.1.5 Gel electrophoresis 40
2.1.6 Quantification of FG-nups on NuPODs 41
2.1.7 Nuclear transport receptors 41
2.2 Surface modification for DNA attachment 43
2.2.1 DNA molecules 43
2.2.2 Polymers and salts for electrostatic attachment 44
2.2.3 Lipid membrane preparation for AFM imaging 44
2.2.4 PEGylated surfaces to minimise non-specific protein adhesion . . . 45
2.3 Atomic force microscopy 46
2.3.1 Tapping mode imaging 47
2.3.2 Force-distance curve imaging 48
2.3.3 Quantitative high-speed imaging of AFM of NuPODs 49
2.4 AFM image analysis 50
2.4.1 Image processing 50
2.4.2 Fast-scanning of FG-nups: autocorrelation analysis 50
2.4.3 Cross-correlation averaging of NuPODs before and after the addition of NTRs 55
2.5 Transmission electron microscopy 60

2.6 TIRF microscopy 61

2.7 Coarse-grained molecular dynamics simulations 68

3 Surface preparation for in-solution AFM imaging of DNA 71

3.1 Introduction 71

3.2 Results 75

3.2.1 Cationic gel-phase lipid membranes for the adsorption of dsDNA . . 75

3.2.2 Polymers as surface modification agents for the adsorption of dsDNA 80

3.3 Discussion 89

4 Mimetic nuclear pore complexes based on DNA origami 92

4.1 Introduction 92

4.2 Results 94

4.2.1 Organising disordered FG nucleoporins using soft scaffolds 94

4.2.2 Cleavage of MBP tags 98

4.2.3 Anchoring different densities of FG nups 99

4.2.4 Surface functionalisation for AFM imaging of NuPODs 103

4.2.5 AFM imaging of FG-nups on DNA origami 106

4.2.6 3D architecture influences FG-nup morphology 108

4.3 Discussion 111

5 Visualising FG-nup dynamics using high-speed AFM 115

5.1 Introduction 115

5.2 Results 117

5.2.1 HS-AFM of NuPODs reveals stochastic dynamics 117
5.2.2 Autocorrelation analysis of AFM kymographs recorded for NuPODs 121
5.2.3 Comparison with HS-AFM on native NPCs 125
5.3 Discussion 129

6 Transport receptor binding to FG-nups housed within NuPODs 132
6.1 Introduction 132
6.2 Results 135
6.2.1 Sample preparation for NTR addition to NuPODs 135
6.2.2 ImportinBeta binding to Nup100 and Nsp1 - an AFM study 137
6.2.3 Replicating transport - NTR binding reversibility 146
6.2.4 TIRF microscopy study 148
6.3 Discussion 155

7 Conclusion 156
7.1 Future Work 158
7.1.1 Understanding FG-nup-NTR interactions 159
7.1.2 Measuring transport through NuPODs 160
7.1.3 Solid-state nanopores 162

Bibliography 167

A Copyright permissions 196

List of Figures

1.1 The structure of the NPC 18

1.2 The impact of cohesive interactions on the morphology of disordered FG nups grafted in a channel. 20

1.3 The classical nuclear import cycle. 23

1.4 Atomic force microscopy studies of native *Xenopus laevis* NPCs 26

1.5 Solid State Biomimetic NPCs as Selective Transport Barriers. 28

1.6 Design of 2D and 3D DNA origami. 30

1.7 Schematic designs of DNA origami nanopores. 31

2.1 Design of DNA origami rings 36

2.2 Design of protein constructs 38

2.3 Protocol for assembling NuPODs from DNA origami and DNA-modified FG nucleoporins. 39

2.4 SDS-PAGE gel analysis of NTRs used in this work. 42

2.5 Schematic setup of an AFM for imaging in liquid. 47

2.6 Drift correction of kymographs. 52

2.7 Interpreting the autocorrelation factor $R(\tau)$. 54

2.8 Analysis protocol for calculating NuPOD height in central channel. 56

2.9 Height increases upon the addition of hsImportin-βmEos2 to NuPODs with Nup100 proteins. 58

2.10 Height increases upon the addition of hsImportin-βmEos2 to NuPODs with Nsp1 proteins. 59

2.11 Total Internal Reflection Fluorescence Microscopy (TIRFM). 62

2.12 Multicolour TIRF imaging 64

2.13 Preliminary processing of importin-β—NuPOD image stacks collected using TIRFM 66

3.1 Protocols to for the adsorption of DNA onto mica 73

3.2 Topographic image and characteristic lipid approach force curves for DNA minicircles on DDAB bilayers 77

3.3 DNA minicircles adsorbed on mica modified with the cationic, synthetic lipid, DDAB 78

3.4 Conformational flexibility of DNA minicircles on cationic DDAB bilayers . 79

3.5 Table expressing molecular weights corresponding to degrees of polymerisation for the polymers used in this study. 81

3.6 Ordering of poly-L-lysine chains on a mica substrate. 81

3.7 AFM images of PLL-mica 82

3.8 Characterisation of the adsorption of DNA plasmid and streptavidin on functionalised mica. 83

3.9 Optimised Poly(L-lysine)-*b*-Poly(ethylene glycol) surfaces for exclusive DNA adsorption. 84

3.10 Additional characterisation of DNA plasmid and streptavidin adsorption on functionalised mica 85

3.11 Streptavidin binding to dual-end biotinylated 672 bp linear dsDNA on mica treated with PLL_{10}-*b*-PEG_{113} / $PLL_{1000-2000}$. 86

3.12 Streptavidin binding to dual-biotin 672 bp linear dsDNA. 87

3.13 Dual-biotin 672 bp DNA pre-incubated with monovalent streptavidin. . . . 88

4.1 Design and assembly of nucleoporins organised on DNA ('NuPOD'). 95

4.2 Representative TEM images of DNA origami rings and assembled NuPODs 97

4.3 Cleavage of the MBP tags from assembled NuPODs 98

4.4 A tunable DNA origami platform capable of housing different numbers of FG-nups 101

4.5 Snapshots of equilibrated molecular dynamics simulations 102

4.6 Adsorption of DNA origami structures on mica using different functionalisation methods. 103

4.7 MBP-FGnup-DNA adsorption on bare mica or on supported lipid bilayers . 104

4.8 AFM images of 48×MBPNsp1 NuPODs adsorbed on mica using different surface functionalisation methods 105

4.9 AFM imaging NuPODs in solution 106

4.10 AFM imaging force affects the appearance of the NuPOD lumen 107

4.11 Grafting of FG-domains on the inside or outside of the DNA scaffold affects their collective morphologies. 109

4.12 Timelapse AFM imaging of outside-grafted NuPODs on a supported lipid bilayer 111

5.1 Timeresolved AFM imaging of NuPODs at 1.6 s per frame 118

5.2 Single-line scanning experiments on NuPODs 120

5.3 Kymographs and autocorrelation analysis of empty DNA origami rings . . 122

5.4 Kymographs and autocorrelation analysis of NuPODs containing FG nups. 123

5.5 Averaged autocorrelation analysis of the pore channel in NuPODs. 125

5.6 Producing kymographs from *Xenopus laevis* oocyte NPCs and from NuPODs. 126

5.7 Kymographs and autocorrelation analysis of NPCs 127

5.8 Kymographs and height fluctuations of NPCs and NuPODs 128

6.1 AFM imaging of supported lipid bilayers and PLL-mica with added importin-β 135

6.2 AFM imaging of 48×MBPNup100 NuPODs on mica functionalised with PLL-*b*-PEG 136

6.3 Addition of human importin-β to NuPOD with 48×Nup100 (MBP tag cleaved) 138

6.4 Importin-βmEos2 binding control experiments with 48×MBP NuPODs . . 139

6.5 Calculated concentrations of FG repeats for NuPODs housing 8, 16, 24 or 48 Nsp1(2-603) or Nup100(2-610). 140

6.6 Importin-βmEos2 addition to 16×MBPNup100 NuPODs 142

6.7 Importin-βmEos2 addition to 24×MBPNsp1 NuPODs 143

6.8 Anti-MBP binding control experiments with 48xMBP NuPODs 144

6.9 Importin-βmEos2 addition to NuPODs containing different numbers of FxFG or GLFG repeats 145

6.10 Importin-βmEos2 forms mobile, fuzzy complexes with FG-nups 147

6.11 Photobleaching traces of NuPODs labelled with Alexa Fluor 647 149

6.12 Colocalisation of hsImportin-βmEos2 to NuPODs containing 16 or 48 MBP-Nup100 proteins 151

6.13 Intensity vs. time traces for importin-βmEos2 molecules interacting with NuPODs containing 16 or 48 MBPNup100 proteins 152

6.14 Colocalisation of importin-βAlexa Fluor 594 to NuPODs containing 8 or 48 MBPNup100 repeats 153

6.15 Single molecule intensity traces of importin-βAlexa Fluor 594 interacting with NuPODs containing 8 or 48 MBPNup100 proteins 154

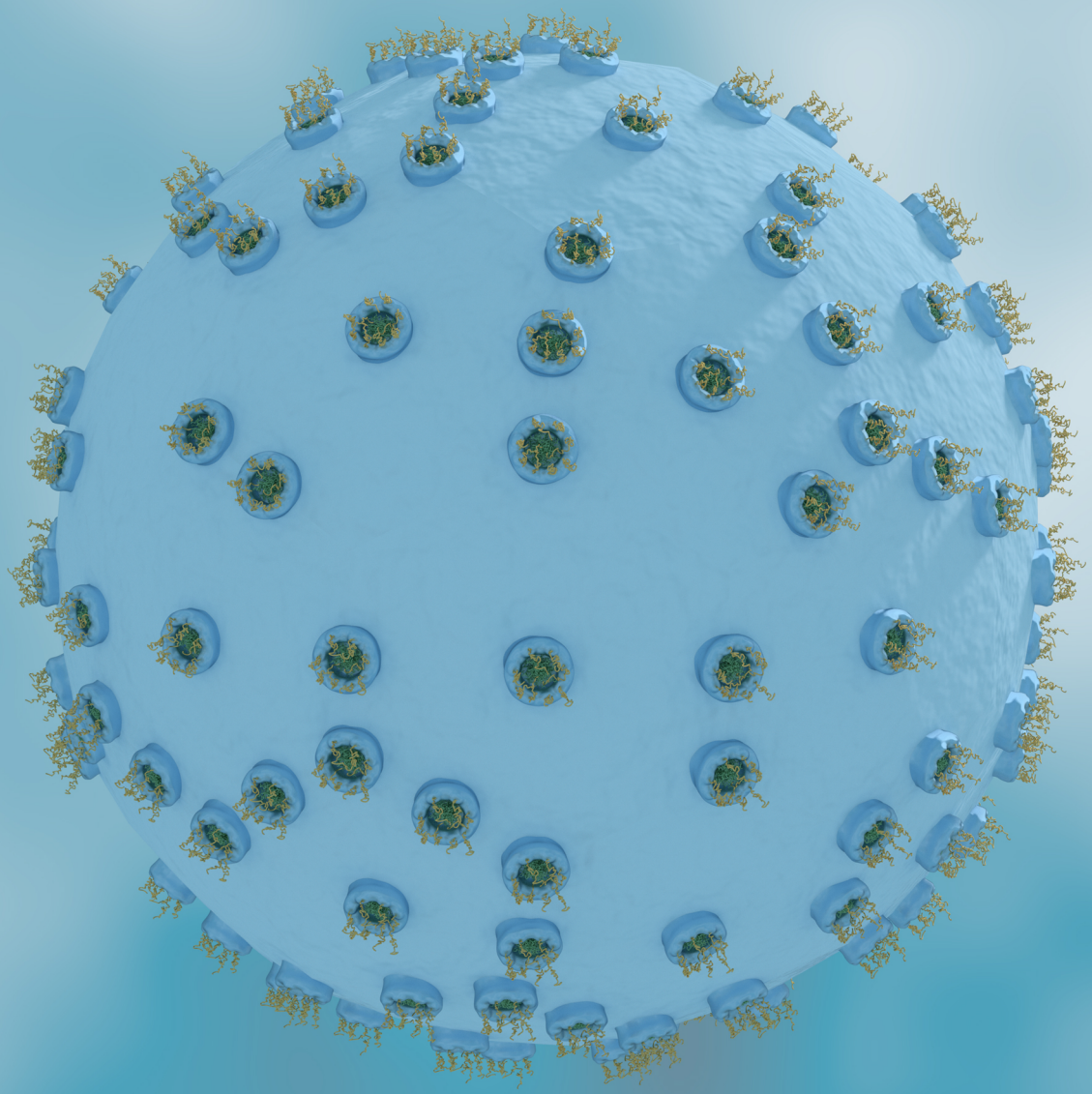
7.1 Incorporating NuPODs into a transport competent platform 161

7.2 Strategies for attaching FG-nups to surfaces and nanopores 162

7.3 Fabricating biomimetic NPCs from nanopipettes 165

List of acronyms and abbreviations

Atomic force microscopy	**AFM**
Bovine serum albumin	**BSA**
Deoxyribonucleic acid	**DNA**
Importin-α	**Imp-α**
Importin-β	**Imp-β**
Intrinsically disordered proteins	**IDPs**
Karyopherin	**Kap**
Maltose binding protein	**MBP**
Nuclear envelope	**NE**
Nuclear export sequence	**NES**
Nuclear localisation sequence	**NLS**
Nuclear pore complex	**NPC**
Nuclear pore protein	**Nucleoporin/Nup**
Nucleoporins organised on DNA	**NuPOD**
Nuclear transport factor 2	**NTF2**
Nuclear transport receptor	**NTR**
PeakForce Quantitative NanoMechanical	**PF QNM**
Phenylalanine-glycine repeat nucleoporin	**FG-nup**
Phosphate buffer	**PB**
Phosphate buffered saline	**PBS**
Poly-l-lysine	**PLL**
Polyethylene glycol	**PEG**
Ras-related nuclear protein	**Ran**
Ran guanosine 5'triphosphate	**RanGTP**
Sodium dodecyl sulphate-agarose gel electrophoresis	**SDS-AGE**
Sodium dodecyl sulphate-polyacrylamide gel electrophoresis	**SDS-PAGE**
Supported lipid bilayer	**SLB**
Total internal reflection fluorescence	**TIRF**
Transmission electron microscopy	**TEM**



Chapter 1

Introduction

Life as we know and see it at the macroscale, is regulated by processes that occur at dimensions orders of magnitude smaller. Living organisms are made up of cellular building blocks 1-100 microns wide, packed with structural and functional elements, bounded by a cellular membrane. The interior of the cell, the cytoplasm, is a complex micro-machine carrying out many functions. In prokaryotes these processes occur freely in the cytoplasm, but eukaryotes have evolved to partition different functions to organelles within the cell. This compartmentalisation has enabled cells to increase their robustness and complexity by simultaneously carrying out different functions within distinct, specialised micro-environments.[1] Arguably the most critical organelle is the nucleus. Bounded by a double membrane, the nucleus separates the cell's genetic material from the cytoplasm, enabling genetic expression to be controlled throughout the cell cycle. To establish and maintain two biochemically distinct compartments, nucleocytoplasmic trafficking occurs exclusively through nanometre-sized pores known as nuclear pore complexes (NPCs), which perforate the nuclear envelope (NE) that separates the nucleoplasm from the cytoplasm. The precise nature of this highly selective barrier is not yet well understood, but mechanistic insights can improve our understanding of a system that is critical for genetic expression, cell growth and replication. By understanding how molecules cross this barrier, we may also shed light on viral import into the nucleus, and guide development of therapeutics that rely on molecular delivery into the nucleus.

1.1 A molecular gatekeeper: the nuclear pore complex

In eukayrotic cells, the nucleus forms a compartment that separates the information required to build cellular proteins from the protein synthesis machinery in the cytoplasm. Thus providing more intricate regulatory control over the production of proteins and their RNA intermediates. It follows that there must be a bidirectional pathway for molecules made in the nucleus, such as messenger RNA, to be exported to the cytoplasm, and nuclear proteins such DNA/RNA polymerases to be imported from the cytoplasm. Nuclear import and export is facilited by hundreds to millions (dependent on cell type and species)[2] of NPCs, which act as molecular gate keepers. Small molecules($\lessapprox$ 40kDa) can travel freely through these nanopores, but larger macromolecules, targetted for nuclear entry, must display a nuclear localisation signal (NLS) and be accompanied by soluble nuclear transport receptors (NTRs) to pass.[3]

Each cylindrical pore is constructed from between 500-1000 copies of approximately 30 different proteins termed nucleoporins or nups.[4–6] Subcomplexes of strongly interacting nups constitute the building blocks of the NPC scaffold, assembling in multiples of eight to yield an approximately ring-shaped structure with eight-fold symmetry. Cross-sectional analysis through the membrane reveals asymmetry with certain nucleoporins preferentially localised to the cytoplasmic or nucleoplasmic faces.[4] Of the $\sim$30 nucleoporins, approximately 15 contribute to the scaffold formation, containing α-solenoid folds and β propeller domain folds.[6] These core proteins form inner and outer rings that connect to a set of nucleoporins with transmembrane domains. An outer luminal ring formed by these hydrophobic domains anchor the NPC into the nuclear envelope. Attached to the interior of the core scaffold, via bridging linker nups, are multiple copies of intrinsically disordered nups (10-15 different types), containing multiple phenylalanine-glycine (FG) repeats.[7] This highly concentrated milieu of FG repeats in the central channel is responsible for mediating nucleocytoplasmic transport and makes up almost one third of the NPC's overall molecular mass.[8] Note that FG repeats are also abundant on cytoplasmic filaments and at the basis of the nuclear basket.[9]

Although there is relatively low interspecies conservation of the amino acid sequences

of nuclear pore proteins, the overall structure of the NPC is highly conserved across eukaryotes.[6,8,10–15] A schematic depiction of the NPC detailing yeast(*S.cerevisae*) and vertebrate counterparts is shown in Figure 1.1. The overall mass of these supramolecular assemblies has been found to be 56.2 MDa in yeast.[8] By contrast, mammalian NPCs have been found to be much larger, at around 110 MDa.[14] It follows that the channel height of vertebrate NPCs is almost twice that of its yeast counterpart, ∼95 nm compared with ∼35 nm, respectively.[16,17] This height discrepancy correlates with the nuclear envelope thicknesses which are approximately 60 nm and 30 nm, respectively.[17,18] However, the inner diameter of the NPC central channel is similar for both, the constriction measueres as 41 nm for *H.sapiens*[13] and 38 nm for *S.cerevisae*.[11]

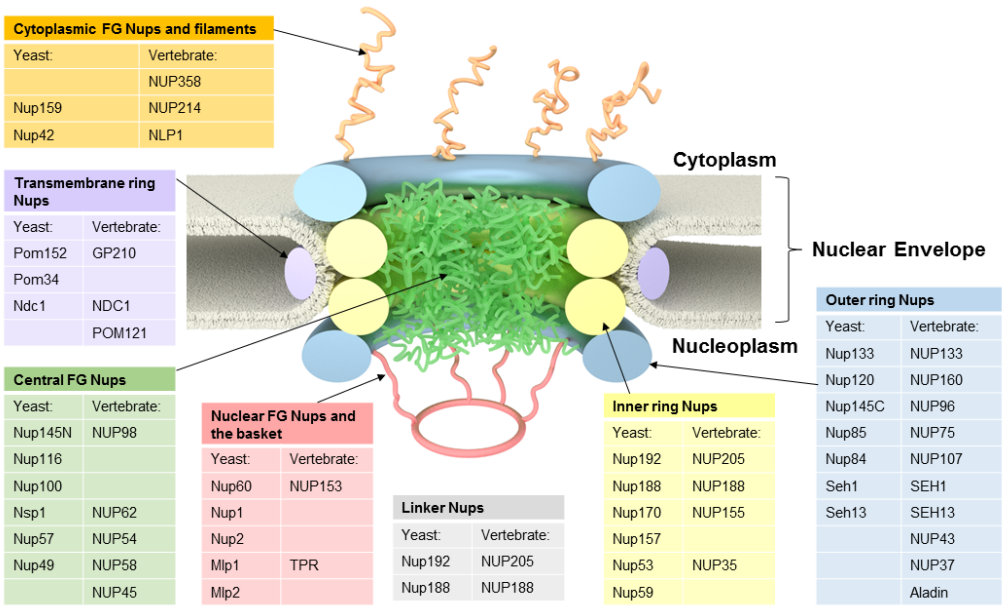


Figure 1.1: **The structure of the NPC** The NPC perforates the inner and outer nuclear membranes of the nuclear envelope, forming a channel through which all material passing between the nucleus and cytoplasm must travel. The pore is anchored into the membrane by a transmembrane ring structure that connects to the core scaffold, which comprises inner and outer ring elements. Linker nucleoporins (nups) connect the central FG-nups, which fill the central channel to form the barrier, to the pore scaffold. Cytoplasmic filaments and the nucleoplasmic basket are peripheral structures that play an important role in the function of the NPC beyond transport such as in cytoskeleton tethering. The nups that are known to constitute each NPC substructure are listed, with *Saccharomyces cerevisae* and vertebrate orthologues indicated.[6]

Owing to its intricate organisation, inherent mobility and membrane association, a com-

prehensive structural characterisation of this proteineous assembly has remained a challenge since its first observation in 1949.[19] By compiling data collected with various techniques, spanning different resolution scales, researchers have been able to resolve the arrangement of structured nucleoporins with sub-nanometre precison.[8]Yet no such detailed structural information exists for the disordered FG-nups that occupy the central channel, as their flexibility and disordered arrangement make them less amenable to traditional structural characterisation using electron microscopy and x-ray crystallography.[20]

1.1.1 The central transport barrier

Visualising the morphology of the FG-network is integral to our understanding of the mechanism of selective transport through the NPC. Hence it has been a topic of much research and debate.[3,21–25] In *S.cerevisae*, there are around 208 individual nucleoporins containing hydrophobic FG repeats in each NPC. These proteins with predominantely disordered domains line the walls of each transport channel creating a highly concentrated millieu of FG moieties (25-150 mM).[8] Sequences of charged amino acids interspersed between FG-domains regulate the cohesivity of intermolecular FG-nup interactions, where a higher ratio of charged to hydrophobic amino acids decreases cohesion and leads to extension of the polypeptide chain. Similarly, a lower ratio affords increased cohesion and compaction into 'molten globules'.[9,21] It is challenging to probe and to understand the impact of sequence heterogeneity on the global arrangement of these intrinsically disordered proteins deep inside the central transport channel, however it is known that not all FG nups are essential for effective barrier formation. Viability studies using minimal NPCs revealed that over half of the total mass of FG domains could be deleted without loss of the NPC's normal barrier function; only certain symmetrically localised FG domains were found to be essential.[26–28]

Efforts to directly examine the conformations adopted by these intrinsically disordered proteins have included *in vivo*,[29–31] *ex vivo*,,[32–34] *in vitro*[35–41] and computational[42–45] approaches. Based on such studies, it has historically been proposed that FG-nups behave either as a weakly interacting polymer brush, dominated by entropic and excluded-volume (repulsive) interactions (Figure 1.2a), or as a hydrogel, dominated by cohesive (attractive) interactions (Figure 1.2b), or — more recently — as an intermediate between such

extremes.

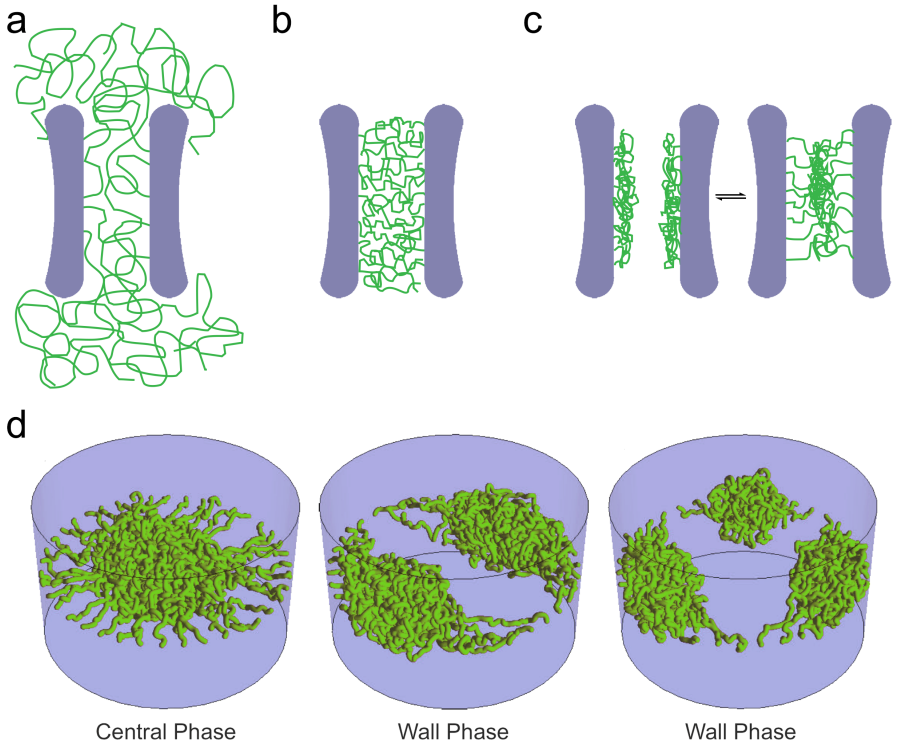


Figure 1.2: **The impact of cohesive interactions on the morphology of disordered FG nups grafted in a channel** A schematic cross-sectional representation of the NPC, based on predictions from polymer theory for flexible, grafted polymers. (a) If repulsive interactions dominate, the polymer chains repel one another and form a polymer brush. (b) As inter-FG-domain interactions become more attractive and cohesive, a denser meshwork forms a 'gel-like' state. (c) Depending on the balance between repulsive and cohesive inter- and intramolecular interactions, there can be large conformational changes for small changes in molecular interactions. (d) Monte Carlo simulations of polymers with the same interaction strength but different starting conditions. 40 polymers of length 100 nm are anchored in a cylinder of radius 25 nm and seen to relax into two distinctly different conformations; the central phase and wall phases. (d) adapted from.[42]

Instrinsically disordered proteins (IDPs) lack a defined three-dimensional structure, instead they adopt a large number of ensemble conformations and resemble flexible polymers. For polymers in a nanopore geometry, it has been predicted that small changes in repulsive and attractive interactions can cause large conformational changes in collective morphology, from collapsed globules near the channel walls to a central condensate where polymers stretch from the walls and collapse in the centre of the pore, Figure 1.2c. Com-

putational simulations have suggested that FG-nups are sufficiently cohesive to seal the transport barrier, yet that fast dynamics permit rapid polymer rearrangements needed for transport events, Figure 1.2d.[42,46]

In addition to the nucleoporins that are integrated into the pore, the NPC's transport barrier is regulated by the interactions that occur between the stationary FG-meshwork and a pool of soluble nuclear transport receptors (NTRs).[25]

1.1.2 Nuclear transport receptors

Whilst NPCs readily allow the diffusion of very small molecules such as nucleotides, entire megadalton assemblies such as viral capsids or proteasomes can also pass. Translocation of these larger molecules is permitted provided that they display a specific nuclear localisation sequence (NLSs; for import) or nuclear export sequence (NES; for export). In some cases the signal-bearing molecule interacts directly with the FG-barrier and passage is allowed. More commonly, additional soluble NTRs (also referred to as transport factors/proteins, karyopherins, kaps, importins, exportins, and transportins) recognise and bind to the NLS/NES, forming a complex that can translocate across the NPC. The karyopherin family comprises 14 different members in yeast and around 20 in metazoan, each sharing only modest sequence homology. Each member is targeted to bind and translocate specific molecules. Some karyopherins bind their cargoes directly whilst others require an adaptor protein, such as importin-β (karyopherin95 in yeast), the archetypal NTR for import. In this classical import pathway shown in Figure 1.3, firstly a heterodimer is formed with cargo-bound importin-α (karyopherin60 in yeast) via an importin-β-binding (IBB) domain. The importin-β \ importin-α \ cargo complex can next translocate through the NPC, facilitated by importin-β's interactions with FG-domains in the central channel.[47] The release of transport-competent cargo complexes into the nucleus is driven by the small GTPase Ran, which cycles between GTP and GDP bound states.[48] The directionality of transport is ensured by the presence of a Ran-GTP gradient across the nuclear envelope, which is maintained by the distinct subcellular localisation of Ran's guanine-nucleotide exchange factor, RCC1, and GTPase-activating protein, RanGAP, to the nucleus and cytoplasm, respectively. The high concentration of RanGTP in the nucleus favours its binding to the NTR•cargo complex as this complex reaches the nuclear

compartment, possibly at the site of nuclear basket nucleoporins.[49] The cargo molecule is then dissociated into the nucleus, importin-β is recycled back to cytoplasm by RanGTP, as is importin-α, which forms complex with CAS and RanGTP. The small homodimer NTF2 also has a role in transport, acting as an importin for Ran, to maintain the Ran concentration gradient, with a higher fraction of RanGTP in the nucleus (approximately 80% of all Ran found in the cell is localised to within the nucleus).[50]

Some studies have also suggested that there is an affinity gradient for NTRs and FG-nups across the NPC, and that this also contributes to transport directionality.[45,51,52] In yeast, Phytila and co-workers found Kap95 binding strongest for cytoplasmic nups (Nup42, K_d = ∼1500 nM) and weakest for nups located on the nucleoplasmic face (Nup1, K_d = ∼8 nM).[52] Such a model would suggest that cargo constructs are released only at the nucleoplasmic face, and that nucleoplasmic nups are therefore essential for viability, an observation that contradicts requirements for minimalist NPCs.[26]

The process of nuclear import requires multiple interactions to take place on millisecond timescales. Binding affinities between FG-nups and NTRs have been found to be in the low micromolar to nanomolar range, using *in vitro* studies based on surface-binding assays such as bead binding, surface plasmon resonance (SPR) and quartz crystal microbalance with dissipation monitoring (QCM-D).[53–57] However, such strong affinities appear — at least at first sight — inconsistent with the fast transport rates observed *in vivo* (where up to 1000 macromolecules are transported per second per NPC).[58] On the other hand, weaker affinities (low millimolar range) were found in studies of isolated FG motifs and NTRs. Such weak individual interactions appear in better agreement with the high rate of transport through the NPC,[58–60] where it should be realised that highly specific transport can result from strong avidities arising from the collective, multivalent nature of NTR binding into FG-nup assemblies.

The NPC central channel contains a high concentration (25 - 150 mM) of FG-binding sites, so the rate of transport is essentially limited by the unbinding of individual NTRs from the FG repeats.[8,61] At physiological concentrations of NTRs (1-10μM), it is plausible that a stable pool of NTRs is incorporated into the FG-meshwork, residing in the central conduit of the NPC.[62] This hypothesis is supported by observance of a central mass highly variable in size and shape, indicative of cargo and NTR molecules caught in transit, in many *ex*

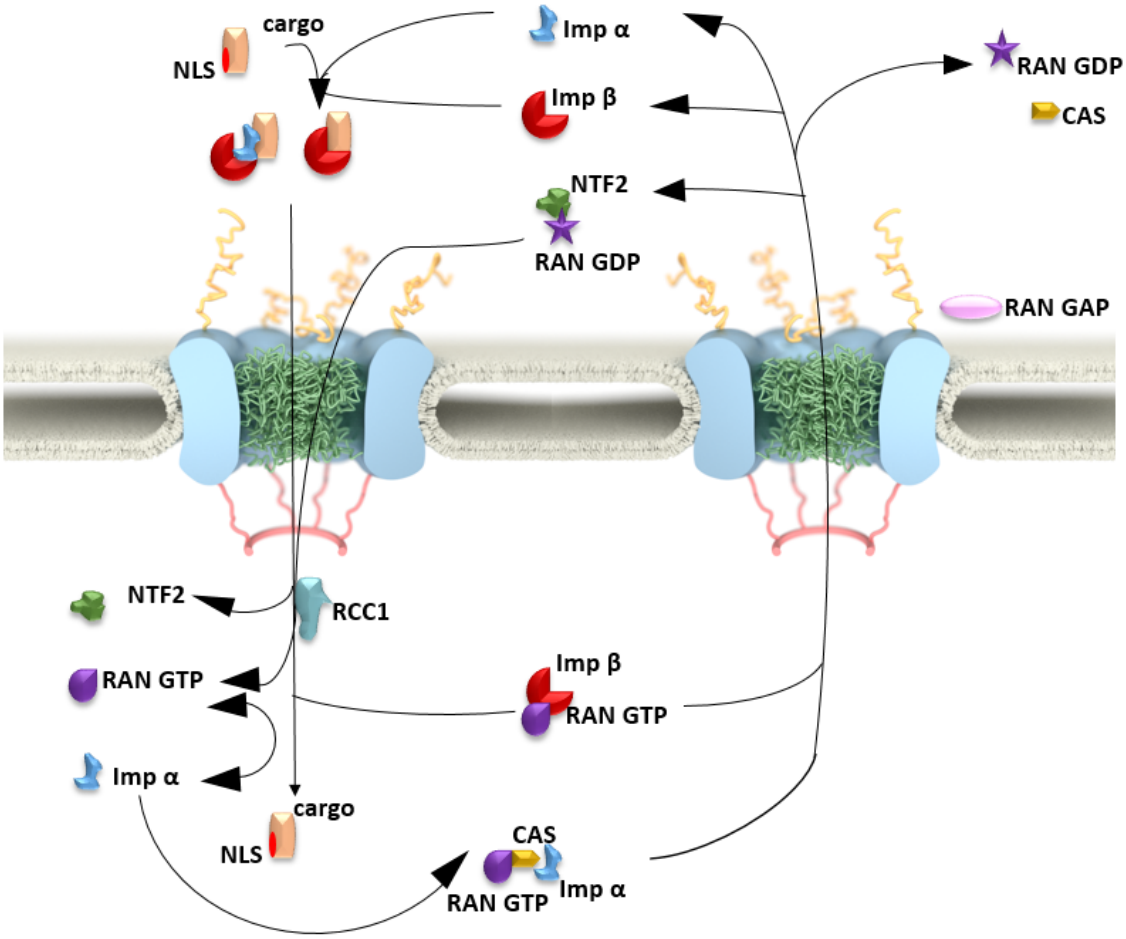


Figure 1.3: **The classical nuclear import cycle** The import cycle begins when a cargo molecule interacts with importin-β or an importin-α/β heterodimer via its nuclear localisation signal (NLS). The complex interacts with the transport barrier and crosses through to the nuclear side where RanGTP binds to importin-β, causing a conformational change that releases the bound cargo. The importin molecules are recycled to the cyctoplasm (importin-β with RanGTP and importin-α with RanGTP and CAS). The importin complexes dissociate at the cytoplasmic face by the hydrolysis of RanGTP to RanGDP using RanGAP.To maintain the RanGTP gradient across the NPC, RanGDP is then imported to the nucleus by the transport factor NTF2 ,where the protein RCC1 converts it to RanGTP.

vivo studies.[33,34,63,64] Recent integrative studies of purified yeast NPCs found around 26 MDa of NTRs and cargo molecules to be associated with each NPC,[8] suggesting NTRs may form an essential component of the transport barrier; a certain fraction of NTRs stably associate with the FG-network whilst another portion are rapidly turned over.[56,65]

1.1.3 Proposed mechanisms for nucleocytoplasmic transport

At the molecular level, the precise nature of NTR—FG-nup interactions remains unclear, although a number of models have been proposed. These models generally are on a continuum between two extreme trains of thought. The first represents FG-nups as non-cohesive entities that form a primarily entropic barrier, the other imagines a cohesive network for the formation of a size-selective barrier. In the non-cohesive model, natively unfolded FG Nups act as a polymer brush, where rapid movements of their disordered domains exert entropic forces that prevent the transport of inert molecules. This 'virtual gate model' allows the passable of specific molecules by stochastic binding between FG repeats and NTRs.[22,58,63,66,67] Similarly, the 'reduction-of-dimensionality' mechanism assumes that the hydrophobic FG-nups are not sufficiently cohesive to occlude the pore, but instead coat only the inner walls of the NPC. A small central channel is left in the centre of the pore to allow the passive diffusion of small molecules whilst larger NTR•cargo complexes bind to the hydrophobic wall of FG-nups in order to pass through the NPC.[29,68]

A very different view is provided by the 'selective phase' model that suggests FG repeat regions are crosslinked with each other through their phenylalanine residues to form a dense cohesive gel-like barrier.[35,36,69–72] The FG-network having a mesh-size of $\lessapprox 5$ nm then allows passive diffusion of small molecules, but excludes larger, inert molecules. NTRs — and NTR-bound cargos — interact with the FG-nups to dissolve FG-FG crosslinks, thus facilitating their passage through the NPC.

More recent studies indicate that FG nup behaviour is balanced between these two regimes, i.e., the selective barrier to transport exists because both of the entropic penalty to polymer compression and of the cohesive interactions between FG nups. In either scenario, only NTRs and NTR•cargo complexes with an affinity for FG-nups can translocate.[25,45,46,73]

1.1.4 Probing the transport barrier of intact NPCs

For the *in situ* characterisation of the NPC's chaotic transport barrier, electron microscopy (EM) combined with immunogold labelling against specific nups has enabled the localisation of central channel nups that are otherwise undetectable by cryo-based-EM. By

detecting the nup-bound gold nanoparticles, the spatial orientation of these disordered proteins can be determined; i.e., whether they extend into the central channel or beyond into the nucleoplasmic or cytoplasmic compartments.[74–79] In this case the sample must be dehydrated, other techniques such as single-molecule fluorescence microscopy enable in solution imaging, thereby facilitating the study of interactions between FG-nups and NTRs.[65,80,81]

Among the various techniques to examine the transport barrier of the NPC, atomic force microscopy (AFM) stands out for being able to record the surface topography of the NPC at nanometre resolution under near-physiological conditions, without the need for drying, fixing, staining or labelling. Since images are generated by raster scanning a sharp tip over the sample, mechanical information can also be extracted by examining the interactions between the probe with known stiffness and the uncharacterised sample.[82] Various developments in AFM technology have also facilitated a large improvement in scan speed and thus temporal resolution, enabling real-time imaging of biomolecules at less than a second per frame.[83]

Most AFM studies of NPCs have been carried out on the nuclear envelope taken from *Xenopus laevis* oocytes, on account of its large nucleus and high NPC density (see Figure 1.4A for an image of the cytoplasmic side of the NE captured in liquid).[25,32–34,64,84–94] By simultaneously monitoring the force response as the AFM tip indents each NPC, the stiffness and elasticity of FG nucleoporins can also be measured. This gives information about FG-nup morphology up to 20 nm below the pore surface, results from these studies have indicated an increased stiffness at the centre of the pore as well as at the pore scaffold (see Figure 1.4H).[25,32,34] Such observed nanomechanical properties in the NPC are consistent with a cohesive barrier to transport. Although it must be noted that since AFM is chemically blind it is unclear whether these measurements are detecting FG-nups alone — or more likely a combination of FG-nups and endogenous cargos/NTRs that are caught in transport.

Other AFM studies have detected rapidly fluctuating features in the pore and interpreted these as individual FG nups moving about their tethers; a signature of the entropic nature of the transport barrier (Figure 1.4I-K).[33,95] However, these features were only $\sim$1 nm in height; such height changes are within the detection limit of the experimental technique.

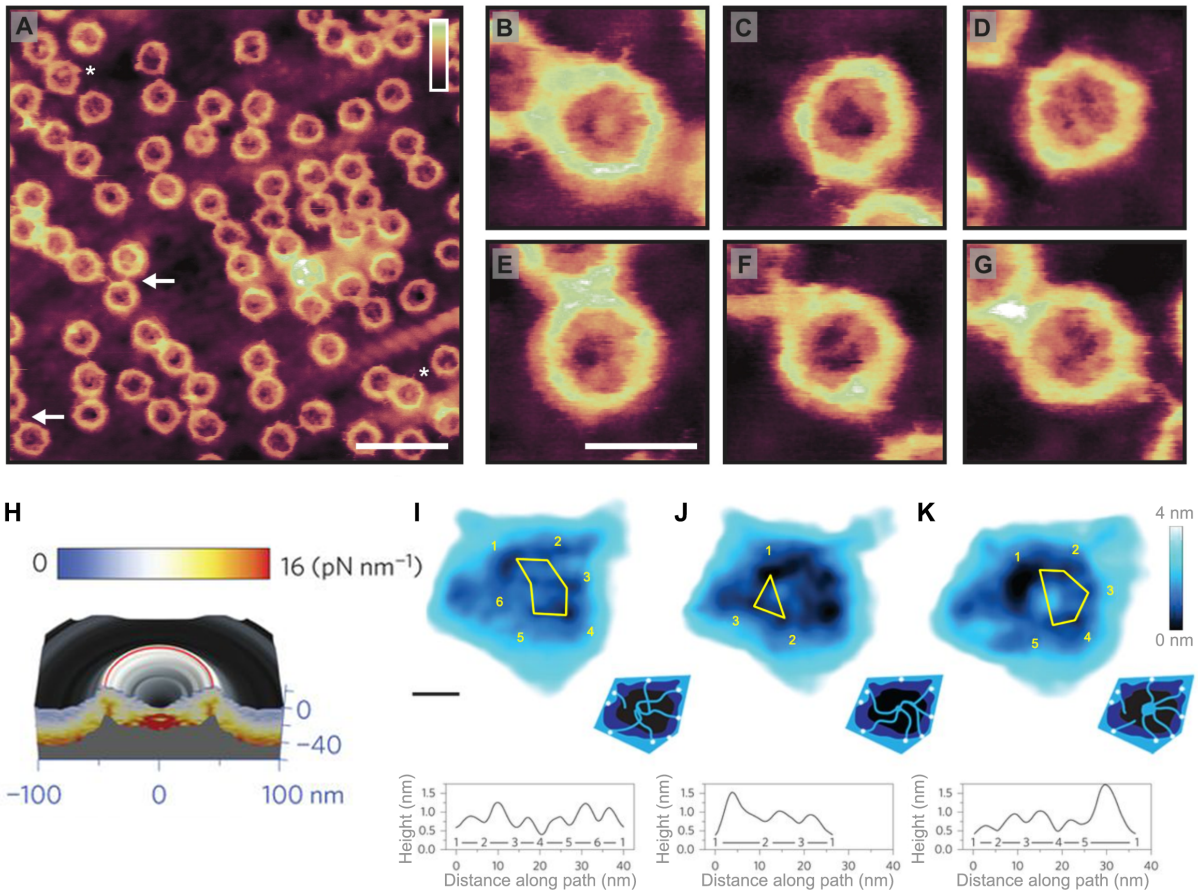


Figure 1.4: **Atomic force microscopy studies of native *Xenopus laevis* NPCs** A) An AFM topographic image of the nuclear envelope viewed from the cytoplasmic side. White asteriks denote lumens filled with central condensates and arrows indicate where two NPCs are connected to one another. (B-G) Magnifications of individual NPCs highlighting variability in the appearance of the central lumen. H) Rotationally symmetrised surface of a single NPC obtained from force spectroscopy measurements. Increased stiffness is observed in the central of the pore and on the pore scaffold structures. (I-K) HS-AFM images captured at 180 ms per frame of an individual NPC showing intermingling FG-nups as they form transient condensates. The height profiles below correspond to the cross-sectional features encountered along the path marked by a polygon (yellow). Scale bars in (A) 300 nm, (B-G) 100 nm and (I-K) 10 nm. Inset colour scale in top row is 100 nm (A) and 60 nm (B-G). All AFM studies presented here were conducted in physiological buffers. (A-G) adapted from,[34] (H) from[32] and (I-K) from[33]

On acccount of these somewhat contradictory observations, along with structural variability in the central barrier of native NPCs (Figure 1.4B-G),[34] it is difficult to identify the nature of the transport barrier even when probing it as directly as possibly by AFM.

1.2 Building synthetic nuclear pore complexes

Due to the complexity of the cellular environment and disordered nature of the network of FG-nups that reside in the central channel, it is a great challenge to probe selective transport at relevant length and timescales. Moreover, since the NPC is assembled from over 30 different proteins and at any given time may contain a significant amount of NTRs and cargos, it is hard to distinguish and identify, which components are interacting during selective transport. Alternative methods to study the NPC take a bottom up approach, creating biomimetic nanopores for *in vitro* studies.[96] Such platforms enable individual components of the barrier to be studied in isolation to build a comprehensive idea of how structure relates to function in the case of these highly selective nanofilters.[97,98] More generally such platforms may also help to establish new ways to design highly selective nanopores, leading to the design of new devices (e.g. for biosensing, medical diagnostics and molecular filtration).

1.2.1 Modification of solid state nanopores

Nanopores can be classified into two categories, namely 'solid state' and 'biological'. Typically the nanopore perforates an insulating membrane that separates two aqueous reservoirs, one of which contains an analyte of interest. Single molecule translocations can be detected by fluorescence, or more commonly through electrical current readout. In the latter case the reservoirs must contain an electrolyte (typically KCl or NaCl) and a non-polarisable electrode. When a constant electrical potential is applied across the membrane a steady state current is generated as ions are exchanged from one side of the nanopore to the other. The applied potential is optimised to drive charged molecules through the nanopore. Experimentally the current is often measured as a function of time where an increase or decrease in current is observed whilst the analyte is confined in the nanopore.[99]

Solid state nanopores are entirely synthetic and can be fabricated by techniques such as ion beam drilling of thin insulating membranes, laser assisted pulling of glass capillaries or track etching of nanopore arrays. By tailoring nanopore design, i.e., size and material, one can achieve large operational flexibility within these systems.[99] Beam milling techniques

produce individual pores where nanopore size can be tuned with nanometre precision (though this is difficult to achieve for sub-10 nm pore diameters), it remains extremely challenging to chemically modify these pores with molecules that are precisely positioned within the pore architecture.[100] Nevertheless the modification of solid-state nanopores with FG-nups has yielded pores that mimic the NPC's selectivity.

One of the first examples of an artificial NPC mimic was fabricated using polycarbonate membranes perforated by ∼30 nm pores, coated with a monolayer of FG-nups surrounding and partially occluding the pore opening (as is the case in the NPC see Figure 1.5a). Membranes were first coated on one face with a ∼15 nm-thick gold layer to which FG-nups were attached through single carboxy-terminal cysteines. Exposed regions of unfunctionalised gold were subsequently passivated with small PEG-thiol molecules, to avoid any unspecific interactions with the gold substrate. This nanoselective filter allowed the transport of NTRs and NTR•cargo complexes but inhibited the passage similarly sized proteins such as bovine serum albumin (BSA) (see Figure 1.5a). By varying experimental conditions in this biomimetic system, the determinants of selectivity were found to include the passageway diameter and the length of the nanopore region coated with FG-nups, both of which could be adjusted by modifications to the construction of the membrane support.[101]

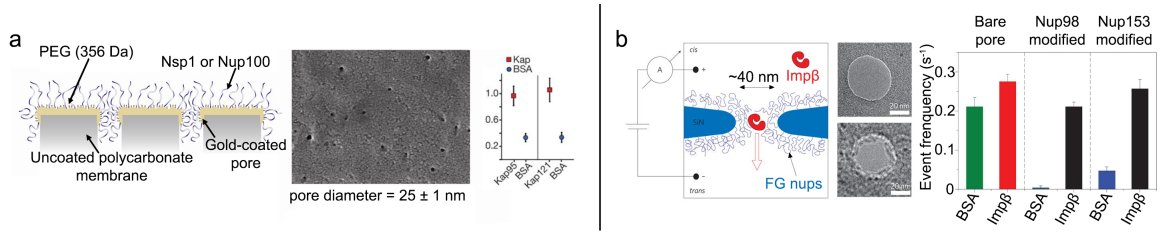


Figure 1.5: **Solid State Biomimetic NPCs as Selective Transport Barriers** a) Gold-coated nanoporous membranes modified with FG-nups as shown schematically and evidenced by SEM. The flux from the translocation of fluorescently tagged proteins across the membrane was much greater for Kap proteins than for a similarly sized non-interacting protein. Figure adapted from.[101] b)A single nanopore coated in FG-Nups as shown schematically and evidenced by TEM with the uncoated(top) and FG-coated(bottom) pores. Single molecule translocations, as measured through transmembrane currents, showed the selective transport of Kaps with respect to unspecific proteins. Figure adapted from.[102]

Cees Dekker's group went on to produce individual nuclear pore complex mimics from

pores milled in silicon nitride membranes, see schematic in Figure 1.5b.[102] By monitoring changes in current across the insulating membrane, the passage of individual molecules translocating through the nanopore could be resolved.[99] In this case pores were modified on both faces of the membrane, as cysteine-terminated nups (Nup98 and Nup153) were crosslinked to amine groups on the surface — the approximate surface coverage was determined as ∼1 nup per 50 nm^2. The modified nanopore demonstrated a high degree of molecular selectivity for the NTR, importin-β, whilst inhibiting the translocation of non-specific proteins. The group later produced a similar mimic modified with the yeast nucleoporin Nsp1 and compared transport selectivity against pores modified with a non-barrier forming Nsp1 mutant (the F residues having been replaced with S residues). In this study they were also able to show selectivity for the passage of Kap95 (the yeast equivalent of importin-β) though Nsp1 coated pores, against a similarly sized non-NTR protein, tcherry (95 and 104 kDa respectively).[40]

Despite technological advancements, it remains challenging to control the exact size and shape of these solid-state nanopores. Moreover, it is nigh impossible to anchor individual molecules at precise locations at the channel walls. By contrast, biological nanopores significantly outperform their solid state counterparts when it comes to the ability to engineer surface functionality.

1.2.2 Designing nanopores using DNA

Biological nanopores are traditionally made by the reconstitution of a membrane spanning protein into a lipid bilayer.[103,104] Although the surface chemistry of protein pores can be precisely engineered,[105,106] they are generally small structures, with only a few examples having a central constriction greater than 2 nm.[107,108]

More recently, 'DNA origami' has evolved as an effective tool to self-assemble and produce well-defined nano-objects, and thus has provided an alternative platform for the production of biological nanopores.[109] The potential of this field dates back to the 1980s,[110] but it was not until 2006 that Paul Rothemund utilised DNA base pairing to design sophisticated nano-structures.[111] The DNA origami method takes a long single scaffold strand of DNA and folds it into a desired shape using hundreds of short staple strands, see Figure

1.6a. Later, the method was extended to build three-dimensional structures formed as pleated layers of helices constrained to a honeycomb lattice, see Figure 1.6d.[112] Although the size of the scaffold strand (M13mp18 genomic DNA,∼7 kb) previously limited the size of DNA origami structures to ∼5 megadaltons, more recently gigadalton structures have also been realised.[113–116]

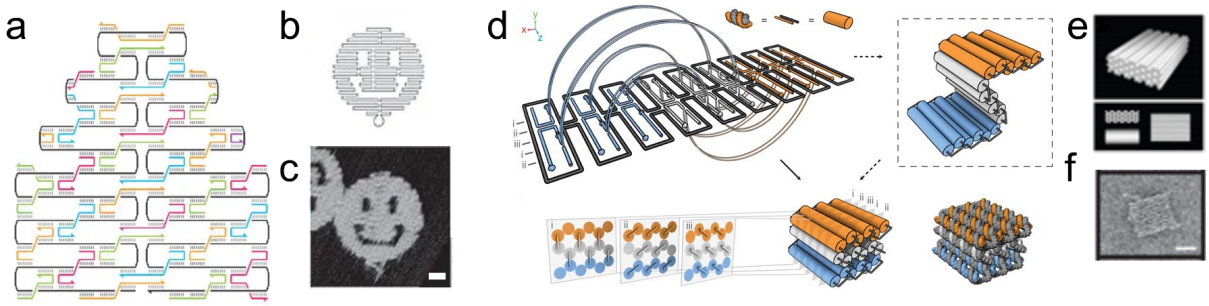


Figure 1.6: **Design of 2D and 3D DNA origami** a) 2D DNA origami using a 7 kb ssDNA template (black) that folds into a predesigned shape directed by short 'staple' strands that from cross-overs between helices. b) design and c) AFM image of a designed smiley face structure. Figure adapted from.[111] d) 3D DNA origami design using double helices comprised of scaffold (grey) and staple strands (orange, white, blue) form an unrolled two-dimensional schematic of the target shape. Phosphate linkages form crossovers between adjacent helices, with staple crossovers bridging different layers shown as semicircular arcs. These linkages cause the structure to assemble into a hexagonal arrangement of helical bundles. e) design and f) TEM image of a monolith structure. Figure adapted from.[112] Scale bars in AFM and TEM images are 20 nm.

Structural design is achieved by matching base sequences of the synthetic staple strands, to hybridise at specific positions on the scaffold strand. This self-assembly technique enables the parallel synthesis of huge numbers of DNA structures in high yield at timescales of less than one day.[117] Furthermore, guest molecules such as gold nanoparticles,[118] proteins[119] and fluorophores[120] can be site-specifically attached to these DNA structures with nanometre precision by incorporating specialised single stranded 'handles'.

DNA origami nanopores can be mounted into solid-state nanopores by the application of an electric field. To aid trapping the structures are deigned with a long DNA tail that is fed into the solid-state devices, see schematic in Figure 1.7a.[121] Once the DNA origami structure is positioned into the nanopore, the translocation of individual dsDNA molecules through the nanopore could also be measured.[121] In addition to nanopores milled into

silicon nitride membranes, DNA origami nanopores can also be mounted onto quartz nanopipettes; although pore size is less well-controlled these devices are much cheaper and quicker to fabriate.[109,122] However, a key challenge for these hybrid platforms is to reduce the leakage currents associated with the formation of a poor seal between the biological and solid-state counterparts.[123] Such leakage currents introduce noise into the current read-out making it difficult to detect single-molecule translocation events.

Alternatively, DNA origami pores have also been inserted into lipid membranes - mimicking nanopores that are ubiquitous in biology. For insertion, the negatively charged DNA must be decorated with an appropriate number of hydrophobic chemical groups (see schematic in Figure 1.7b).[124–126] The largest example of such pores has an inner central diameter of just ∼4 nm, which is an order of magnitude smaller than the inner diameter of the native NPC.[126] The self-assembly of larger DNA origami structures into lipid bilayers is complicated by the ability to incorporate enough hydrophobic moieties to make intertion entropically favourable. Moreover, the decorated structures are also prone to aggregation, which complicates their handling.[127]

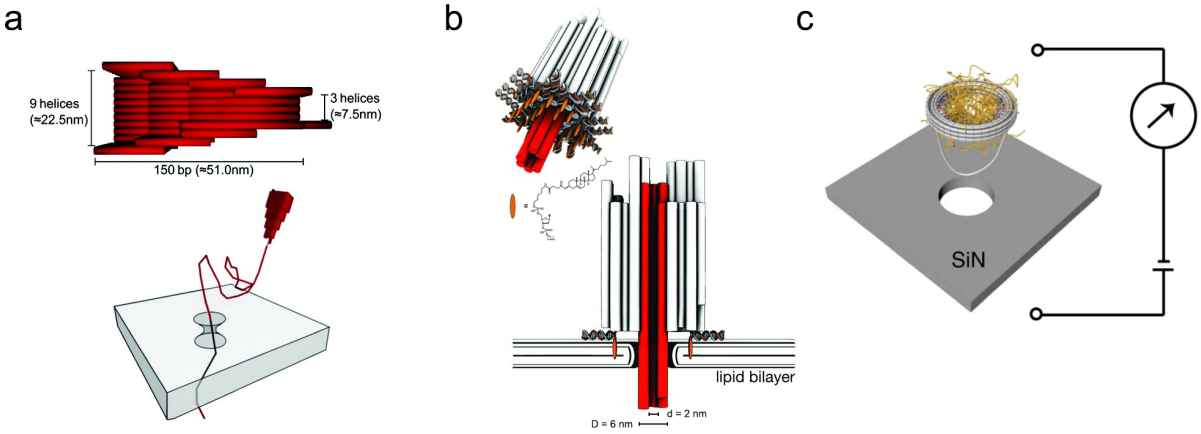


Figure 1.7: **Schematic designs of DNA origami nanopores** a) A DNA origami designed with a long-single stranded tail to allow for docking onto solid-state nanopores (13-18 nm). Figure adapted from.[121] b) DNA origami cylinders modified with chloesterol moieties (shown in orange) allow for insertion into lipid bilayers. Figure adapted from.[124] c) DNA origami nanopores modified with disordered nucleoporins mounted onto solid-state nanopores. Figure adapted from.[41]

In recent work carried out by Ketterer *et al.*, DNA origami structures functionalised with intrinsically disordered proteins were mounted onto solid-state devices (see schematic in

Figure 1.7c). However, unlike modified solid-state nanopores (see discussion in 1.2.1), selectivity for transport was not explicitly shown. It should be noted that this platform was developed at the same time as that developed by Fischer and Shen which is used and discussed in this work.

DNA-nanotechnology offers a powerful platform by which architecturally accurate mimics of the NPC can be built. Furthermore, since one can precisely control the anchoring sites of individual proteins onto the DNA scaffold, the effect of the number and position of FG-nups on the permeability barrier can also be explored.[39,41]

1.3 Concluding Remarks

This thesis describes the development and characterisation of a biomimetic platform to probe the behaviour of FG-nups confined in a nanopore geometry that is similar to the NPC. The overarching aim of this work is to gain insights into the mechanism of nucleocytoplasmic transport. My collaborators at Yale University had established a method to reconstitute select FG-nups from the yeast NPC into a well-defined and tuneable pore geometry, designed using biological building blocks (DNA). However, this system was yet to be characterised at nanometre resolution in physiologically relevant conditions.

In order to study the dynamic organisation of these disordered FG-nups, in solution atomic force microscopy was used as a label free technique capable of biomolecular imaging with sub-nanometre resolution.[128] Preliminary findings using single-molecule total internal reflection fluorescence microscopy (TIRFM) to detect the binding of NTRs in the NPC-mimics are also presented. Since both techniques are surface-based, a significant effort was directed to design and test different surface functionalisation strategies for the in-solution imaging of dsDNA, of which our synthetic NPCs are constructed.[129] Following a description of the materials and methods used in Chapter 2, this surface functionalisation is the focus of Chapter 3.

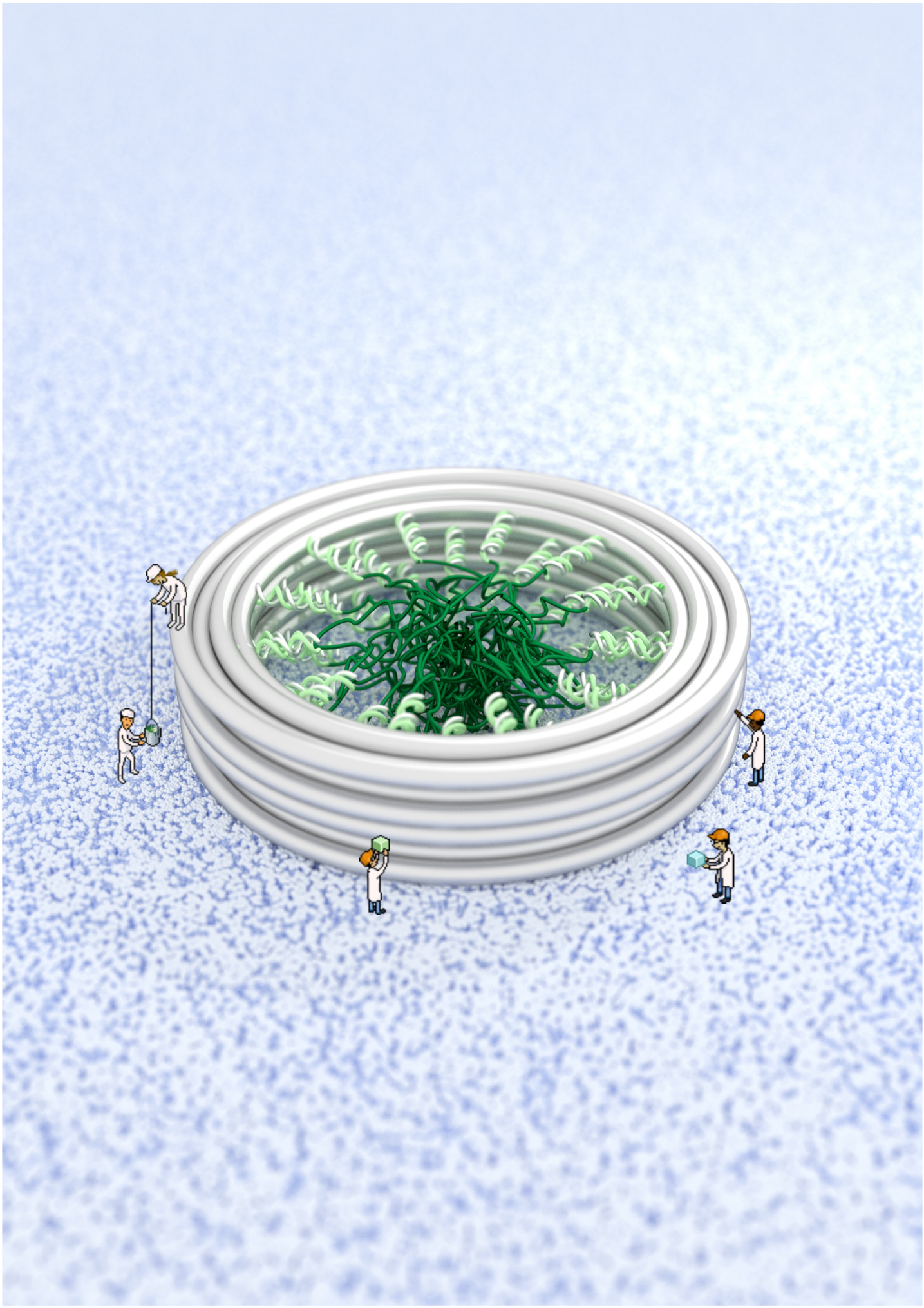
Next, in Chapter 4, the design of the mimetic platform to study interactions between two different FG-nups with different cohesivity is described. Modifications to the the scaffold design are made to anchor the proteins to the inside or outside of the ring, and in different

copy numbers to study the affect of grafting sites and density on FG-nup arrangement.[39]

To probe the dynamic organisation of FG-nups in these NPC mimics, we developed and carried out high-speed AFM analysis, as described in detail in Chapter 5. Pores containing biologically relevant concentrations of FG-nups revealed local and reversible FG-domain condensation, in line with computational simulations.[39,46] Quantification of observed dynamics and their biological significance was further explored by comparison with analogous experiments on native NPCs.[130] Although collective dynamics of FG-nups in the biomimetic pores were unambiguously detected, no significant fluctuations were seen in native NPCs. This difference may be due to the presence of endogenous cargo and NTR molecules, trapping the FG-nups into a given conformation in the *ex vivo* case.

In Chapter 6, the effects of added NTRs to synthetic NPCs are explored, where FG-nups are anchored at different densities within the pore scaffold. AFM data shows importin-β molecules binding to FG-nups, in line with previous observations that a stable pool of NTRs may be intrinsic to the NPC's selective barrier.[8,56,62,65,131] Since, using AFM, super-fast transient interactions that are also predicted to occur between FG-nups and NTRs[59] are unable to be detected, TIRFM is also used as an alternative non-invasive, light-based microscopy technique. Preliminary results using these two techniques although more work is required to verify their biological relevance.

Finally, Chapter 7 summarises the results and provides a brief outlook based on the findings presented in this thesis.



Chapter 2

Materials and methods

2.1 Building NuPODs

All the developmental work to design the DNA origami structures and protein constructs were performed by Patrick Ellis Fisher (P.D.E) and Qi Shen (Q.S), Yale University. They conducted all experiments that led to the design of the NuPODs (NucleoPorins Organised on DNA) and showed me how to perform the experiments myself. In general the purified proteins (see methods section 2.1.2) and DNA origami structures (see methods section 2.1.1) were supplied to me, I then performed the hybridisation to assemble the NuPODs for further analysis which I performed independently.

Molecular dynamics (MD) simulations to compliment the experimental finding on the NuPODs were performed by Luke Davis, UCL. The methods are described in section .

All analysis scripts to further analyse AFM data described in section 2.4.2 and 2.4.3 were written in MATLAB by George Stanley, UCL.

2.1.1 DNA origami scaffold

P.D.E and Q.S used CaDNAno software to design ring structures with an inner diameter of 46 nm to mimic the structure of a native NPC (see Figure 2.1). Firstly, a M13mp18

bacteriophage-derived circular ssDNA strand (8064 nt) and oligonucleotides (Integrated DNA Technologies, IDT) were annealed using a 36 hr 85°C-25°C temperature gradient. The fully assembled rings were purified with rate-zonal centrifugation through a 15-45% glycerol gradient in 1× TE, pH 8.0 (5 mM Tris-Cl, 1 mM EDTA) + 10 mM $MgCl_2$ in a SW 55 swinging bucket rotor (Beckman Coulter) at 50k rpm for 1 hr at 4°C.[132] After collecting fractions, purified structures were buffer exchanged into 1× TE + 10 mM $MgCl_2$ and stored at -20°C prior to use. Concentrations were determined using the absorbance values obtained on a NanoDrop 2000 (Thermo Scientific).

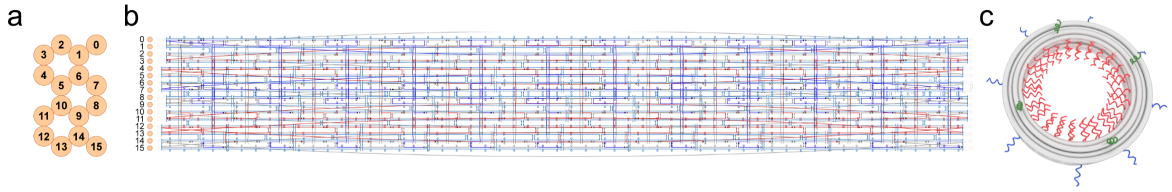


Figure 2.1: **Design of DNA origami rings** a) Cross section through DNA origami ring showing the hexagonal arrangement of helical bundles b) caDNAno design for the 48 inner handle NuPOD and 48 outer handle NuPOD. Scaffold strands are shown in blue, staples for inner handles in red and outer handles in dark blue. c) Schematic of assembled 48 inner handle DNA origami ring. 8 outer ssDNA handles shown in blue for the attachment of fluorescent dyes. 4 handles on the base of the ring shown in green typically hybridised with complementary biotinylated ssDNA. 48 ssDNA inner handles shown in red for the attachment of ssDNA modified proteins, different DNA origami rings have been designed to contain 1, 8, 16, 24, 32 and 48 inner handles. Note handle locations are flipped on the 48 outer handle NuPOD.

2.1.2 Modified Nucleoporins for scaffold attachment

This protocol was developed and performed by P.D.E and Q.S. FG-domains from *S. cerevisiae* Nsp1 (a.a. 2-603) and Nup100 (a.a. 2-610) were cloned into 10×His-MBP-SUMO-TEV-(FG-nup)-Cys constructs in a pET-28a-derived vector (Novagen) and expressed in *E. coli* strain BL21-Gold(DE3) (Agilent)(see Figure 2.2 for the full protein sequence). Cells were grown in LB media at 37°C to an OD≈0.8. Protein expression was induced with 1 mM IPTG for 4-5 hr at 25°C. Cells were harvested by centrifugation and stored at -80°C until use. Cell pellets were resuspended in lysis buffer (1× PBS, 0.5 mM TCEP, 0.1 mM PMSF, 1× Roche complete protease inhibitors), and lysed in a cell disruptor.

Lysate was spun at 35k rpm for 45 min in a 45 Ti rotor (Beckman Coulter) and supernatant was decanted and filtered through a 0.45 μm cellulose acetate membrane. Filtered soluble lysate was applied to a 5 mL HisTrap column (GE) on an ÄKTA system (GE) at 1 mL/min. The column was washed with wash buffer (1× PBS, 0.1% Tween-20, 25 mM imidazole) and eluted on a gradient of elution buffer (1× PBS, 0.1% Tween-20, 500 mM imidazole). Protein concentration was determined by BCA assay (Pierce). Protein fractions were spiked with 10% glycerol, flash frozen in liquid nitrogen, and stored at -80°C until use.

Maleimide-DNA was prepared separately to react with the terminal cysteine on the nucleoporin constructs. 5'-labeled amino-DNA oligonucleotides were purchased from IDT, resuspended in Milli-Q water, and buffer exchanged into 10 mM HEPES, pH 7.4 using a Micro Bio-spin 6 column (Bio-Rad) to remove free amines. Sulfo-SMCC (Pierce or G-Biosciences) was resuspended in double-deionised water (MilliQ, Merck Millipore) at 50°C to a concentration of 22.5 mM. 2 mM sulfo-SMCC was reacted with 200 μM amino-DNA for 3-5.5hr at 37°C in 100 mM HEPES, pH 7.4, and purified by ethanol precipitation. Dried maleimide-DNA pellets were stored at -20°C until use.

For the final protein-DNA conjugation step maleimide-DNA pellets were resuspended in 10 mM HEPES, pH 7.4 and mixed with affinity purified FG-nups in FG-nup buffer (1× PBS, 0.1% Tween-20, 10% glycerol) at a final concentration of ∼250 μM maleimide-DNA and 50 μM FG-nup (5:1). This reaction was incubated at 37°C for 3-5.5hr, then stored at 4°C overnight. Excess DNA was purified away from conjugated proteins using Size Exclusion Chromatography (SEC) on a Superdex Increase 10/300 column (GE) at a flow rate of 0.15 mL/min in FG-nup buffer. Conjugation efficiency was verified by SDS-PAGE using Coomassie or SYPRO Red stain (Thermo Fisher).

2.1.3 Hybridisation of FG-nups to DNA origami

A schematic of the hybridisation procedure developed by P.D.E and Q.S which I used to attach proteins to the DNA scaffold is shown in 2.3. DNA-conjugated FG-nups were added to DNA origami rings at 7.5× excess over the number of handles (e.g. 5 nM origami × 48 handles × 7.5 = 1.8 μM FG-nup-DNA) in 1x PBS, 0.1% Tween-20, 10%

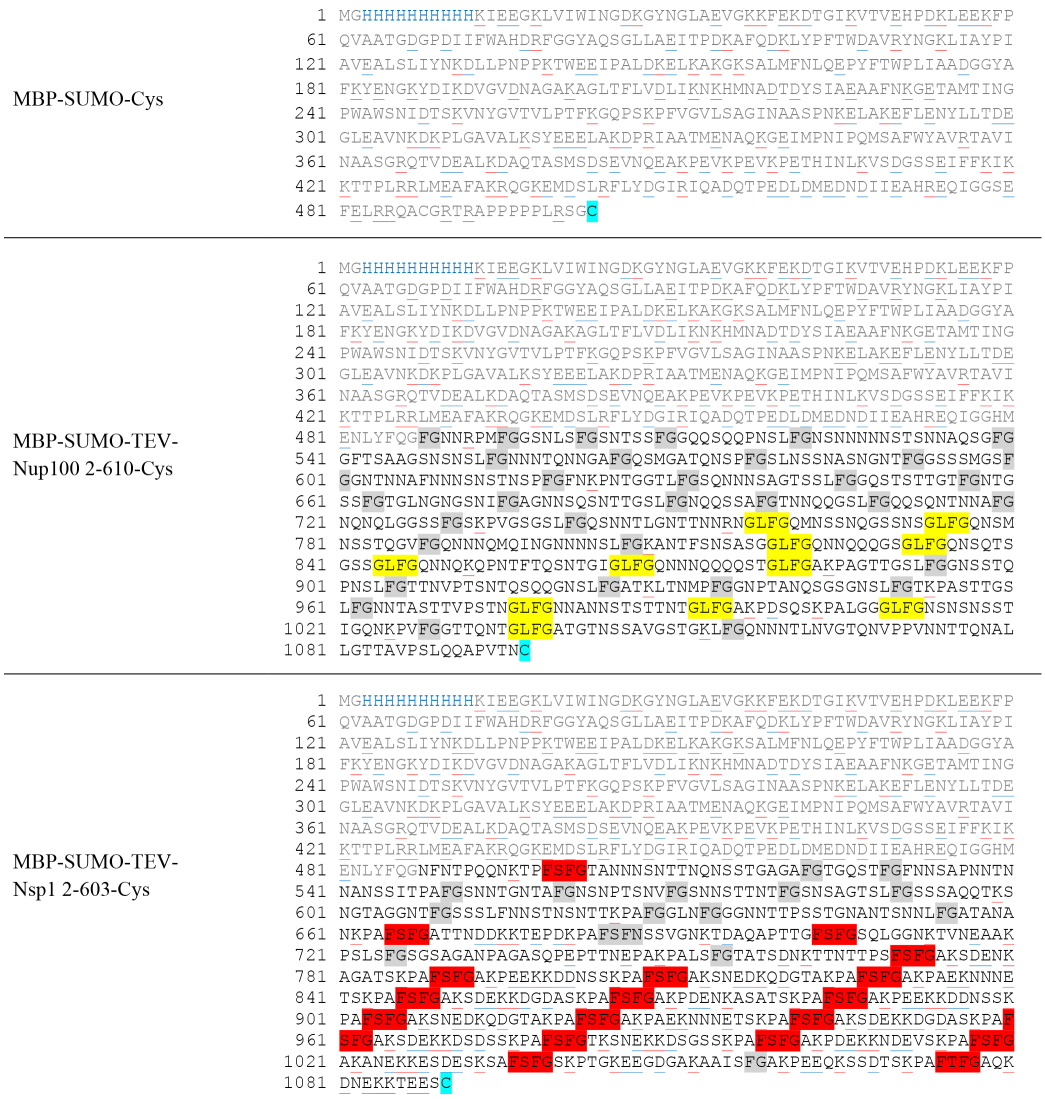


Figure 2.2: **Design of protein constructs** Amino acid sequence of constructs used in this study. FG-domains (Nup100 2-610 and Nsp1 2-603) are in black text, 10× his tag in blue text, and all other features in grey text. Negatively charged residues (D/E) are underlined in blue, positively charged residues (R/K) in red. GLFG repeats are highlighted in yellow, FXFG in red, other FGs in grey (including 2 FXFX repeats in Nsp1). C-terminal cysteine residues are highlighted in cyan.

glycerol, 16 mM $MgCl_2$ buffer and incubated for 3 hr at 37°C. Note that the DNA origami rings could also be decorated with biotin molecules (via 4×handles at the base of the structure) or dye molecules (we chose Alexa Fluor 647 via 8×outer handles), see Figure 2.1c. Modified oligonucleotides 5'-TAGATGGAGTGTGGTGTGAAG-3'-Alexa Fluor 647

and 5'-GAATCGGTCACAGTACAACCG-3'-biotin with HPLC purification were ordered from Integrated DNA Technologies. Hybridisation reactions (55 μl volume) were loaded onto a 15-45% glycerol gradient in the hybridisation buffer (0.62 ml total volume in a 0.8 ml Ultra-Clear tube from Beckman Coulter) to purify the assembled structure from excess protein. After centrifugation in a SW 55 swinging bucket rotor (Beckman Coulter) at 48k rpm for 1 hr at 4°C, 11-12×55 μl fractions were collected from the gradient. The purified product is called a NuPOD (NucleoPorins Organised on DNA) and will be referred to according to the number and type of FG-nup/protein they house. For example a DNA origami ring with 48 copies of Nsp1MBP proteins anchored to the inside will be referred to as 48×MBPNsp1 or 48×MBPNsp1(in). Assembled NuPODs were kept at 4°C for up to 2 weeks for further characterisation.

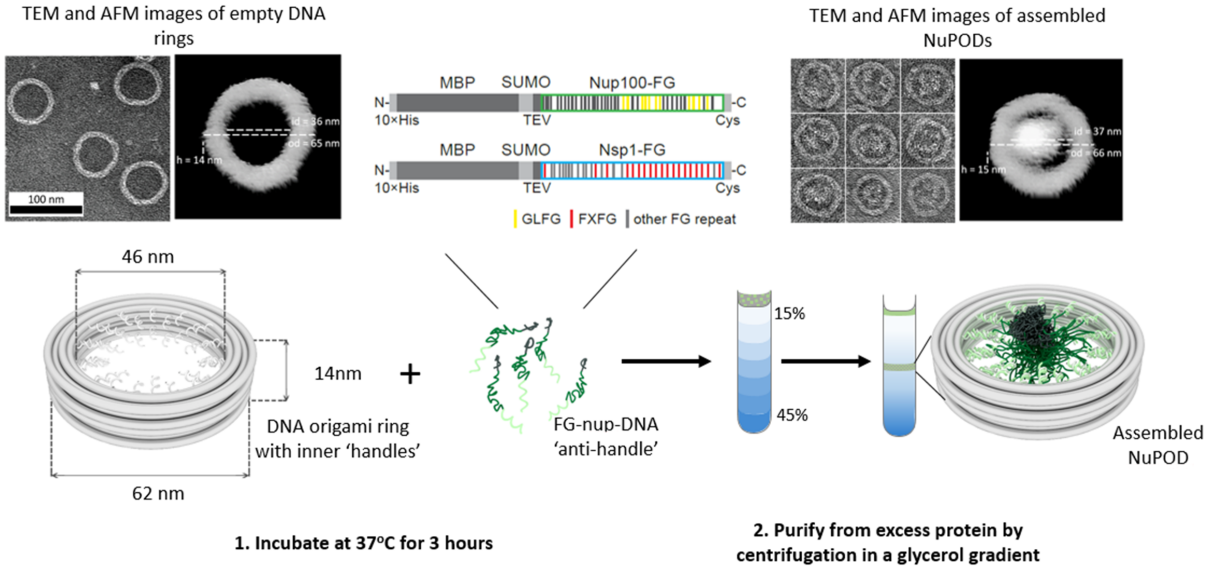


Figure 2.3: **Protocol for assembling NuPODs from DNA origami and DNA-modified FG nucleoporins** DNA origami are incubated with MBP-Nup100-DNA or MBP-Nsp1-DNA for 3 hrs at 37°C. The reaction mixture is then loaded onto a glycerol gradient and spun in a swing bucket rotor at 48,000 rpm (269,000 g) for 1 hr at 4°C, the unbound proteins remain at the top of the gradient whilst the large assembled NuPOD elutes to a separate fraction. AFM and TEM characterisation show the presence of FG-nups in the centre of DNA origami after purification.

2.1.4 Cleavage of MBP tags

Cleavage of the MBP tag was conducted prior to purification of the assembled NuPODs. Conditions necessary for cleavage were developed by me. TEV-protease (Promega) was added to the hybridisation reaction (after being held for 3 hrs at 37°C). Stock TEV-protease was diluted 20× and 1 μl of this was added for every 250 nM of protein. The mixture was held at 4°C for 30 mins and at room temperature for a further 1.5 hrs before purification of excess protein via rate-zonal centrifugation. After purification, partially cleaved free proteins were collected in the early fractions, but the assembled NuPODs collected in later fractions appeared to contain only the cleaved protein (i.e., Nup100 or Nsp1 without the MBP tag, see Chapter 4.2.2 and Figure 4.3).

2.1.5 Gel electrophoresis

For SDS-agarose gel electrophoresis (SDS-AGE), 1.5% agarose gels were made with with 0.05% SDS to elute the protein-conjugated DNA origami structures. Gels were made with and run in running buffer (0.5 × TBE [44.5 mM Tris, 44.5 mM boric acid, 1 mM EDTA], 10 mM $MgCl_2$, 0.05% SDS). Gels were run at 60 V for 3 hr in Thermo Owl B2 system or 38 V for 3.5 hrs in BioRad sub gel GT mini system (the difference in operating voltage was due to the differences in electrode spacing, both yield an applied voltage over distance of ∼2.5 V/cm). SDS was removed by shaking the gel in MilliQ water, typically overnight. For ethidium bromide (EtBr) staining at Yale, gels were then stained with 0.5 μg/ml EtBr and destained for 10 min in MilliQ before scanning with a Typhoon gel scanner (GE Healthcare). For gel staining at UCL gels were stained in 3x GelRed (Biotium) for 45 minutes before detaining in MilliQ for ∼2 hrs and imaged under UV illumination.

For SDS-polyacrylamide gel electrophoresis (SDS-PAGE), bis-Tris, pH 6.5, 8% acrylamide gels were made in house or 4-20% mini-PROTEAN TGX pre-cast gels were purchased from Thermo Fisher. Samples were boiled in Laemmli buffer for 10 mins and run in MOPS-SDS buffer (50 mM Tris, 50 mM MOPS, 1 mM EDTA, 0.1% SDS) or TGS buffer (25 mM Tris, 192 mM glycine, 0.1% SDS) at 200 V for 30 mins-1 hr. Gels were stained using Coomassie or SYPRO Red stain (Thermo Fisher, following manufacturer's instructions) and imaged.

2.1.6 Quantification of FG-nups on NuPODs

P.D.E and Q.S performed western blots to quantify the number of proteins attached to the DNA origami rings. For purified NuPODs, the DNA origami concentration was determined from the band intensity after EtBr staining of the SDS-AGE gel, as compared to known concentrations of empty DNA origami rings. Immunoblots were run with either equivalent NuPOD concentration (equal DNA origami, different amounts of protein) or equal protein concentration (different amounts of DNA origami, equal DNA handle number). SDS-PAGE gels were run as above, and transferred to nitrocellulose membranes at 100 V for 1 hr in transfer buffer (25 mM Tris, 192 mM glycine, 0.1% SDS, 20% methanol). Membranes were washed in TBS-T buffer (25 mM Tris, 150 mM NaCl, 0.05% Tween-20, pH 7.5), labeled with an αPentaHis-HRP conjugate (Qiagen), and developed with standard western blot enhanced chemiluminescence reagents (Pierce). A concentration curve of MBP-Nup100, run on the same blot, was fit in GraphPad Prism to a quadratic curve and was used to interpolate total moles of protein, which was then divided by moles of DNA origami to convert to copy number per NuPOD.

2.1.7 Nuclear transport receptors

A number of transport receptors were used in this study, their purity was confirmed by running an SDS-PAGE gel as shown in Figure 2.4. They were provided from collaborators or purchased as follows. The recombinant human importin-β subunit was purchased from Novoprotein (catalogue number: CE62), and the recombinant human importin-α subunit was purchased from Flarebio, CusAb (Catalogue number: CSB-EP622929HU). Both were re-suspended in import buffer (20 mM Hepes, 110 mM potassium acetate, 5 mM magnesium acetate, 0.5 mM EGTA, pH 7.4). Human NTF2 was supplied by George Stanley (Hoogenboom Lab, UCL). Human importin-β conjugated to the photoconvertible dye, mEos2 (25.8 kDa) was expressed and purified by Roxana Mironska(Lowe lab, UCL) in 50 mM sucrose, 10 mM HEPES pH 7.7, 1.3 mM NaOH, 5 mM DTT, 0.1 mM $CaCl_2$, 100 mM KCl, 1 mM $MgCl_2$. Human importins labelled with synthetic fluorophores (in this work I present data using hsImp-β labelled with Alexa Fluor 594 at position 213), along with RanQ69L (residues 1-180, preloaded and locked with GTP) were provided by Sofya Mikhaleva(Lemke lab, Heidelberg). The importins were in 37 mM Tris, 500 mM

NaCl, 3.8 mM $MgCl_2$ buffer and the truncated RanQ69L in 50 mM Tris, 0.5 M NaCl, 5 mM $MgCl_2$, both buffers contained 20% glycerol and were at pH 7.3. *S.cerevisae* Kap95 was

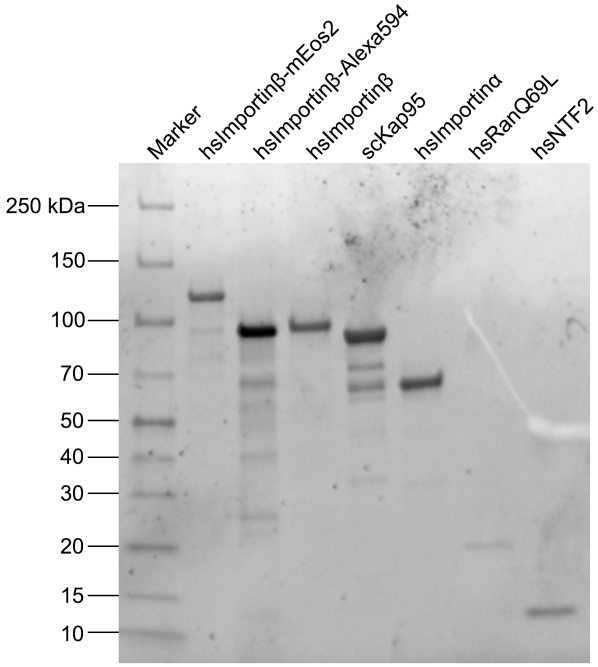


Figure 2.4: **SDS-PAGE gel analysis of NTRs used in this work.** Bands were eluted at positions corresponding their expected molecular weights. Some impurities are seen but the gel was stained with extremely sensitive SYPRO-Red stain (and only ∼1-2 μg is loaded in each well).

kindly provided by Fouzia Bano(Richter lab, The University of Leeds). The protein was supplied in 44 mM Tris-HCl, pH 7.5, 290 mM NaCl, 4.4 mM $MgCl_2$, 10 mM DTT. Monoclonal AntiMBP (NEB) was also used for some control experiments to look at binding to MBP tags on the DNA origami rings.

The proteins were diluted to lower concentrations in their corresponding buffer containing some sucrose or glycerol, flash frozen and aliquoted such that 5 μl of this solution could be added to a 60 μl droplet for AFM imaging to yield the different concentrations for titration experiments. For example 250 nM for a droplet concentration of 20 nM, these aliquots were stored at -80°C before use.

2.2 Surface modification for DNA attachment

To study the NuPODs by single-molecule imaging techniques like AFM and TIRFM, it is imperative that their DNA scaffolds are adhered to a solid support. However, this support should not affect the behaviour of FG-nups or NTRs inside the NuPODs, i.e., care must be taken to minimise undesirable interactions between the surface and biomolecule. This section describe different protocols for the adsorption of dsDNA to a mica substrate used for subsequent nanoscale characterisation. dsDNA in addition to DNA origami nanostructures were used to verify surface-DNA interactions.

2.2.1 DNA molecules

DNA molecules used for AFM imaging experiments to verify surface interactions were supplied as follows. Relaxed plasmid pBR322 DNA (M_w = 4361 bp) was purchased from Inspiralis LTD, UK. 339 bp DNA minicircles were purchased from Twister Biotech, USA. A 672 bp length of DNA, biotinylated at both ends for streptavidin binding assays was prepared by Nicholas Bell (Francis Crick Institute) using PCR amplification of a section of lambda DNA (New England Biolabs) using a forward primer 5'-CGATGTGGTCTCACAG-

-TTTGAGTTCTGGTTCTCG-3' and reverse primer 5'-GGAAGAGGTCTCTTAGC--GGTCAGCTTTCCGTC-3' purchased from Integrated DNA Technologies. Each primer was labelled at its 5' end with a single biotin, thereby resulting in a double-stranded DNA PCR product labelled at both ends with biotin. The PCR product was purified using a QIAquick PCR purification kit (Qiagen). Tetravalent streptavidin was purchased from Sigma Aldrich and monovalent streptavidin was produced by the Howarth lab.[133]

For AGE of dsDNA, a 1% agarose gel in 1× TBE was made and run using the BioRad Wide Mini-Sub Cell GT Electrophoresis System. To check Biotinylated DNA binding to mono and tetravalent DNA 5 μl of pre-incubated samples were mixed with 1 μl of 6× loading dye (Thermo Scientific) before loading onto the agarose gel. The samples were allowed to migrate for 90 minutes (running buffer: 1× TBE; 90 V). The gel was stained as described above using 3× GelRed.

2.2.2 Polymers and salts for electrostatic attachment

For mica functionalisation with poly-L-lysine (PLL) freshly cleaved mica discs (diameter: 5 mm, supplied by Agar Scientific) were covered in 10 μl of aqueous solution containing either 0.01% or 0.001% w/v of the solvated polymer. PLL (M_w = 150,000-300,000 kDa) with approximately one HBr molecule per lysine residue was purchased from Sigma-Aldrich. Mica discs were incubated for 1 minute in a humid chamber with the PLL solution before thoroughly rinsing with double-deionised water (MilliQ, Merck Millipore) and then washing into imaging buffer (10 mM PB for dsDNA and 10 mM PB, 10 mM $MgCl_2$ for DNA origami) to minimise surface contamination. For imaging of dsDNA, an aliquot of 5 μl of 2 nM dsDNA was added to the imaging droplet, whose total volume was maintained at approximately 60 μl . For imaging empty DNA origami rings, these were diluted from the stock to a concentration of approximately 4 nM and 5 μl of this solution was added to the mica. DNA rings with conjugated protein (i.e., assembled NuPODs) were purified as described in section 2.1.3 and then added to mica discs (2-7 μl of the fraction containing NuPODs at an approximate concentration of 1-5 nM).

2.2.3 Lipid membrane preparation for AFM imaging

The preparation of supported lipid bilayers (SLBs) mostly followed procedures described elsewhere.[134] 1,2-dihexadecanoyl-sn-glycero-3-phosphocholine (DPPC; zwitterionic head group) and dimethyldioctadecylammonium Bromide Salt (DDAB; cationic head group) were purchased from Avanti Polar Lipids. The lipids were dissolved in chloroform and mixed in a variety of molar ratios afford different degrees of positive charge on the resultant bilayer. Next, the solvent was slowly evaporated by passing a steady stream of nitrogen in a fume hood for 1 hr and often also then placing under vacuum for at least 4 hr. The dry lipid film was resuspended in MilliQ water to a concentration of 1 mg/ml and was transferred to bath sonicator, maintained 15°C above the gel-liquid transition temperature (41°C and 45°C for DPPC and DDAB, respectively[135,136]) of the constituent lipids. The large multilamellar vesicles were disrupted by 15 min sonication treatments at frequencies between 37 and 80 kHz. The solution containing the lipid dispersion was loaded into an Avanti mini-extruder kit (Avanti Polar Lipids) and kept above the gel-liquid transition temperature of the lipids at all times. The lipid solution was forced

through a polycarbonate filter (GE Healthcare Lifesciences, Buckinghamshire, UK) with a 100 nm nominal pore diameter and the extrusion process repeated at least 20 times to yield small unilamellar vesicles.

2 μl of the small unilamellar vesicles (prepared as described above) along with 1 μl 1 M $MgCl_2$, 1 μl 1 M $CaCl_2$ and 16 μl of MilliQ water were deposited onto a freshly cleaved mica disc. The disc was placed in a humid chamber and heated to 65^{o}C for 10 minutes before slowly cooling to room temperature over 20 minutes. This process induced vesicle rupture and yielded a positively charged, gel-phase SLB. Excess vesicles in the supernatant were removed by rinsing first with water and then exchanged with buffer (10 mM Tris, 1 mM EDTA, pH 7.4 for dsDNA minicircles and 10 mM PB, 26 mM $MgCl_2$ pH 7.0 for NuPODs). The rinsing process was gently repeated five to ten times to ensure a clean and uniform surface before addition of DNA structures. For dsDNA, 339 bp DNA minicircles (2 μl of a 7.8 ng/ml solution) were added to the $\sim$60 μl droplet. For imaging of DNA origami or assembled NuPODs, 2-7 μl of 1-5 nM solution was added.

2.2.4 PEGylated surfaces to minimise non-specific protein adhesion

Block copolymers poly(L-lysine hydrochloride)-block-methoxy-poly(ethylene glycol)(PLL_x-*b*-PEG_y) with varying degrees of polymerisation of the poly-L-lysine and polyethylene glycol blocks were purchased as lyophilised powders from Alamanda polymers. The polymers used for this study were PLL_{10}-PEG_{22}, PLL_{10}-PEG_{113}, PLL_{100}-PEG_{113} and PLL_{10}-PEG_{454} where the subscript refers to the degree of polymerisation, i.e., the number of monomer repeats. For the preparation of copolymer films, freshly cleaved mica discs (diameter: 5 mm) were covered in 10 μl of solution comprising only PLL_x-*b*-PEG_y (1 mg/ml in MilliQ water) or a mixture of 5 μl of the PLL_x-*b*-PEG_y solution and 5 μl $PLL_{1000-2000}$ (0.01% w/v). Mica discs were incubated with these solutions for 45 minutes in a humid environment, before washing 5 times with MilliQ water and 5 times with imaging buffer (10 mM phosphate buffer pH 7.4 with additional $MgCl_2$ at 10 mM for DNA origami structures). 5 μl of DNA plasmid (1.5 ng/μl), 3 μl biotinylated DNA (3.5 nM) or 2-7 μl of 1-5 nM DNA origami was immediately added to the disc and allowed to equilibrate for approximately 10 minutes prior to imaging.

2.3 Atomic force microscopy

Atomic force microscopy is a scanning probe microscopy technique that raster scans a sharp tip mounted at the end of a flexible cantilever over the surface of a sample, see Figure 2.5. Lateral drag forces that are exerted by this raster scanning can be minimised using alternate contact (AC) modes, where the vertical tip-sample distance is modulated whilst scanning. The movement of the probe or the sample is controlled by a piezoelectric scanner. The interaction force between the tip and sample is modulated by the distance between them. As the cantilever presses into the sample it is deflected. The is typically detected via a laser that reflects off the back of the flexible cantilever and is recorded on a position-sensitive detector. The deflection of the laser on the photodiode is fed back into the feedback loop so that the probe remains in contact with the sample and records the height changes of the sample to build a topographical image. By monitoring the interaction forces between the tip and the sample AFM can be used not only to quantify the height with high accuracy (z axis on the order of Ångströms in certain conditions), but also to look at mechanical deformation of the sample, or derive its elastic modulus and energy dissipation.[128,137]

All AFM measurements were performed in liquid on either a Multimode 8 with 'E' scanner or a FastScan Bio AFM system (Bruker, Santa Barbara, CA). The former operates by scanning of the sample where the FastScan uses a tip-based scanner scanning the tip with respect to the sample. Both AFMs were isolated from sources of vibrational noise by placement upon an anti-vibration table, modulated by a bed of compressed air. Additional acoustic isolation for the FastScan was achieved by placement inside an insulated hood. For imaging using the Mulitmode 8 and sometimes with the FastScan, Biolever mini (Olympus, Tokyo, Japan) cantilevers with typical measured parameters of; resonance frequency 25 kHz in water, and spring constant 0.1 Nm^{-1} were used. For higher speed imaging on the FastScan Bio AFM, miniturised FastScan D cantilevers (Bruker) were used, with a resonance frequency of ∼110 kHz in water and a nominal spring constant of 0.25 Nm^{-1}.

Biological samples were deposited onto cleaved mica disks prior to imaging in liquid (see detailed descriptions in previous section 2.2). The mica disks were glued (with Araldite® rapid two-part epoxy) to magnetic stainless steel sample disks (Agar Scientific) covered

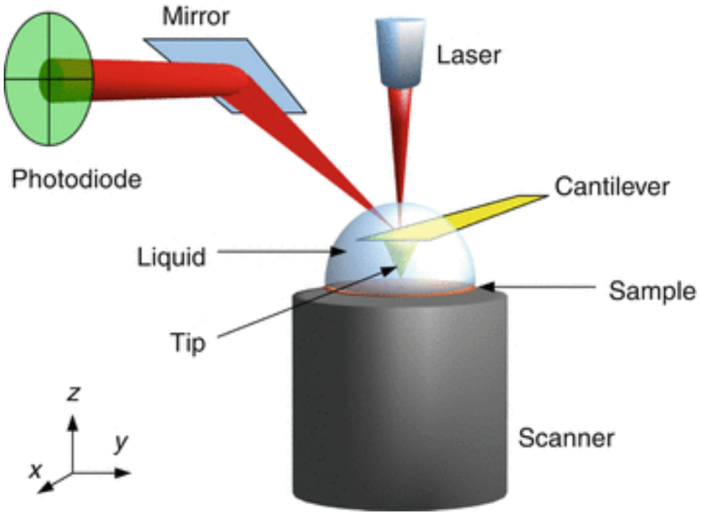


Figure 2.5: **Schematic setup of an AFM for imaging in liquid** The sample for imaging is hydrated in a liquid droplet and mounted on a magnetic sample disc and placed on a stage. The setup here shows a tube scanner as in the Multimode AFM system (Bruker, Santa Barbara, CA). The AFM probe is lowered into a droplet and a laser aligned on the back of the cantilever onto a photodiode detector, the signal of which is fed into a feedback loop. Figure reproduced from.[138]

in hydrophobic Teflon (Bytac®, Sigma-Aldrich) to avoid droplet spillage. The sample was then placed on the sample stage and held in place via magnetic attachment. Imaging buffer was also added to the AFM tip prior to lowering onto the sample to ensure adequate hydration. Between samples the AFM tip holder and tips were thoroughly cleaned in detergent, MilliQ water and isopropanol.

2.3.1 Tapping mode imaging

In conventional tapping mode the cantilever oscillates near its resonance frequency (driven by a piezoelectric actuator, here acoustically although excitation by light and magnetic waves is also possible[139,140]). The tip then intermittently touches the sample at the end of its downward movement. In close proximity to the sample surface, the interactions between tip and sample change both the cantilever amplitude and resonance frequency allowing them to be used as feedback parameters. In liquid, although the tip-sample

interaction is unaffected by capillary forces as present in ambient conditions (air), the cantilever resonance is highly dampened by hydrodynamic interactions. This dampening reduces the quality factor, Q of the cantilever making it less sensitive to small changes in amplitude. Related to this lowered quality factor, it is common that cantilever actuation also drives excitations in the fluid cell/cantilever holder that results in a convoluted excitation spectrum often referred to as a 'forest of peaks'.[141] The piezo-acoustic actuation employed by the FastScan suffers from this problem, the peaks shifting during the course of the measurement as the overall mass and geometry of the fluid cell changes due to liquid evaporation. Care must therefore be taken to re-optimise drive frequency as imaging quality deteriorates. Another disadvantage is that it is not trivial to accurately quantify the tip-sample interaction from changes in the cantilever oscillation, given the high hydrodynamic damping in solution.[128]

Material contrast can be achieved by recording the phase shift of the cantilever oscillation while imaging. That is the difference between the phase angle of the excitation signal and the phase angle of the cantilever deflection. Differences in surface properties of the material can cause a change in the phase of the oscillation, thereby affecting the phase lag. Phase lag images are not shown in this work although contrast was observed whilst imaging, where the phase lag is greater for 'softer' materials.

Using miniaturised cantilevers with oscillation frequencies in the kiloHertz to megaHertz range, it is possible to acquire images at several frames per second using tapping mode (providing the instrumentation support this speed of data acquisition). For this work all tapping mode imaging was carried out on the FastScan Bio using FastScan Ds (frequency $\sim$110 kHz). The force applied to the sample was minimised by setting the highest possible amplitude set-point voltage at which the pores could be tracked with sufficient accuracy. This was typically above 85% of free oscillation just close to the sample surface.

2.3.2 Force-distance curve imaging

By driving the cantilever at frequencies well below its resonance frequency and continuously detecting the cantilever deflection, one can measure the force as a function of tip-sample distance. In so-called PeakForce tapping (PF QNM, Bruker, Santa Barbara,

CA) mode, this is implemented by driving the cantilever in a sinusodial manner in the low kilo Hertz range.[142] The maximum force is monitored by the maximum deflection of the cantilever during the oscillation. A feedback loop adjust the sample (or tip) position to keep this maximum force constant to a defined setpoint during imaging. This allows imaging at forces as low as ∼10 pN.[143] Both the height at maximum indentation and a force curve are recorded; whilst the former is used to generate a topographic image the latter can be used to extract information about the material properties such as the stiffness.

For imaging in PeakForce Tapping mode, the amplitude was adjusted in line with the feature heights. Typically an amplitude of 10 nm was used for imaging dsDNA and 40 nm for imaging NuPODs. An operating frequency of 2 or 4 kHz was used for imaging on the Multimode 8, and 2 or 8 kHz for imaging on the FastScan.

2.3.3 Quantitative high-speed imaging of AFM of NuPODs

In AFM measurements of whole NuPODs recorded on the second to minute timescale, fluctuations of FG-nups within the central channel were observed. The imaging speed (operated in tapping mode) was primarily limited by the propensity for the NuPODs to become dislodged from the substrate at high tip velocities. By detecting individual scan lines instead of full images as a function of time, the temporal resolution can be enhanced by 2-3 orders of magnitude. Thereby allowing monitoring of fluctuations that occur on the millisecond timescale, (as reportedly observed by others when imaging native NPCs[33,95]). For these experiments tapping mode AFM was performed using a Dimension FastScan (Bruker) (see Methods section 2.3.1) and a FastScan-D cantilever (Bruker; nominal resonance frequency (f_0) in water = 110 kHz, nominal k = 0.25 Nm^{-1}, nominal tip radius = 5 nm, and tip half opening angle of $\leq 20°$). Briefly, the sample was prepared as described in detail in Chapter 4.2.4 on a mica disc coated in a positively charged supported lipid bilayer (3:1, DPPC:DDAB). The sample was setup on the AFM with both the sample and cantilever immersed in approximately 60 μl of solution. For single-line recordings individual NuPODs were centred in the field of view and the scan size reduced to 120×120 nm with 128×128 pixels. As the tip rastered over the centre of the pore, the slow scan axis was disabled such that the same scan line could be recorded as a function of time,

see Figure 5.2 in Chapter 5.2.1. The scan speed was systematically increased from 5 Hz to 10 Hz to 20 Hz (200, 100 and 50 ms per scan line respectively).

This data was later compared with recordings acquired on native NPCs from *Xenopus laevis* oocytes. Experiments on native nuclear envelopes were conducted by George Stanley (UCL) and the methods are described in full elsewhere.[34,130] Briefly the nuclei were mechanically isolated from cells, and the nuclear envelopes spread across a PLL-coated glass coverslip. AFM imaging was conducted in an import buffer (20 mM Hepes, 110 mM potassium acetate, 5 mM magnesium acetate, 0.5 mM EGTA, pH 7.4). For single-line recordings a 300×300 nm image at 304 samples/line of a single NPC was captured to ensure capture of background nuclear envelope as well as the NPC. As before, the slow scan axis was disabled as the tip rastered over the centre of the NPC to generate kymographs. All data collected in this way (i.e. slow scan disabled imaging of NuPODs and native NPCs) was further analysed by George Stanley (UCL) using the custom scripts described in section 2.4.2.

2.4 AFM image analysis

2.4.1 Image processing

All AFM images presented in this thesis were at minimum processed using first-order line-by-line flattening and zeroth order plane fitting to remove sample tilt in the Nanoscope Analysis software (Bruker AXS, CA, USA) or Gwyddion. Colour scales we chosen and adjusted to give the most contrast between features.

2.4.2 Fast-scanning of FG-nups: autocorrelation analysis

To provide information on the timescale of FG-nup fluctuations, an analysis code was developed by George Stanley (UCL) that quantifies the correlation of pixel height as a function of time-lag. The script was written in MATLAB and a full version has been deposited online, https://doi.org/10.5281/zenodo.3565763. Results from this analysis are described in Chapter 5.

The analysis script runs as follows: (1) A sequence of kymographs (generated by disabling the AFM slow scan axis) recorded from one pore (NuPOD or NPC), at a given line rate, was loaded into MATLAB, and the kymograph width (nm), samples/line, and line rate (Hz) were entered manually. A first-order plane background subtraction was applied to each kymograph individually to flatten the data with respect to the background (either nuclear envelope or lipid bilayer). If the 'Down Scan Only' feature during data capture was not enabled, the capture direction of the first image must be entered (up or down). All images captured in the 'up' direction are then vertically flipped such that the traces are in chronological order. If the Down Scan Only feature was enabled, this step is skipped. All images are then vertically concatenated. This gives one large matrix with position along the x-axis (fast-scan axis), and time along the y (slow-scan axis). This is called a kymograph.

(2) Even when using an AFM system with a closed-loop scanner (here: Dimension FastScan, Bruker), in which the sample position is continuously verified to $\sim$1 nm accuracy, lateral drift still occurs due to scanner hysteresis and thermal equilibration. In order to ensure the same point in space is referred to for future analysis, a drift correction protocol was implemented by shifting the data with respect to static features (the outer edges of the pore scaffold). The concatenated kymograph was shown as a figure and the two outer edges of the scaffold (for either the NuPOD or NPC) were selected manually. Windows (usually 10-20 nm in width) of kymograph data, centered around the two selected points, were cropped. The height data within these two windows were averaged to create a template. Each line (fast-scan axis) within the kymograph, at the same window positions, was then compared with the template using the sum of absolute differences (SAD) method, that is, the sum of absolute difference in height values between all relevant pixels was calculated, with a lower SAD score meaning greater correlation. Each line (or height array) was shifted in 1 nm intervals to both the left and right by half the window width. The SAD score was calculated at each position. Whichever position gave the lowest SAD score was considered to have the best correlation with the template, and the height array was moved to this position. If shifted, however, this resulted in missing data points at one end of the height array (if a row was shifted 3 nm to the left, for example, there would be 3 nm of missing data points at the extreme right end of the array). As it is assumed that this region is either background lipid bilayer (for NuPODs) or background nuclear envelope (for NPCs), these pixels were filled in with random noise

between the values of –1 and 1 nm. This process is repeated for each row of height data to produce the drift-corrected kymograph in Figure 2.6. Experimental drift for the NuPODs was typically less than 10 nm over the course of 100 seconds (see Figure 2.6E) and was greater than observed for native NPCs (compare with Figure 2.6). This can be in part attributed to some movement of the NuPOD's DNA origami scaffold on top of the bilayer (adhered via electrostatic atraction) whereas native NPC are stably embedded into a double lipid bilayer.

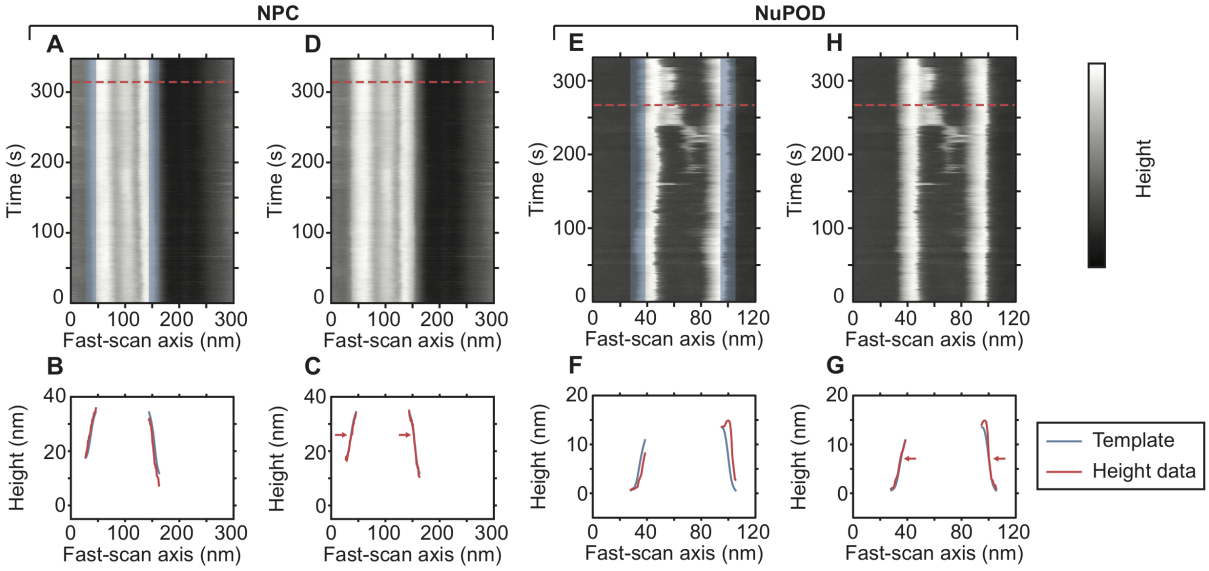


Figure 2.6: **Drift correction of kymographs.** (A) A kymograph of the cytoplasmic side of an NPC (scanned at 5 Hz). The outer edges of the pore scaffold are selected, and windows (typically of ∼20 nm width) centred around these areas are cropped (blue, transparent regions). These regions are height-averaged to produce a template (B and C, blue lines). Each line in the kymograph is then compared against this template within the window regions (red lines, B, corresponding to the red-dashed line in A). The data is then shifted in 1 nm intervals to both the left and right, for ∼10 nm, and the sum of absolute difference of height values (SAD score) is calculated at each position. Whichever shift results in the best height correlation (or minimum SAD score), is used to correct that particular line (C). (D) This operation is performed on every line in the kymograph to correct for lateral drift in our experiments. (E-H) Same as for (A-D) but demonstrated on a NuPOD containing 48 Nsp1 molecules.

(3) With the kymographs corrected for experimental drift, we can assess how a particular position in/near the pore changes as a function of time. To this end, the autocorrelation

function, $R(\tau)$, was defined and next applied to each position in the kymograph:

$$R(\tau) = R(m\Delta t) \equiv R_m = \frac{1}{N-m} \sum_{n=1}^{N-m} \left[(z_n - \overline{z}) \, (z_{n+m} - \overline{z}) \right] , \tag{2.1}$$

where m and n refer to line numbers in the kymograph, N is the total number of scan lines in the kymograph, and Δt is time between consecutive scan lines. z_n denotes the pixel height (in nm) of a given position as a function of time ($n\Delta t$), and $\overline{z}$ denotes the average pixel height at that position. In brief, $R(\tau)$ quantifies the similarity in height values for a given pixel (in nm^2) at a certain time-lag, τ. It can detect a periodic signal shrouded by noise and the persistence time of stochastically fluctuating signals (see Figure 2.7 for the $R(\tau)$ outputs from various simulated fluctuations).

It should be noted that it is possible to normalise $R(\tau)$ values by dividing by the pixel'd variance (σ^2). This would give $R(\tau)$ values between –1 and 1, at each time-lag, for each pixel, in which –1 is perfect anti-correlation and 1 is perfect correlation. However, to facilitate a quantitative comparison between experiments (in which all will have different σ^2 values for each pixel), this was not done. The $R(\tau)$ values were calculated for each pixel for $\tau = n\Delta t$ to $\tau = 100$ s (or until the maximum time of the kymograph if recorded for <100 s), in increments of $n\Delta t$. The results from the autocorrelation analysis are then plotted as an intensity map as a function of both position in the x-axis (fast-scan axis) and time-lag.

To average autocorrelation heatmaps, at a given line rate, from several NuPODs, the heatmaps must be aligned spatially. This was done by selecting the two inside edges of the scaffold structure as seen in the concomitant kymograph (akin to the drift correction routine, in which both outer edges are selected). These two values were used to define the center of the kymograph (and thereby the center of their autocorrelation heatmaps). All autocorrelation heatmaps were then aligned by this point, and the $R(\tau)$ values 15 nm either side of this position were cropped. All heatmaps to be averaged were then scaled by their overall time contribution and then summed. The data were then binned as a function of radial position and averaged to produce an autocorrelation heatmap as a function of radius, with 0 nm being the center of the channel and 15 nm approaching the inner-wall of the scaffold as shown in Figure 5.5 in Chapter 5.2.2.

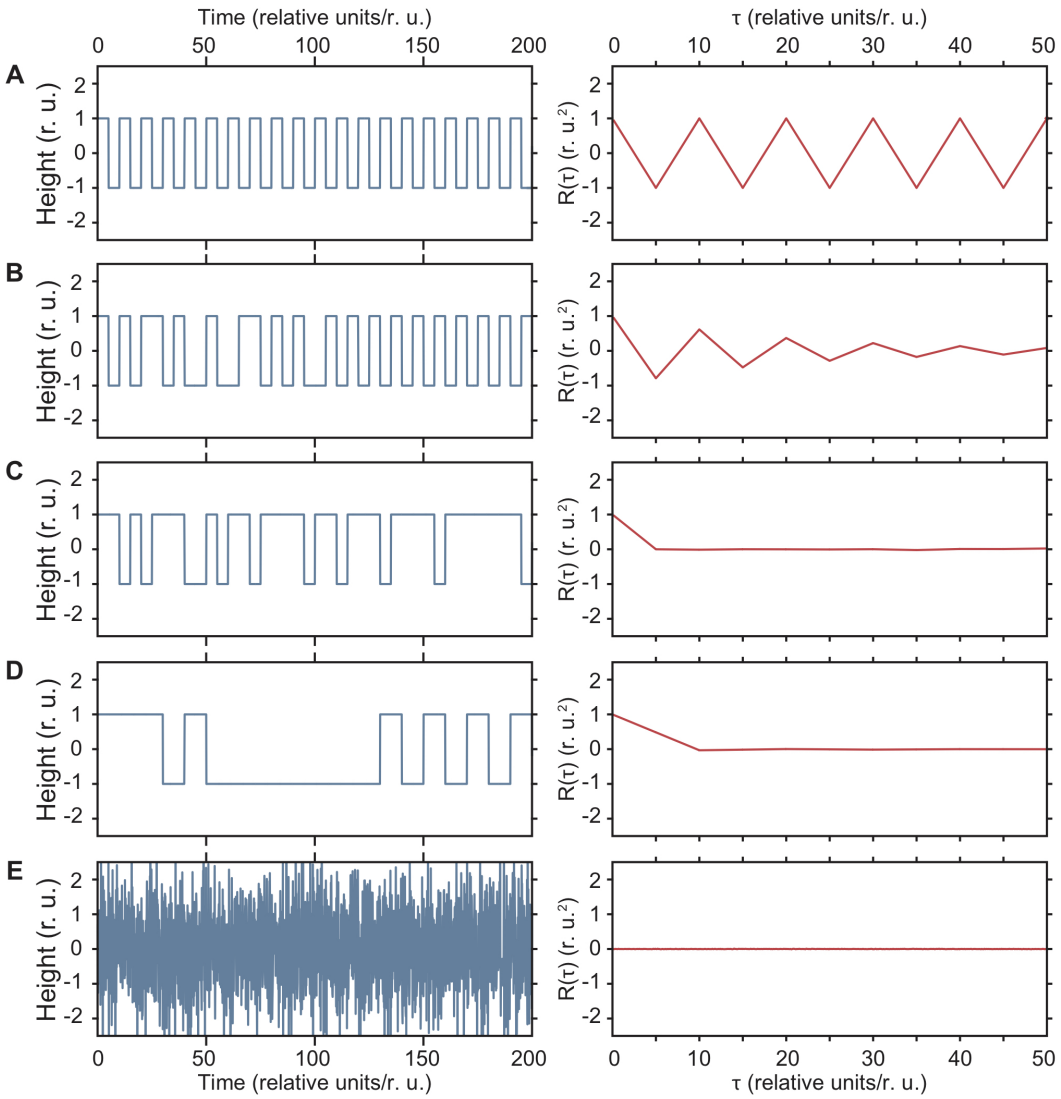


Figure 2.7: **Interpreting the autocorrelation factor $R(\tau)$.** (A) A simulated step function that changes between the values –1 and 1 at intervals of 5, therefore having a period of 10 (left panel), and calculated $R(\tau)$ (right panel). $R(\tau)$ is maximum for lag times, τ, that match integer multiples of the period of the original signal (i.e., for $\tau = 0$, 10, 20, etc.), indicating high correlation. By contrast, for half-integer multiples of the period ($\tau = 5$, 15, 25, etc.), there is maximum anti-correlation. (B and C) Increased randomness in this function reduces long-scale autocorrelation, here shown when the flipping probability at each interval is reduced from 100% to 90% (B) and 50% (C). In the case of (C), no correlation is observed beyond a single half-period. (D) Same as (C), but the interval length is increased from 5 to 10. Now correlation is observed up until $\tau = 10$ instead of $\tau = 5$. (E) For white noise, $R(\tau)$ is zero.

2.4.3 Cross-correlation averaging of NuPODs before and after the addition of NTRs

To quantify and compare the change in height of the NuPOD's central channel upon the addition of NTRs and other proteins to the imaging solution, George Stanley wrote the following analysis protocol. The protocol crops and extracts height data from each DNA origami ring identified in a given AFM image. In this way the height at the centre of the NuPOD can be compared before and after the addition of transport receptors and used as a measure of binding. Note that this data is acquired on NuPODs adsorbed onto PLL_{10}-*b*-PEG_{113} coated mica, not SLBs as before. When adsorbed onto this surface the FG-nups (or MBP) moieties are repelled and therefore undetectable by the AFM tip. The NuPODs only appear 'filled' when they are cross-linked by gluteraldehyde (see discussion in 6.2.1 and Figure 6.2) or after the addition of NTRs (or AntiMBP) which bind to the FG-nups (or MBPs). George Stanley wrote the script which I then used to process all the data.

The first step in the script loads the image file into MATLAB, the width of the image (fast-scan axis) is entered manually in nm (typically 6000 nm, recorded with 2000 pixels per line). A 1^{st} order plane flattening is applied to the image. Circles are found within the image using the 'imfindcircles' function to identify all NuPODs. The function uses a sensitivity parameter which measures how circular an object must be to be detected and must optimised to best find all pores. Objects were also disregarded if they were less than 50 nm in outer diameter. An example of an image processed using this function is shown in Figure 2.8a and b). All identified NuPODs are cropped (100 nm$\times$100 nm), another 1^{st} order plane flattening is applied to each NuPOD individually. This both straightens each pore individually and sets them all against the same background height. The centre of each pore is located and averaged height data is collected in concentric bins that radiate out in 4 nm intervals.

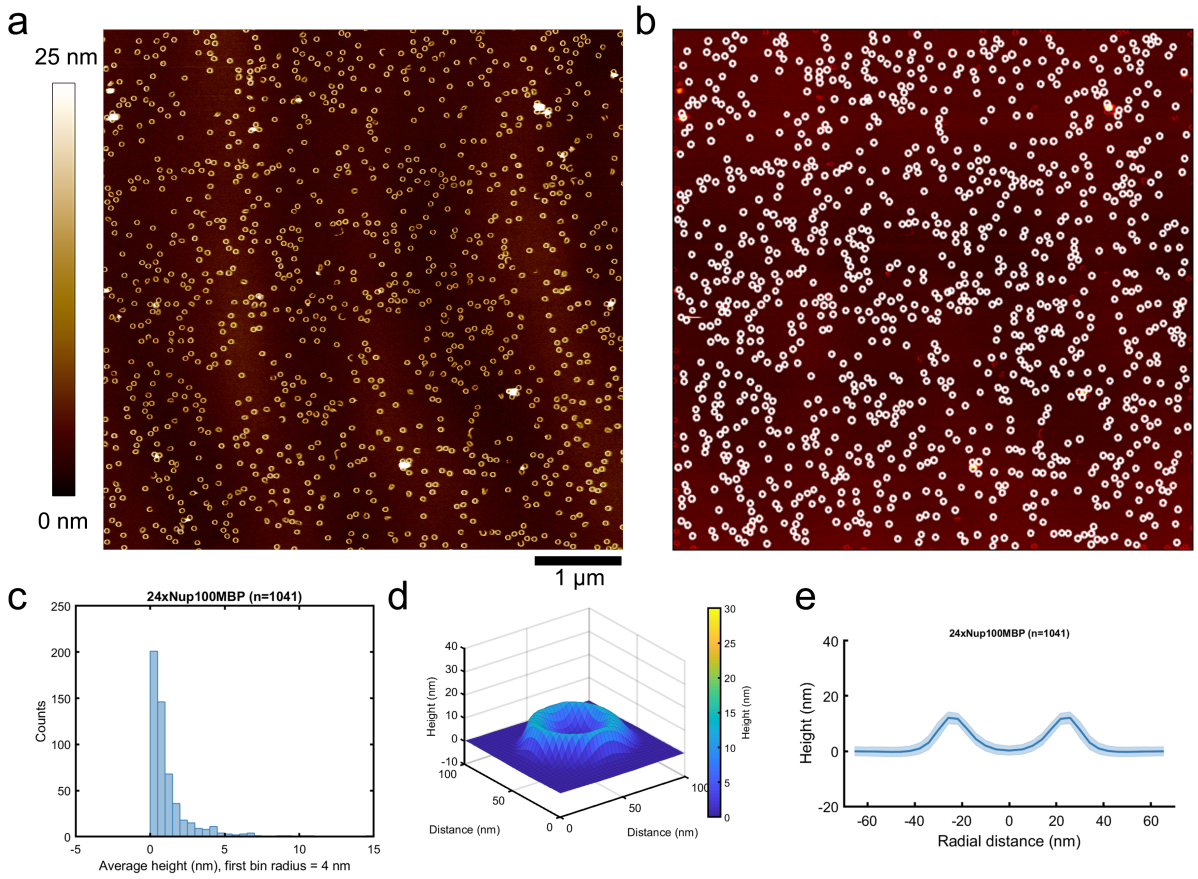


Figure 2.8: **Analysis protocol for calculating NuPOD height in central channel.** (a) An image loaded into MATLAB (here image of 24×MBPNup100 NuPOD on PLL-*b*-PEG coated mica). (b) Circles are found within the image (for this image, $n = 1041$).(c) Height data is radially binned with distance from the centre of the pore, here is a histogram of the first bin, i.e., 8 nm circle in the centre of the pore, this small bin size was chosen to ensure that the pore scaffold was not included. (d-e) Each circle is cropped as a separate image and compared against one another to give a rotationally symmetric profile of the height across the pore. The shading on the height profile in (e) represents the standard deviation for the height recorded at 4 nm intervals across the 1041 pores.

In order to create averaged radial projections of the data a cross-correlation averaging procedure is implemented. The first pore recognised by 'imfindcircles' working from upper left of the image is used as the template for the cross-correlation averaging. The template is masked such that only image data within a 50 nm radius of the centre of the cropped image is kept for the correlation — this region is kept tight to the pore scaffold and should contain only the NuPOD, ignoring other possible neighbouring NuPODs. A second pore is

then compared against the template (this is also masked such that only data within an 50 nm radius of the centre is kept) using the sum of absolute differences (SAD) method, i.e., the absolute difference in height between each overlapping pixel is taken, and the sum of all differences saved. The image is then rotated 5° and the SAD score is calculated and saved. This is repeated until the image has been rotated 45°, this assumes an eight-fold symmetry, note that the image was not found to be significantly different if allowed to rotate the full 360° and so this was found to be sufficient. The rotation of the image corresponding to the lowest SAD score is defined as having the greatest correlation with the template and is therefore averaged with the template to create a new template. This process is repeated until all pores have been averaged. The averaged image is then rotationally symmetrised to produce the plots shown in Figure 2.8d and e.

The height data from the first 4 nm bin as extracted for all of the pores in a given image can then be plotted as a metric for pore-filling (see Figure 2.8c). As the AFM images were captured with sampling every 3 nm the central radial bin contains 5 data points, one in the centre and four surrounding. By including only the first bin, i.e. the 8 nm in the very centre of the pore, any influence from poor-tracking of the AFM tip over the pore scaffold is excluded. Owing to errors in image flattening some of the data in the centre of the pore appeared to be slightly below zero, ideally the data should have an absolute minimum of zero. Histograms of the raw data extracted from experiments adding importin-βmEos2 to NuPODs containing various numbers of Nsp1 or Nup100 proteins are plotted in Figures 2.10 and 2.9. Distributions can be approximated as normal, yet the spread of the data increases with increasing hsImp-β concentration. Two-tailed Welch's t-tests were performed on the data in Origin Lab. Owing to the large sample size and nature of the data, when comparing height changes before and after the addition of importinβ p values obtained were by and large very small, indicating a significant change despite similar mean values and overlapping standard deviations (see box plots in Figure 2.10 and 2.9). Non-parametric Mann-Whitney U-tests, which do not assume a normal distribution were also performed on the data, the outcomes were consistent with welch's t-test therefore the results from the parametric tests were used.

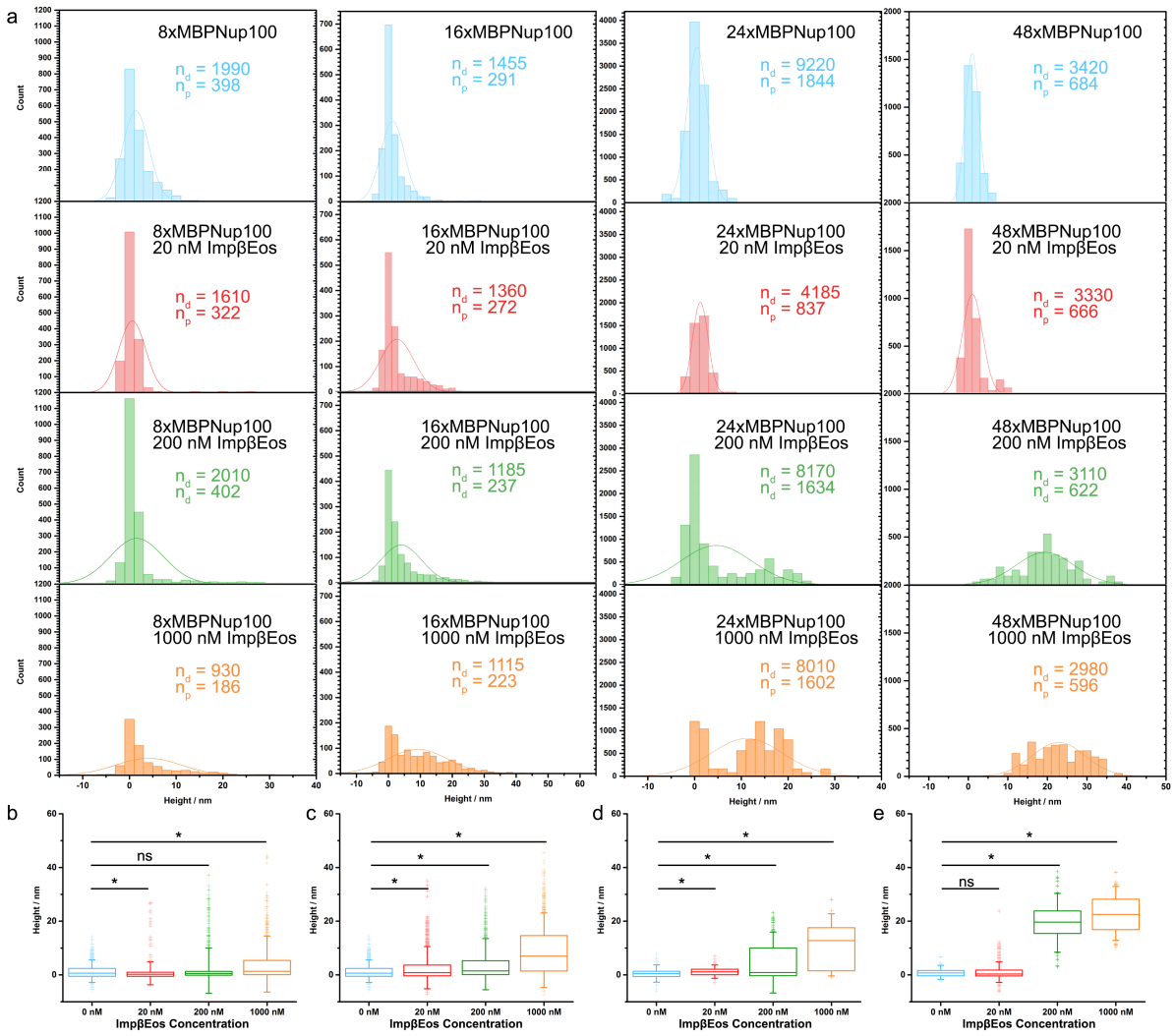


Figure 2.9: **Height increases upon the addition of hsImportin-βmEos2 to NuPODs with Nup100 proteins.** a) Distribution of height data in the central 4 nm of NuPODs with varying numbers of MBPNup100 proteins and increasing concentration of exogenous Imp-βEos protein. n_d is the number of data points and n_p is the number of rings sampled. Data was binned in 2 nm bins, the normal distribution is overlaid on the histograms. Box plots for the data is shown for NuPODs containing 8 (b), 16 (c), 24 (d) or 48 (e) MBPNup100 proteins. The central line indicates the median and the upper and lower bounds the 75th and 25th percentiles. Welch's t-tests were performed to compare the data before and after addition of Imp-β *, p ¡ 0.001; ns, p ¿ 0.05.

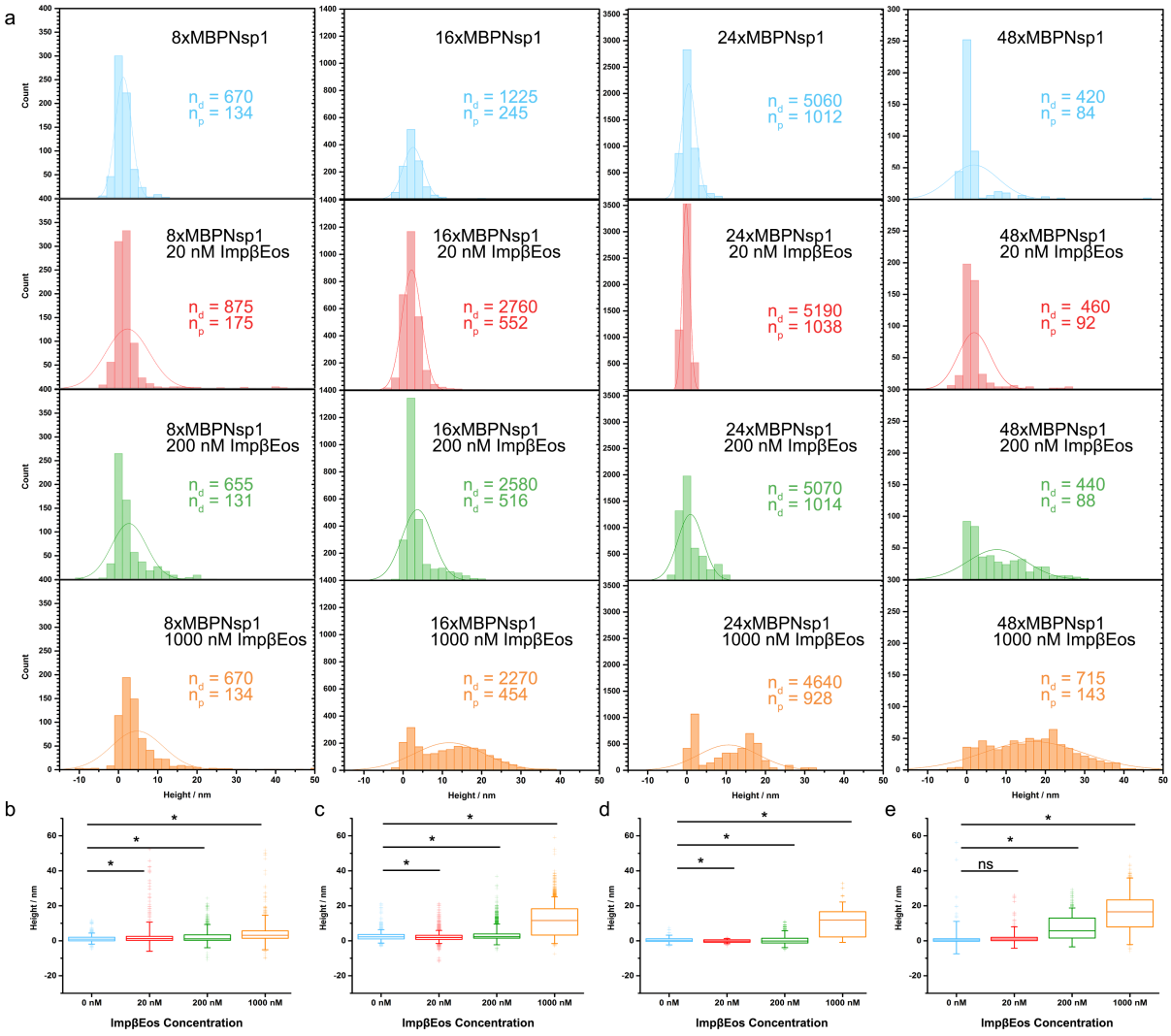


Figure 2.10: **Height increases upon the addition of hsImportin-βmEos2 to NuPODs with Nsp1 proteins.**Distribution of height data in the central 4 nm of NuPODs with varying numbers of MBPNsp1 proteins and increasing concentration of exogenous Imp-βEos protein. n_d is the number of data points and n_p is the number of rings sampled. Data was binned in 2 nm bins, the normal distribution is overlaid on the histograms. Box plots for the data is shown for NuPODs containing 8 (b), 16 (c), 24 (d) or 48 (e) MBPNsp1 proteins. The central line indicates the median and the upper and lower bounds the 75th and 25th percentiles. Welch's t-tests were performed to compare the data before and after addition of Imp-β *, p ¡ 0.001; ns, p ¿ 0.05.

2.5 Transmission electron microscopy

Transmission Electron Microscopy (TEM) is a technique that focuses electrons, via a series of electromagnetic lenses, onto a thin sample (50-150 nm thick) of interest. By using an electron beam which has a very small wavelength (100,000-fold shorter than photons in visible light), sub-nanometer resolution is attainable - whereas the highest super-resolution light microscopes typically resolve to 20-50 nm.[144] Upon reaching the sample the electrons collide with atoms within the specimen, producing a variety of elastic and inelastic collisions. Larger atoms (i.e higher atomic number) have a greater cross-sectional area, therefore cause more scattering of the electrons and increased mass contrast in the image. Since biological matter generally contains atoms of low and similar atomic number, electrons do not interact strongly and steps have to be taken to increase the contrast when imaging such samples. After passing through the thin specimen the electrons are captured using a CCD camera.[145]

For TEM imaging, the biological samples consisting of DNA and proteins were adsorbed onto hydrophilised carbon-coated copper grids. In order to have sufficient electron contrast for imaging, samples were negatively stained with a heavy metal stain. Here the particle of interest is shrouded in an amorphous matrix of electron dense stain such that the particles, having a lower electron scattering power, appear as light areas. Whereas the surrounding stain, which scatters electrons more appears darker, providing a high contrast. Note that biomolecules can also be imaged by freezing them in vitreous ice in a technique known as cryo-electron microscopy (cryo-EM). Although this can afford the highest resolution by averaging thousands of molecules to create an electron map, intrinsically disordered proteins are not amenable to detection using this method since they are highly flexible. This flexibility lends poor contrast to the images whilst heterogeneity between the protein conformations means no meaningful structure can be obtained from class averaging. For negative staining of FG-nups within the NuPODs, the MBP terminal tag is thought to help improve electron contrast (see Chapter 4) although FG-nups can also be observed in the TEM images after MBP tag removal (as shown in Figure 4.3).

Typically, 5 μl of $\sim$1 nM NuPODs (diluted in buffer not containing Tween-20 surfactant) was deposited for 1 minute on a glow-discharged formvar/carbon coated copper grid (Electron Microscopy Sciences). A piece of filter paper was used to wick away the

specimen droplet before adding 5 μl of 2% uranyl formate stain. The stain was blotted immediately and a further 5 μl of stain added and left for 1 minute before it was removed and the grid left to dry fully. Imaging was performed under vacuum on a JEOL JEM-1400 Plus microscope operated at 80 kV with a bottom-mount 4k×3k CCD camera (Advanced Microscopy Technologies). Patrick Ellis Fisher (Yale), Qi Shen (Yale) and Joe Beton (Birkbeck) obtained some of the images presented in this thesis, where this is the case, it is noted in the figure captions.

2.6 TIRF microscopy

Total Internal Reflection Fluorescence (TIRF) microscopy is a light microscopy based technique that requires molecules of interest to be labelled with a fluorescent dyes.[146] The process of fluorescence is induced by excitation with a particular wavelength of light. This energy is absorbed by the fluorophore as it creates an excited electronic singlet state. Amongst other energy transfer processes, a relaxed singlet state is formed from which fluorescence originates. A photon of light is emitted as it returns to the ground state although this is of lower energy and longer wavelength, this change is referred to as the Stokes shift. A single fluorophore is able to generate many thousands of photons, but after a period of excitation, they eventually loose their ability to fluoresce as the result of photochemical degradation (known as photobleaching).[147]

TIRFM offers a particularly high sensitivity since it only excites and captures fluorescently labelled molecules that are located very close to the samples surface. In a typical setup, light is transmitted through two adjacent materials of differing refractive indices. Figure 2.11 shows a typical set up where incident light is passed through a glass coverslip (n = 1.52) and then into a water-based physiological buffer (n = 1.33) that contains molecules of interest. As light passes through the media, it is partially reflected and refracted depending on the incident angle. By using two materials with different refractive indices, a critical angle can be reached where all the light is refracted parallel to the interface of the two materials; a phenomenon known as total internal reflection (TIR). Although light no longer passes through the second medium, the reflected light creates an evanescent electromagnetic field that decays exponentially with the depth of penetration into the less

refractive material. This evanescent field can be limited such that most of the intensity is limited to the first ∼100 nm, so only fluorophores very near to the coverslip are excited and detected. As a consequence, the contribution of out-of-focus background fluorescence is much reduced.[148]

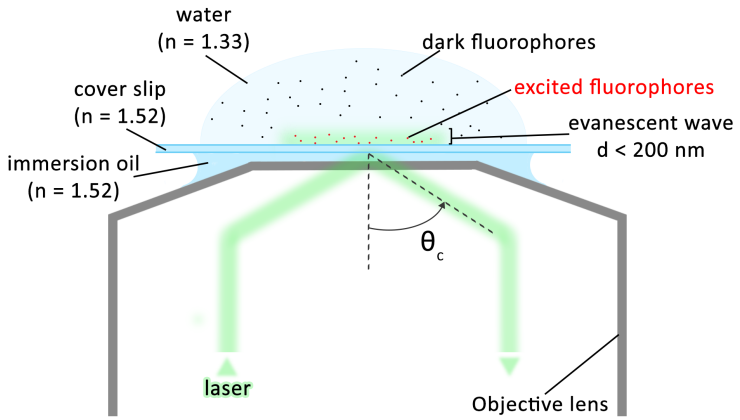


Figure 2.11: **Total Internal Reflection Fluorescence Microscopy (TIRFM).** A laser beam passing through two materials of differing refractive indices (namely glass and aqueous solution) is directed at a critical angle, θ_c to induce total internal reflection. An evanescent wave forms at the glass-solution interface, penetrating the sample to a depth of 100-200 nm allowing for highly selective illumination. Only fluorophores very close the surface are excited, resulting in a particularly high signal-to-noise ratio.

TIRF imaging was performed with the assistance of Kwasi Kwakwa (Lowe Lab, UCL) who focused the samples and acquired images whilst I prepared the samples and helped identify optimised parameters for data collection. A custom built microscope was used, based on an Olympus IX81 frame (Olympus, Japan) with a high NA oil objective (Olympus 100× UPON TIRF 1.49 N.A. oil). An sCMOS camera (Orca Flash4.0V2, Hamamatsu, Japan) was coupled to the camera port of the microscope via a magnifying relay to achieve an effective pixel size of 115 nm. Appropriate bandpass filters were placed in front of the camera to filter the fluorescence emission. The Semrock FF01-692/40-25 single band filter was used for Alexa Fluor 647 dyes and the Semrock FF01-523/610-23.3-D dual band filter was used for mEos2 and Alexa Fluor 594 imaging. A fiber-coupled CW laser (iChrome HP, 488, 561, and 640 nm, Toptica, Germany) was expanded using a collimating lens and relayed via the camera port of the microscope via a scanning galvo mirror system (GVSM002-EC/M, Thorlabs, USA). The fast-steering mirrors are steered to the critical

TIRF angle or near critical angle at the back focal plane of the objective. The camera and galvo mirrors were synchronised using a TTL pulse and analog signal from an external D/A converter (DT9834, Data Translation, Germany). A quarter-wave plate was used to circularly polarize the beam before it was injected into the microscope. The beam was directed to the objective lens via a multi-edge dichroic filter (Di01-R405/488/561/635-25x36, Semrock, USA). The field of view was set to ∼40 μm×40 μm such that it was evenly illuminated. The resolution is diffraction limited so one cannot distinguish between two fluorophores located within 200 nm.

Samples for TIRF microscopy studies were prepared on PLL-*b*-PEG coated glass coverslips to replicate the conditions used for AFM imaging NTR addition to NuPODs. Briefly circular glass coverslips (25 mm diameter, thickness 0.16-0.19 mm from Thermo Fisher) were cleaned in excess isopropanol and MilliQ water, before drying under a stream of nitrogen. To contain the liquid droplet, apertures with a 10 mm diameter were punched into sticky-backed Teflon (Bytac®, Sigma-Aldrich). The Teflon was cleaned in detergent and MilliQ water before sticking onto the cleaned coverslip. Coverslips with Teflon were then hydrophilised by plasma treatment at 70% power for 2 minutes in a plasma cleaner (Zepto, Diener Electronic). To cover the larger sample size, the droplet volume was increased to ∼80 μl during imaging. For functionalisation, 10 μl of PLL_{10}-*b*-PEG_{113} and 10 μl of $PLL_{1000-2000}$ was added to the coverslip and left to adsorb for 45 minutes. The solution was washed with 5× MilliQ water and then 6× with imaging buffer (10 mM PB, 10 mM $MgCl_2$, pH 7.2). Since the association rate for NTR-FG-nup interactions has been estimated as $\sim 1.5 \times 10^9$,[59] and is much faster than the ∼30 ms resolution possible for our TIRF setup; to monitor the binding of fluorescently tagged importin-β molecules to nucleoporins housed within labelled NuPODs we allowed the system to equilibrate prior to imaging. Firstly 10 μl of a ∼0.1 nM solution of NuPODs was added to the functionalised glass slide. At this concentration NuPODs are sparsely distributed such that the chance of two NuPODs being within 200 nm of one another is minimised. The DNA origami rings had also been hybridised to Alexa Fluor 647 molecules prior to purification (see description in section 2.1.3). Each DNA origami ring was designed to anchor 8× Alexa Fluor 647 dyes to its outer circumference, the synthetic dye can be excited by laser lines between 633 and 650 nm and its emission maximum is at 665 nm. For equilibration with the NTR, 10-15 minutes prior to imaging a solution of fluorescently labelled importin-β was added to the 80 μl droplet to a typical concentration between 1 and 10 nM. We

attempted experiments with two variants of hsImp-β. The first was expressed and purified by Roxana Mironska (Lowe Lab, UCL) and had an a photoconvertible protein tag, mEos2 (mEos2 is a monomeric variant of the fluorescent protein Eos). This protein is referred to throughout this work as hsImportin-βmEos2 or Imp-βEos. In its unconverted state, the protein has an excitation peak at 506 nm and an emission peak at 519 nm. Its fluorescence is red shifted when it is subject to near UV radiation ($\sim$390 nm), the shifted excitation peak is at 573 nm and the emission peak is at 584 nm.[149] The other hsImp-β used had been labelled at a.a. position 213 with the synthetic dye Alexa Fluor 594 by Sofya Mikhaleva (Lemke Lab, EMBL). This dye, while optimally excited by a 594 nm laser can also be excited by the 561 nm laser line, and emits at a maximum of 617 nm. We also included an oxygen scavenging system (Oxyfluor (Sigma Aldrich) diluted 1:100 with 18 mM sodium lactate substrate) to ensure stable fluorescence from the dye molecules during imaging.

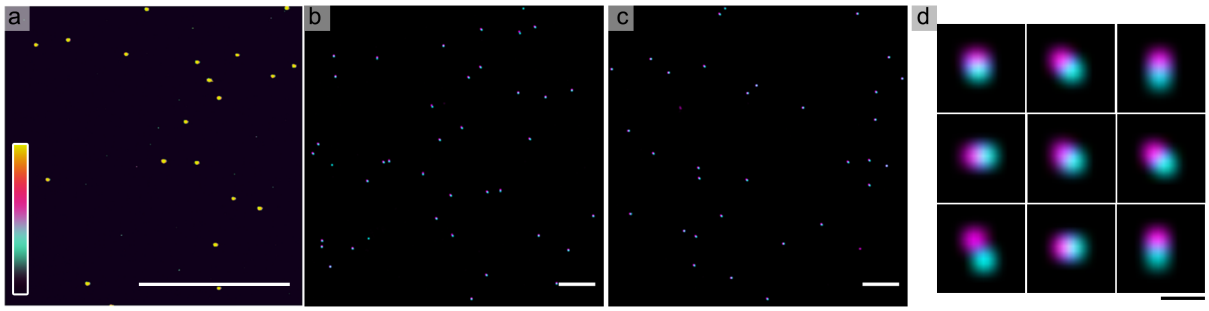


Figure 2.12: **Multicolour TIRF imaging.** TetraSpeck™ microspheres loaded with 4 dyes were used to check for the alignment between colour channels. a) an AFM image of 200 nm diameter TetraSpeck™ beads on mica, analysis gave an average diameter of 210 nm (n = 82) b and c) TIRFM image stacks processed using the ThunderSTORM plugin for ImageJ and visualised using the average shifted histograms method of TetraSpeck beads on glass. Visualisations in the 640 nm (magenta) and 561 nm (cyan) channels have been overlaid without any offset. d) Magnified regions from b) and c) illustrating inconsistent offsets. The scale bars in (a-c) are 5 μM and 500 nm in d). The colour scale in the AFM image in a) represents 50 nm.

The imaging procedure was as follows; firstly fluorescence from the 8× Alexa Fluor 647 dyes anchored to the outside of the DNA origami ring was recorded to identify the positions of the NuPODs. Typically a stack of 100 images were recorded with the 640 nm laser power at 8% and an acquisition time of 100 ms. To check that there were indeed

multiple dyes per NuPOD, photobleaching experiments were also performed by recording 2000 frames at 100 ms per frame(see Section 6.2.4 and Figure 6.11). Next the bandpass filter was manually switched and frames were captured with the 561 nm laser power set to ∼30% to image importin-β molecules labelled with Alexa Fluor 594 at position 213 or expressed with the mEos2 tag (for imaging importin-βmEos2 the UV power was also set to 3% to induce photoconvertion). For these experiments, 10,000 frames were recorded with an exposure time of 30 ms per frame.

Alignment differences between the optical filters can lead to problems with colour registration in fluorescence imaging. Misregistration was assessed using TetraSpeck^{TM} microspheres(Sigma), processed image stacks are shown in Figure 2.12 b and c. The 200 nm beads (see AFM image in Figure 2.12a) were stained with four fluorescent dyes, $^{365}/_{430}$ nm (blue), $^{505}/_{515}$ nm (green), $^{560}/_{580}$ nm (orange) and $^{660}/_{680}$ nm (dark red). Note that despite trying to improve the system alignment, there was an offset between channels, that was not consistent between different fields of view in a given image (see spot magnifications in Figure 2.12d). However the offset was typically less than 500 nm and so larger regions of interest could be chosen or the whole image shifted by a few pixels to account for this.

For the analysis, image stacks were processed to obtain spot localisations using the ThunderSTORM plugin for ImageJ.[150] First the image is filtered and the features enhanced with a wavelet filter using the default settings (B-spline basis function of the third order with a scaling factor s = 2). Next the approximate positions of the molecules are found by determining if the intensity of each pixel is greater than a user-specified threshold. This was set to default as the standard deviation of the first wavelet level. At the same time the intensity value must be greater than or equal to all values within a 8-connected neighborhood. If both of these conditions hold, the point is accepted as a candidate molecule for further processing. Sub-pixel localisation of the molecules was carried out using an integrated form of a symmetric 2D Gaussian function with a pixel fitting radius of 3. The data was then visualised using the average shifted histogram method with the number of lateral shifts set to 2 and the pixel size retained at 115 nm.[150]

For image stacks collected of NuPODs (in the 640 nm channel) and importin-β (in the 561 nm channel), despite colour misregistration, there is clearly a colocalisation of inten-

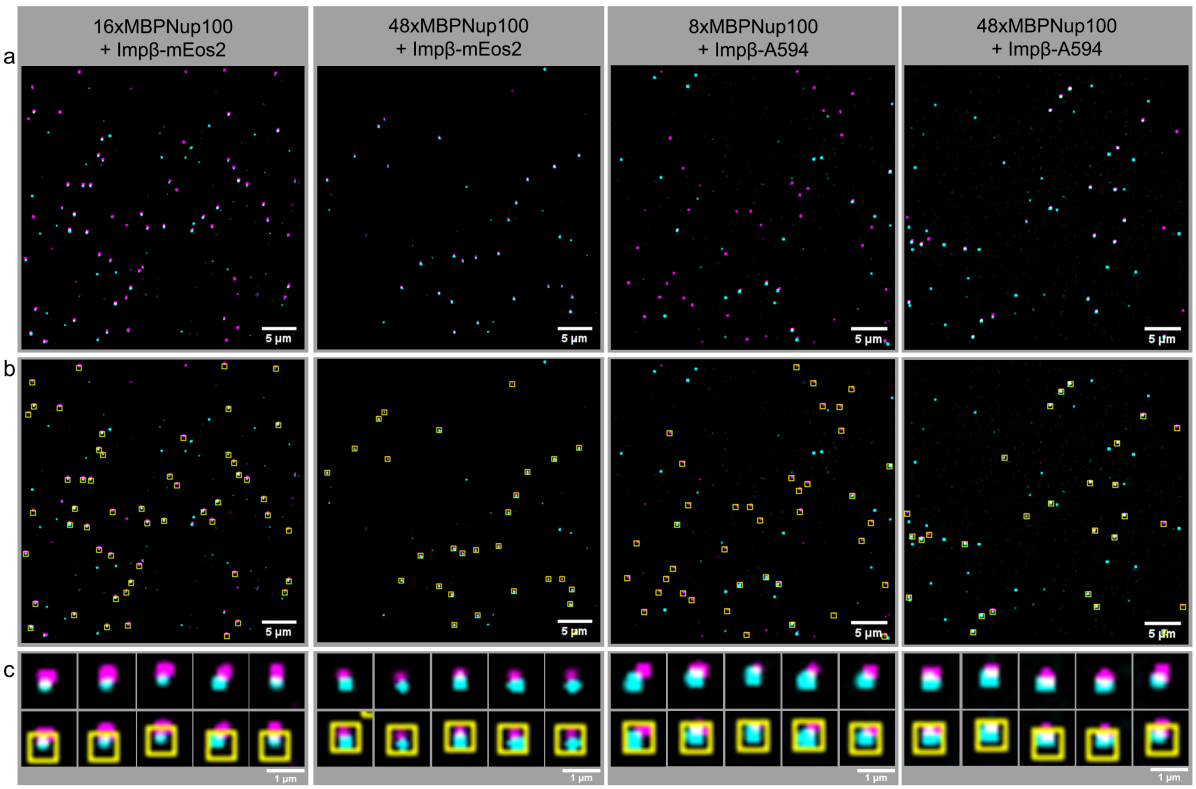


Figure 2.13: **Preliminary processing of importin-β—NuPOD image stacks collected using TIRFM** Images shown are visualisations using the average shifted histograms method of image stacks run through ThunderSTORM, i.e. they are a mean projection of multiple frames. a) NuPODs labelled with Alexa Fluor 647 are shown in magenta (100 frames recorded at 100 ms in the 640 nm channel) are overlaid importin-βmEos2 or importin-βAlexa Fluor 647 localisations shown in cyan (10,000 frames recorded at 30 ms per frame). b) 6 pixel regions of interest are drawn around the localised NuPODs (magenta) but shifted accordingly by a few pixels in the x and y direction such that their positions align with the importin-β localisations (cyan). The intensity of each of these windows can be monitored with each frame to detect for single molecule binding events of labelled Imp-β. c) Magnifications of individual NuPODs with co-localised Imp-β showing offset between 640 and 561 nm channels(top-row). The location of the 6-pixel window is optimised to capture the fluorescence in the 561 nm channel corresponding to Imp-β molecules(bottom-row).

sities when single molecule positions from ThunderSTORM processing are overlaid (see Figure 2.13). Since the fluorophore spots are spaced relatively wide apart by shifting the whole image one could clearly see that the spots overlapped. By counting the number of colocalised spots whether NuPODs with less FG-nups showed a lower propensity to

bind labelled Imp-β could be assessed (see further figures and discussion in Section 6.2.4). To isolate single molecule events for both Imp-β molecules binding to NuPODs and of the dyes attached to the NuPODs themselves, regions of interest were created around localised spots. This processing was done with the use of a custom macro in ImageJ. A region of interest (ROI) was drawn around the labelled DNA ring positions (i.e., in the 640 nm channel) after the ThunderSTORM processing. The ROI was set to 6×6 pixels to fully encapsulate the emitted intensities whilst limiting overlap between adjacent ROIs. To assess the photobleaching of the dyes attached to the NuPODs, the multimeasure tool in ImageJ was used to record the 'RawIntDen' i.e., the sum of intensity values in the ROI for each frame in the stack (here 2,000 in the 640 nm channel). Plotting 'RawIntDen' for each ROI against time could facilitate the observation of single dyes (see Figure 6.11 in Section 6.2.4).

To look at how labelled importin-β molecules interacted with the NuPODs, the ROIs identified for NuPOD positions in the 640 nm were offset to account for misregistration between the colour channels. Offsetting of the ROIs was carried out manually using the visualisation of the 561 nm channel obtained by ThunderSTORM processing and adjusting the position of the 6 pixel box (typically by 1 or 2 pixels in the x and y directions) to ensure the full Gaussian intensity was recorded (see bottom row of Figure 2.13c which shows shifted 6×6 pixel ROIs around importin-β spot localisations in cyan overlaid with un-shifted spot localisations of NuPODs in magenta). The intensities of the shifted ROIs were then integrated with time as before but for the 10,000 frames recorded in the 561 nm channel. Due to heterogeneity within the intensity data sets the fluorescence intensity and average bleach times for the labelled importin-β molecules was not able to be identified. Note that the fluorescence of importin-β molecules in the absence of NuPODs on non-passivated glass was also recorded as a control to try to gather this information, however intensities were found to be heterogeneous. Scripts were written in MATLAB by George Stanley (UCL) to plot histograms of the single molecule intensities but their values were non-uniform and overlapped with the large background peak (despite attempts at background subtraction). Given more time I would hope to better analyse the data to obtain these values, perhaps instead using a step-finding function and thus use this information to quantify the number of importin-β molecules bound per NuPOD. Moreover, by additionally extracting photobleaching times, one could resolve to establish whether in fact any importin-β molecules unbind from the NuPODs — as unbinding events are non-trivial

to distinguish from bleaching events.

2.7 Coarse-grained molecular dynamics simulations

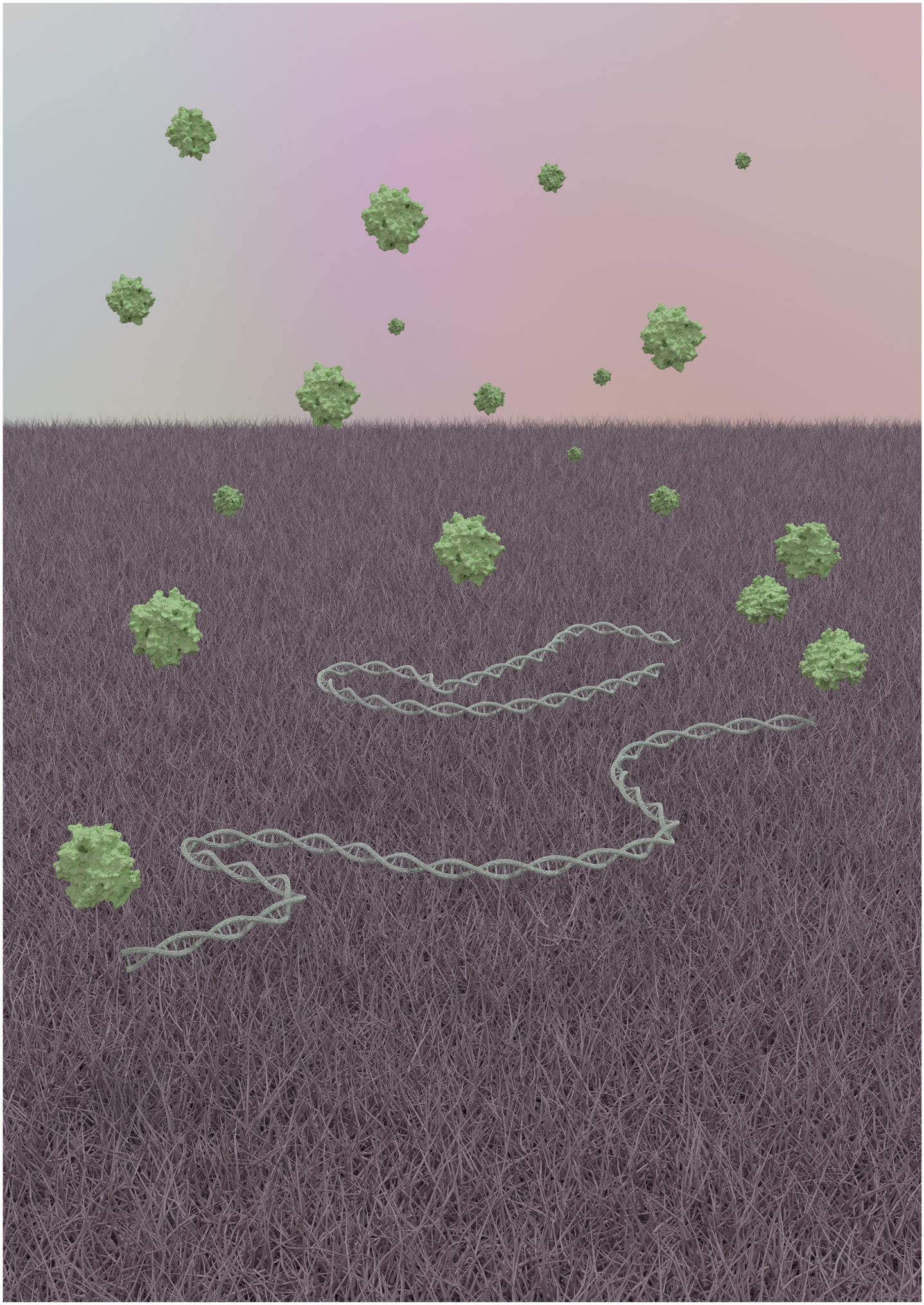
Molcular dynamics (MD) simulations were performed to complement *in vitro* studies of the NuPOD system by Luke Davies (UCL). The simulations were a combination of an *NVE* (constant number of particles N, constant volume V, constant energy E) time integration algorithm and a Langevin thermostat, with the LAMMPS package (version 5 Nov 2016; 78).

The DNA origami ring was modelled as an open cylinder comprised of neighbouring spheres with diameter = 2.0 nm and arranged as to mimic the experimental setup, with the sphere centres positioned along a cylinder of radius 23.9 nm and height 9.0 nm, and of a radius of 29.9 nm and height 11.5 nm for the inside and outside grafted NuPODs, respectively. The cylinder was kept fixed throughout the simulation and was excluded from the integration scheme. The DNA linkers were modelled as stiff chains of beads with diameter = 2.2 nm, connected by harmonic springs (stiffness 1000 k_BT /nm^2) and angular potential (stiffness 1000 k_BT /rad^2) between nearest-neighbours. The linkers were kept fixed at one end at specific points along the inner cylindrical wall, as defined by the designs of the DNA origami NuPOD, and were free to rotate around that anchor. The FG-nup proteins were modelled as beads-on-a-chain, connected by harmonic springs with stiffness 1000 k_BT /nm^2.[42,73] Each bead had a diameter of 0.76 nm, corresponding to two amino acids, a choice that yielded the correct persistence length for FG-nups. Individual FG-nup polymers had one end attached to the tip of a DNA linker rod via a stiff harmonic spring. MBP at its other end was modelled as a sphere with a diameter of 4.83 nm to match its approximate absolute volume (PBD ID: 1OMP);[151,152] this was attached to the free-end of the FG-Nup polymer via a harmonic spring (stiffness 1000 k_BT /nm^2). The ring, DNA linker rods, FG-nup polymers and MBP all experienced excluded-volume (short-range repulsive) interaction, implemented through a truncated and shifted repulsive Lennard Jones potential as shown in equation 2.2.

$$U^{rep}(r) = 4\varepsilon_{LJ}\left[\left(\frac{\sigma_{ij}}{r}\right)^{12} - \left(\frac{\sigma_{ij}}{r}\right)^{6}\right] + \varepsilon_{LJ} \tag{2.2}$$

This is true for $r < 2^{1/6}\sigma_{ij}$ and zero elsewhere, with r the centre-to-centre distance between particles i and j with respective diameters d_i and d_j, and $\sigma = \frac{1}{2}(d_i + d_j)$. ε_{LJ} was set to 500 k_BT. In addition, an attractive FG-nup polymer-polymer (pp) interaction was implemented with a roughly exponential decay (dropping to zero at a centre-to-centre distance of $r_c^{att} = 2\sigma_{ij} = 2d_i = 1.56$ nm here) with strength ε_{pp} (in units of k_BT) at contacts between the beads making up the FG-nups. Specifically, the attractive potential was based on $U^{att}(r) = -\varepsilon_{pp} exp\big(-\frac{r-\sigma ij}{\lambda}\big)$, with $\lambda = \sigma_{ij} = d_i = 0.76$ nm here, shifted and truncated to yield a total pair potential for the polymer beads of the form $U_{pp}(r) = U^{rep}(r) - \varepsilon_{pp}$ for $r < 2^{1/6}\sigma_{ij}; U_{pp}(r) - U^{att}(r = r_c^{att}) - (r - r_c^{att})\big(\frac{dU^{att}(r)}{dr}\big)_{r=r_c^{att}}$ for $2^{1/6}\sigma_{ij} \leq r < r_c^{att}$; and zero elsewhere. The phenomenological parameter ε_{pp} was set through a comparison of MD polymer brush simulations and experimental thickness data of FG-nup films, following a procedure previously applied by Zahn et al.[73] This yielded $\varepsilon_{pp} = 0.41\ k_BT$ for Nsp1 and $\varepsilon_{pp} = 0.45\ k_BT$ for Nup100, for the here chosen shape of the interaction potential.

All simulations were equilibrated for 7 × 106 timesteps (roughly equivalent to 48 μs) and a further 8 × 106 timesteps (∼54 μs) were used for data analysis. Each simulation was run 5 times with different initial conditions and random seeds to verify equilibration and to obtain reliable statistical sampling.



Chapter 3

Surface preparation for in-solution AFM imaging of DNA

This chapter is based in part upon the manuscript "PEGylated surfaces for the study of DNA-protein interactions by atomic force microscopy" by B. Akpinar, P. J. Haynes, N. A. W. Bell, K. Brunner, A. L. B. Pyne, and B. W. Hoogenboom, which has been published in *Nanoscale* vol. 11, pp. 20072-20080, 2019. An earlier version of the manuscript was also deposited on the *bioRxiv* preprint server, DOI: 10.1101/680561.

3.1 Introduction

Single-molecule techniques such as AFM (but also TIRF microscopy) rely on the adsorption of biomolecules onto a solid substrate, such as mica or glass cover slips. This represents a significant disadvangate, because in many cases such a surface-adhered state may not be representative of *in-vivo* conditions. For AFM, this disadvantage is balanced by its ability to image biomolecules such as DNA at $\sim$1 nm resolution in physiologically relevant conditions.[153] Importantly, such resolution can be achieved without sample staining or labelling.[82,154] Muscovite mica is the substrate of choice for AFM imaging of biomolecules, because of the ease of preparing an atomically flat mica surface via cleavage along the basal plane, and because of the polar, hydrophilic nature of the cleaved surface,

facilitating the adsorbing and retention of biomolecules in aqueous solution. When mica is hydrated, K^+ ions dissociate from interstitial sites within mica's aluminium phyllosilicate lattice, resulting in a net negative charge on the surface. *A priori*, this hampers the adsorption of negatively charged biomolecules and biomolecular complexes, which applies in particular to DNA and the DNA origami structures that play an important role in this thesis.

To permit the adsorption of DNA with its highly negatively charged phosphate backbone, the negative surface charge of mica therefore needs to be screened or compensated for.[155,156] Figure 3.1 shows schematically a number of different adsorption protocols that have been established for adsorbing DNA on mica.[157] One of the most commonly adopted methods is the use of transition metal cations such as Ni^{2+}, $Co^{2+}$and Zn^{2+}, which can substitute into vacant sites within the mica lattice, yielding positively charged regions to which the negatively charged DNA can adhere (see Figure 3.1b).[158]The strength of the electrostatic attraction can be modified by the presence of additional ions and chelating agents within imaging buffer.[159,160] Note that ions such as Ni^{2+} kinetically trap dsDNA in a given conformation on the surface, whilst the similarly sized Mg^{2+} ion binds DNA less strongly leaving it in a more dynamic and therefore harder to resolve state (unless the sample is dried).[160] Other methods to facilitate DNA absorption include the silanization of mica to introduce positively charged surface groups (normally amines),[161] the formation of positively charged lipid bilayers,[162,163] and the electrostatic adsorption of positively charged polymers such as poly-L-lysine (PLL),[164,165] see Figure 3.1c-e.

Whilst many of these methods simply screen the surface charge of the underlying mica, the formation of supported lipid bilayers, provide a means to completely coat the underlying solid substrate in a biomimetic membrane.[166,167] Lipids are small amphiphilic molecules comprising a hydrophilic head and a hydrophobic tail: when suspended in aqueous solution, they arrange themselves to form vesicles. The adhesion and rupture of these vesicles onto a mica support results in bilayer formation, yielding an atomically flat plane of densely packed lipid head groups. The head group of the synthetic lipid can be modified to tune the surface charge, whilst the length and degree of saturation of the hydrophobic hydrocarbon tail can be modified to tune lipid packing and hence lipid order. Closely packed, 'gel-phase' bilayers are formed when the hydrophobic hydrocarbon chains of the lipids are ordered and relatively immobile. Above some critical transition temperature,

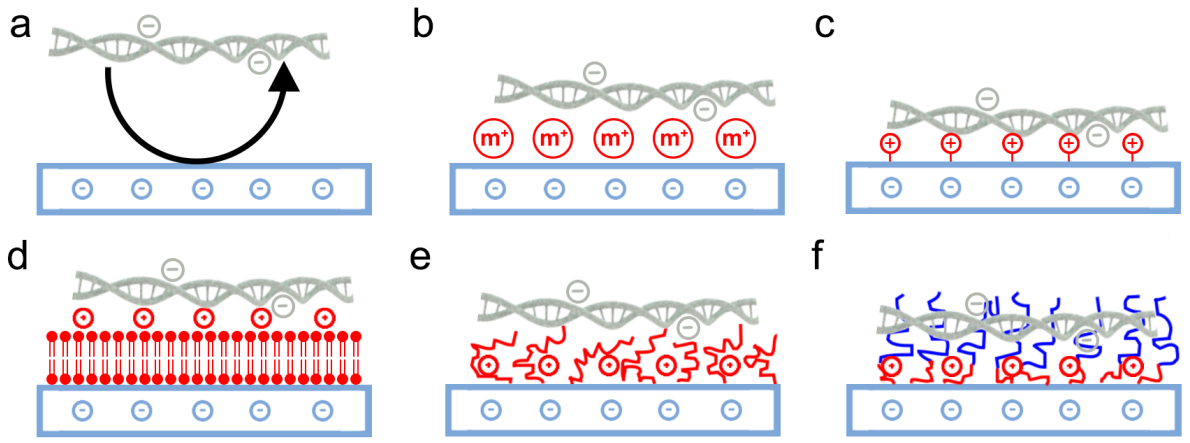


Figure 3.1: **Protocols to for the adsorption of DNA onto mica for AFM imaging** Both mica and DNA are negatively charged in aqueous solutions at physiological pH. Different methods have been used to adsorb DNA onto mica to facilitate AFM imaging. a) Negatively charged DNA is repelled from negatively charged mica. b) Metal cations are added to the buffer to mask the charge difference and promote DNA absorption, where e.g. Ni^{2+} binds more strongly and facilitates imaging of DNA in solution, whereas Mg^{2+} ions are more weakly bound, causing the dsDNA to be less well attached to the substrate and thus resulting in poor quality in-solution imaging (note Mg^{2+} is most effective for imaging DNA on dried samples). c) Silanization of mica to covalently link positively charged surface moieties (typically 1-(3-aminopropyl) silatrane is used to introduce amine groups). d) A supported bilayer can be deposited onto the mica from unilamellar vesicles, where lipids with cationic head groups result in a positively charged bilayer for the adsorption of DNA. Note that the bilayer must be in the gel phase, to provide a stable substrate for adsorbing the DNA. e) Highly positively charged, non-toxic polymers such as polyquaternium and poly-l-lysine adsorb to mica to form a positively charged film for the adsorption of DNA f) Co-polymers that comprise a surface-binding domain as well as a separate domain that extends into the solution, forming a polymer brush. These biphasic films are able to bind DNA to the underlying positively charged layer, whilst the polymer brush inhibits the non-specific adsorption of other, less-highly charged biomolecules.

the lipids become more mobile and hydrocarbon chains become randomly oriented, forming 'fluid-phase' bilayers. Lipids in the gel-phase are characterised by very low mobility in the bilayer plane,[168] which is favourable to high resolution imaging of adhered dsDNA molecules. AFM studies have shown that dsDNA can be adsorbed and imaged on both zwitterionic[169] and cationic[163] gel phase bilayers, while the use of liquid-phase membranes is restricted to AFM of larger assemblies of dsDNA.[170,171] DNA modified with chloresterol can aid insertion into the bilayer, although such modifications tend to induce aggregation

and require careful handling.[172]

The surface functionalisation becomes more complicated if there is a need for selective adsorption. E.g., for AFM imaging of FG-nups in NuPOD NPC mimics, the DNA origami scaffold needs to adhere onto the substrate, but ideally the substrate does not affect the FG-nups inside the pore — to avoid substrate-induced artefactual behaviour. Similar constraints apply more generally for studies on DNA-protein binding, where the aim may be to resolve specific binding of the protein to adsorbed DNA from a background of unspecific protein binding to the substrate, which may be non-trivial if such unspecific binding is abundant.

The problem of non-specific adsorption can be addressed by the use of surface coatings that are protein repellent, for example polymer brushes that suppress protein binding by steric repulsion.[173] One approach to suppress protein binding is to create an interfacial layer of polyethylene glycol (PEG) brushes. The high degree of hydration and flexibility of these brushes causes surface passivation when the chains are of sufficient length and grafted at high density.[174] Facile preparation of PEGylated surfaces is achieved using multifunctional copolymers comprising both surface binding domains and surface passivating domains. Graft-copolymers with a cationic PLL backbone and PEG side chains (PLL-*g*-PEG) have proven particularly effective at self-assembling into densely packed polymeric brushes to form non-fouling surfaces.[175–177] In addition, bio-recognition sites, such as RGD-peptides, have been incorporated into these films to promote cell adhesion whilst suppressing the non-specific adsorption of serum proteins.[178,179] Similarly, the incorporation of biotin-terminated PEG chains has been used to form small molecule biosensors that selectively bind streptavidin, neutravidin and avidin.[180] Unmodified PLL-*g*-PEG films have also shown the ability to selectively adsorb DNA polyelectrolytes to the underlying positively charged PLL layer, whilst the PEG layer remains impervious to other proteins, as confirmed by fluorescence imaging.[181]

The well-studied graft copolymer (PLL-*g*-PEG) adopts a comb-like conformation in solution comprised of a long PLL backbone with randomly distributed PEG side chains, whilst the block copolymer (PLL-*b*-PEG) exhibits a linear worm-like conformation comprised of regions of lysine repeats followed by regions of ethylene glycol repeats. Both copolymers can form protein repellent PEG brushes on a variety of substrates through

the spontaneous electrostatic attachment of their lysine residues. In the case of the graft copolymer, the length of the PEG block as well as the grafting ratio affects the density and hence efficacy of the non-fouling brushes.[177] The diblock copolymer has been less widely employed for surface passivation, but has been shown to be effective at inhibiting cell adhesion on glass surfaces micro patterned with PLL_{100}-*b*-PEG_{22}.[182] The passivation properties of the diblock copolymer (PLL_x-*b*-PEG_y) can be tuned by varying the degree of polymerisation of both the PLL (x) and PEG (y) chains that in turn affect the packing density onto the underlying substrate, although as of yet variations of these have not been explored.

This chapter explores different methods to adsorb DNA onto differently functionalised mica sheets for AFM imaging. Firstly, cationic lipid membranes were prepared using the synthetic lipid dimethyldioctadecylammonium bromide(DDAB). The lipid was seen to pack into two different membrane structures upon which dsDNA could be stably adsorbed, facilitating AFM imaging in a low-salt buffer. Next, different block copolymers of PLL_x-*b*-PEG_y were tested to functionalise mica in a way that selectively adsorbs DNA, whilst inhibiting the adsorption of proteins present in the imaging buffer. This allows for the high resolution AFM imaging of dsDNA, and dsDNA-protein complexes in solution whist resisting non-specific protein adsorption. These preparations will next be applied for studying the NPC-mimicking NuPODs in the following chapters.

3.2 Results

3.2.1 Cationic gel-phase lipid membranes for the adsorption of dsDNA

To create a positively charged supported lipid bilayer, the synthetic, cationic lipid dimethyldioctadecylammonium bromide (DDAB) was used, which has a gel transition temperature of 45°C.[136] This is not a phospholipid as found in biological membranes, but a double-chained quaternary ammonium surfactant. Small unilaminar DDAB vesicles were deposited onto freshly cleaved mica above their transition temperature, and allowed to slowly cool (see methods section 2.2.3). Upon cooling, DDAB assembled into closely

packed layers of two different heights (see Figure 3.2a), previously identified as two types of lipid phases, the 'gel-phase'(L_β)and the 'interdigitated gel-phase'($L_\beta I$).[183,184] The higher regions measured here extend approximately 4.3 nm from the background mica and correspond to the (L_β) bilayer where both ends of the hydrocarbon chains meet in the membrane midplane, forming a thick hydrophobic core (see schematic in Figure 3.2b). In the other phase observed, the membrane thickness/height is reduced to ∼2.7 nm as the membrane midplane is lost; there is an increase in spacing between the cationic lipid head groups and the ends of the hydrocarbon tails become more exposed to the aqueous solution.[185] These observed heights for the L_β and $L_\beta I$ phases are in agreement with simulation data that estimated the thicknesses as 4.0 and 2.4 nm for the two phases respectively.[186]

Figure 3.2b-d shows force-distance curves, acquired by ramping the AFM tip towards the surface as a constant rate of 0.5 Hz while detecting the cantilever deflection. Since regions of three different heights were observed across the sample, this procedure was performed on each region to probe their mechanical properties. Characteristic 'breakthrough curves' were observed when the tip pushed through regions coated in supported lipid bilayers (Figure 3.2b and c), whereas the approach on the lowest-height area (bare mica) showed no breakthrough(Figure 3.2d).[187] This procedure confirmed the deposition of a lipid bilayer whilst the difference in the force required to punch through the highest and second highest phase suggests different mechanical characteristics. The higher L_β phase required $\sim$ 0.7 nN more force to disrupt than the lower $L_\beta I$ phase. It should be noted that more data would be required to confidently quantify the forces required to puncture through these membranes.

As further demonstrated by the AFM images of 339 bp dsDNA minicircles in Figure 3.3, DNA can adsorb and be stably imaged on top of both phases of the DDAB membrane in low salt buffer, owing to the cationic charge on the lipid head group. Under these conditions, the DNA preferentially adsorbs onto the lipid as opposed to the mica at z = 0 nm (coloured black in the images). At the edge of the lipid membranes, the minicircles are seen to form less open conformations, one strand often following the contour of this outer edge. It is reasonable to assume that there is a higher concentration of hydrophilic head groups at these interfaces and therefore greater positive surface charge for the electrostatic attraction of DNA.

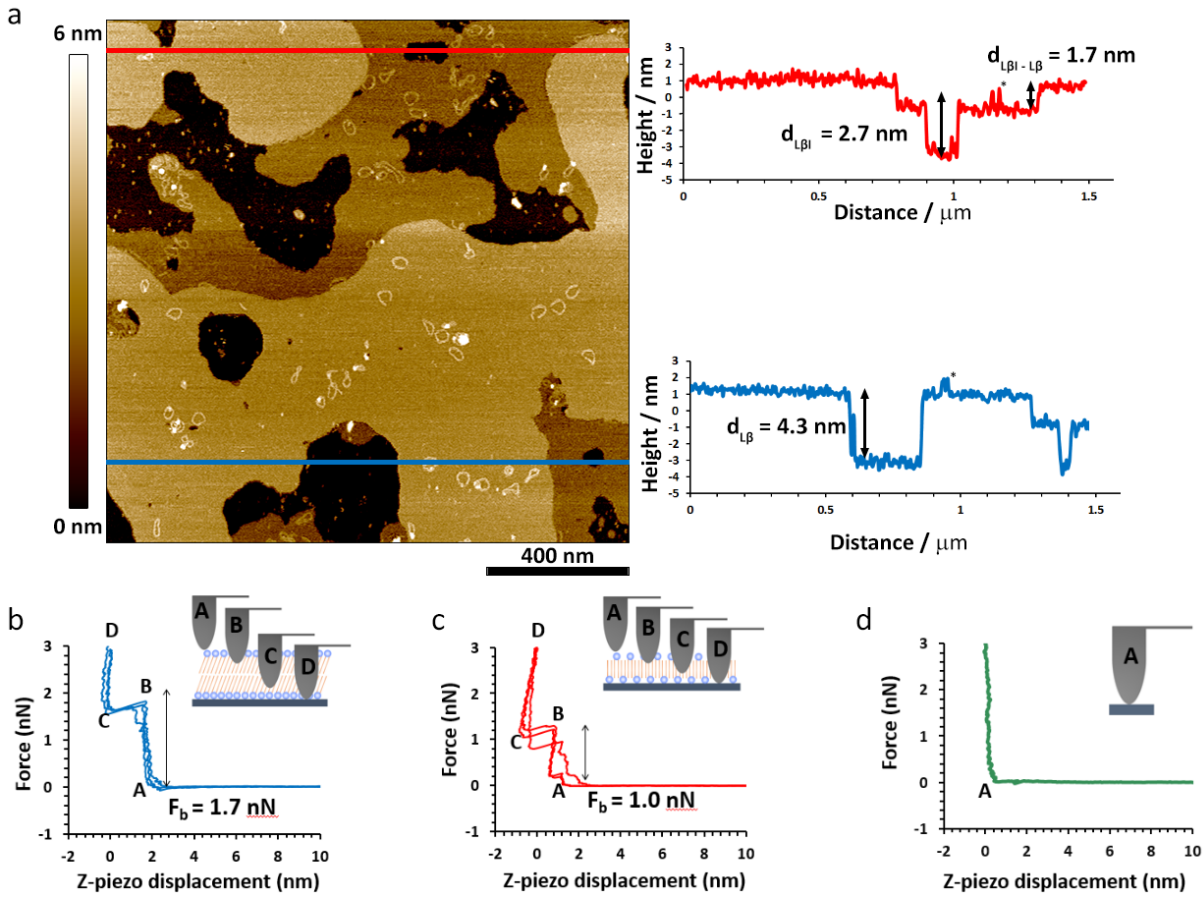


Figure 3.2: **Topographic image and characteristic lipid approach force curves for DNA minicircles on DDAB bilayers.** a) An AFM image of 339bp DNA minicircles adsorbed on DDAB lipid bilayers in 10 mM Tris, 1 mM EDTA pH 7.4. Height profiles demonstrate that DDAB assembles into two distinct bilayer structures at room temperature. b) AFM approach force-distance curve for highest phase, assumed to be the L_β phase. As the AFM tip approaches, it first interacts with the top surface of the bilayer at A. As the force is increased, there is elastic compression of the bilayer until rupture of the upper surface of the bilayer at B. The tip continues to tip transition through the central portion of the bilayer (B-C) until it contacts the mica surface at D.[187] b) As for a), but on the regions lower in height, corresponding to DDAB in the L_βI phase. Note an additional breakthrough is observed at much lower force, possibly due to differences in compressibility for the L_βI phase. c) As for a-b), but on the lowest height regions (no membrane), here the tip comes into contact with the mica at point A. The colour bar in the AFM image corresponds to 6 nm and the scale bar 400 nm.

dsDNA is a highly flexible molecule that must be tightly packaged to fit long lengths into a single nucleus (6 billion base pairs, or over 2 m of DNA fits into the nucleus of each

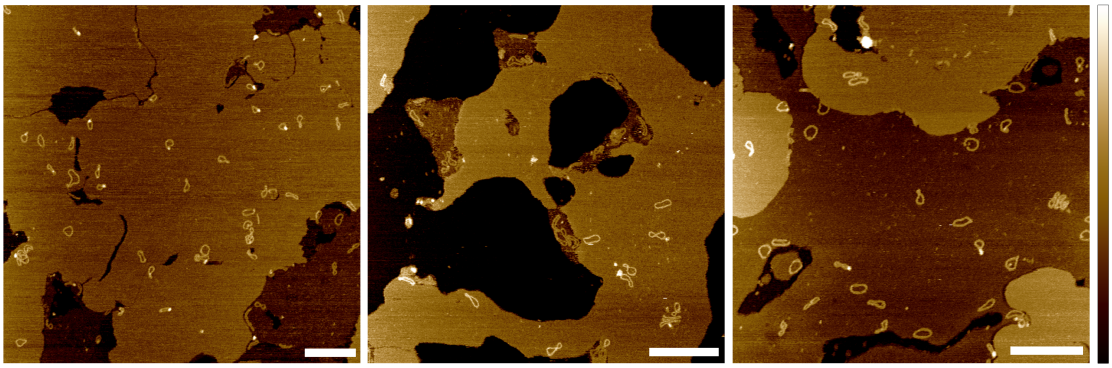


Figure 3.3: **DNA minicircles adsorbed on mica modified with the cationic, synthetic lipid, DDAB** 339 bp minicircles readily adsorb onto two phases of DDAB assumed to be the gel-phase(L_β) and interdigitated gel-phase($L_\beta I$). Scale bars 200 nm, height scale 6 nm. Images recorded in 10 mM Tris, 1 mM EDTA buffer pH 7.4.

human cell that is just ∼5 μm wide). Therefore DNA is highly compacted to fit into this small space via a number of processes. However, cellular processes require changes in DNA topology which require the charged polymer to revolve about its axis in a process known as supercoiling.[188]In most organisms DNA is underwound (i.e., less than one turn of the helix per 10.5 base pairs) from its normal relaxed state. Whilst overwound DNA is transiently generated during replication and translation processes. The minicircles used in these experiments are often used to study supercoiling processes since they are small enough to allow for the isolation of individual topoisomers. Although a detailed study of such processes is beyond the scope of this project, the conformations of these closed loops of DNA are well-studied and therefore one can use this knowledge to ensure that surface-induced changes to the dsDNA are minimised.[189,190]

The 339 bp minicircles used in this study were purified in a mixture such that their helical strands were negatively linked together 1 or 2 times compared to the normal relaxed state, Lk_0. This negatively linking difference, ΔLk is accommodated by over-winding or under-winding of the DNA helix about its helical axis (twist, T_w), or by the helix coiling upon itself (writhe, W_r). Since DNA is highly charged, the tendency for a DNA molecule to writhe is highly influenced by the presence of counter-ions which permit the close approach of DNA strands. Although the ΔLk number is known to influence the

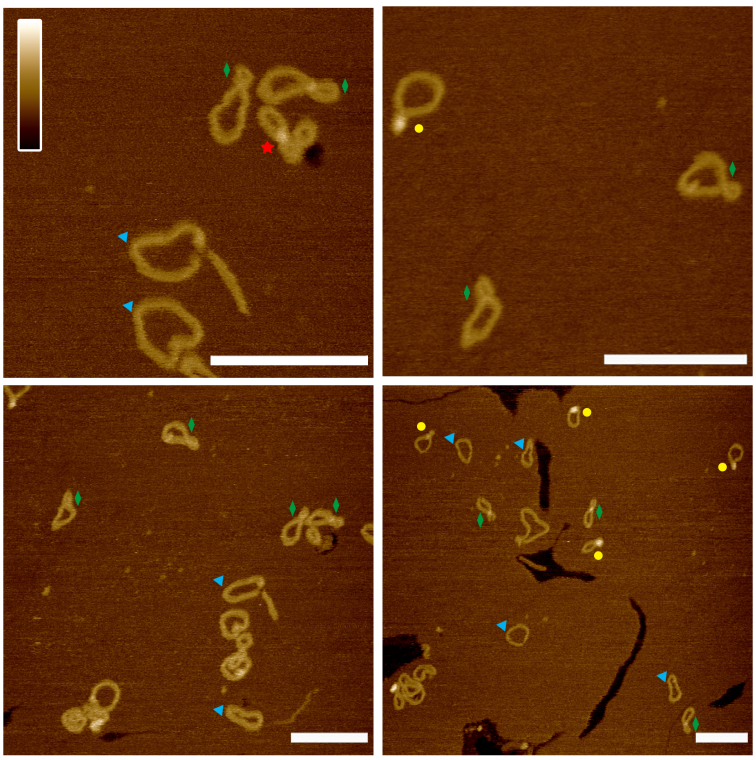


Figure 3.4: **Conformational flexibility of DNA minicircles on cationic DDAB bilayers** The 339 bp minicircles adsorb as 'open circles'(blue ▲), 'figure-8'(green ♦), 'racquet' (yellow •), 'handcuffs' (red ★), onto DDAB gel phase bilayers. The scale bars are 100 nm and the height scale is 7 nm. The images were obtained in 10 mM Tris 1 mM EDTA pH 7.4 imaging buffer.

minicircle conformation, different degrees of twist and writhe can simultaneously exist within one population. Therefore one might expect to observe a range of structures in these AFM images; provided the molecules are not highly influenced by the underlying surface.[160,189,190]

Figure 3.4 shows the range of conformations adopted by the 339 bp minicircles (on average ΔLk = -1.6) when adsorbed onto the gel phase(L_β) DDAB bilayer. In line with cryo-EM and AFM studies their arrangements can be broadly classified into the following categories, in order of increasing compaction: open circle, figure-8, racquet and handcuffs.[189,190] Interestingly, the DNA is imaged in a low salt buffer, yet significant writhe is accommodated even in these conditions. This could be attributed to a high positive surface charge on the lipid bilayer that facilitates the close approach of negatively charged

DNA strands.

Taken together, these data demonstrate that positively charged DDAB membranes can be used to adsorb dsDNA for AFM imaging. Further experiments in Chapter 4 will further confirm their suitability for the study of DNA-origami-protein hybrid systems which mimic the nuclear pore complex.

3.2.2 Polymers as surface modification agents for the adsorption of dsDNA

Poly-L-lysine (PLL) has been used frequently to immobilise DNA on a mica surface by forming an interfacial layer of positively charged long-chain polymers which bind DNA through electrostatic attraction.[164,165] The nature of the binding is dependent on the pH and solution conditions and hence must be tuned accordingly to limit aritifically induced DNA supercoiling. When both PLL and DNA are in the solution the cationic polymer is known to induce DNA condensation, forming aggregates known as polyplexes.[191] Furthermore PLL-coated surfaces also promote the non-specific adsorption of proteins, thus complicating the identification of targeted interactions between DNA and proteins which are of great importance for a number of cellular processes.[192]

Contrastingly, copolymers comprising both PLL and PEG domains achieve reduced non-specific protein adsorption through an additional PEG component, which acts as a steric barrier to protein binding (see Figure 3.1f). As a point of comparison for functionalisation using diblock PLL_x-*b*-PEG_y copolymers, firstly DNA adsorption on a mica functionalised with PLL only was characterised. PLL spontaneously attaches to the negatively charged mica surface via its highly charged lysine residues (pKa $\sim$ 10.5) to yield homopolymer films that are stable over a range of salt concentrations and pH.[193] The PLL used here was $PLL_{1000-2000}$, where the subscript refers to the number of lysine repeats in the homopolymer, corresponding to a molecular weight of 150-300 kDa. See Table 3.5 for molecular weights of the other polymers used in this study.

PLL surface functionalisation is obtained by incubation of a cleaved mica surface in PLL solution. Deposition at low solution concentrations ($\sim$0.001% w/v), allows relaxation of the lysine chains which adsorb in flattened, stretched out conformations where individual

Notation as degree of polymerisation	Notation as molecular weight / Da
$PLL_{1000-2000}$	$PLL_{150-300k}$
PLL_{10}-*b*-PEG_{22}	$PLL_{1.6k}$-*b*-PEG_{1k}
PLL_{10}-*b*-PEG_{113}	$PLL_{1.6k}$-*b*-PEG_{5k}
PLL_{100}-*b*-PEG_{113}	PLL_{16k}-*b*-PEG_{5k}
PLL_{10}-*b*-PEG_{454}	$PLL_{1.6k}$-*b*-PEG_{20k}

Figure 3.5: Table expressing molecular weights corresponding to degrees of polymerisation for the polymers used in this study.

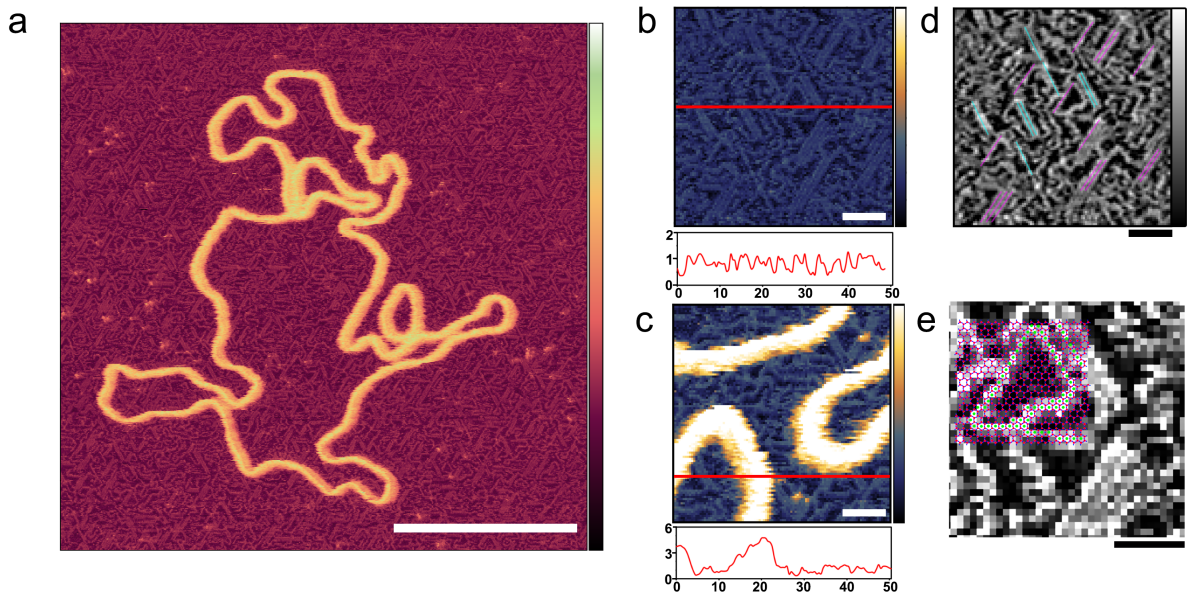


Figure 3.6: **Ordering of poly-L-lysine chains on a mica substrate** (a) AFM image (with a pixel size of ∼0.5 nm) showing a DNA plasmid adsorbed onto $PLL_{1000-2000}$-functionalised mica. (b,c) At higher magnification, PLL chains are unambiguously resolved. Height profiles underneath provide an indication of the respective protrusions of the PLL chains and of the DNA. (d) The axis of alignment observed in (b) are highlighted. (e) The mica lattice geometry is here aligned and overlaid with the resolved lysine chains, demonstrating that their alignment and spacing is consistent with alignment to the mica lattice. Inset colour scale for (a) is 8 nm and inset colour scales for (b) and (c) 4 nm, for (d) and (e) 0.8 nm. Scale bar for (a) is 100 nm, 10 nm for (b), (c) and (d).

PLL molecules can be resolved (Figure 3.6).[193] High resolution imaging of the individual lysine chains was achieved in 10 mM phosphate buffer, a relatively poor solvent for poly-L-lysine, reducing repulsion of the AFM tip, which can thus contact the collapsed

chains (Figure 3.6).[194] The PLL chains are seen to preferentially align along three orientations, with an angular difference of about 60°C (Figure 3.6d). PLL chains appear better resolved when aligned at larger angles with respect to the fast scan axis (left to right in these images). When aligned along fast scan axis itself, PLL chains are more difficult to resolve as their apparent width (here convoluted by the width of the AFM tip[153]) is approximately equal to the width of one scan line (0.5 nm) and therefore more sensitive to the precise position of consecutive lines. While the underlying atomic lattice of the mica substrate cannot be resolved in these images, the observed orientations are consistent with a molecular arrangement in which the lysine residues occupy interstitial sites on the mica lattice vacated by K^+ ions (Figure 3.6e).[195] When deposited from the stock solution at high PLL concentration (0.01% w/v), the lysine chains adopt a more globular form, resulting in a homogeneous surface functionalisation (Figure 3.7).

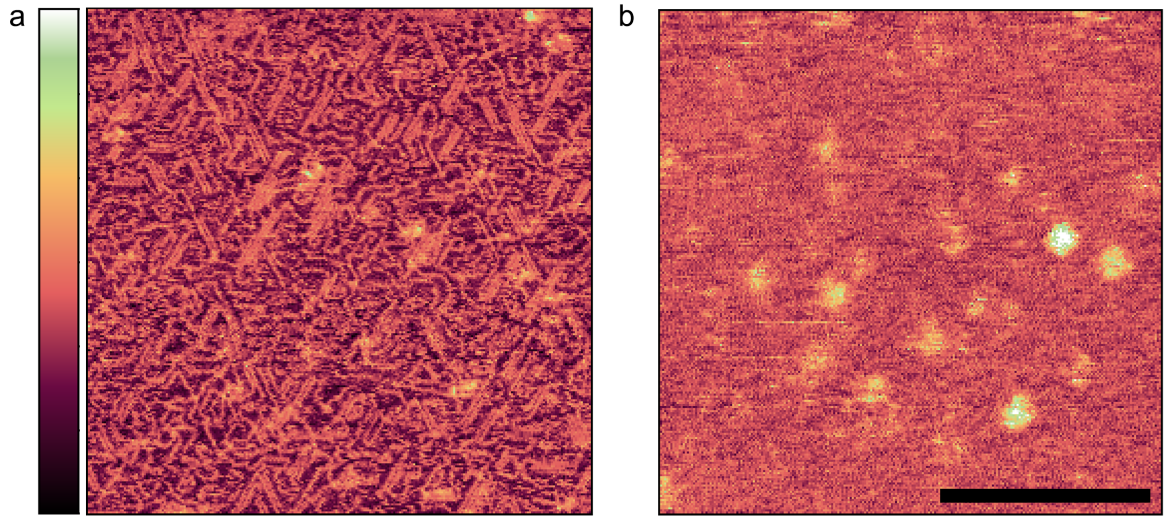


Figure 3.7: **AFM images of PLL-mica** (a) Mica after 5 minutes incubation with 0.001% PLL solution and subsequent washing. (b) Mica after 1 minute incubation with 0.01% PLL solution and subsequent washing. Both images were taken in solution with 0.5 nm pixel size. Scale bar (same for both images) is 50 nm. Height scale is shown on the left and is 3 nm.

PLL functionalised mica enhances the adsorption of DNA, but also of other biomolecules that may be present in solution, including those of reduced charge. This is demonstrated in Figure 3.8a by the immobilisation of both the highly negatively charged plasmid DNA and the slightly negatively charged streptavidin (pKa ∼5.0-6.0, at pH 7.4).[196] We show

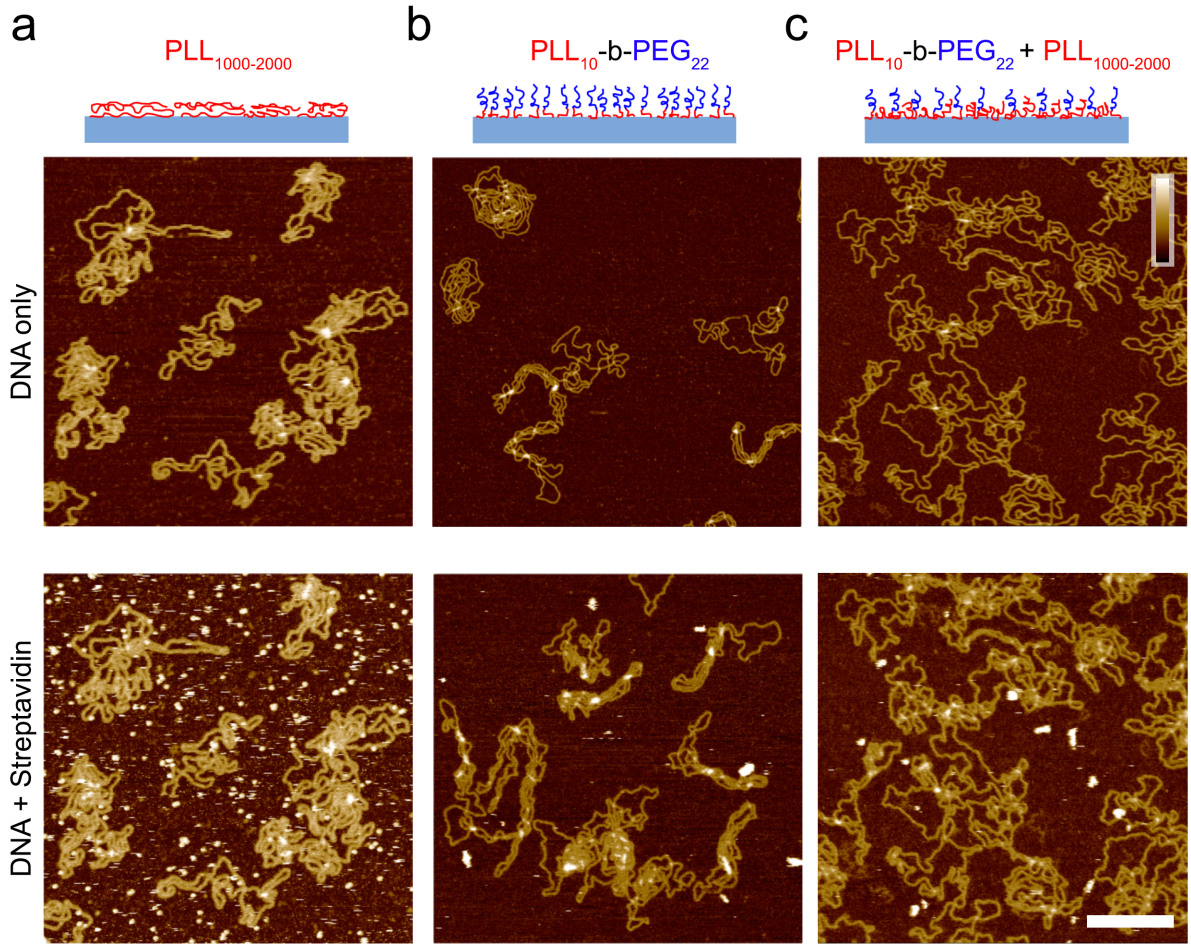


Figure 3.8: **Characterisation of the adsorption of DNA plasmid and streptavidin on functionalised mica** Streptavidin (160 nM) was added after DNA immobilisation, DNA was incubated for 10 minutes prior to imaging and streptavidin was left to equilibrate for 10 minutes prior to imaging on (a) $PLL_{1000-2000}$ only surface, (b) PLL_{10}-*b*-PEG_{22} and (c) a mixed PLL_{10}-*b*-PEG_{22}/$PLL_{1000-2000}$ surface. Colour scale (inset in top right) 10 nm; scale bar 200 nm.

that the surface can be modified to achieve a more preferential, selective adsorption of DNA, based on functionalisation with PLL_{10}-*b*-PEG_{22} alone or on functionalisation with a combination of PLL_{10}-*b*-PEG_{22} and long-chain $PLL_{1000-2000}$. In the presence of the block copolymer, streptavidin adheres as sparse clusters (Figure 3.8b and c), perhaps due to heterogeneous surface coverage of the protein-repellent PEG. In both cases, large areas of functionalised mica are visible without any protein adsorbed. This can be explained by the effective repulsion that arises when the polyethylene-glycol chains form a sufficiently

dense steric barrier.[174]

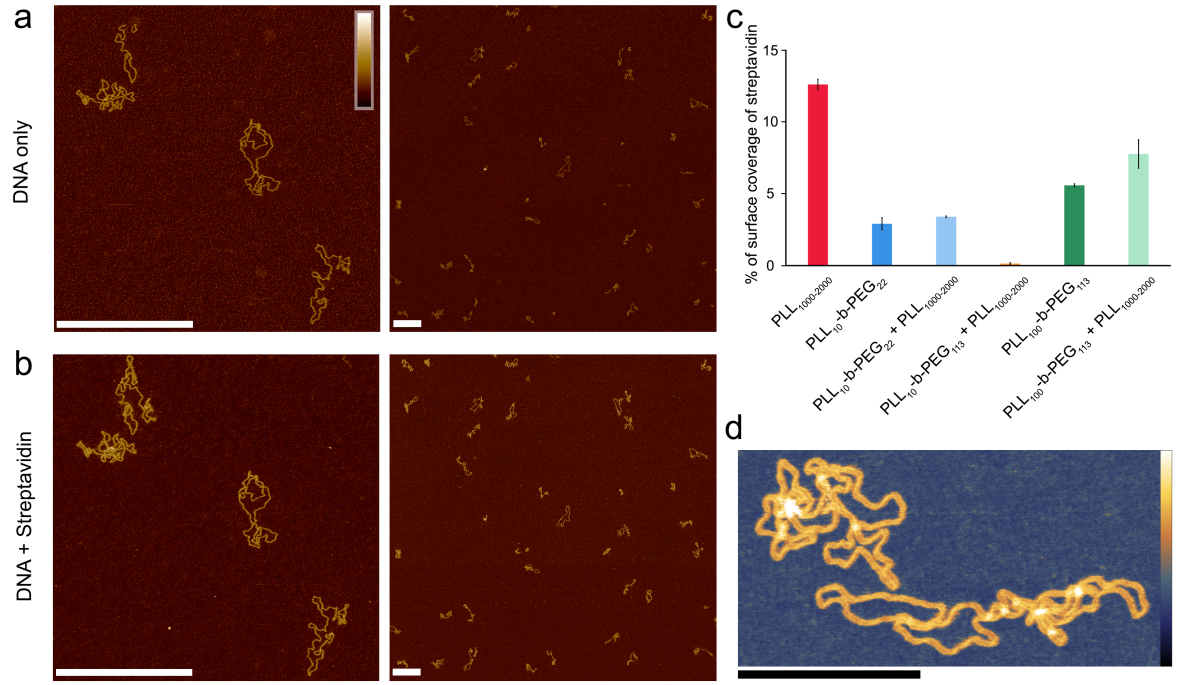


Figure 3.9: **Optimised Poly(L-lysine)-*b*-Poly(ethylene glycol) surfaces for exclusive DNA adsorption** AFM images taken in solution showing selective DNA adsorption on PLL_{10}-*b*-PEG_{113} / $PLL_{1000-2000}$ surfaces. (a) DNA plasmid only. (b) The same area following the addition of 160 nM streptavidin. (c) Percentage background streptavidin coverage at 160 nM for functionalisation protocols using different PEG chain lengths, error bars correspond to the minimum and maximum values as determined from two different areas. (d) A higher resolution image of DNA on the PLL_{10}-*b*-PEG_{113} / $PLL_{1000-2000}$ surface. Colour scales for (a) and (b) with inset scale bar are 7 nm, (d) with scale shown on the right is 9 nm. Scale bars in (a) and (b) are 500 nm and in (d) 200 nm.

To achieve a homogeneous surface that resists protein adsorption across the entire sample, the PEG molecules should be grafted at a density that is large enough to facilitate overlap between different chains, resulting in the formation of a dense polymer brush.[197] This requires the radius of gyration R_G for the polymer to be comparable with or larger than the mean distance between grafting sites. It follows that longer PEG chains are more effective in passivating a surface against protein binding, provided that they are grafted at sufficient densities.[198] By increasing the PEG block length (y) in the PLL_x-*b*-PEG_y diblock copolymer, we generated an optimised surface functionalisation that resisted non-specific protein adsorption in a solution of 160 nM streptavidin (Figure 3.9). PLL_{10}-*b*-PEG_{113} con-

structs were more effective than PLL_{10}-*b*-PEG_{22} in preventing streptavidin binding, but co-deposition with $PLL_{1000-2000}$ was required to facilitate the adsorption and imaging of DNA. Finally, for even longer PEG chains (PLL_{10}-*b*-PEG_{454}), DNA adsorption appeared to be prevented altogether, even in the additional presence of $PLL_{1000-2000}$ chains (Figure 3.10c). This comes with the caveat that we cannot fully exclude that DNA absorption to the underlying PLL layer is obscured by the PEG layer: the hydrodynamic radius of the PEG_{454} is ∼13.7 nm and therefore the film thickness is expected to be much greater than the height of the DNA.

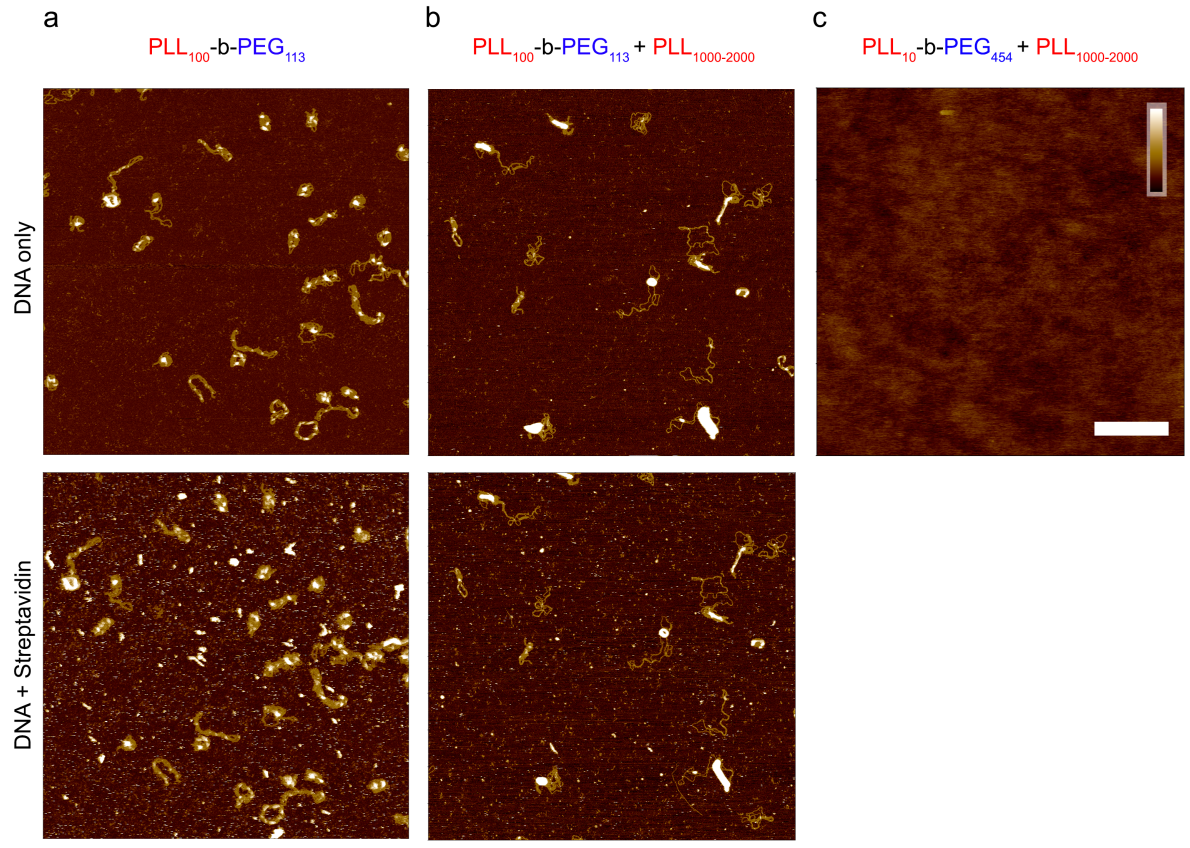


Figure 3.10: **Additional characterisation of DNA plasmid and streptavidin adsorption on functionalised mica** Streptavidin (160 nM) was added after DNA plasmid immobilisation on (a) PLL_{100}-*b*-PEG_{113} surface, (b) a mixed PLL_{100}-*b*-PEG_{113} and $PLL_{1000-2000}$ surface and (c) PLL_{100}-*b*-PEG_{454} surface. Inset colour scale 8 nm and scale bar 200 nm. Images taken in solution.

In addition to varying the PEG block length, we studied the effect of changing the PLL chain length x in the diblock copolymer PLL_x-*b*-PEG_{113} (Figure 3.10a and b). By contrast

to PLL_{10}-*b*-PEG_{113}, PLL_{100}-*b*-PEG_{113} facilitated DNA adsorption without additional long chain PLL, however this surface was less selective, also showing higher affinity for streptavidin. This implies that the longer lysine block (in the PLL_x-*b*-PEG_{113}) increases the spacing between the passivating PEG moieties. In this case the effective grafting distance between these moieties becomes larger than their extension, such that they adopted collapsed coil conformations and no longer form an effective steric barrier.[173] It should also be noted that with the increased length of PLL in the block copolymer, the DNA plasmids appear more condensed than on PLL_{10}-*b*-PEG_y, forming toroid and rod-like structures, as seen in Figure 3.10a and b.[191]

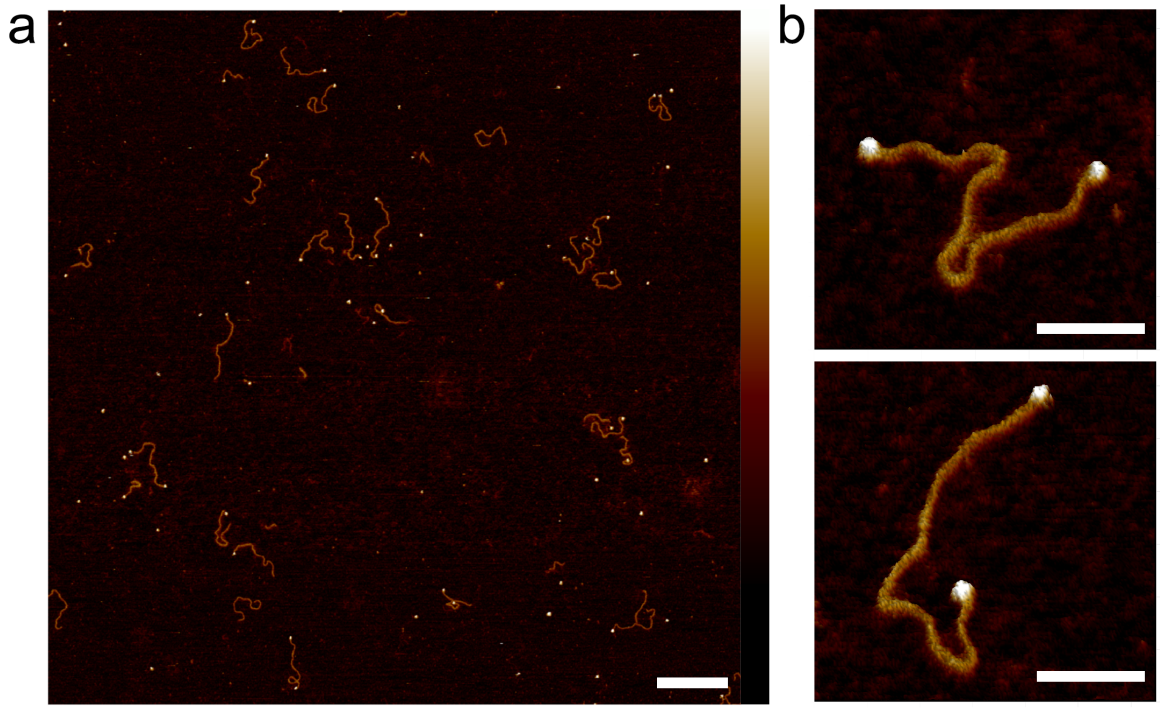


Figure 3.11: **Streptavidin binding to dual-end biotinylated 672 bp linear dsDNA on mica treated with PLL_{10}-*b*-PEG_{113} / $PLL_{1000-2000}$.** (a) AFM image taken in solution of 672 bp DNA after pre-incubation with ∼50× molar excess of monovalent mono-streptavidin over the biotin tag. (b) High-resolution images showing mono-streptavidin bound to both ends of dual-biotin DNA. Colour scale (see inset) is 5 nm. Scale bar for (a)is 200 nm and for (b) 50 nm.

By qualitative comparison of the images and by quantification (Figure 3.9c), PLL_{10}-*b*-PEG_{113} / $PLL_{1000-2000}$ treatment emerges as the most effective in suppressing streptavidin binding whilst allowing visualisation of DNA by AFM. To determine if this functional-

isation is also effective to study protein interactions, a biotinylated DNA construct to which streptavidin could bind was designed. Biotin binds to streptavidin with a high affinity (K_d on the order of femtomolar). These binding partners were also chosen for their relatively low dissociation rate (less than 10% of molecules were shown to dissociate after 12 hours at 37°C).[133] Two streptavidin variants were considered: tetravalent streptavidin and monovalent streptavidin. Although both exhibit a similar binding affinity, monovalent streptavidin has only one functional biotin binding subunit, compared with four in wild-type streptavidin. This well-established interaction was used as a proof of concept model, whereas the surface modification strategy presented may also be of interest to others wishing to directly probe DNA-protein interactions that are important for the regulation of cellular function.

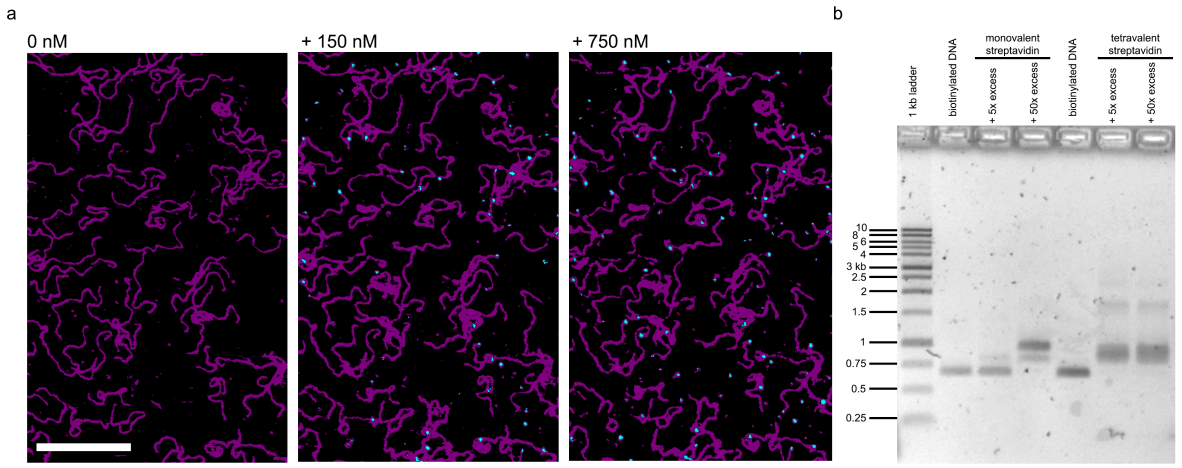


Figure 3.12: **Streptavidin binding to dual-biotin 672 bp linear dsDNA.** (a) An AFM image with the colour scale adjusted to highlight immobilised DNA (magenta) and added tetravalent streptavidin (cyan) for streptavidin concentrations of 0 nM, 150 nM and 750 nM (from left to right). (b) Clear band shifts confirm binding of monovalent streptavidin when pre-incubated for 5 minutes at ∼50× excess and tetravalent streptavidin when at ∼5× excess over the number of biotin binding sites. Scale bar in (a) is 200 nm.

For this study, Nicholas Bell (Francis Crick Institute) created a 672bp length of dsDNA with a single biotin at each end by using PCR amplification with biotinylated primers (see Methods section 2.2.1). The binding of streptavidin with either one or four binding sites to the dsDNA construct was confirmed by electrophoretic band shift assay shown in Figure 3.12b. DNA incubated with a 50× excess of monovalent streptavidin was adsorbed on

the PLL_{10}-*b*-PEG_{113} / $PLL_{1000-2000}$ functionalised mica surface (See Figure 3.11). DNA molecules with streptavidin bound to both biotinylated ends were specifically adsorbed to the surface (Figure 3.11b). The excess monovalent streptavidin in solution was not observed at high concentration on the surrounding background, implying good non-specific protein passivation. Overall around 40% of adsorbed streptavidin molecules were found at the ends of DNA ($n = 531$). The advantages of PLL_{10}-*b*-PEG_{113} / $PLL_{1000-2000}$ functionalisation were further demonstrated by comparison with the traditional $PLL_{1000-2000}$-only functionalisation, which yielded increased adsorption of non-DNA-bound streptavidin on the surface shown in Figure 3.13.

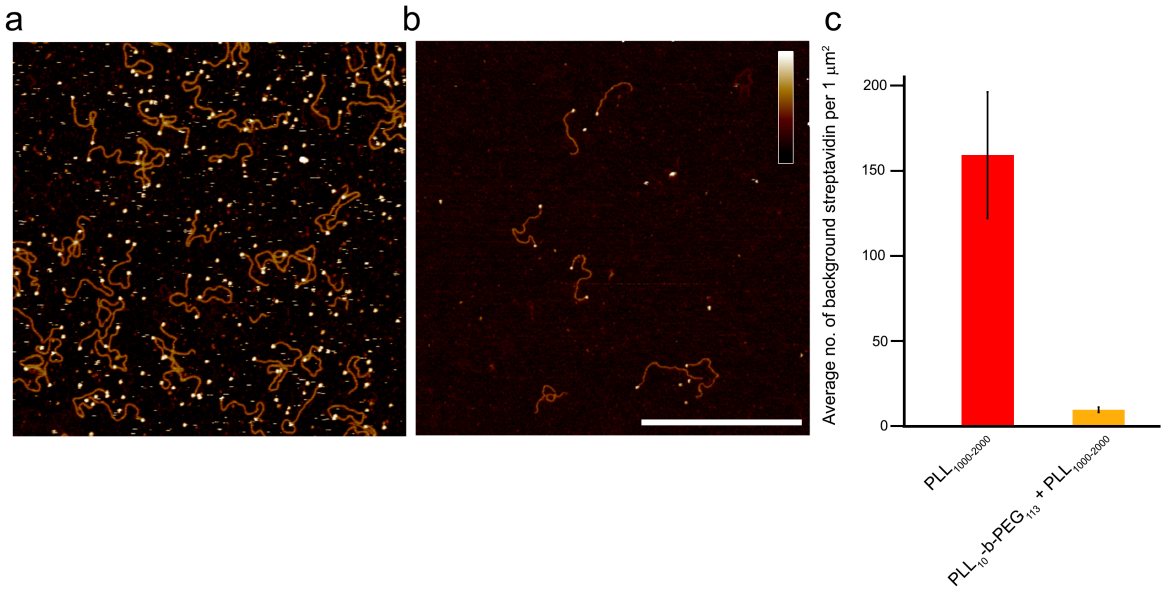


Figure 3.13: **Dual-biotin 672 bp DNA pre-incubated with monovalent streptavidin.** added to (a) $PLL_{1000-2000}$ and (b) PLL_{10}-*b*-PEG_{113} / $PLL_{1000-2000}$ surface. (c) a graph of the average number of streptavidin molecules bound to the background (i.e., not on the end of a DNA molecule) per 1 μm^2 analysed for passivated surface (mean $\pm$ standard deviation, n = 8 images, 32 μm^2) and for the PLL surface (n = 7 images, 28 μm^2). Scale bar is 400 nm and height scale is 6 nm.

It is of considerable interest to study the dynamics of DNA-protein interactions. To determine whether this method can be used to study the binding of streptavidin to biotinylated DNA strands *in situ*, tetravalent streptavidin was flowed over biotinylated DNA that had already been immobilised on PLL_{10}-*b*-PEG_{113} / $PLL_{1000-2000}$ functionalised mica (see Figure 3.12a). To enhance the differentiation the AFM images were thresholded by height to

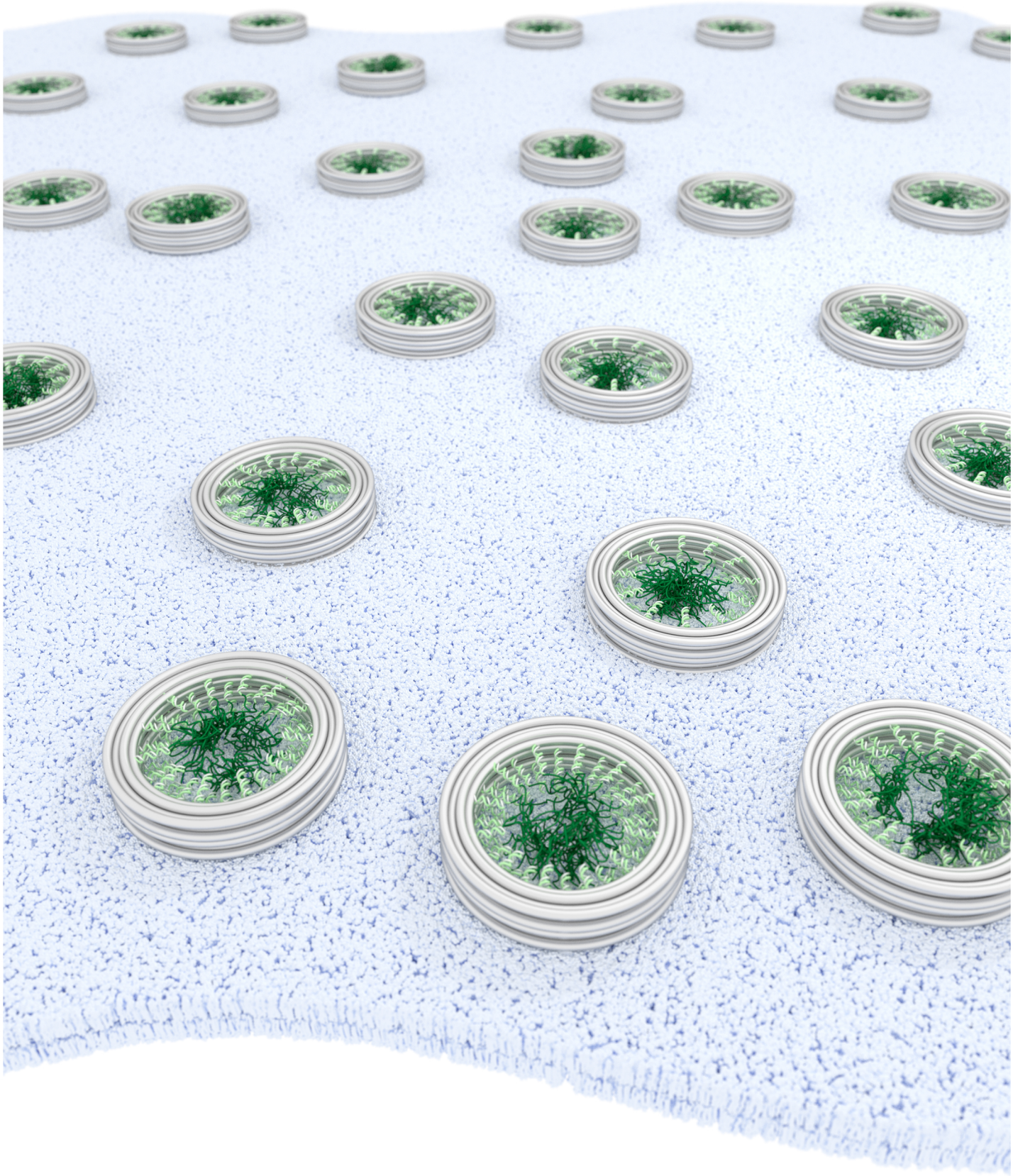
differentiate between streptavidin ($\sim$ 4 nm), DNA molecules ($\sim$ 2 nm) and the substrate (at 0 nm). The colour scale was then adjusted to colour DNA molecules in magneta and streptavidin in cyan. Binding is observed as the formation of cyan protrusions at the ends of the immobilised biotinylated DNA substrates (magenta). These can seen to accumulate as the solution concentration is increased from 150 nM to 750 nM. A higher concentration of streptavidin is required to show significant binding to immobilised biotinylated DNA, as compared with biotinylated DNA in solution. This suggests limited accessibility of the biotin binding site, presumably due to the lack of conformational flexibility of the ends of the immobilised DNA molecules; in addition, the streptavidin may be repelled to some degree by the PEG moieties, introducing an additional barrier to binding. In this instance tetravalent streptavidin was used as opposed to monovalent streptavidin to increase the surface area for binding, thus reducing steric hinderance effects.[199]

3.3 Discussion

This work has shown that dsDNA can be adsorbed onto gel-phase lipid membranes formed from the synthetic cationic lipid DDAB. In addition, it has been demonstrated that hydrophilic diblock copolymers comprising both a cationic surface binding domain (PLL) along with a neutral protein repellent domain (PEG) can be used to functionalise mica for the selective binding of biomolecules. The chain lengths of both blocks were optimised to reduce the non-specific adsorption of streptavidin in solution, whilst adsorbing highly charged DNA molecules. The surface-passivating properties of this PEG film are demonstrated through the selective binding of biotinylated DNA-streptavidin complexes, minimising non-specific streptavidin surface binding. Furthermore, this functionalisation strategy lends itself more generally for the study of DNA interactions with other proteins. The PLL_{10}-*b*-PEG_{113} / $PLL_{1000-2000}$ surface functionalisation could also be used to study the protein-protein interactions, where one binding partner is anchored to an immobilised DNA scaffold. This methodology is indeed applied and reported later in Chapter 6 where interactions between FG-nups (anchored on DNA origami nanopores) and NTRs (free in solution) are studied.

It is important to be aware of different surface adsorption protocols for AFM and their af-

fect on a given biomolecule's confinement, particularly when hybrid protein-DNA systems are probed. Specifically, the surface functionalisations presented in this chapter provide a basis for AFM and TIRF microscopy studies on NPC mimicking nanopores formed from DNA origami scaffolds, as described in the following chapters.



Chapter 4

Mimetic nuclear pore complexes based on DNA origami

This chapter is based in part upon the paper "A programmable DNA origami platform for organizing intrinsically disordered nucleoporins within nanopore confinement" by P. D. Ellis Fisher, Q. Shen, B. Akpinar, L. K. Davis, K. K. H. Chung, D. Baddeley, A. Saric, T. J. Melia, B. W. Hoogenboom, C. Lin, and C. P. Lusk, published in *ACS Nano* vol. 12, no. 2, pp 1508-1518, 2018.

The experimental work in this chapter was carried out in collaboration with Patrick Ellis Fisher (P.D.E) and Qi Shen (Q.S) at Yale University, who designed and produced the DNA origami and protein constructs which I then hybridised and purified for further characterisation (see methods section 2.1 for further details). The computational simulations were carried out by Luke Davis (UCL).

4.1 Introduction

Located within the central channel of the NPC, the transport barrier consists of ∼12 types of nucleoporins, denoted as FG-nups. This FG-nup assembly contains thousands of repetitive peptide motifs, the major types being FG/FxFG and GLFG. Subtle differences in these repeat sequences are also thought reflect their differing roles in the maintenance

of the NPC's barrier. Whilst FxFG/FG repeats are known to dock RNA for export and are enriched in the nuclear and cytoplasmic peripheries, GLFG are essential for the exclusion of non-specific molecules and are localised near the walls of the NPC and at the cytoplasmic entrance.[8,9,21,22] Owing to the disordered nature of these proteins that occupy the central channel and the added complexity of the presence of endogenous NTRs and cargos, its biophysical nature remains hard to assess and its organisation has remained ill-defined. This contrasts with the 8-fold radially symmetric NPC scaffold, which has been visualised, for a number of species, with ∼3 nm resolution using cryo-EM data along with integrative structural analysis.[8,13,15] These structures, in combination with extensive biochemical analyses of nup-nup interactions[5,11,200–202] and nup stoichiometry[4,5,5,14,203] are revealing the fundamental and evolutionarily conserved mechanisms that constitute the NPC, but have not yet been able to define its permeability properties.

In addition to *in vivo* and *ex vivo* experiments, efforts have also been directed at explaining FG-nup behaviour within conceptually simple polymer models that ignore many of the underlying chemical details of the FG-nups.[45,73] These models can explain the behaviour of FG-nups grafted onto planar films, which is impacted by the type of FG-nup, grafting density, and the concentration of NTRs in solution.[38,53,54,56] However, such polymer models[42,204] also predict qualitatively different collective behaviours depending on the exact architecture and geometry that the FG-nups are grafted in. This prediction remains to be explored experimentally.

Hence, important outstanding questions include: how FG-nups organise within nanopore confinements that mimic the NPC channel, how this organisation depends on the grafting geometry, density and stoichiometry, how it depends on the type of FG-nup — given that not all FG-nups are alike[9,35,36,205] — and to what extent such behaviours can be captured by generic polymer physics. Ideally, this is explored in a system that also offers a perspective to investigate how such behaviours translate into transport properties in a pore geometry. Encouragingly, NPC transport properties have been recapitulated in nanopore devices containing grafted FG-nups.[40,96,101] Moreover by measuring the permeability of ions and molecules through these nanopores, in varying conditions, some insight into the underlying behaviour of the FG-nups can be inferred. However, our knowledge of configurations adopted by these disordered proteins confined within nanopores remains fragmentary, primarily because it is challenging to visualise protein dynamics inside a

nanopore, and because — when designing the nanopores — it is hard to precisely control where the FG-nups are anchored to the nanopore wall, at at what density.

The following chapter describes the use of DNA nanotechnology to tackle this problem, and specifically the technique termed 'DNA origami', which can fold a long, single-stranded DNA (ssDNA) with many short, synthetic DNA strands into designer shapes.[111,117] Importantly, the resulting shape-controlled DNA origami nanostructures can be chemically modified at specific positions, making them particularly useful as nanoscale scaffolds for organising guest molecules with precisely controlled stoichiometry and spatial positioning. For example, a defined number (usually less than 10) of well-folded proteins, such as SNAREs,[206] motor proteins,[207,208] enzymes,[209] and ephrins,[210] have been assembled on DNA origami structures, for studying diverse molecular interactions and collective biochemical functions.[211] Here this technology is utilised to construct biomimetic nanopores in which FG-nup anchor points and stoichiometry can be precisely controlled within a cylindrical architecture that mimics the native NPC geometry. This work provides evidence that cylindrical confinement impacts the collective properties of FG-nups, and establishes an experimental system that allows the direct visualisation of FG-nup dynamics within pore architectures.[39]

4.2 Results

4.2.1 Organising disordered FG nucleoporins using soft scaffolds

To mimic the native NPC channel of ∼40 nm inner diameter,[13] a DNA origami cylinder with an inner diameter of 46 nm and a height of 14 nm was designed by P.D.E, see Figure 4.1a and b. The cylinder consists of 16 DNA double helices and contains 21-nucleotide ssDNA handles that extend inward from the inner wall in up to four layers, providing anchor points for the FG-nups. These handles are flexible; when annealed with the complementary anti-handles, they form 7 nm long double-stranded DNA rods that can rotate around their anchor points at the DNA origami cylinder. Hence the effective diameter of the FG-nup grafting points inside the DNA origami will be between 32 and 46 nm. The scaffold also incorporated 12 additional ssDNA sites, with two separate

sequences for the attachment of biotin or fluorophores (see design in section 2.1.1).

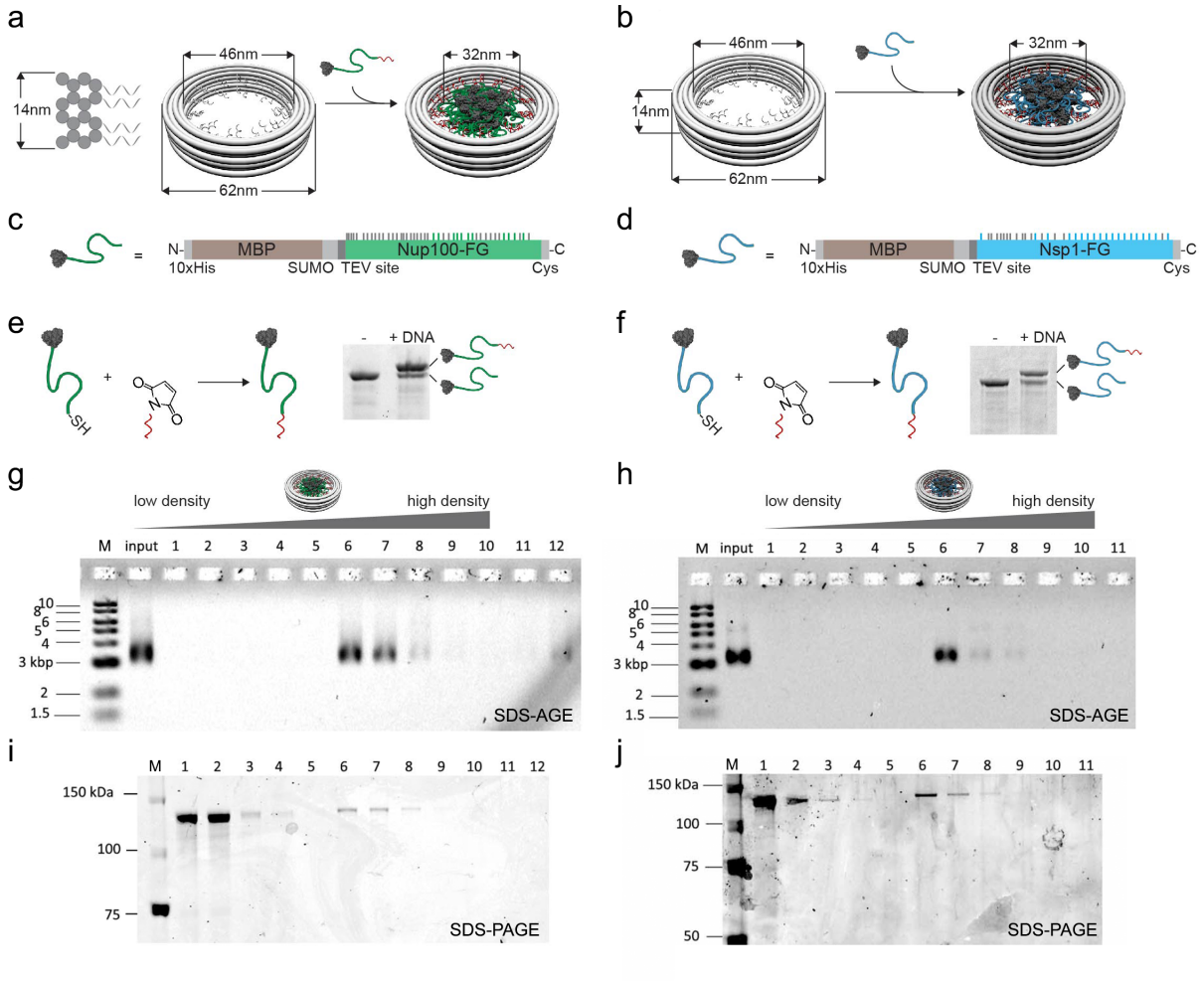


Figure 4.1: **Design and assembly of nucleoporins organised on DNA('NuPOD').** A cross section and a cartoon of the DNA origami cylinder with protruding inner DNA handles hybridised to DNA labelled MBPNup100 (a) or MBPNsp1(b). MBPNup100-FG (a.a. 2–610)(c) and MBP-Nsp1-FG (a.a. 2–603)(d) protein constructs. FG-repeats are shown as vertical lines (with green, blue,and grey lines representing GLFG repeats, FxFG repeats, and other FG-repeats, respectively). The strategy for thiol-maleimide linkage between FG-nups and DNA, with SDS-PAGE showing the separation between proteins (-) and protein-DNA conjugates (+), MBPNup100 proteins stained by SYPRO Red (e) or MBPNsp1 proteins wih Coomassie (f). Rate-zonal centrifugation shows hybridised NuPODs enriched in fraction 6, (M, molecular weight marker; input, before centrifugation.) SDS-agarose with EtBr stain for MBPNup100 (g) and MBPNsp1 (h). SDS-PAGE with SYPRO red stain for MBPNup100 (i) and Nsp1 (j).

Due to design restraints imposed by the length of the scaffold strand, 8-fold symmetry could be maintained for DNA cylinders containing 8, 16, 24, and 32 FG-nups, but had to increase the number of anchor points to 12 per layer to accommodate a maximum of 48 proteins. Thus, these DNA cylinders provide a platform for studying physiologically relevant FG-nup copy numbers in a pore geometry; in the budding yeast NPC, for example, Nsp1 is found in 48 copies.[5,8,11] Moreover, the DNA cylinders have a grafting density of ∼3 FG-nup molecules per 100 nm^2 for the 48 handle version, which is comparable to previously-studied planar monolayers of FG-nups, typically in the range of ∼2-6 molecules per 100 nm^2.[38,53,54,56,73] The DNA cylinders can thus house FG-repeats at physiologically relevant concentrations (100-200 mM[4,17,26]).

The DNA origami cylinders were functionalised with purified FG-domains that represent the two major repeat classes of FxFG and GLFG, by expressing and purifying the *S. cerevisiae* orthologues of metazoan Nup62 (Nsp1) and Nup98 (Nup100), respectively. Importantly, the FG-domains chosen were truncated from the full length protein to have virtually identical molecular masses but unique chemical composition in their amino acid sequences (notably in their charge content). Nsp1(2-603) has a higher content of charged amino acids than Nup100(2-610) and thus adopts a more extended conformation in solution.[9] The FG-domains were recombinantly expressed with a TEV-cleavable 10×His-MBP-SUMO tag to ensure solubility in physiological buffers.[71] Additionally, DNA origami cylinders could be hybridised with 10×His-MBP-SUMO proteins alone (where MBP is an acronym for maltose binding protein), providing a useful experimental control.

To incorporate FG-domains into the DNA cylinder in the correct orientation (i.e., anchored at their C-termini[212]), the constructs were conjugated to maleimide-modified DNA 'anti-handles' (21-nucleotide strands of complementary sequence to the 'handles') via an engineered C-terminal cysteine, producing a site-specific, stoichiometric protein-DNA conjugate (see Figure 4.1c-f). The FG-domains were incorporated into the ring by the formation of a 21 bp double helix between the 'handles' and 'anti-handles' to generate what we term Nucleoporins Organised on DNA, or 'NuPODs'. Following hybridisation in a 7.5× excess of protein over DNA handle, the NuPODs were purified by rate-zonal centrifugation, which separated assembled NuPODs from free proteins (see verification by the observance of well-defined bands SDS-AGE and SDS-PAGE gels (Figure 4.1g-j).

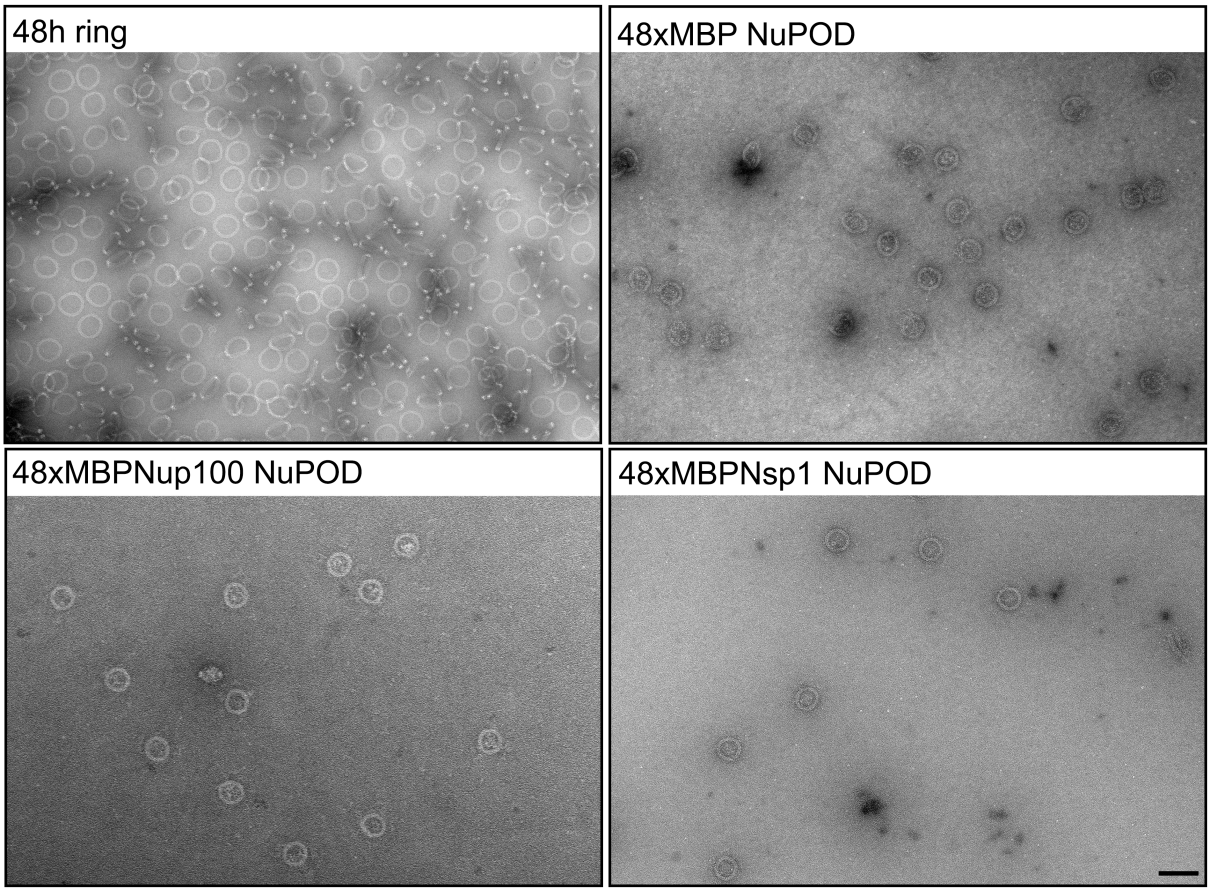


Figure 4.2: **Representative TEM images of DNA origami rings and assembled NuPODs** Images were taken at 25,000× magnification and the full field of view is shown here for empty rings and rings containing 48 copies of MBP, MBPNup100 or MBPNsp1 proteins. Scale bar is 100 nm. The image of 48×MBPNup100 was taken by Qi Shen (Yale) and others by myself.

Figure 4.2 shows representative TEM images of empty DNA origami cylinders alongside assembled NuPODs with 48 copies of either MBP, MBPNup100 or MBPNsp1. The MBP protein alone along with MBPNup100 can be easily visualised with negative stain TEM. Where MBPNup100 proteins appear to fully occlude the central lumen, MBP proteins cluster more towards the pore edge and form a less dense mass. Rings with 48 copies of MBPNsp1 proved more difficult to stain with sufficient contrast and would often extend beyond the DNA ring, reflective to the fact that Nsp1 is less cohesive than Nup100.[73] Note that for TEM imaging the samples are dried onto a hydrophilised carbon-coated grid and stained, therefore this sample-surface interaction also affects the conformation

observed for the anchored proteins.

4.2.2 Cleavage of MBP tags

The FG-nup constructs were designed with their solubilising MBP tags facing into the centre of the DNA origami scaffold, such that they can be cleaved after the proteins are stably anchored to the ring (see schematic in Figure 4.3a). The time needed for complete tag cleavage by TEV protease was found to be 1.5 hours at room temperature, despite

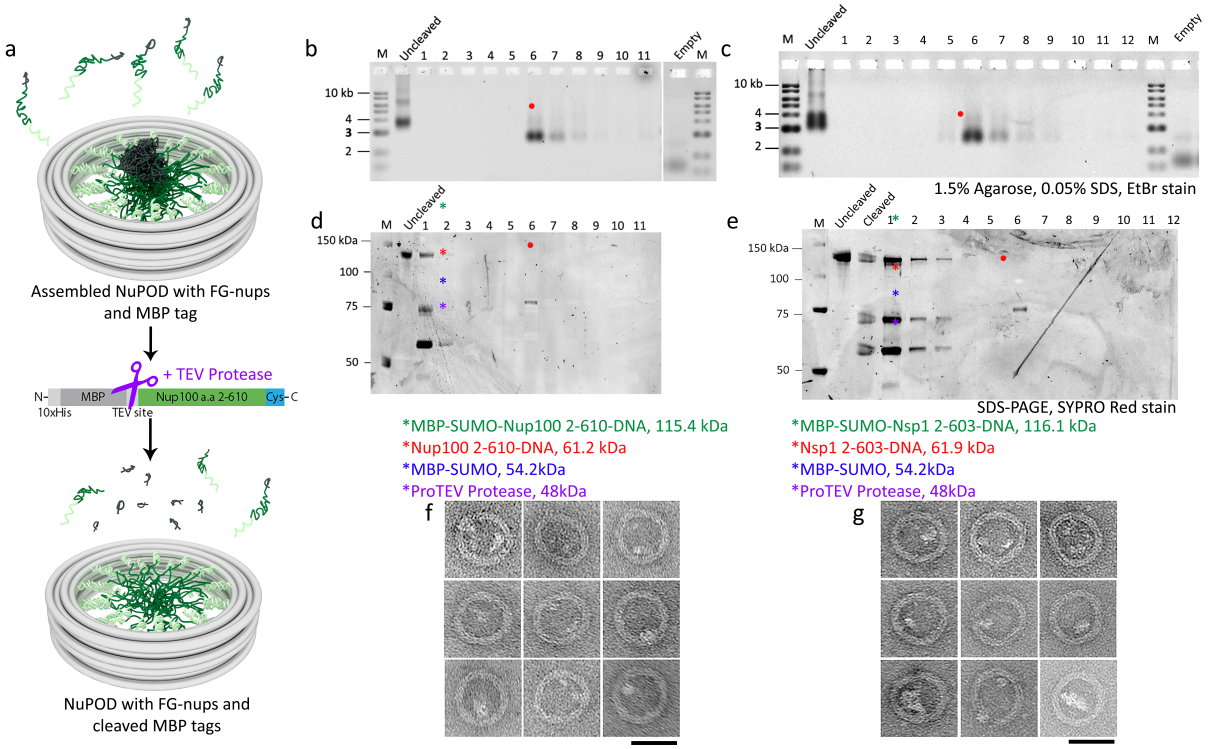


Figure 4.3: **Cleavage of the MBP tags from assembled NuPODs.** (a) Schematic showing cleavage of MBP tags from MBPNup100. TEV-protease was added to the hybridisation reaction and held at room temperature for 1.5 hours before purification of excess protein via rate-zonal centrifugation. (b-e) SDS-AGE and SDS-PAGE gels of rate-zonal centrifugation fractions of NuPODs with 48 copies of Nup100 or Nsp1. The uncleaved and unpurified reaction contained only the MBP-Nup100 or MBP-Nsp1 construct. After purification, partially cleaved free proteins were collected in the early fractions and the Nup100-NuPOD (b and d) or Nsp1-NuPOD (c and e) construct in fraction 6. Representive negatively stained TEM images of (f)48×Nup100-NuPODs and (g)48×Nsp1-NuPODs. The scale bars in the TEM images represent 50 nm.

the fact that the unpurified reaction mixture indicated incomplete cleavage (see multiple bands in the 'cleaved' lane of the SDS-PAGE gel in Figure 4.3e). The 6th fraction, containing the purified NuPOD contains only Nup100/Nsp1 (see Figure 4.3d and e). SDS-PAGE analysis of the first fractions collected following rate-zonal centrifugation (i.e., free-protein in the reaction mixture) shows bands corresponding to the molecular weights of MBP-Nup100/MBP-Nsp1, Nup100/Nsp1 and MBP. This indicates that the TEV protease selectively cleaves the MBP-tags from protein constructs that are attached to the DNA ring, over those that are free in solution. This can be attributed to the increased concentration and therefore density of TEV cleavage sites once the proteins are anchored onto the DNA origami scaffold.

Following removal of the MBP-tag, NuPODs show a decrease in density inside the cylinders and in many cases the proteins appear to collapse against the DNA origami walls, as visualised in the TEM images in Figure 4.3f-g. A priori, this collapse may be attributed to electrostatic DNA-protein interactions, since at neutral pH and in the absence of counter-ions, the DNA surface is more negatively charged than one would anticipate for the inside of the NPC central channel. However, in our experiments, counter-ions are present and we expect the DNA charge to be largely screened.[213] Specifically, all these experiments were carried out in the presence of 10-26 mM of the divalent electrolyte $MgCl_2$: this implies that the DNA surface charge is screened over a (Debye) length scale of <2 nm. Therefore the surface charge is expected to be relatively unimportant in determining the observed FG-nup morphology.

4.2.3 Anchoring different densities of FG nups

To ensure that purified NuPODs with 0-48 handles housed the predicted number of FG-domains, Patrick Ellis Fisher and Qi Shen first performed SDS-agarose gel electrophoresis (SDS-AGE) and looked at the relative band shifts, as a measure of molecular weight increase. As anticipated, the increase in polypeptide copy number led to a corresponding gel mobility shift (see Figure 4.4a and e). Moreover, the NuPODs were resolved as single, sharp bands, indicating that the samples were homogeneous. They next loaded equivalent amounts of NuPODs onto SDS-PAGE gels and immunoblotted for the 10×His tag with an antibody raised against a 5×His peptide. By comparing signal intensities to an

internal FG-nup concentration standard curve, one could see that there was a quantitative agreement with the design prediction, for example, the 48-handle NuPOD had 45.1 ± 5.2 (mean ± standard deviation) copies of MBPNup100 (see Figure 4.4c). Immunoblots were also performed on samples normalised to the concentration of DNA handles and thus theoretically, to the concentration of FG-nups. The resultant signal intensity was nearly identical between samples, further demonstrating that the number of grafted FG-nups scaled with the number of DNA handles and thus with the design prediction, see Figure 4.4b and f.

Negative-stain transmission electron microscopy (TEM) was used to visualise FG-domains, at different densities, in the confinement of the DNA cylinder. Protein density (appearing as white clumps) was only observed in NuPODs with at least 8 copies of MBPNup100 or MBPNsp1 (see Figure 4.4d and g). As the protein copy number was increased to 48, the center of the cylinder became completely filled for MBPNup100 whereas the less cohesive MBPNsp1 overflowed the cylinder, as evidenced by a wider spread of white puncta, interpreted as MBP moieites outside of the ring (arrowhead in Figure 4.4f, see also larger fields of view in Figure 4.2). Furthermore, the morphology of the 48×MBPNup100 or 48×MBPNsp1 was distinct from 48×MBP alone, which accumulated mostly at the channel walls, forming a donut with a distinct lack of density in the center (see Figure 4.2 and further discussion in Section 4.2.5).

To help interpret experimental observations, Luke Davies (UCL) performed coarse-grained molecular dynamics simulations for the respective grafting geometries, as shown in Figure 4.5. In these simulations, Nup100-FG and Nsp1-FG were modeled as homogenous polymers that experienced volume-exclusion as well as an attractive intra-/intermolecular interaction. The strength of the attractive, also termed 'cohesive',[38] interaction was set by comparing computational and experimental data for FG-nup assemblies that were grafted in a planar geometry.[73]

The resulting FG-nup arrangements appear in good overall agreement with the TEM data, notably in the distributions of the MBP domain (grey spheres in the MD snapshots in Figure 4.5) as a function of FG-nup copy number, and specifically in the larger spread of the Nsp1 variant in the 48-handle system, compared with Nup100. This difference between the Nsp1 and Nup100 FG-domains is fully consistent with previous reports[38,53]

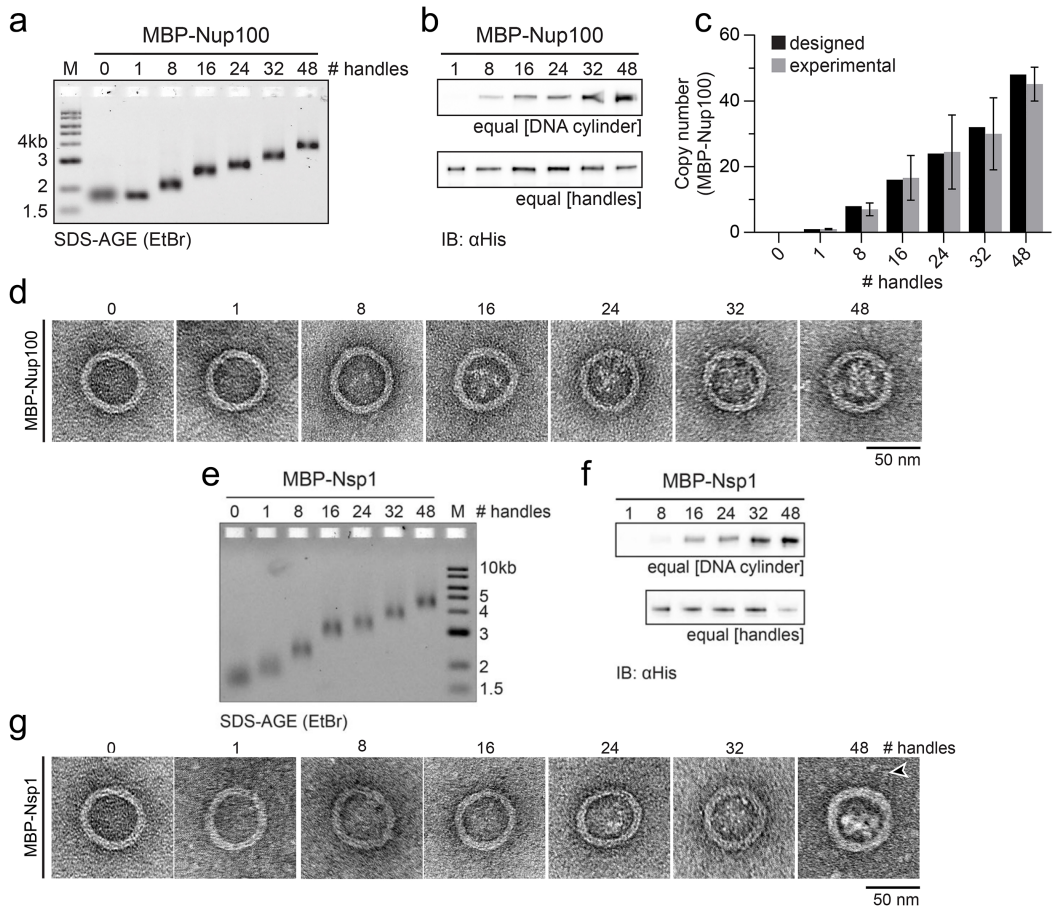


Figure 4.4: **A tunable DNA origami platform capable of housing different numbers of FG-nups.** Step-wise mobility shift of NuPODs as the number of FG domains increases for MBPNup100 (a) and MBPNsp1 (e) (M, molecular weight marker; SDS-agarose, EtBr stain). Immunoblots (αHis) loaded with either equal amount of DNA cylinders or number of DNA handles for MBPNup100 (b) and MBPNsp1 (f). Additional quantification of copy numbers of MBP-Nup100 in NuPODs are shown in (c)(N = 4 independent measurements for 1 and 8 handles, N = 5 for others; error bars show mean ± SD). Negative-stain TEM showing an appearance of protein clumps with increasing handle number in MBPNup100 (d) and MBPNsp1 (g) NuPODs. All measurements were carried out by Patrick Ellis Fisher and Qi Shen (Yale).

and indeed with the data underpinning the parameter settings for these simulations,[73] showing Nsp1 to be less cohesive than Nup100 (or its metazoan orthologue Nup98), and thus able to sample a greater volume.

Simulations shown in Figure 4.5 with and without the terminal MBP yielded largely

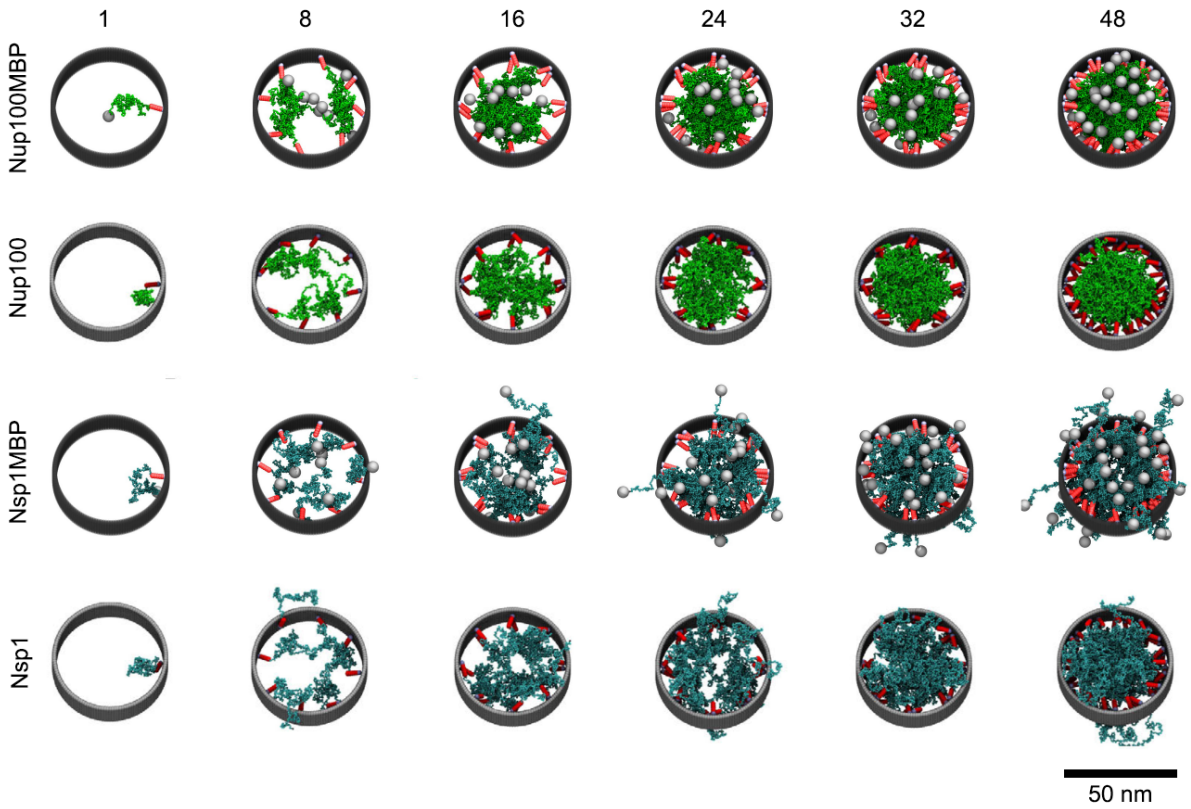


Figure 4.5: **Snapshots of equilibrated molecular dynamics simulations** The FG-domains are approximated as homogeneous polymers (green for Nup100 and blue for Nsp1) and modelled as 'beads-on-a-chain' consisting of beads, each representing two amino-acids, connected by harmonic springs. The phenomenological parameter of interaction strengh, ϵ_{pp} was set through a comparison of MD polymer brush simulations and experimental thickness data of FG-nup films.[73] Individual FG-nup polymers had one end attached to the tip of a DNA linker rod via a stiff harmonic spring. The DNA linkers were modelled as stiff chains and were kept fixed at one end at specific points along the cylindrical scaffold, although they were free to rotate about that anchor. Note that the cylinder was kept fixed throughout the simulation and was excluded from the integration scheme. Simulations were conducted with and without the terminal maltose binding protein (MBP). The MBP moiety is connected to the free-end of the FG-nups via a harmonic spring and is modeled as a sphere (light grey). Molecular dynamics simulations were carried out by Luke Davis and a full description can be found in the methods section 2.7.

similar results, indicating that the presence of the (inert) MBP — while beneficial for highlighting the presence of proteins attached to the NuPODs in the TEM images — did not greatly affect the FG-nup morphology in the NuPODs. This is further supported by

in vivo experiments that have shown, as an approximately globular, stable protein, MBP has little or no interactions with native proteins in the yeast NPC.[214]

4.2.4 Surface functionalisation for AFM imaging of NuPODs

For label-free and high-resolution measurements of FG-nup morphologies in solution, we imaged surface-immobilised NuPODs using AFM. To this end, a surface functionalisation strategy was developed that allowed adhesion of the DNA origami rings on a mica substrate, whilst interaction with the FG-nups was minimised to reduce the risk of surface-induced artefacts. The protocol deemed most effective for imaging FG-morphologies within NuPODs was that based on cationic supported lipid bilayers as described in

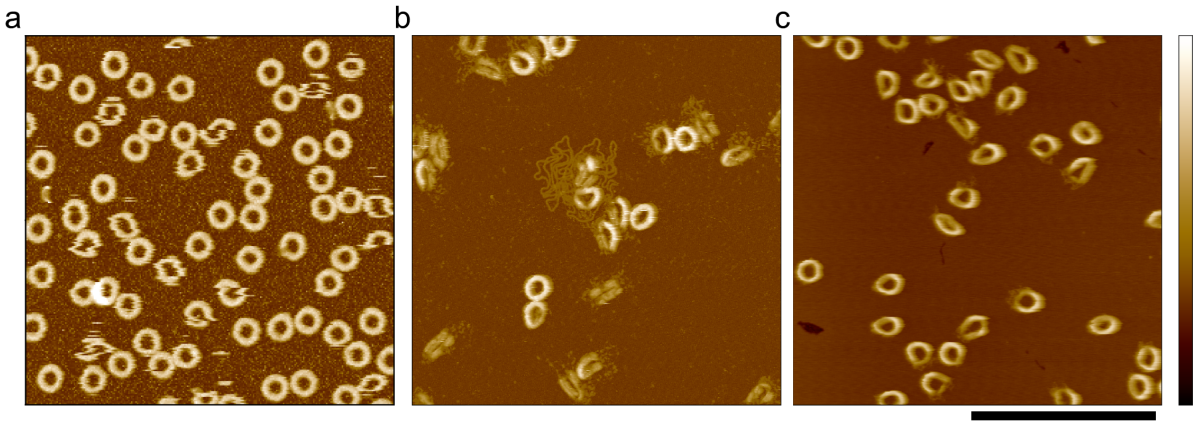


Figure 4.6: **Adsorption of DNA origami structures on mica using different functionalisation methods.** AFM imaging of empty DNA origami rings, prepared as described in section 2.1.1. a) On mica treated with 20 mM $NiCl_2$ and imaged in 1× PBS buffer containing 16 mM $MgCl_2$. b) A solution of 0.01% PLL was incubated on mica for one minute before thorough washing into buffer containing 1×TE, 16 mM $MgCl_2$. The interaction between the DNA origami and lysine is so strong that the DNA origami (held together by magnesium ions) is seen to fall apart, note scaffold strand and small staple strands around structures. c) Empty DNA origami rings are adsorbed on top of a cationic lipid bilayer (DPPC:DDAB, 3:1) and imaged in 10 mM PB, 26 mM $MgCl_2$. The black regions in the image are defects in the supported lipid bilayer. Images a) and b) were taken using Peak Force tapping mode, c) was taken in tapping mode. Height scale is 25 nm, scale bar is 500 nm.

Section 3.2.1. For these experiments, the supported lipid bilayer comprised a 3:1 ratio of

zwitterionic to cationic lipid (DPPC:DDAB). The composition was optimised to facilitate immobilisation of the DNA scaffold (via electrostatic attraction) whilst minimising the interactions of the FG-nups with the AFM substrate.

The effect of surface functionalisation was first explored by AFM imaging of DNA origami ring containing no protein. DNA origami structures can be adsorbed to mica discs in a variety of ways. Depending on the method used, rings were seen to absorb face up (see Figure 4.6a) or in more collapsed conformations (see Figure 4.6b and c). Clearly, the strength of the adhesion can induce instability in the DNA origami structure, which is held together by intercalating magnesium ions. Figure 4.6b shows how the DNA origami

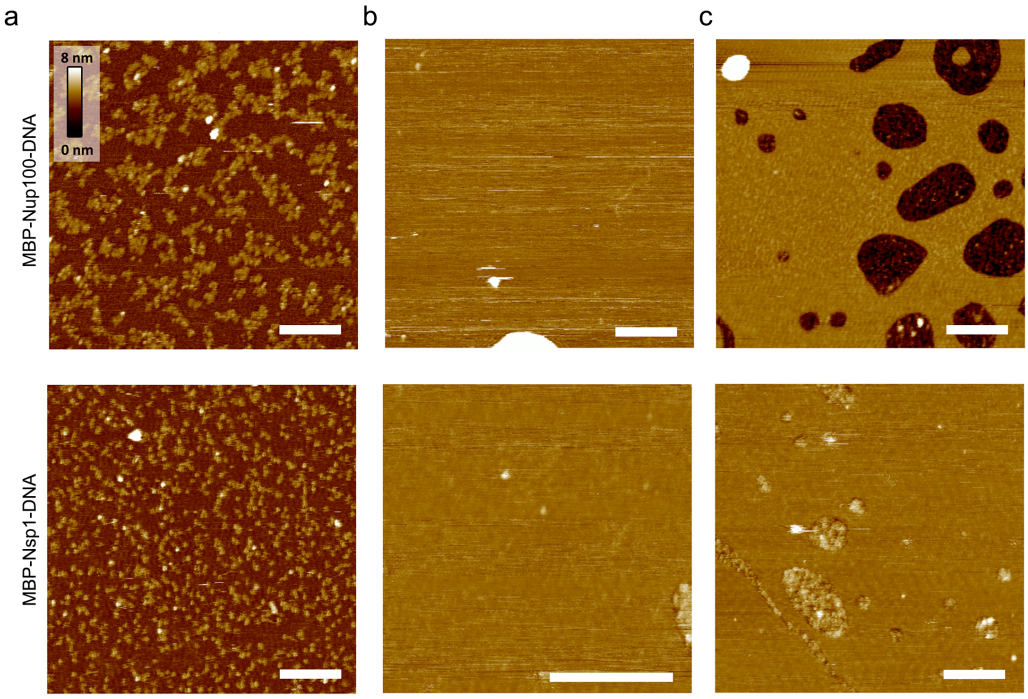


Figure 4.7: **MBP-FGnup-DNA adsorption on bare mica or on a supported lipid bilayers.** AFM topographs of protein-DNA conjugates on mica and on supported lipid bilayers.a) On a cleaved mica surface, as commonly used for AFM, both MBP-Nup100-DNA and MBP-Nsp1-DNA readily adsorb. b) A supported DPPC:DDAB (3:1) bilayer effectively passivates the mica substrate, showing practically no adsorption of protein (under otherwise identical conditions). c) When the mica substrate is only partially covered by the lipid bilayer, proteins adsorb and/or aggregate on the exposed mica surface only, while the bilayer surface remains free of protein. For these experiments, 1 μl of 100 nM MBP-FGnup-DNA was added and left to equilibrate for ~20 minutes before imaging in buffer (10 mM PB, 26 mM $MgCl_2$ pH 7.0). Scale bars are 200 nm.

structure can fall apart entirely upon adorption to a highly charged PLL surface (note DNA origami can be adsorbed stably to mica functionalised with PLL at lower concentrations).

For effectively imaging DNA origami conjugated to FG-nups, control experiments were conducted to evaluate the interaction strength between the FG-nups and the underlying substrate, being either freshly cleaved mica or a supported lipid bilayer, see Figure 4.7. The proteins are effectively repelled from supported lipid bilayers, but strongly adhere to the bare (i.e., not functionalised) mica surface. Furthermore, Figure 4.8 shows the appearance of 48×MBPNsp1 NuPODs adsorbed onto either PLL-mica (a) or a positively charged lipid bilayer (b). In the case of the PLL-mica, protein moieties can be seen extending beyond the confinement of the DNA origami ring, which can be attributed to non-specific adsorption of the proteins to the underlying substrate. By contrast, on the lipid bilayer, the surface charge (in these buffer conditions) is sufficient to adhere the DNA scaffold, yet the anchored nucleoporins retain conformational flexibility appearing to occupy the central lumen of the DNA scaffold as their interaction with the lipid surface is limited (see Figure 4.7).

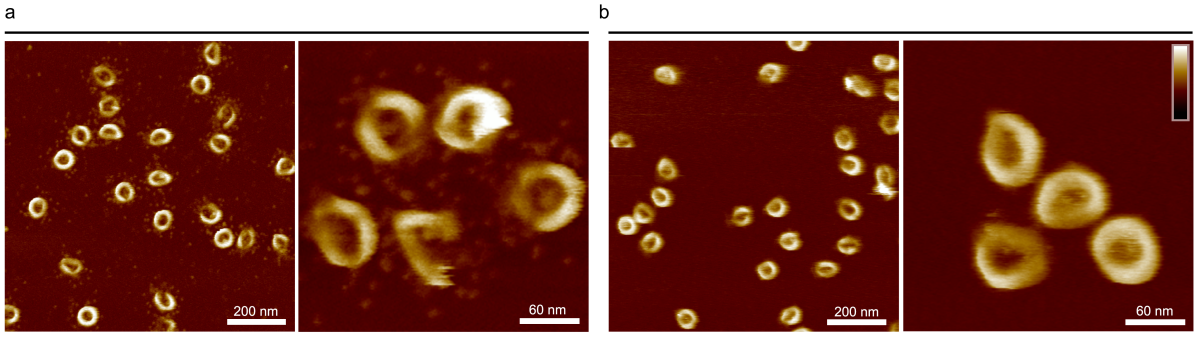


Figure 4.8: **AFM images of 48xMBPNsp1 NuPODs adsorbed on mica using different surface functionalisation methods** (a) Mica functionalised with an aqueous solution of 0.05% $PLL_{150-300k}$ for 1 minute before washing and imaging in 1×PBS,10% glycerol, 0.1% Tween-20, 10 mM $MgCl_2$. (b) A supported lipid bilayer (3:1, DPPC:DDAB) imaged in 10 mM PB, 26 mM $MgCl_2$ buffer. Colour scale is 24 nm.

On account of these observations, to best mimic *in vivo* conditions all images presented in the rest of this Chapter and in Chapter 5 were performed on NuPODs adsorbed on top of supported lipid bilayers, using a ratio of 3:1 of zwitterionic DPPC to cationic DDAB. The

imaging buffer for these experiments was 10 mM PB, 26 mM $MgCl_2$ pH 7.0, the higher concentration of magnesium was found to be important for integrity of the DNA origami structures.

4.2.5 AFM imaging of FG-nups on DNA origami

Figure 4.9 shows AFM images of NuPODs containing 48 copies of either FG-nucleoporins (with and without the MBP tag) or MBP alone. Consistent with the TEM and MD simulations, we find that in the absence of disordered FG domains, the MBP tags are frequently resolved lining the pore walls, whereas MBP-Nup100 and MBP-Nsp1 NuPODs have greater density in the central lumen (Figure 4.9b-c vs. f). This difference in

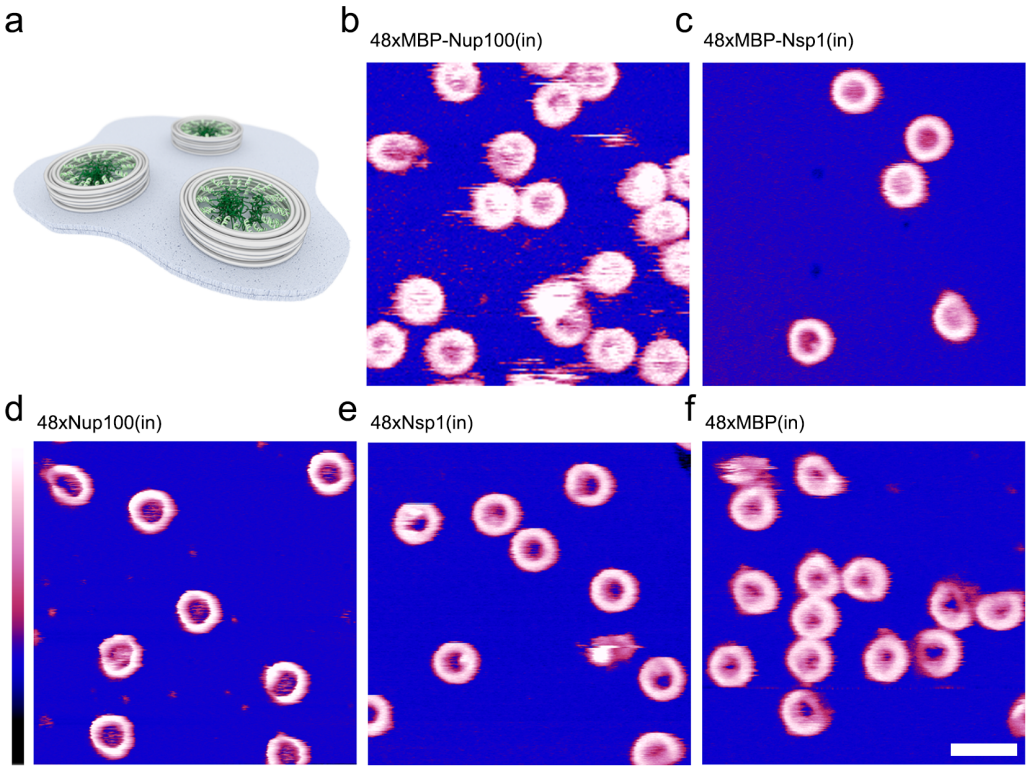


Figure 4.9: **AFM imaging NuPODs in solution**(a) Schematic depicting setup for AFM imaging with NuPODs adsorbed on top of a supported lipid bilayer. (b-f) AFM images of inside-grafted NuPODs adsorbed on a supported DPPC:DDAB (3:1) bilayer. (b) for 48×MBP-Nup100 (c) 48×MBP-Nsp1 (d) 48×Nup100 (e) 48×Nsp1 (f) 48×MBP. Scale bar is 100 nm, colour scale is 24 nm.

appearance can be attributed in part to the much greater mass of proteins in the latter case (∼5.5 MDa for 48×MBP-Nup100, ∼5.6 MDa for 48×MBP-Nup100 versus ∼2.7 MDa

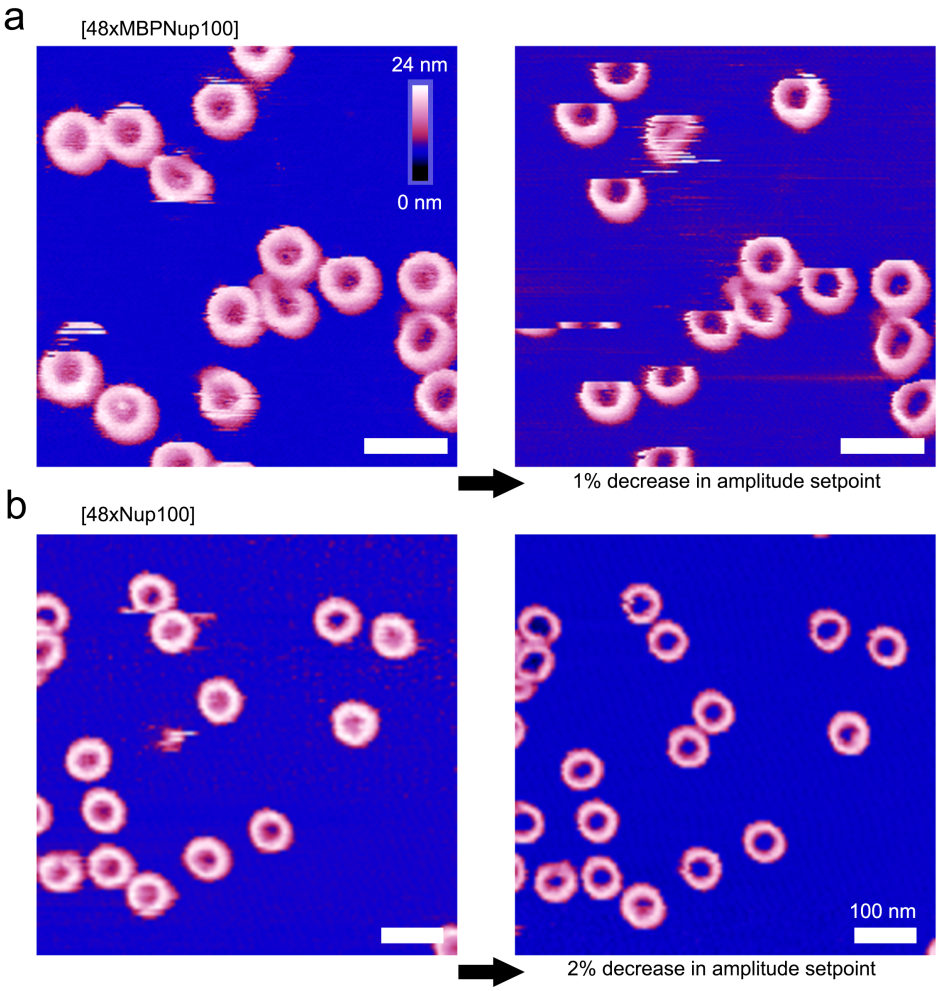


Figure 4.10: **AFM imaging force affects the appearance of the NuPOD lumen** In tapping mode AFM, as used here,the amplitude setpoint governs the tip-sample interaction and is a compromise between, on one hand, the need to minimise invasiveness (i.e., requiring a high setpoint, close to the free amplitude of the AFM probe as measured just above the surface) and, on other hand, the need to detect surface features with sufficient signal-to-noise ratio (a priori requiring a lower setpoint). (a) Imaging of the same area with 48×MBPNup100(in) NuPODs, recorded at an amplitude of ∼15 nm, for optimised parameter settings (left) and for an only marginally reduced setpoint (right). The optimum parameter range was rather narrow, and minor changes in setpoint (∼1%) could change the appearance of proteins in the NuPOD lumen. (b) As in a, for 48×Nup100(in) with the MBP tag cleaved off.

for 48×MBP). However, even after MBP-tag removal (such that there mass is now similar to MBP alone) the FG-nucleoporins show some density at the centre of the pore as well as larger clumps, presumably on account of cohesive interactions between FG repeats.[9]

Overall, we found significant variation in the appearance of the lumen of individual NuPODs for a given sample (see Figure 4.9a-e). DNA rings appeared to be diffusely filled, completely occluded with large central plugs, or almost empty. Although these observations suggest heterogeneity in the number of proteins bound to each ring, the narrow band observed in electrophoresis assays, along with quantification by western blot suggests uniform filling. Since the proteins are anchored onto the scaffold via a stable 21 base pair double helix, we assume that the proteins remain attached during the duration of the experiment where tapping forces of the AFM tip are maintained at around 100 pN. A much larger force would be needed to shear the proteins from the DNA by the downwards moving AFM tip; a shear force of ∼50 pN is required to rupture a 20 base pair length of DNA, but this is measured by magnetic tweezers which exert a direct pulling force as they stretch apart opposite ends of dsDNA.[215] However, the overall appearance of the FG-nups does depend strongly on the imaging conditions: NuPODs could be made to appear mostly empty upon a small increase in imaging forces (Figure 4.10). This indicates that the FG-nups are at the detection limit of these AFM experiments as conducted in solution.

The exact origin of this variation between different NuPODs could not be determined in our experiments, but we speculate that it is partly due to the intrinsically disordered nature of the FG-nups, due to the constraints imposed upon the FG-nups during adsorption of the NuPODs on the supported lipid bilayer, and/or due to the invasiveness of the AFM measurement. It should be noted that such heterogeneity in the appearance of FG-nups has also been observed for AFM imaging of native NPCs.[34]

4.2.6 3D architecture influences FG-nup morphology

Given the prediction from polymer models that pore geometry is a major determining factor for FG-nup behaviour and in particular molecular extension in the NPC,[42,204] we next compared NuPODs with 48 copies of MBP-Nup100 or MBP-Nsp1 grafted on the

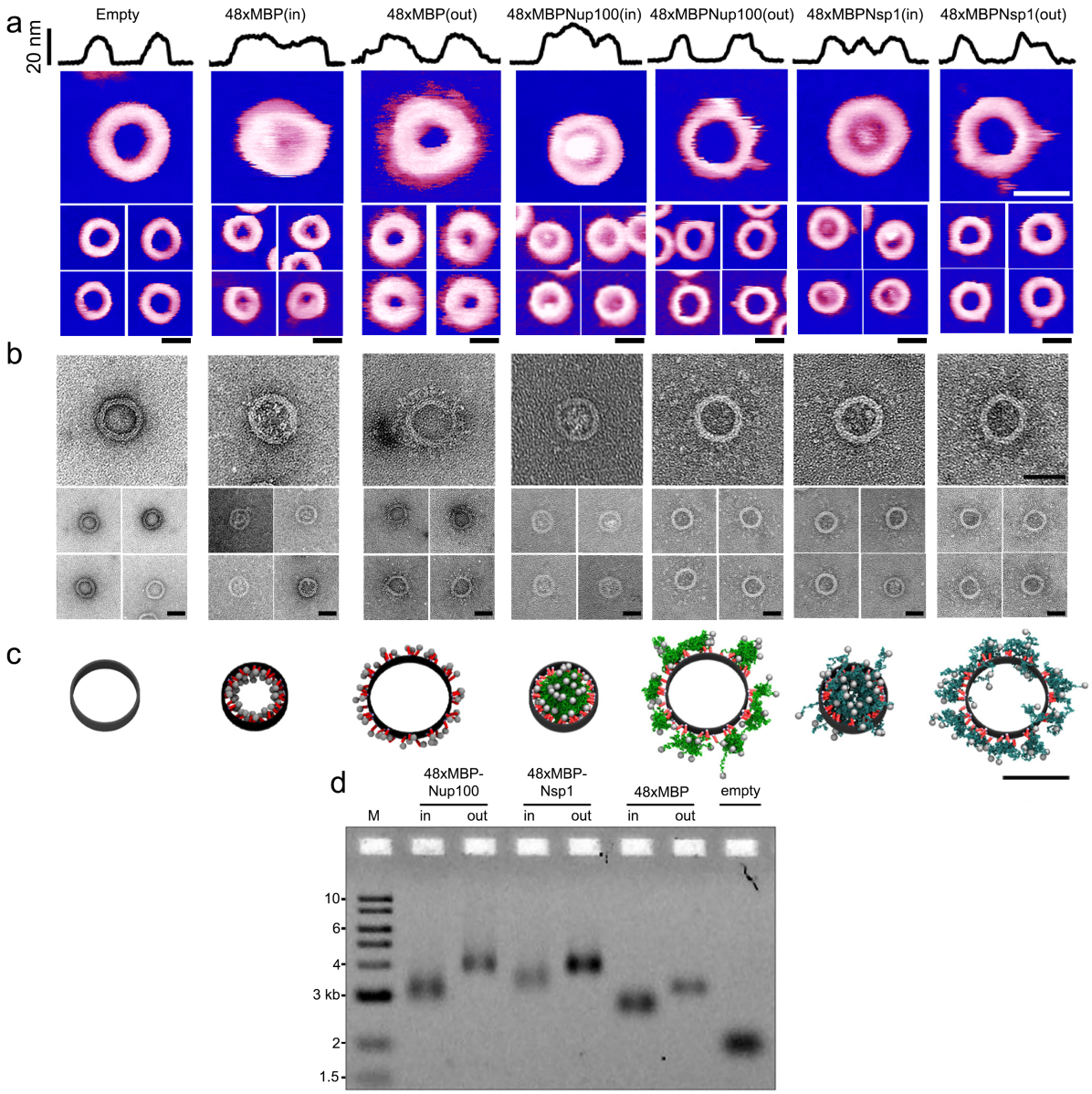


Figure 4.11: **Grafting of FG-domains on the inside or outside of the DNA scaffold affects their collective morphologies.** (a) AFM images, including height profiles (as measured across the center of the pore in the top image) and (b) Negative-stain TEM images showing an accumulation of protein inside and outside the DNA rings for the indicated proteins in NuPODs (c) Snapshots of equilibrated molecular dynamics (MD) simulations of the corresponding inside and outside grafted NuPODs (with Nup100 and Nsp1 in green and blue, respectively, and grey spheres representing MBP; all MD snapshots are displayed at the same length scale; observed differences in diameter of the rings between the inside- and outside-grafted NuPODs reflect that only the inner and outer wall of the DNA ring are shown, respectively). (d) SDS-AGE (EtBr stain) showing mobility shifts between different NuPOD constructs. NuPODs with proteins grafted outside run slower than their inside-grafted counterparts. Colour scale for AFM images (top right) is 24 nm. All other scale bars are 50 nm. TEM images were captured by Joe Beton (Birkbeck), Patrick Ellis Fisher and Qi Shen (Yale). MD simulations were carried out by Luke Davis (UCL). The SDS-AGE gel was run by Patrick Ellis Fisher.

inside and outside of the DNA cylinder, annotated as 48×MBP-Nup100(in) or (out) (see Figure 4.11). As determined from the cylinder dimensions, the inside versus outside grafting corresponds to a difference in grafting density of only ∼30%. In all cases the NuPODs with proteins grafted outside run slower during electrophoresis than their inside grafted counterparts, owing to their larger hydrodynamic diameters (see Figure 4.11d).

By comparison with empty DNA rings, AFM clearly resolved conjugated protein for 48×MBP(in), 48×MBP(out), 48×Nup100(in) and 48×Nsp1(in), but only identified a few clumps of attached protein for the NuPODs with the FG-nups grafted at the outside of the DNA rings (48×Nup100(out) and 48×Nsp1(out), see Figure 4.11a). This suggests that the FG-nups were too mobile to be fully resolved by AFM, in contrast to MBP alone, which can be clearly resolved as a shoulder encircling the outside of the DNA ring. By contrast, protein densities could be resolved for all variants via TEM where the samples are dehydrated (see Figure 4.11b). In snapshots from MD simulations for FG-nucleoporins anchored to the outside of the ring as shown in Figure 4.11c, there are a number of condensed 'clumps' as opposed to a uniform distribution for the case of MBP alone. These computational predictions are in agreement with the AFM data, if we assume that individual FG-nups were too flexible and/or mobile to be fully resolved by AFM, but that they could be visualised when of sufficient density and sufficiently compacted.

By collecting a number of sequential images of 48×MBPNup100(out) and 48×Nsp1(out), collective rearrangements of the FG-nups can be resolved, as shown in Figure 4.12. When grafted on the outside of the DNA origami scaffold, clumps are seen to form and rearrange. Generally, we detect only one or two condensates per ring, i.e., it appears that whilst some of the FG-nups interact to form compacted structures, others remain sufficiently diffuse not to be detected by the AFM tip. By high-speed AFM imaging of two 48×MBPNup100(out) NuPODs in close proximity to one another, we also find cases in which entanglements of FG-nups form between neighbouring NuPODs (Figure 4.12c). By increasing the temporal resolution (for (c) 1.6 seconds per frame as opposed to 14.2 seconds per frame in (b)), we can begin to better track FG-nup dynamics. This high-speed AFM imaging of NuPODs will be further developed in the following chapter.

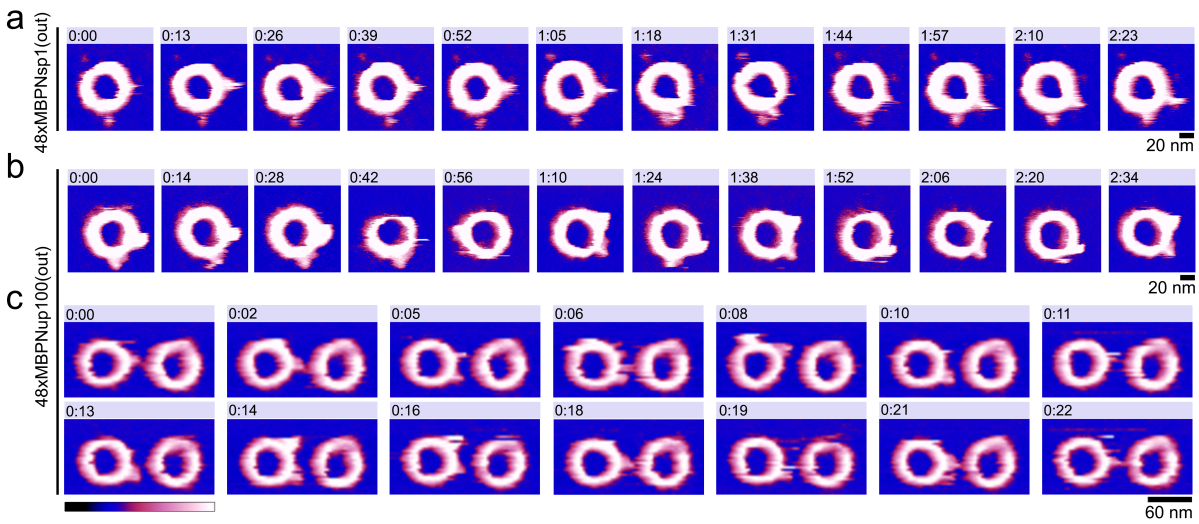


Figure 4.12: **Timelapse AFM imaging of outside-grafted NuPODs on a supported lipid bilayer.** (a) for 48xMBPNsp1(out) recorded at 13.2 seconds per frame (b) and (c) for 48xMBPNup100(out) at 14.2 and 1.6 seconds per frame respectively. Time stamps are shown at the top of the images. Colour scale 15 nm for (a) and (b) and 19 nm for (c).

4.3 Discussion

A bottom-up engineering approach has been taken to examine the collective properties of precise numbers of FG-nups that are confined within a cylindrical architecture mimicking the geometry of the native NPC channel (Figure 4.1). This has enabled a direct experimental investigation of how concepts such as FG-nup cohesiveness are affected by nanopore confinement at physiologically relevant densities of FG-nups.

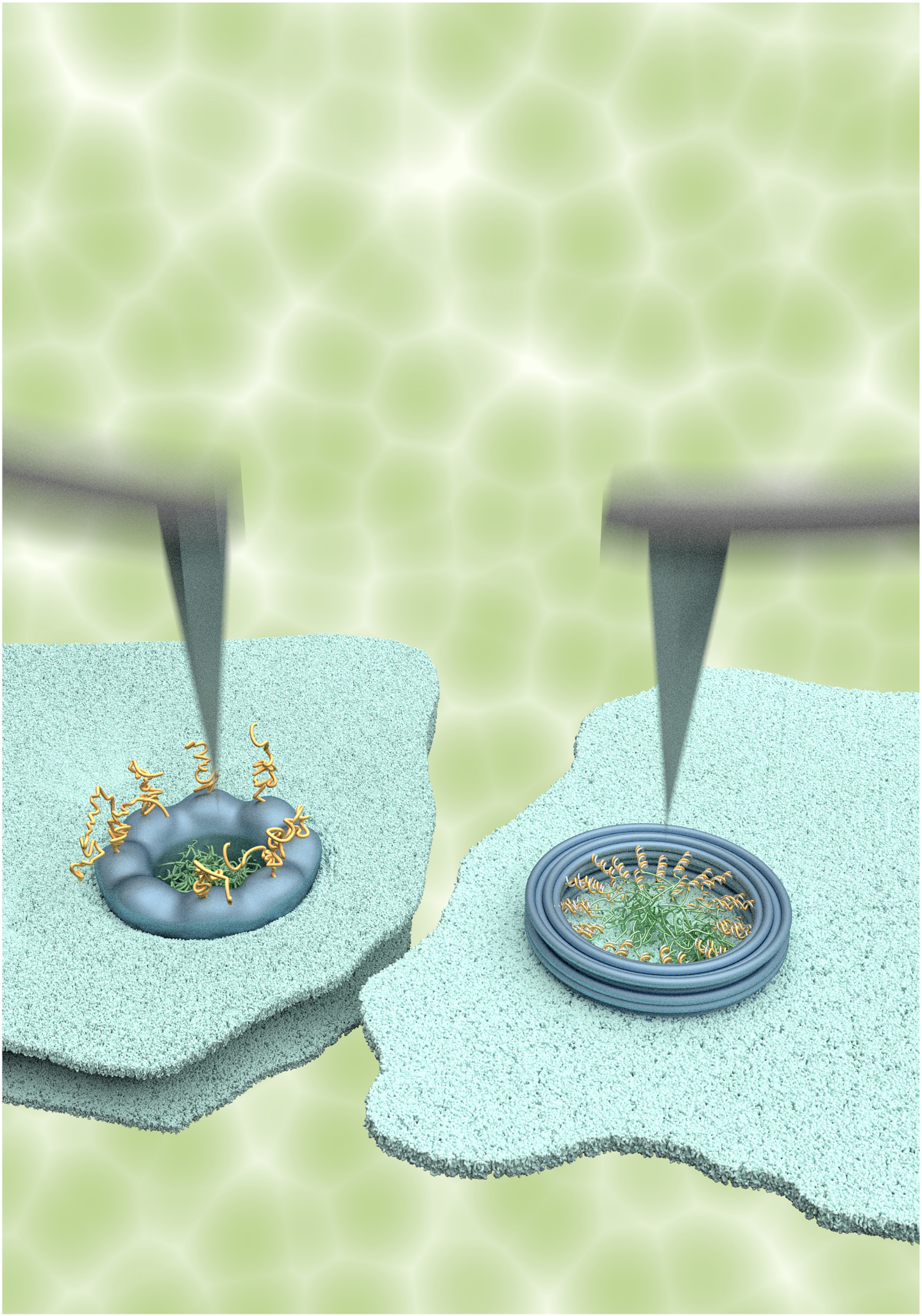
In general, the coarse-grained MD simulations facilitated the interpretation of our experimental data in terms of FG-nup morphology within the NuPODs. While some computational simulations may take into account precise amino-acid sequences of FG-nups,[27,216] a good agreement with protein distributions in the TEM and AFM images is obtained by modelling the FG-nups as homogeneous polymers that experience an overall attractive (or 'cohesive') inter- and intramolecular interaction. This indicates that the collective FG-nup morphology can largely be understood based on rather generic polymer physics, ignoring many of the underlying chemical and structural details. This conclusion is fully consistent with recent observations based on experiments with FG-nups grafted in a planar

geometry.[24,38,45,73]

Those prior experiments on planar, 2D surfaces were unable, however, to address how FG-nup confinement within a cylindrical architecture impacts their collective behaviour. This concept is best exemplified by the difference in morphology of the Nup100 FG-domains when grafted on the inside versus the outside of the DNA cylinder (Figure 4.11). Pore confinement appears to facilitate the condensation of Nup100, confirming predictions from polymer physics;[42,204] but when grafted on the outside of the NuPOD cylinder, the Nup100 FG-domains form somewhat smaller condensates as they interact with adjacent nups as opposed to those anchored across the centre of the pore. Our data overall suggests that these GLFG and FxFG-rich nups have unique biophysical/biochemical properties that are clearly influenced by grafting density and spatial confinement.

Taken together, these biomimetic 'NuPODs' introduce a powerful and flexible experimental system to probe the biophysical properties of FG-nups within cylindrical architectures that mimic the ∼40 nm NPC channel. Although this work demonstrates a proof-of-concept using only two types of FG-nups, the platform presented here can be applied to organise other FG-nups or other intrinsically disordered proteins capable of phase separation, thus presenting opportunities to generate more sophisticated and diverse biomimetic constructs. In that sense, the NuPOD platform paves the way to extend the applications of DNA nanotechnology to both cell biology (*in vitro* modelling of nuclear transport) and synthetic biology (designing macromolecule sorters with tunable selectivity). Indeed, this study highlights the power of the DNA origami technique to build synthetic macromolecular structures with biologically relevant concentrations of proteins; the future goal of such designs is to reconstitute a fully synthetic NPC mimic in a configuration that also facilitates transport measurements. Ketterer *et al.* recently designed an analogous biomimetic platform as presented here, but added a long dsDNA lesh to the base of the DNA origami scaffold such that it could be docked into a solid-state nanopore.[41] By measuring the conductance through these hybrid nanopores they showed that the presence of 32×Nsp1 molecules decreased the flow of ions moreso than an empty DNA origami ring or a ring containing 32×Nsp1 non-barrier forming mutants. However, they were unable to show whether molecules (as opposed to individual ions) were selectively excluded by these hybrid systems.[41]

AFM characterisation of this NuPOD system will be explored further in the following chapter. Collective arrangements of FG-nups inside the pore lumen will be tracked using high-speed imaging such that the dynamics of both the 'less-cohesive' and 'more-cohesive' Nsp1 and Nup100 variants can be compared. Moreover, by comparing results with measurements obtained on native NPCs this work will attempt to explicate the relationship between FG-nup dynamics and nucleocytoplasmic transport.



Chapter 5

Visualising FG-nup dynamics using high-speed AFM

This chapter is based in part upon the paper "Quantification of biomolecular dynamics inside real and synthetic nuclear pore complexes using time-resolved atomic force microscopy" by G. J. Stanley, B. Akpinar, Q. Shen, P. D. Ellis Fisher, C. P. Lusk, C. Lin and B. W. Hoogenboom, published in *ACS Nano*, vol. 13, no. 7, pp 7949-7956, 2019.

The experimental work on native nuclear envelopes from *Xenopus laevis* oocytes in this chapter was carried out by George Stanley, who also wrote custom MATLAB scripts for the data analysis and processed the data. I collected all the data on the NuPODs.

5.1 Introduction

With its ability to resolve biomolecules in aqueous solution at a spatial resolution of ∼1 nm,[153] AFM has a unique potential to observe dynamic biological processes at the single-molecule level. Thanks to technological advances in microscope hardware, cantilevers, and imaging modes, this high spatial resolution has become compatible with a temporal resolution on the order of 100 milliseconds per frame (often denoted as high-speed AFM, or HS-AFM),[82] or 0.5-1 millisecond for monitoring individual scan lines.[217–219] Over the years, AFM has allowed real-time visualisation of diverse biological systems,[220]

from the binding/unbinding of GroEL molecules,[217] to molecular motors walking along actin filaments,[221] Cas9-mediated DNA cleavage,[162] and a range of protein assembly processes.[134,218,222,223]

When the observed dynamics are progressive in nature and have a magnitude well above the noise floor of the AFM, they can be unambiguously associated with molecular motion, binding, or conformational change. However, at molecular length scales, such dynamics invariably contain a stochastic component, and when the magnitude of these dynamics is $\lesssim$1 nm, they are not trivial to distinguish from AFM measurement noise or feedback errors that may arise when tracing molecular contours at high scan speeds. Such stochastic dynamics are arguably most pronounced for natively unfolded and intrinsically disordered proteins.[224] Unlike structured proteins, intrinsically disordered proteins have low sequence complexity and fluctuate rapidly over an ensemble of conformations ranging from extended statistical coils to more collapsed globules. Such proteins play a central role in a number of cellular processes: one important example being those that line the NPC and regulate the selective filtering of macromolecules between the nucleus and the cytoplasm.[25]

AFM has proven itself a useful tool for probing the dynamics of FG-nups inside real NPCs, with high-speed experiments potentially revealing dynamic movement of individual FG-nups at the cytoplasmic periphery of the pore,[33,95] and high-resolution studies revealing many different metastable collective morphologies of FG-nups and soluble NTRs inside the central channel.[34] Both of these results support the notion that the 'cohesivity' of the FG-nups is tuned such that the energetics of stable FG-nup morphologies lie near transition states, as has been postulated in computational studies.[42,45,73] One of the caveats with these experimental results, however, is that the exact chemical composition of the NPC's transport barrier is ill-defined. Structural studies indicate that, by mass, the FG-nups only comprise (approximately) one third of the material inside the channel — the majority of the pore lumen is filled with NTRs and cargo molecules caught in transit.[8] Mimetic NPCs made using DNA origami described in Chapter 4 and also in published work[39,41] instead offer a model platform better understand the behaviour and function of isolated FG-nups that form part of this complex system.

The NuPOD platform was designed to mimic the dimensions of the NPC's central transport channel, providing a means to study the behaviour of pure FG-nups in the cylindrical

geometry.[39] This system has been used to accommodate two different *S. cerevisiae* FG-nups: Nup100, which is a cohesive GLFG-repeat nucleoporin; and Nsp1, a less cohesive FxFG-repeat nup. NuPODs therefore house purely the disordered FG-nups, of a known composition and grafting density (i.e., concentration).

In the following chapter, HS-AFM is used to probe the dynamic behaviour of disordered FG-nups within mimetic NPCs (NuPODs) and later compare those to analogous experiments performed on native NPC's from *Xenopus laevis* oocytes. This work presents analysis, procedures, and criteria to distinguish between the stochastic dynamics of these proteins (often on length scales of $\lesssim$1 nm), and that of the (also largely stochastic) AFM measurement noise. By applying a drift-correction routine, and a subsequent autocorrelation analysis to the pixel heights with time, both the timescale of any dynamic behaviour, and the effect of the tip-sample interaction force on the behaviour of the system can be probed — thus providing a more rigorous approach to interpreting HS-AFM data. In doing so, the timescale of collective dynamics of the pure FG-nups inside the NuPOD system can be evaluated, thus further elucidating their precise role in nucleocytoplasmic transport.[130]

5.2 Results

5.2.1 HS-AFM of NuPODs reveals stochastic dynamics

Having established the scope (and limitations) of AFM for imaging the FG-nup morphology in Section 4.2.5 within the confinement of the DNA scaffold structure, I next set out to probe the dynamic behaviour of the confined FG nups by increasing the AFM imaging speed and recording frames of individual NuPODs as a function of time (Figure 5.1). Since AFM is a raster scanning technique, two images can be generated for every frame recorded; one where the tip is scanning from left-to-right (the 'trace' direction) and another where the tip scans from right-to-left (the 'retrace' direction). By systematically recording both trace and retrace images one can verify the robustness of the AFM data and measurement process. From image to image ($\sim$1.6 s between each frame), significant changes within the NuPOD lumen could be observed. These were qualitatively similar for

both GLFG and FxFG containing proteins. Specifically, local enhancements of protein density that shifted position as time evolved were identified, often, appearing to extend and make contact with analogous densities emanating from multiple positions along the channel walls. The height of these fluctuations observed in the NuPOD lumens are at the scale of 1-10 nm.

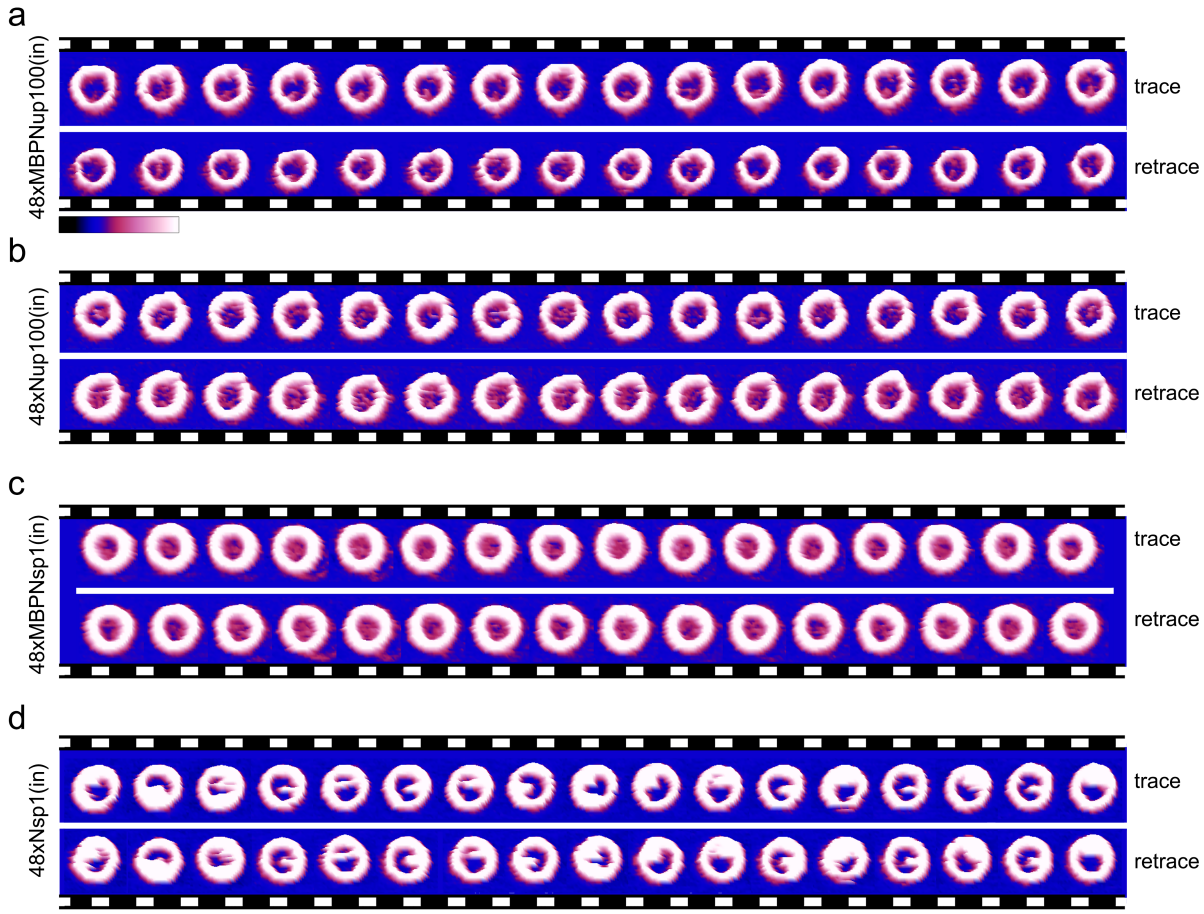


Figure 5.1: **Timeresolved AFM imaging of NuPODs at 1.6 s per frame.** Comparison of trace and retrace AFM images of a NuPOD containing (a) 48×MBP-Nup100(in), (b) 48×Nup100(in) with MBP cleaved off, (c) 48×MBP-Nsp1(in), and (d) 48×Nsp1(in) with MBP cleaved off, with 1.6 s between subsequent scans. Features that reproduce between trace and retrace images can be attributed to changes in the sample, as opposed to noise in the measurement. Each frame consists of 32 scan lines recorded at 50 ms/line. The colour scale represents 0-15 nm in height.

While the data presented here does not directly address the establishment of a permeability barrier inside the NuPODs, it is nonetheless tempting to interpret these results within

this context. First, it is clear that 48 copies of either FG-nup are capable, in principle, of occluding a ∼40 nm diameter cyclinder. Most strikingly, however, is that the FG-nups can undergo local and reversible condensation, including transitions from pore-occluding to more open configurations (see in particular Figure 5.1d). These AFM experiments must be interpreted with the caveat that more mobile and/or diffuse FG-nup arrangements may not be fully resolved because of the inherent invasiveness of the AFM measurement (see the dicussion in section 4.2.5). These results imply FG-nup condensation as expected for gel/selective-phase models,[36,69] as well as, at the nanometre length scale dynamics that are in line with descriptions that emphasize entropy-dominated behaviour.[56,66]

As supported by previous experimental work,[214] and predicted by MD simulations (see discussion in Chapter 4.2.3 and Figure 4.5), the behaviour of the FG-nups i.e. their ability to form transient condensates was not appreciably affected by removal of the MBP moieties. However, to ensure that only the behaviour of isolated FG-nucleoporins at physiologically relevant concentrations was recorded, subsequent data presented in this chapter was recorded on NuPODs containing only 48×Nup100 or 48×Nsp1 molecules (following MBP tag removal, see section 4.2.2).

The behaviour of disordered FG-nucleoporins was resolved at higher temporal resolution by repeatedly scanning the same single line across the centre of a single NuPOD to generate kymographs (see Figure 5.2).[217] By scanning the AFM tip at different frequencies we generated trace and retrace line profiles separated by 100, 50 and 25 ms, shown in Figure 5.2c, d and e respectively. With this increased temporal resolution the movement of condensates, forming both at the walls and at the centre of the channel, can be tracked with time. This is consistent with earlier speculations on how such rearrangements may facilitate selective transport across the NPC, in particular for large cargos.[42] It must be noted that since only a single line is scanned across the centre of the pore, clumps of nucleoporins that form at positions *not* occupying the centre of the pore will not be detected in the kymograph (see schematics in Figure 5.2f).

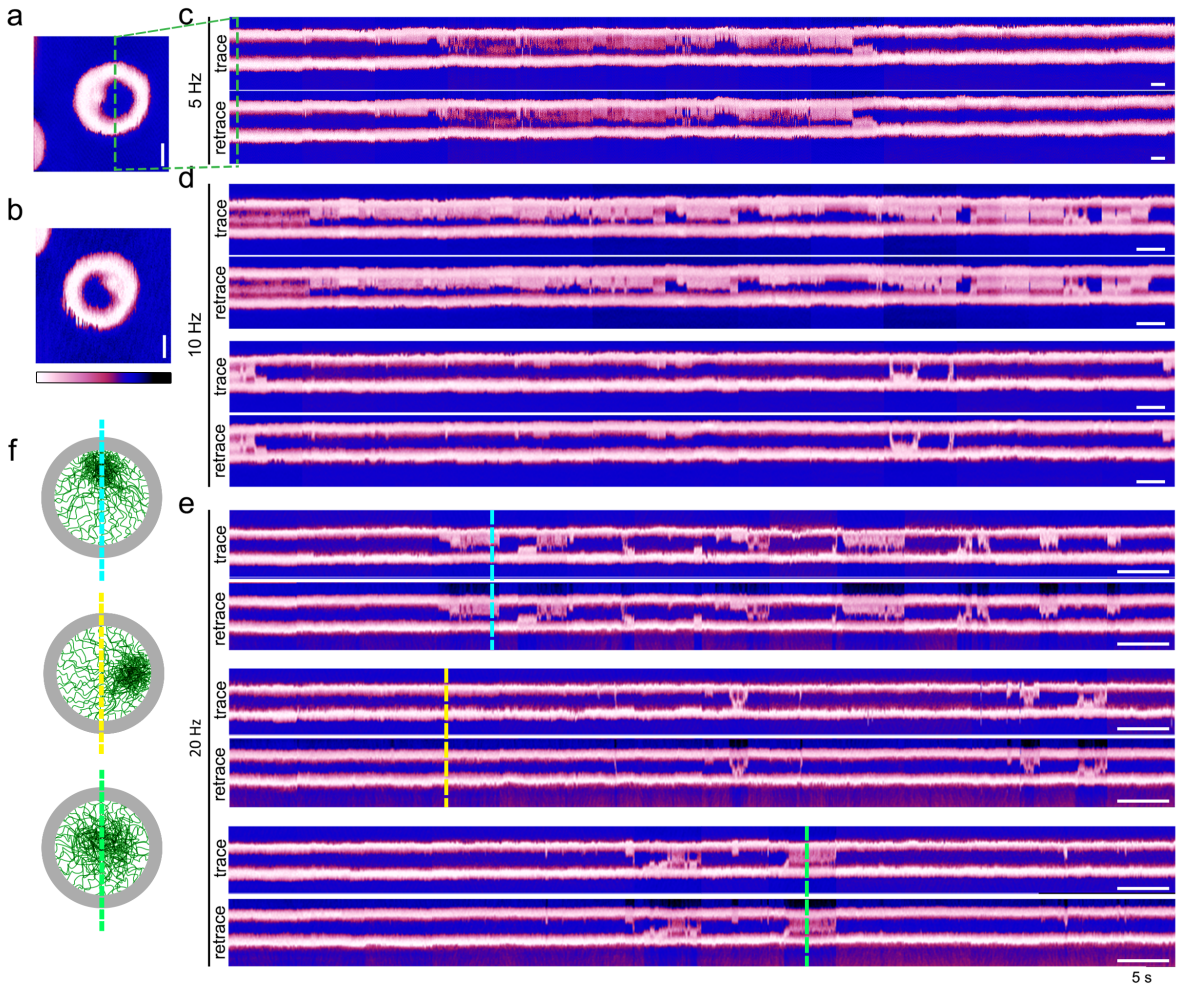


Figure 5.2: **Single-line scanning experiments on NuPODs.** (a) AFM image of an inside grafted 48×Nup100 NuPOD with the MBP tag cleaved off (frame time: 26 s, recorded before starting the single-line scans). (b) AFM image of the same 48×Nup100 NuPOD after single line scanning experiments, showing that the central clump is still present and the pore is intact (frame captured over 6 s) (c-e) Kymographs are obtained by recording the same scan line across the centre of the pore (green-dashed line) as a function of time (horizontal axis of the kymographs). Kymographs (raw data after flattening) captured at different scanning speeds, showing the AFM height profile across the NuPOD as a function of time, with trace (top) and retrace (bottom) shown separately to validate the robustness of the observed fluctuations; with (c) 200 ms, (d) 100 ms and (e) 50 ms between subsequent scan lines. (f) schematic interpretations of kymograph recordings where the dashed line corresponds to the path of the AFM tip; the top image shows a clump of nups formed on one wall, captured by the single line scan; the middle image showing a clump of nups formed out of the path of the single line scan, the lumen thereby appearing empty in the kymogaph; the bottom image shows the nups occluding the entirety of the channel. Colour scale is 20 nm for all images. Single lines for the kymograph were captured across a length of 120 nm. The scale bars in (a) and (b) are 20 nm.

5.2.2 Autocorrelation analysis of AFM kymographs recorded for NuPODs

The generation of kymographs also facilitates data averaging and the application of analysis protocols described in the Methods section 2.4.2 to quantify the time-dependence of the collective fluctuating behaviour of the clumped FG-nups; and furthermore, to verify if any difference in behaviour can be detected between the two different proteins. Firstly, as a control, the analysis protocol was applied to NuPODs containing no anchored nucleoporins, where no fluctuations should be detectable in the central lumen.

The autocorrelation function, $R(\tau)$, measured in nm^2 (see Methods section 2.4.2 and Equation 2.1), was used to quantify the similarity in height values for a given pixel at a certain time-lag. It can detect a periodic signal shrouded by noise, and the persistence time of stochastically fluctuating signals (see Figure 2.7 in Methods section 2.4.2). For analysis, $R(\tau)$ was determined for each pixel in a kymograph, and represented as a heatmap as a function of both position (nm) and time-lag (τ), with red showing greater correlation and blue representing no correlation (see Figure 5.3).

After drift correction, the kymographs show the empty DNA origami rings as rather static objects, as expected (see Methods 2.4.2). However, both the $R(\tau)$ heatmaps and standard deviation plots reveal that there are significant fluctuations at positions that coincide with the edges of the DNA origami scaffold structure. At these edges, the AFM tip needs to trace over the protruding ∼14 nm high scaffold walls, which is where it is most prone to tracking/feedback errors. Moreover, small lateral shifts from one line to the other may result in relatively large height fluctuations, because of the steep slope of these edges. This is in spite of the lateral drift correction. Hence, these fluctuations are attributed to artefacts of the AFM imaging process; importantly no significant $R(\tau)$ signal is recorded at the centre of the pore for the control scaffolds containing no FG-nups (see Figure 5.3).

By contrast, when the DNA origami rings contain grafted FG-nups, fluctuations are detected in the pore centre that greatly exceed those observed at the same positions in the empty 'NuPODs', or at the background supported lipid bilayer. This is here illustrated in Figure 5.4 for NuPODs each containing 48 copies of one of two types of FG-nup domains. If 48 Nsp1 molecules are present (Figure 5.4A-C), fluctuating clumps inside the central

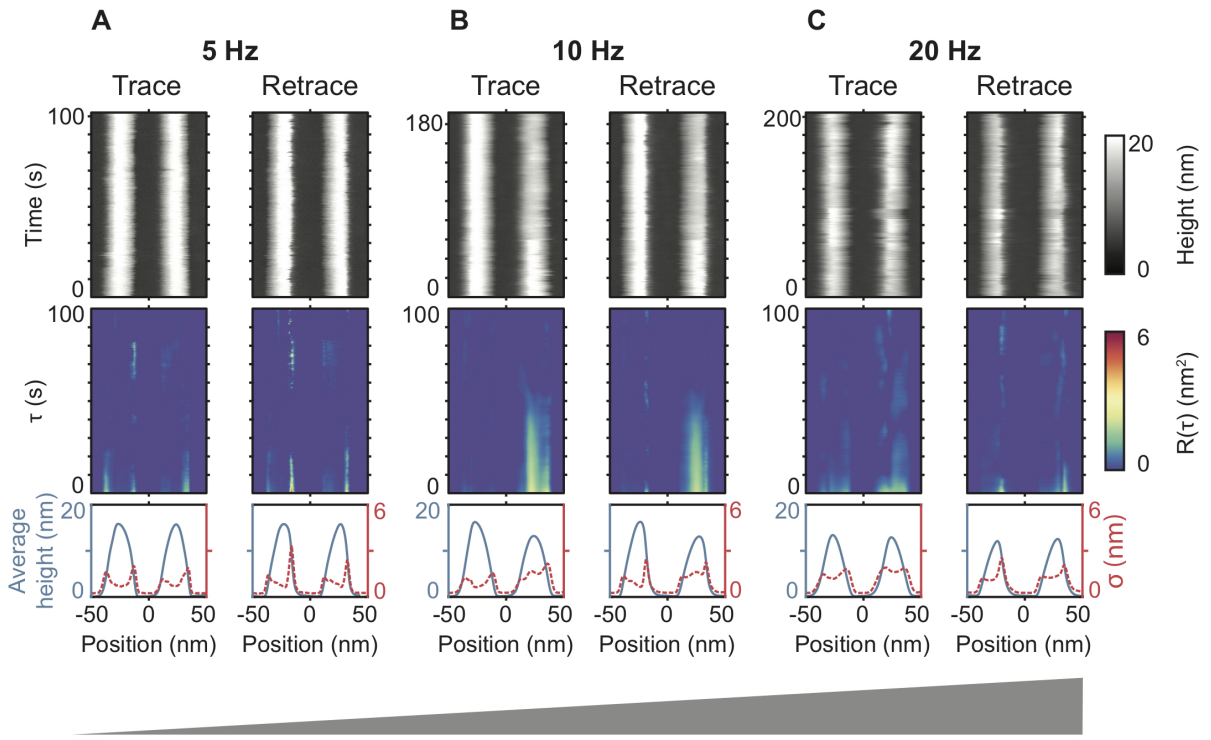


Figure 5.3: **Kymographs and autocorrelation analysis of empty DNA origami rings.**(A-C) Kymographs of DNA origami rings without FG-nups (top row), recorded at 5 (A), 10 (B), and 20 Hz (C), showing both trace and retrace data. The light features are the DNA scaffold and the dark background the lipid bilayer. The autocorrelation heatmaps (second row) show background noise in the central lumens, and weak signatures of stochastic fluctuations at the edges of the DNA scaffold structure. Average height profiles of each pixel in the kymograph with time (bottom row, blue line), plotted with their respective standard deviation, σ (bottom row, red-dashed line), show maximum σ where the slope of the height profiles is steepest.

channel are observed in the kymographs. For kymographs recorded at line frequencies of 5 and 10 Hz (Figure 5.4A and B, respectively), the autocorrelation heatmaps show correlation up to ∼10 s; for the 20 Hz kymographs, little significant correlation is detected beyond 1 s (see Figure 5.4C, logarithmic plot). A similar pattern is observed for NuPODs containing 48 Nup100 molecules (Figure 5.4D-F); for 5 and 10 Hz, correlation is observed up to ∼10 s, but for 20 Hz, this appears to be reduced. Furthermore, for all $R(\tau)$ heatmaps, no significant periodicity is detected — all heatmaps show signals more akin to stochastic fluctuating behaviour.

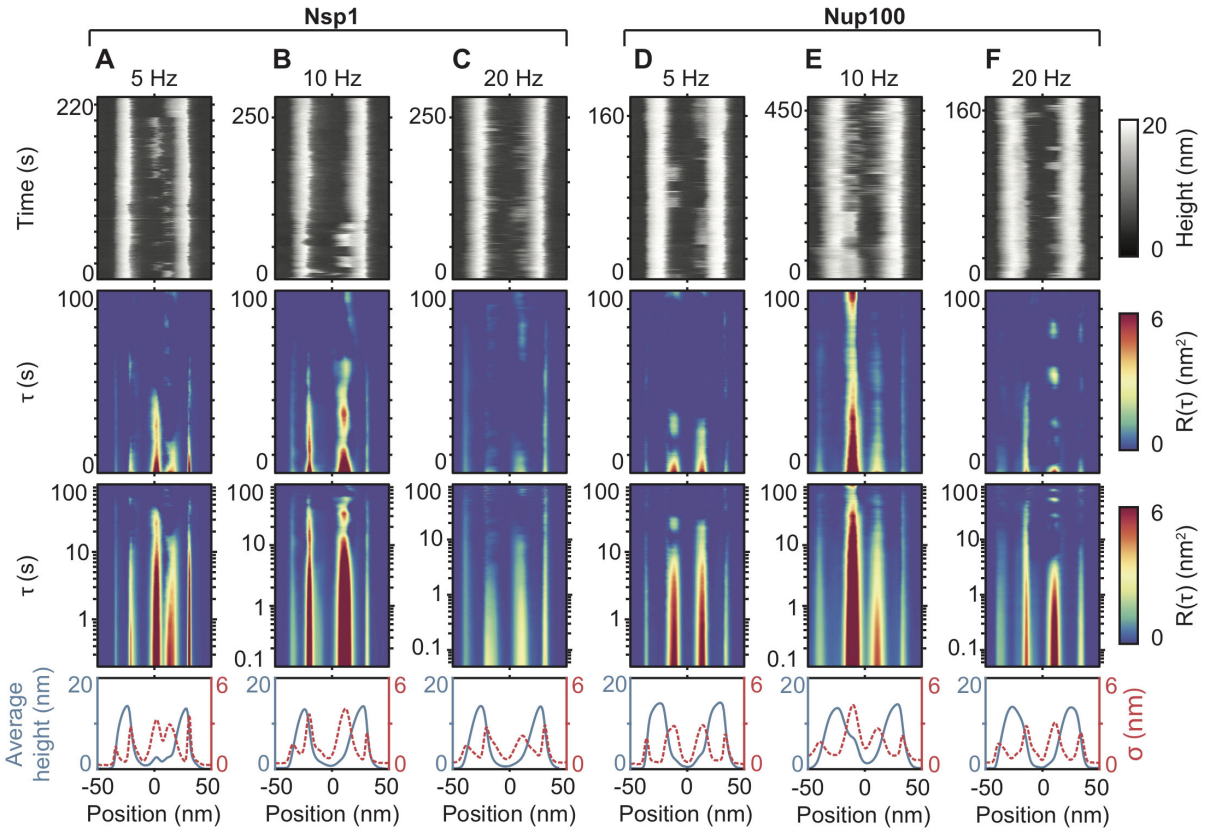


Figure 5.4: **Kymographs and autocorrelation analysis of NuPODs containing FG nups.** Kymographs recorded with time now displayed on the vertical axis. The concomitant autocorrelation factor, R, is displayed as a function of position with respect to the pore center and as a function of time-lag, τ, with τ plotted on linear (second row) and logarithmic (third row) scales. The average height profiles (blue) and respective standard deviations (red) are plotted in the final row. For NuPODs containing 48 copies of Nsp1 (A-C), and for NuPODs containing 48 copies of Nup100 (D-F). The data of protein-containing NuPODs were recorded at scan line frequencies of 5, 10, and 20 Hz (200, 100, and 50 ms per scan line). (A-C and F) Each data set displayed is from different NuPODs. (D and E) The same NuPOD scanned at 5 and 10 Hz.

To explain the observed differences between data recorded at lower and higher line scan frequencies, it is noted that at higher scan speeds, more invasive feedback settings are required to track the NuPODs (data here were all obtained using Tapping Mode AFM, with the applied force minimised as much as possible without losing track of the pores). As a consequence, the flexible and mobile FG-nups may increasingly drop below the detection threshold of the AFM, perhaps in addition to being perturbed by the AFM tip.

In this context, it is not trivial to quantify the peak forces applied and energy dissipated into the sample;[223] and it is nigh impossible to translate such forces and energies into plausible molecular deformations without knowledge of the dissipative mechanisms in the sample. To exclude that the observed dynamics are due to the invasiveness of the AFM measurements, the best approach remains to validate the observations at different scan speeds.

The results presented in Figure 5.4 are from individual NuPODs. It is also possible to average over many autocorrelation heatmaps (produced from kymographs scanned at a given line rate), to build up a picture of the collective behaviour of each FG-nup, from many different NuPODs, over longer, aggregate recorded times. Furthermore, by cropping only a 30 nm window, which is smaller than the inner-diameter of the NuPOD ($\sim$46 nm[39]), it is ensured that only contributions from the FG-nups are considered. This eliminates any artefacts produced by tracking errors from the AFM tip scanning over the DNA scaffold structure. Next, by assuming the NuPODs display rotational symmetry, the data can be binned as a function of radial position, and averaged. This produces autocorrelation heatmaps as a function of radius, with 0 nm being the centre of the channel and 15 nm approaching the inner-wall of the scaffold, as show in Figure 5.5.

The NuPODs containing 48 Nsp1 molecules (Figure 5.5 A-C) exhibit similar behaviour to that shown from the individual kymographs (Figure 5.4A-C), i.e., stochastic fluctuations with a decreasing persistence time as the scan rate increases from 5, to 10, to 20 Hz. A very similar picture is seen for the NuPODs containing 48 Nup100 molecules (Figure 5.5D-F). At 5 Hz, significant correlation is seen to up to $\sim$10 s (Figure 5.5A and D); and at 10 Hz, it is seen to persist into the 1-10 s range (Figure 5.5B and E). At 20 Hz, however, the correlation does not persist much beyond 1 second (Figure 5.5C and F, logarithmic plots). All six heatmaps (Figure 5.5A-F) show stochastic, fluctuating behaviour, and more correlation at the edges of the transport channels (i.e., nearer radial values of 15 nm) as opposed to the centre (i.e., at 0 nm). Empty NuPOD controls confirm that these fluctuations are related to FG-nup fluctuations (refer to Figure 5.3). These observations indicate that the FG-nups spend more time clumped towards the inner-walls of the NuPODs, rather than in the middle of the transport channel; and that their rate of collective transitioning is recorded to increase with faster line scanning. Furthermore, at equal scan speeds, the more cohesive GLFG-repeat Nup100 tends to persist for longer

before transitioning when compared to the FxFG-repeat Nsp1(Figure 5.5D-F vs A-C).

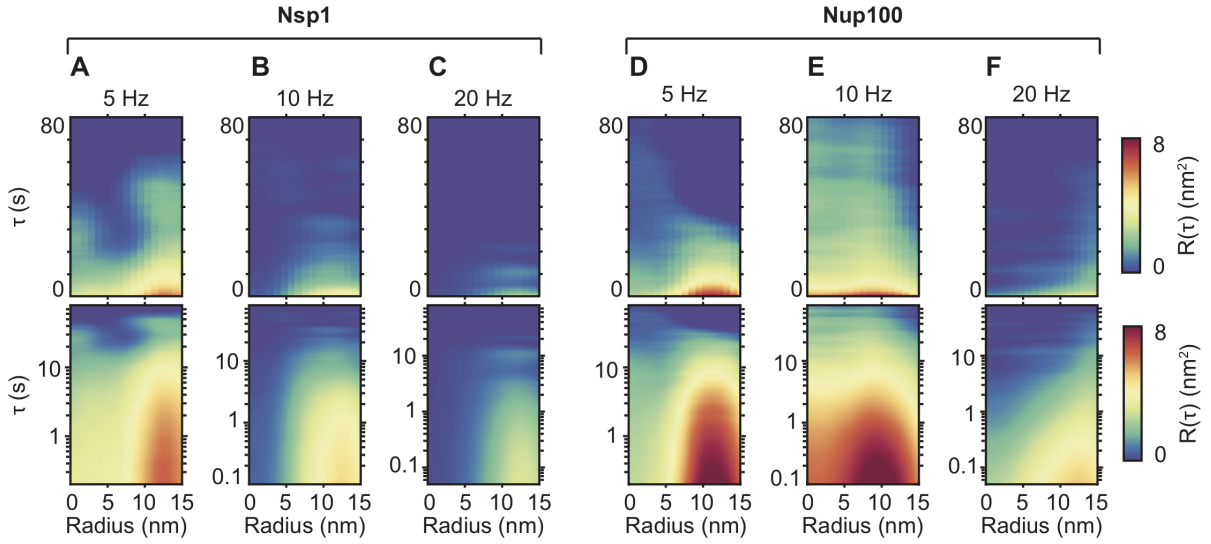


Figure 5.5: **Averaged autocorrelation analysis of the pore channel in NuPODs.**(A-C)$R(\tau)$ heatmaps averaged over nNuPODs, each containing 48 Nsp1 molecules, plotted as a function of radial position from the center of the pore, scanned at line rates of 5, 10, and 20 Hz. τ is plotted on both linear (top row) and logarithmic scales (bottom row). (D-F) Same as for (A-C) but the NuPODs contain 48 Nup100 molecules. From (A-F): n = 3, 4, 2, 3, 5, and 3; total duration of each kymograph = 739, 1050, 365, 586, 1907, and 1664 s.

5.2.3 Comparison with HS-AFM on native NPCs

Given the physiological context of FG-nups, it is also worthwhile to compare the NuPOD data with AFM data collected on intact *Xenopus laevis* NPCs. For these experiments, the nuclear envelope is spread onto a glass coverslip such that either the cytoplasmic or nucleoplasmic side (see Figure 5.6A and B respectively) is facing upwards and imaged by the AFM tip.[25,34] As opposed to the NuPODs which have ∼14 nm high scaffolds and are probed when adsorbed on top of a lipid bilayer, the native NPCs protrude ∼40 nm from the background nuclear envelope in which they are fully embedded (see schematics in Figure 5.6).

When the same analysis protocol applied to kymographs produced from the NuPODs (see previous Section 5.2.2) is applied to kymographs collected on the cytoplasmic and

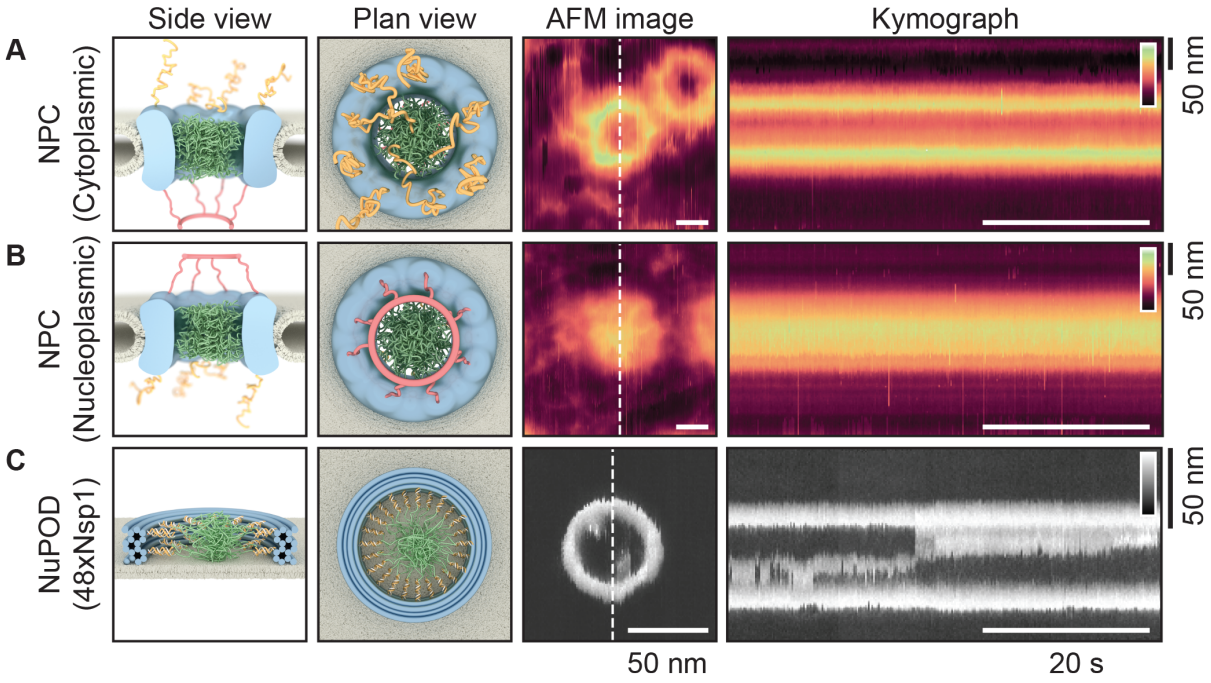


Figure 5.6: **Producing kymographs from *Xenopus laevis* oocyte NPCs and from NuPODs.** Schematics (side and top views) and representative AFM images of NPCs with the cytoplasmic (A) and nucleoplasmic (B) sides facing the AFM tip and of a NuPOD that contains 48 Nsp1 proteins, resting on a supported lipid bilayer (C). The NPC is asymmetrical when viewed through the mirror plane of the nuclear envelope: From the cytoplasmic face, cytoplasmic filaments are seen (yellow filaments), and from the nucleoplasmic face, the nuclear basket protrudes (red filaments). The disordered FG-nups are shown in green (A-C). Note the differences in scale bars between the NPC and NuPOD data. Height scales (insets in kymographs): 80 nm for the NPCs and 20 nm for the NuPOD.

nucleoplasmic sides of intact NPCs (Figure 5.7), at different scan speeds, no significant fluctuations are detected in the positions of the central transport channel (i.e., around the 0 nm position). That is, the recorded fluctuations for positions occupied by the disordered FG-nups are not distinguishable from those at the positions of the nuclear envelope (a double membrane and lamin filaments, here supported by a glass substrate[34]). It remains possible that FG-nup dynamics inside the central channel yield Ångström-scale height variations (as have previously been reported for the cytoplasmic face of the transport channel of NPCs[33,95,225]), but in these experiments, based on a similar sample preparation as for,[33,225] height fluctuations do not exceed the experimental noise floor.

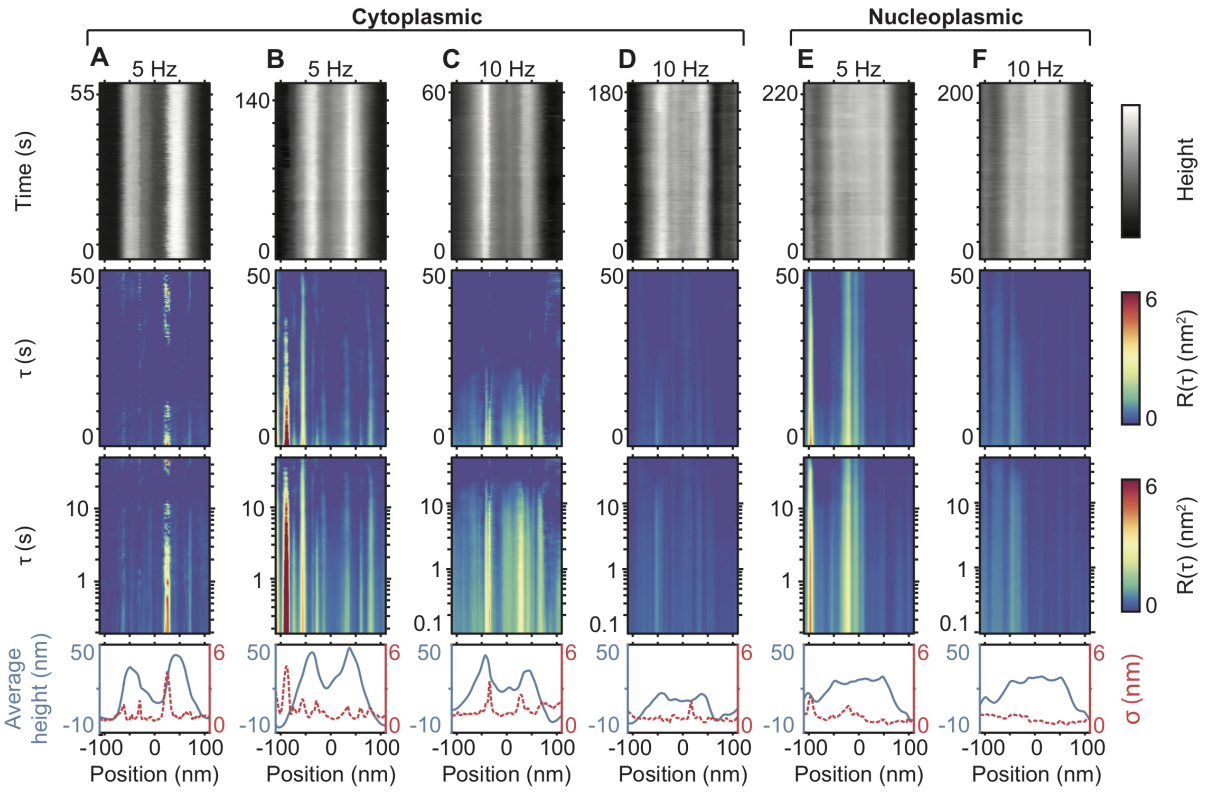


Figure 5.7: **Kymographs and autocorrelation analysis of NPCs.**(A-D) Kymographs of NPCs at the cytoplasmic face (top row), recorded with time on the vertical axis (recorded at line frequencies of 5 and 10 Hz). The concomitant autocorrelation factor, R, is displayed as a function of position with respect to the pore centre and as a function of time-lag, τ, with τ plotted on linear (second row), and logarithmic (third row) scales. The average height profiles (blue) and respective standard deviations (red), are plotted in the final row. (E and F) Same as for (A-D) but for the nucleoplasmic face of NPCs. Kymograph height scales: 50 nm (A and C), 60 nm (B), 25 nm (D), 40 nm (E and F). (A-D) show data each from different NPCs; (E and F) is the same NPC scanned at 5 and 10 Hz.

This can be further confirmed by plotting sample height at different locations in and around the pores as a function of time (Figure 5.8). For the NuPOD system, fluctuations inside the channel exceed those measured on and outside the pore scaffold by more than an order of magnitude (Figure 5.8B and C), whereas, for the native NPC, no noticeable difference in the magnitude of fluctuations is detected for different positions inside and outside the transport channel (Figure 5.8A). It is plausible that the discrepancy in behaviour observed between the native NPCs and NuPODs (i.e., non-fluctuating and fluctuating be-

haviour) is due to the presence/absence of endogenous NTRs (present in the real NPCs). In the preparation of native nuclear membranes from *Xenopus laevis* oocytes, the nuclei are repeatedly washed to remove cellular material — including cargoes and NTRs — that may be caught in transit. However, it is safe to assume that many NTRs and possibly cargo molecules bound to the FG-nups will not be removed by our washing steps.[34] In the case of the NuPODs, in the complete absence of NTRs, and in the symmetry of the pore geometry, there are many different possible metastable conformational states with small activation energy barriers between them, thus leading to the observed fluctuating behaviour. However, in the presence of multivalent NTRs (such as importin-β[226]), the FG-nups could wrap around these proteins, thereby becoming energetically trapped in a given conformation (as was observed for FG-nups at low grafting densities in planar films[227]). To this end, it would be interesting to acquire further AFM data of NuPODs in the presence of NTRs — presumably, upon addition of importin-β, FG-nup fluctuations

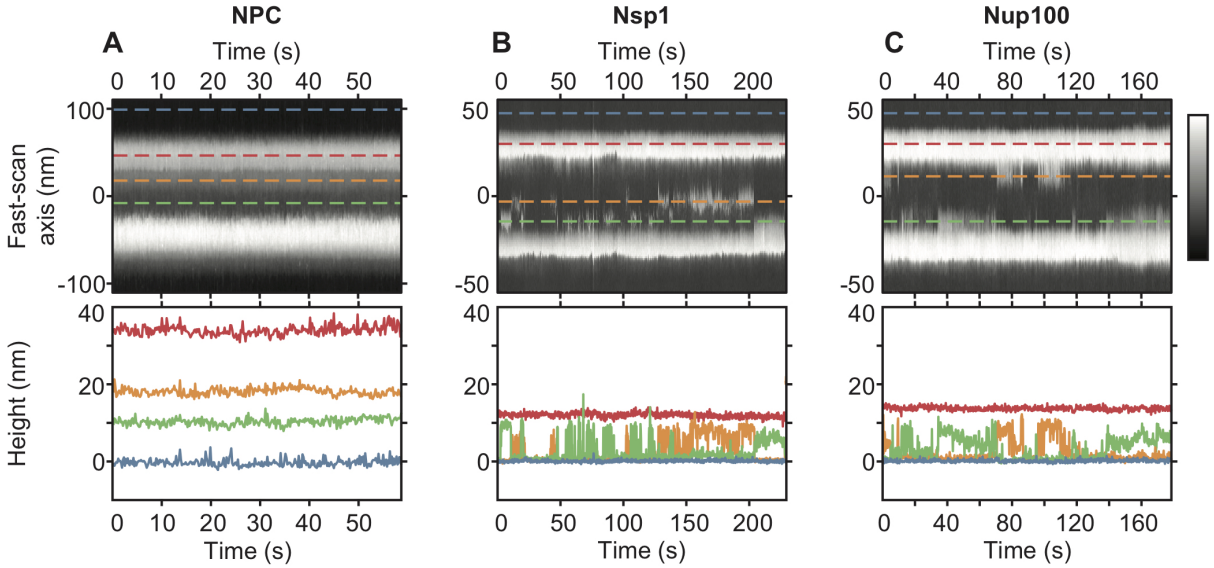


Figure 5.8: **Kymographs and height fluctuations of NPCs and NuPODs.** (A) Kymograph of a native NPC (cytoplasmic face) with the height profiles of selected pixels shown underneath, scanned at 5 Hz. Blue-dashed line is the background nuclear envelope; red-dashed line is the NPC scaffold structure; and orange- and green-dashed lines are different locations inside the transport channel. (B and C) Same as for (A) but of NuPODs containing 48 Nsp1 molecules (B) or 48 Nup100 molecules (C). Blue-dashed lines are the background lipid bilayer; red-dashed lines are the DNA scaffold structure; and orange- and green-dashed lines are different locations inside the channel. Color scales: 50 nm (A) and 20 nm (B and C)

would stop. Preliminary data on the effect of the addition of NTRs will be explored further in the following Chapter 6.

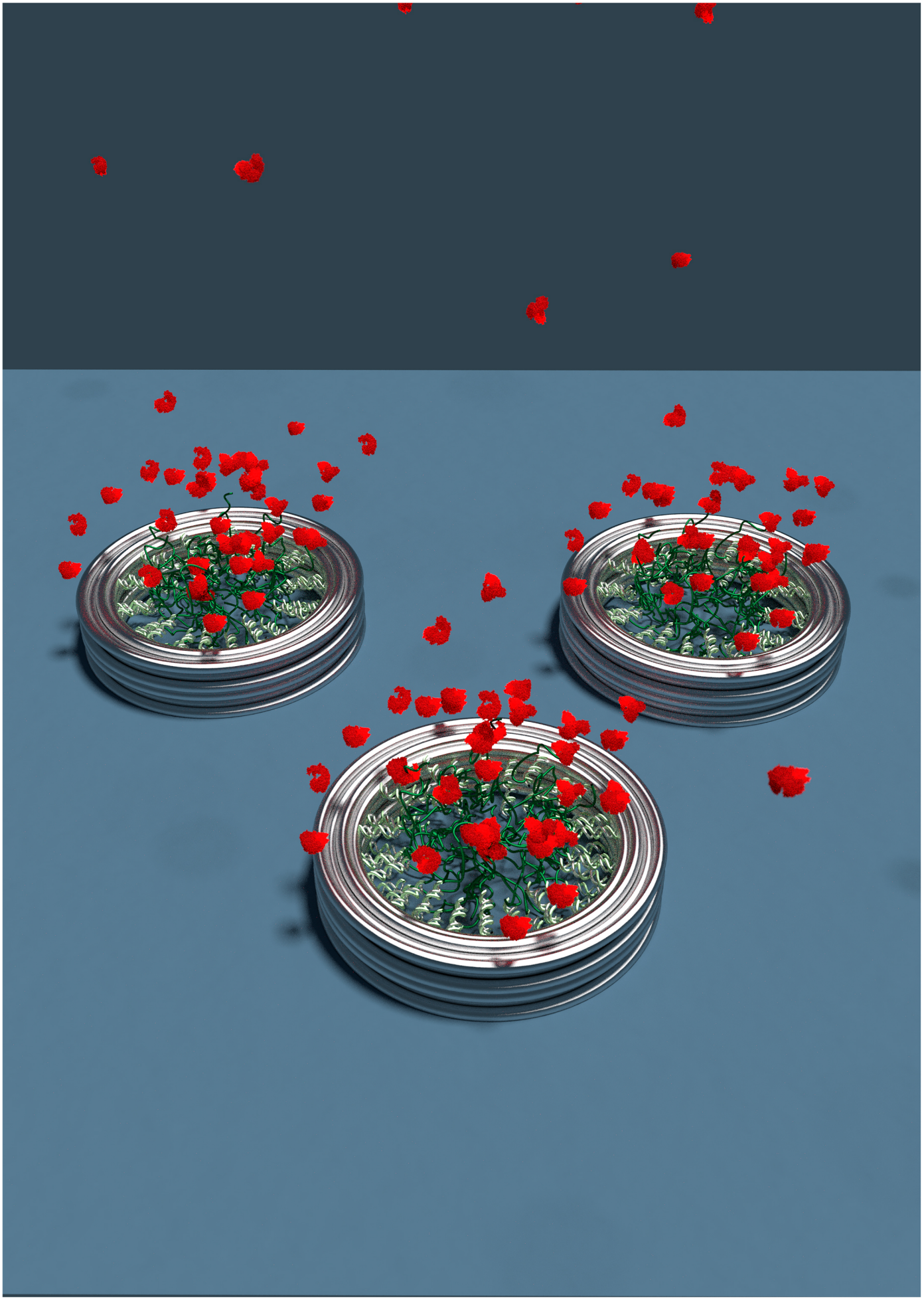
5.3 Discussion

This work demonstrates that purified FG-nups, grafted inside a cylinder, interact collectively to form clumps that persist for ∼1 s before transitioning. Furthermore, a subtle difference in behaviour between the FxFG-repeat Nsp1 and the more cohesive GLFG-repeat Nup100 is observed, with Nup100 persisting for longer times before transitioning (at comparable scan speeds; see Figure 5.5). While this result is expected,[9] it further emphasizes the importance of cohesion — alongside molecular-scale dynamics — to the collective behaviour of the FG-nups. For example, Nsp1, which on its own adopts a more extended, i.e., less condensed state than Nup100,[9] is nevertheless shown to form clumps that can persist for several seconds before transitioning. In the native NPC, however, the static appearance of the FG-nups is probably due to the presence of other macromolecular contents (namely NTRs and cargoes) that interact with the FG-nups and trap them in given morphologies.[8,34]

More generally, these results highlight several criteria that can be applied to facilitate the interpretation of nanometre-scale fluctuations in time-resolved AFM data, especially of dynamic data obtained from biological systems exhibiting a stochastic, rather than progressive nature. First, data must be background corrected, referenced to stable and flat areas of the sample (as is a common procedure for AFM images), and, separately, corrected for lateral drift. Second, if fluctuations are observed in the vicinity of protruding features on the sample, additional controls are needed (e.g., the empty DNA scaffold control in Figure 5.3 to rule out any artifactual nature). Third, to rule out white noise, dynamic features should be observed to persist over multiple subsequent scan lines (in unfiltered data), such as observed here in the kymographs recorded on NuPODs (Figure 5.2), and further articulated by the autocorrelation analysis (Figure 5.4), demonstrating and quantifying the persistence time of the observed molecular dynamics. Fourth, any such fluctuations should be significantly larger than fluctuations at other, presumably immobile positions on the sample (Figure 5.8). Finally, like any experimental method

that probes individual molecules, AFM is an invasive technique. To identify the effect of the tip upon induced molecular dynamics, the observed movements should be shown to be relatively robust against variations in imaging parameters and/or speed.

It is possible that differences dynamic behaviour of the intrinsically disordered FG-nups for NuPODs and native NPCs could be due to interactions between NTRs and FG-nups; in the following chapter the affect of the addition of exogenous NTRs on the NuPOD system will be studied. Tuning the type and density of nucleoporin along with the solution concentration of NTR will also facilitate greater insight into the physical nature of these interactions and how they contribute to the NPC's selective barrier. The next chapter will study how these molecules interact with FG-nups anchored within DNA origami scaffolds. Using single-molecule detection techniques this work will strive to understand how their binding affects the morphologies adopted by the FG-nups. Such fundamental studies will form an important foundation for any further development of the NuPOD platform, namely into a functional synthetic bio-filter.



Chapter 6

Transport receptor binding to FG-nups housed within NuPODs

All of the experimental work in this chapter was carried out by me. Kwasi Kwakwa (UCL) assisted with operation of the TIRF microscope and data collection. I performed all data analysis using ImageJ and custom MATLAB scripts written by George Stanley (UCL).

6.1 Introduction

Transport through the NPC is rapid; NTRs bind to their cargo, shuttle them through the central channel and release them into the nucleus within only a few milliseconds.[228] The whole process relies upon NTRs being able to pass through the selective barrier formed by a highly concentrated milieu of intrinsically disordered FG-nups that emanate into the centre of the NPC. Intrinsically disordered proteins (IDPs) are of biological importance for a number of processes in eurkaryotes. Their ubiquity (making up 30-50% of the entire proteome) owed to their functional plasicity; where structured proteins are optimised for one specific task, one can imagine IDPs are easily repurposed since they possess no secondary or tetiary structure, instead rapidly interconverting between a number of confomations.[229] Unlike most IDPs, the nucleoporins in the centre of the NPC are relatively hydrophobic and have a low net charge. Composed of multiple FG repeats,

these proteins are classified based upon the amino acid residues that flank that the F residue; FxFG, GLFG, PxFG, SxFG and FG being the most abundant FG repeats (where x is any amino acid).[230] The repeats are typically spaced by ∼10-20 amino acids, these regions having low complexity and relatively high hydrophilicity. However, it still remains unclear as to how these biochemical properties relate to their function. Moreover, it is highly debated whether these proteins predominantly interact cohesively or repulsively with one another and if there are any conformational changes that occur upon association with NTRs.[23] A molecular description of these fundamental properties of the transport barrier is required to fully comprehend how NTRs are selectively, rapidly translocated through the NPC.

Although many IDPs fold into a specific structure upon binding to their receptor — reestablishing the classical structure-function paradigm, some do not. Instead the IDP retains its disorder even in the bound state, forming a 'fuzzy' complex.[231] Recent studies indicate that 'random fuzzy' complexes are formed between NTR and FG-nups, i.e., the disordered FG-nups retain their dynamic flexibility, refusing to adopt a particular binding conformation, while continuing to interact specifically with transport receptor proteins.[59,60,230,232]

A number of different transport receptors are involved in the shuttling of cargo molecules, many of these belonging to the Karopherin super-family.[233] Although its members have vastly different sequences their structural features are highly conserved. One of the founding members of this family is importin-β, composed of HEAT repeats that form two amphiphilic alpha helices coiling in an anti-parrallel manner to adopt a helicoidal structure.[233] Structural studies of importin-β have shown its ability to change the pitch of the helicoid upon binding to different binding partners. Noteably, the change in pitch upon RanGTP binding to Imp-β is thought to facilitate the realease of FG-motifs from its binding pocket.[234] Other NTRs such as importin-α (which forms a heterodimer with importin-β) also adopts a solenoid structure, yet is comprised of ARM repeats that share their evolutionarily origin with HEAT motifs. However not all NTRs are structurally similar, for example NTF2 is a small homodimer formed of a bent β-sheet and three α helices.[235] In spite of structural dissimilarities, all NTRs have the ability to cross the ∼30 nm deep channel of the NPC by interacting directly or indirectly with FG-motifs.

Many NTRs contain multiple hydrophobic pockets that are involved in binding FG-motifs, one NTR may therefore bind multiple residues on the same nucleoporin or adjecent nucleoporins.[236] Up to nine binding sites have been identified for the archetypal transport receptor importin-β, which may be important in explaining how transport of these molecules through the NPC is so finely tuned.[226] On account of this multivalency, one must consider both the avidity ($K_{D,global}$) and the affinity ($K_{D,individual}$) of binding to FG-nupd. The avidity being an ensemble of simultaneous binding events occurring between multiple FG-residues and an NTR whilst the affinity is a measure of the binding of a single FG repeat to a single pocket on the NTR. As NTR•cargo complexes are able to pass through such a dense network of FG-repeats so rapidly, interactions between NTRs and FG-nups are expected to be very weak (on the order of mM).[55,69] However, paradoxially, *in vitro* measurements of $K_{D,global}$ values are often in the nanomolar to micromolar range.[53–55] Since $K_D = k_{off}/k_{on}$, given a typical protein-receptor on-rate ($k_{on} = 10^7$ M^{-1} s^{-1}), an interaction with $K_D \sim 1$ μM would exhibit an off-rate corresponding to a dissociation half-life of $\sim$70 ms. This would be too slow to explain the $\sim$5 ms transport times observed *in vivo*.[228]

Recent stopped-flow spectroscopy measurements showed that k_{on} values for interactions between NTRs and FG-nups are in fact much faster than those observed in other systems.[59] Values of $\sim 10^9$ M^{-1} s^{-1} suggest NTR-FG-nup binding occurs upon collision, without the need of rearrangement, further highlighting the unique properties of these disordered proteins.[236] Considering both these fast k_{on} values and low affinties that have been measured for interactions between NTRs and individual FG-repeats($K_{D,individual}$) one can start to recapitulate how ultrafast transport may occur.[58–60,232,237]

The NuPOD design is unique in its ability to monotonically increase the number of FG-nups anchored in a nanopore geometry. Note that thus far only two nucleoporins comprising either FxFG or GLFG repeats have been studied in this work, owing to their indispensability for selective barrier formation,[26] but this platform could easily be extended to house other relevant nups.

Thus far, the majority of experiments probing interactions between NTRs and FG-nups have used detection methods which measure over macroscopic dimensions and hence report an average over a large number molecules of such as QCM-D,,[53,57,73,238] SPR[56,131,238]

NMR.[60,232] Uniquely in this work, single-molecule detection techniques will be used to detect NTR binding in individual nanosized NuPODs, thereby detecting NTR-FG-nup interactions at a scale more proportionate with that of isolated nuclear transport. AFM imaging of individual NuPODs will enable the direct visualisation of NTR-FG-nup complexes, furthering understanding in the field on whether NTRs do trap otherwise highly dynamic FG-nups (as proposed in the previous chapter). This work also presents the first steps towards using fluorescence microscopy to probe the timescales of these interactions.

6.2 Results

6.2.1 Sample preparation for NTR addition to NuPODs

Although the supported lipid bilayers provided an appropriate substrate to adsorb and characterise NuPODs alone (see Section 4.2.4), they proved less suitable when NTRs were added. Specifically, the addition of hydrophobic NTRs caused disruption of the gel phase bilayers (see Figure 6.1a and b). Note that NTRs did not disrupt fluid-phase bilayers which form the basis of FG-nup film platforms,[53] but NuPODs could not be stably immobilised on top of these fluid phase SLBs. Alternatively, for NuPODs adhered on

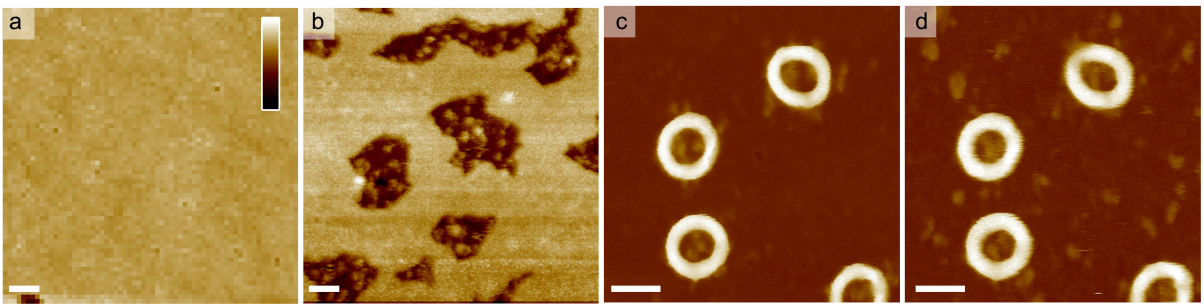


Figure 6.1: **AFM imaging of supported lipid bilayers and PLL-mica with added importin-β** a) DPPC:DDAB (3:1) SLB in 10 mM PB, 26 mM $MgCl_2$ buffer b) a different area on the same bilayer in the presence of importin-β at ~3 nM, the gel-phase bilayer is disrupted by the hydrophobic NTR c) 48×MBPNup100 on PLL-mica, imaged in 10 mM PB, 10 mM $MgCl_2$ d) the same area with importin-βmEos2 at ~25 nM, where it is difficult to differentiate whether the NTRs are interacting with the FG-nups or with the surface itself. Colour bar is 15 nm for a-b and 30 nm for c-d, scale bar is 50 nm.

PLL-functionalised mica, the addition of NTRs resulted in non-specific surface binding even concentrations as low as ∼25 nM (see Figure 6.1c and d). Since physiologically relevant NTR concentrations are in the micromolar range[239](∼3 μM for importin-β[240]), this was not a viable surface functionalisation to proceed with.

Therefore, an alternative surface preparation was employed to minimise NTR adhesion to the underlying substrate. PEGylated surfaces, as described in the methods section 2.2.4 and Chapter 3, were prepared by the co-deposition of PLL_{10}-*b*-PEG_{113} and $PLL_{1000-2000}$. Purified NuPODs were immediately added to the PEGylated surface and imaged in Peak Force tapping mode (mostly on the FastScan Bio, as its closed-loop scan system is more suitable for scanning larger areas). FG-nups or MBP moieties appeared differently in NuPODs absorbed onto PEGylated surfaces as compared with NuPODs on supported lipid bilayers. This may attributed to the FG-nups being repelled by the surface-grafted

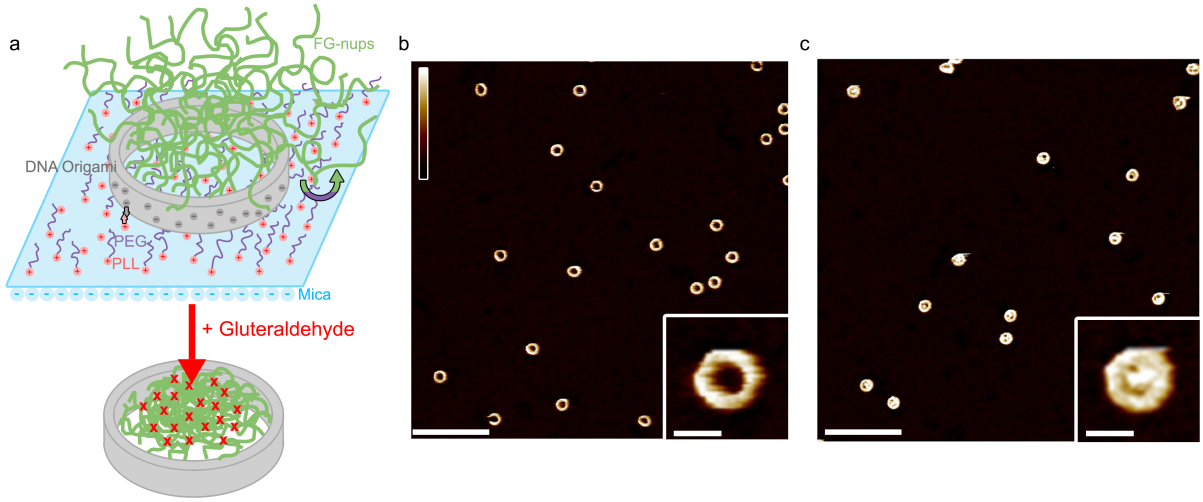


Figure 6.2: **AFM imaging of 48×MBPNup100 NuPODs on mica functionalised with PLL-*b*-PEG** a) A schematic detailing proposed surface interactions. Negatively charged mica is coated in PLL_{10}-*b*-PEG_{113}, the positively charged PLL attracts the negatively charged DNA origami whilst the PEG chains form a dense brush that repels the FG-nups from the surface, thereby eluding detection by the AFM tip. b)An AFM image of 48×MBPNup100 NuPODs, their lumen appearing 'empty' c) After incubation in a solution of ∼0.1% gluteraldehyde for 5 minutes and then washing extensively, the disordered proteins with their MBP moieties are crosslinked and can be detected as central condensates by the AFM tip. Colour bar 30 nm, scale bar in larger images is 400 nm and is 50 nm on the magnified insets.

PEG chains, whilst the DNA origami remains adhered to the surface via its electrostatic interactions with the underlying PLL. Hence the unsupported and dynamic proteins may be harder to detect by AFM. To verify this, the NuPODs were also imaged on this surface after addition of the crosslinking agent gluteraldehyde. After fixation, the central lumen of the NuPODs appeared filled in the AFM images, confirming the presence of the FG-nups (see Figure 6.2b and c).

6.2.2 ImportinBeta binding to Nup100 and Nsp1 - an AFM study

Upon addition of human importin-β (hsImp-β) to NuPODs containing 48× Nup100 molecules, the central lumens are seen to be increasingly filled with increasing concentration of hsImp-β in solution (see Figure 6.3). By contrast, no hsImp-β is seen bound to the substrate elsewhere, indicating that the surface functionalisation method, as described previously, is effective in inhibiting the importin-β from sticking to the background. Interestingly, when the solution contains ∼230 nM hsImp-β, some NuPODs appear to contain a number of bound hsImp-β molecules, as the height in the centre of the pore is greatly increased, while others still appear empty. A hypothesis for this observation could be that upon binding the disordered nucleoporin undergoes some compaction, concentrating the FG binding sites hence making the binding of further importin-β molecules more favourable. As the solution concentration is increased further, all pore lumens become filled. The observed binding of importin-β appears irreversible: even extensive washing (10× washes to leave an approximate concentration of ∼1 nM in the bulk solution) hsImp-β molecules remain bound (see far right image in Figure 6.3, note that the appearance of large tails going right to left on the NuPODs is due to poor tracking of the large features by the AFM tip). Failure to remove bound hsImp-β via simple buffer exchange is consistent with previous *ex vivo* experiments on *Xenopus laevis* NPCs, which showed that hsImp-β binds strongly and stably to the central FG-nup meshwork.[34] Indeed for Imp-β to unbind, other components of the transport system maybe required.[65,131,241]

After thus resolving interactions between importin-β and FG-nups, control experiments were conducted with NuPODs containing 48 copies of MBP to confirm there is no interaction between the two proteins and that NuPODs with the MBP tag attached could be used

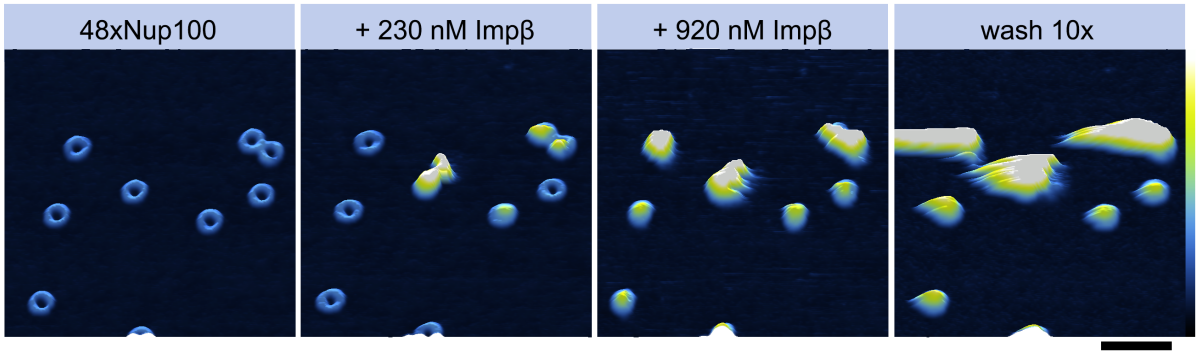


Figure 6.3: **Addition of human importin-β to NuPOD with 48×Nup100 (MBP tag cleaved).** AFM topographic images over the course of the hsImportin-β titration show NuPODs being filled with bound Imp-β. Although all pores are filled at higher concentration, at lower concentrations some lumens appear to fill up more readily with — presumably multiple (see below) — importin-β molecules. This suggests that at least initially, once one Imp-β molecule has bound, it becomes easier for others to bind. The hsImp-β used in these experiments was purchased from Novoprotein. The height colour scale shown on the right is 55 nm and the scale bar represents 200 nm. Images have been low-pass filtered with a Gaussian filter with 3 pixels FWHM, corresponding to 9 nm.

for future studies. As shown in Figure 6.4, there appears be be no discernible interaction between MBP and importin-βmEos2 as the central lumen continue to appear empty over the course of the titration, and the radial profiles do not appear much changed. When the concentration of hsImportin-βmEos2 in solution is increased from 0, to 200 and then to 1000 nM, the mean height of the central channel (radial position ¡ 4 nm) changes from 1.9 ± 1.7 nm to 1.1 ± 1.0 nm to 3.8 ± 2.1 nm (mean ± standard deviation). Two-tail Welch's t-tests, indicate a statistically significant difference between the channel heights for 200 and 1000 nM vs 0 nM(p = 9×10^{-6} and 7×10^{-18}). However, such AFM data sets can show systematic differences due to, e.g., differences in AFM tip shape and applied force during the experiments; and the numbers of independent experiments are typically insufficient (for practical reasons) to completely rule out that the observed height differences are due to such systematic differences between data sets. When comparing the height data on NuPODs containing Nsp1 and Nup100 proteins before and after the addition of importin-β, where an increase in height due to binding would be expected, Welch's t-tests indicated p-values far below 0.001 in almost all cases (refer back to Figures 2.10 and 2.9 in Methods section 2.4.3).

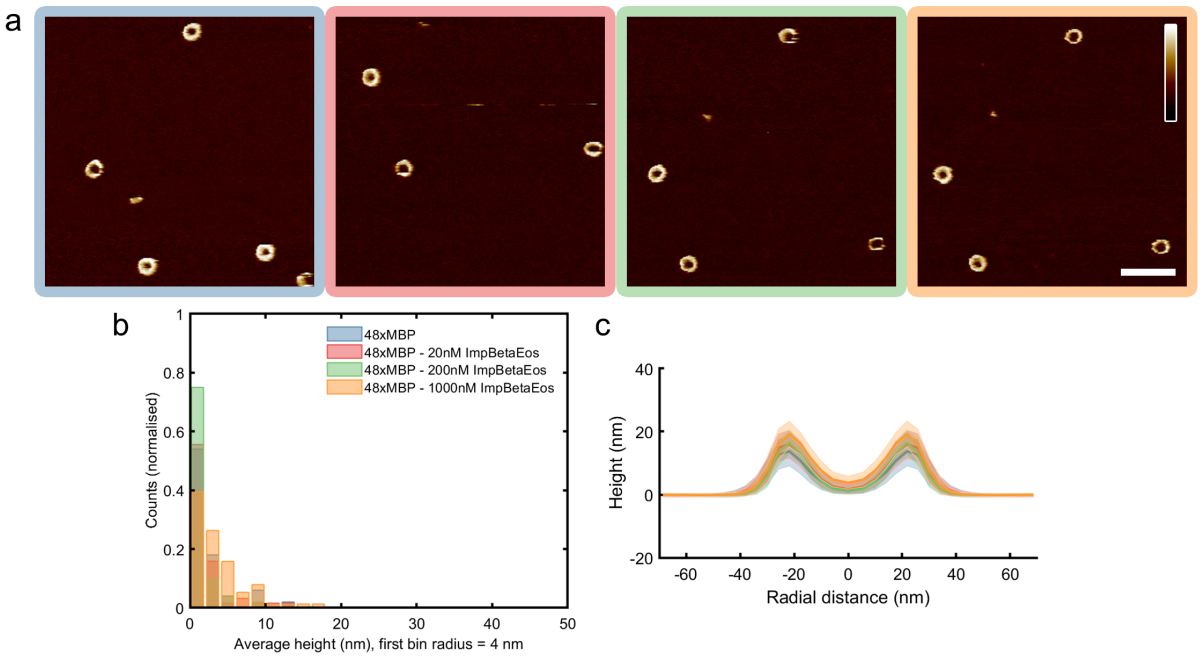


Figure 6.4: **Importin-βmEos2 binding control experiments with 48×MBP NuPODs.** a) AFM images showing that hsImportin-βmEos2 does not appear to bind to 48×MBP proteins anchored inside DNA origami scaffold. Left to right increasing concentration of importin-βmEos2 from 0-1000 nM (see colour key in b) b) Histogram of heights in the centre of the pore for n=100, 126, 104 and 156 NuPODs for Imp-βEos concentrations 0,20,200 and 1000 nM respectively. c) Averaged radial profiles of 48×MBP NuPOD with importin-βmEos2 addition, the shaded region represents the standard deviation. The scale bar in the AFM images is 200 nm and the colour bar represents 40 nm.

The concentration and type of FG repeats housed within each NuPOD can be well-controlled (see Chapter 4.2.3). Table 6.5 shows the total concentration of FG repeats (which includes FG along with FxFG for Nsp1 or GLFG for Nup100) housed within the different NuPODs, estimated as follows. Assuming that the 21 bp DNA handles that anchor the FG-nups also exclude them, the effective diameter of the DNA scaffold is 32 nm. This extends to 46 nm if one assumes that the FG-nups are able to occupy the entire inner diameter of the DNA origami ring and are not excluded by the DNA handles. Concentrations in mM have been calculated for both cases where the effective concentration of FG-nups is approximately halved when assuming the larger diameter. The height is approximated as the height of the DNA scaffold (14 nm), although one might expect the disordered proteins to extend beyond this, it is non-trivial to estimate

to what extent. The Nsp1 (2-603) segment used here contains a total of 34 FG repeats of which 19 are FxFG repeats, whereas the Nup100 (2-610) segment contains 44 repeats of which 11 are GLFG. GLFG repeats are essential for cell viability and are the dominant repeat type of yeast NPCs, although Nsp1 is the most abundant FG nup in yeast,[8] an absence of FxFG repeats can still lead to cell viability.[26] ScImportin-β (also known as Kap95) and its vertebrate orthologue hsImportin-β bind to both FxFG and GLFG repeats. Although some studies have also suggested that binding is stronger for FxFG repeats,[55,242] the magnitude of this difference is unclear. Futhermore, *in vitro* experiments have shown that the influx of scImportin-β into FG-repeat hydrogels is greater for those containing GLFG repeats over FxFG repeats.[70]

	Number of Nups			
	8	16	24	48
Nsp1				
# FG repeats	272	544	816	1632
[FG repeats] / mM	19–40	39–80	58–120	116–241
Nup100				
# FG repeats	352	704	1056	2112
[FG repeats] / mM	25–52	50–104	75–156	151–311

Figure 6.5: **Calculated concentrations of FG repeats for NuPODs housing 8, 16, 24 or 48 Nsp1(2-603) or Nup100(2-610)**.Concentrations of FG repeats are indicated as ranges determined from minimum and maximum estimates of the NuPOD inner diameter (see text). For entire amino acid sequences of the constructs used, see Figure 2.2

Importin-βmEos2 was used for further studies, as the presence of a photoconvertible dye did not lead to noticeable differences (with respect to wild type) in FG-nup binding, and since this will facilitate a comparison with additional fluorescence microscopy experiments (as described later, in Section 6.2.4). Figure 6.6 shows hsImp-β-Eos binding to NuPODs that house 16 copies of MBPNup100. Consistent for results with hsImp-β binding to 48×Nup100 NuPODs (refer to Figure 6.3), some pores appear to fill up more readily than others at low importin-β concentrations, whereas at higher concentrations, most pores showed a similar degree of filling. This suggests that at least initially, importin-β binding is somewhat cooperative. Throughout this titration the pores become more and more filled, indicative of multivalency since the binding sites do not appear to become saturated, with pores continuing to fill up even when the concentration is in the micromolar range

(see Figure 6.6a and b). To facilitate AFM imaging in the 5 μM hsImp-βEos experiment, the 60 μl droplet was replaced 5×, to yield a total dilution of approximately 32× after an initial incubation of approximately 15 minutes. Given the irreversibility of importin-β binding as reported above, I do not expect this washing step to change the overall results. Moreover although the concentration in the bulk solution is diluted, the concentration near the FG-nups is still expected to be high.[238] For AFM imaging, when the sample droplet contains a high concentration of soluble protein, the ability of the AFM tip to image the features clearly can be affected. This is due to the propensity for proteins to stick to the AFM probe, leading both to tip artefacts on the recorded image and impaired sensitivity due to changes to the laser reflection on the back of the cantilever.[128]

A similar trend is observed for hsImportin-βmEos2 addition to NuPODs housing 24×MBP--Nsp1 proteins (Figure 6.7). These pores contain a similar density of FG-repeats as the 16×MBPNup100 system shown previously. It follows that the central bin heights detected at respective importin-βmEos2 concentrations of 20, 200 and 1000 nM are similar (see Figure 6.6b-d vs Figure 6.7b-d). Here, experiments were carried out up to a concentration of 2 μM importin-β in solution; at this concentration binding does not appear to be fully saturated as the AFM images and data show a few apparently empty pores. It would be useful to image the pores again at a solution concentraion of 5 μM, it should also be noted that here imaging at 2 μM was still possible without need of a washing step.

The observed behaviour for hsImportin-β—FG-nup binding can be compared with the binding of monoclonal antibody (AntiMBP) to 48×MBP NuPODs, noting that AntiMBP is approximately 150 kDa in size, compared with 129 kDa for hsImportin-βmEos2. For this case, there are 48 binding sites per DNA origami ring and so a maximum of 48 AntiMBP molecules are able to bind. Upon saturation, all the central lumen fill up to the the height of the pore scaffold but no further. More strikingly, for a given concentration, the variability of the NuPOD filling appears much less, i.e., all pores appear to be similarly filled, as can be seen in the AFM images as well as via the narrow distributions of the measured heights in the pore centre. However, it was not tested if wider distributions occurred for lower AntiMBP concentrations.

To comprehensively study the effect of FG-nup type and copy number on NTR binding, hsImp-βEos was titrated onto samples of NuPODs housing 8, 16, 24 or 48 MBPNsp1 or

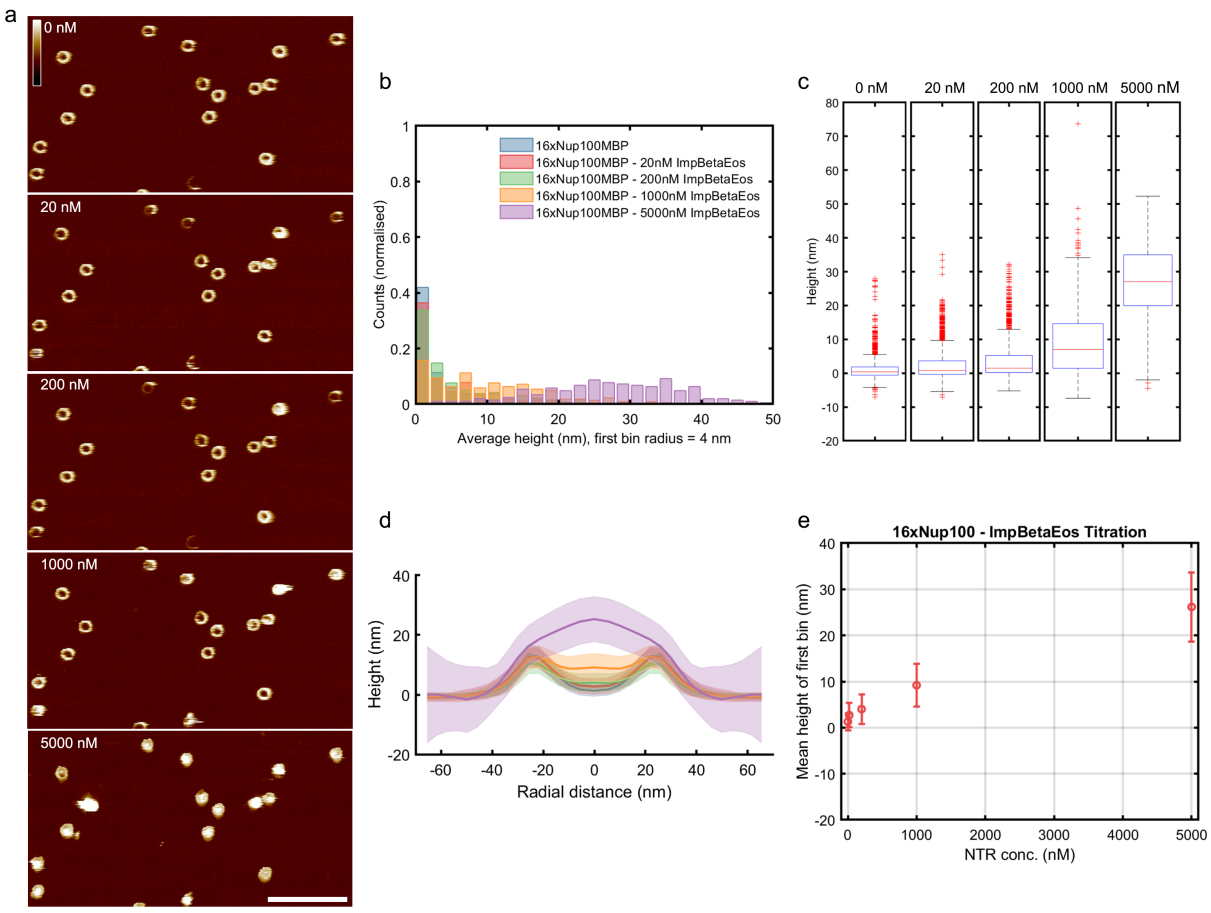


Figure 6.6: **Importin-βmEos2 addition to 16×MBPNup100 NuPODs.** a) AFM images as hsImportin-βmEos2 is titrated (0-5000 nM). b) Histogram of heights in the centre of the pore for n=291, 272, 237, 223 and 207 NuPODs for Imp-βEos concentrations of 0, 20, 200, 1000 and 5000 nM respectively. c) Box plots for the same data as in b), the central line indicates the median and the upper and lower edges of the box indicate the 25th and 75th percentiles. d) Averaged radial profiles of 16×MBPNup100 NuPOD with Imp-βEos addition. The shaded regions indicate the standard deviation e) Titration curve for the addition of Imp-βEos to 16×MBPNup100 NuPODs where the mean height in the centre of the pore is plotted and error bars are the standard deviation. AFM scale bar is 400 nm and the colour bar represents 40 nm.

MBPNup100 molecules. The results from these experiments are summarised in Figure 6.9. As before, the height measured in the very centre of the channel was used as a metric for importin-β binding. NuPODs remain 'empty' in appearance when 20 nM hsImp-βEos is present in solution. When the concentration is increased to 200 nM hsImp-βEos, the DNA origami rings with 24× or 48× MBPNsp1 or MBPNup100 appear to fill with NTRs

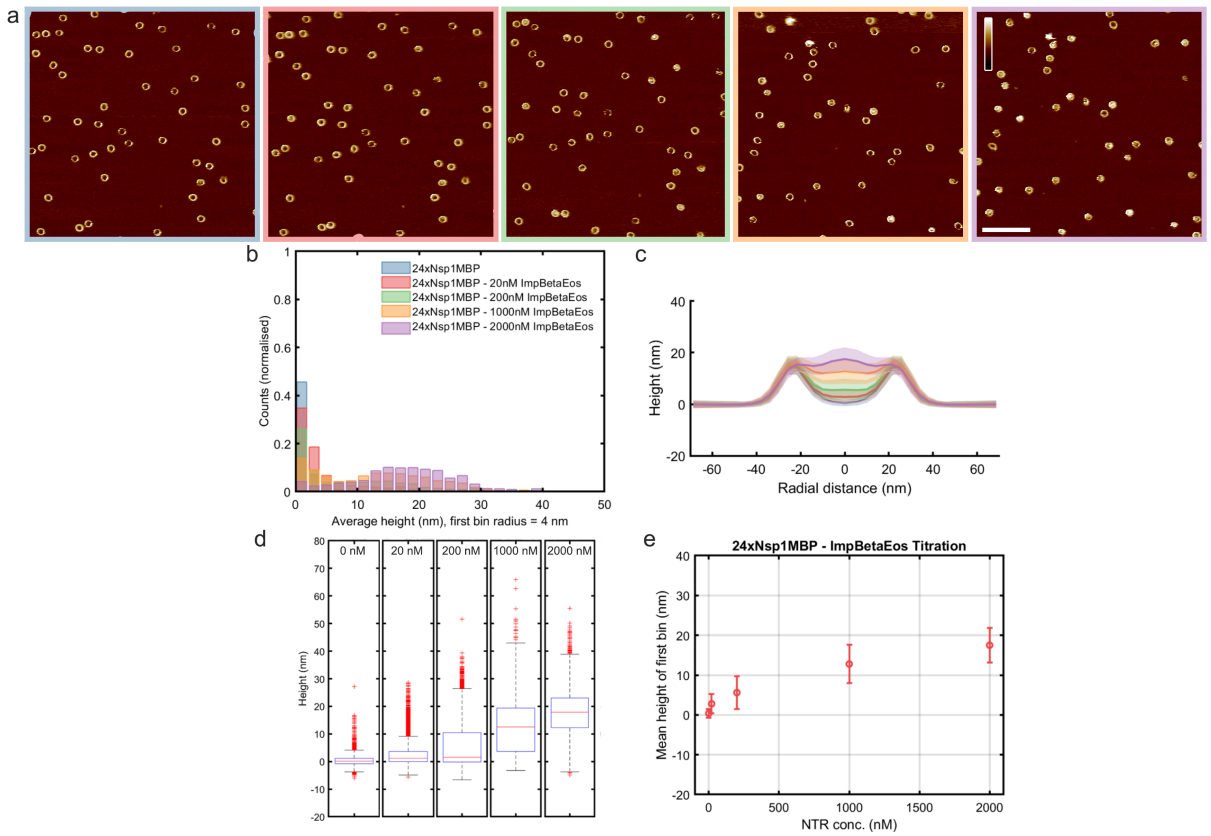


Figure 6.7: **Importin-βmEos2 addition to 24×MBPNsp1 NuPODs.** a) AFM images as hsImportin-βEos is titrated (0-2000 nM). b) Histogram of heights in the centre of the pore for n=1012, 1038, 1014, 928 and 760 NuPODs for Imp-βEos concentrations of 0, 20, 200, 1000 and 2000 nM respectively. c) Averaged radial profiles of 24×MBPNsp1 NuPOD with hsImp-βEos addition, the shaded region indicates the standard deviation d) Box plots for the same data as in b), the central line indicates the median and the upper and lower edges of the box indicate the 25th and 75th percentiles. e) Titration curve for the addition of hsImp-βEos to 24×MBPNsp1 NuPODs where the mean height in the centre of the pore is plotted and error bars are the standard deviation. AFM scale bar is 400 nm and the colour bar represents 40 nm.

(see Figure 6.9a-d). Overall the trend across the data is as expected, i.e., the greater the copy number, the higher the mass observed in central lumen for a given concentration of hsImportin-βmEos2. NuPODs housing 48 copies of MBPNup100 appear more filled than those that house 48 copies of MBPNsp1 — this may be due to the higher concentration of FG repeats in the former construct (see Table 6.5). However more experimental repeats would be needed to confirm this is the case. Furthermore, it would be interesting to gather more data at even higher concentrations of NTRs, to detect a saturation point. Although

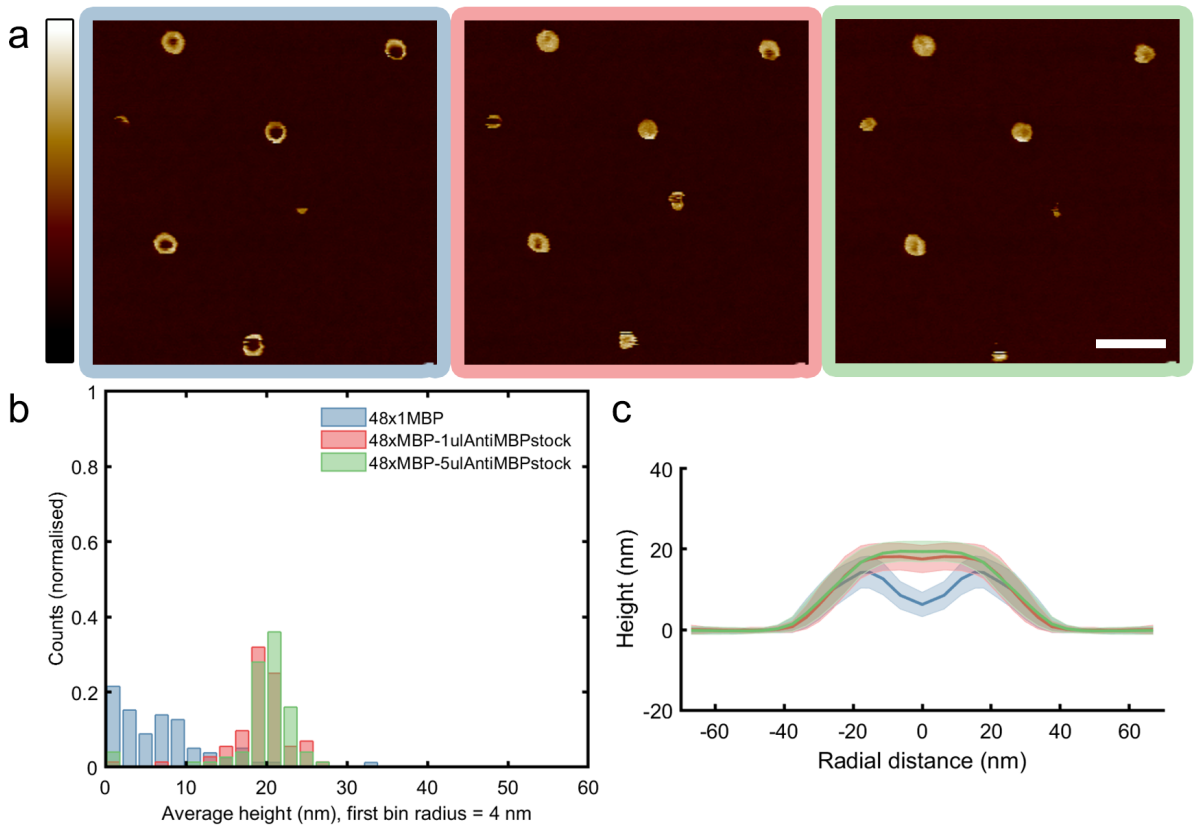


Figure 6.8: **Anti-MBP binding control experiments with 48×MBP NuPODs.** a) AFM images showing that monoclonal antibody against MBP binds to the 48×MBP proteins and fills up the pores (images are boarded with colours corresponding to the colour key in b)). b) Histogram of heights in the centre of pore for n=79, 72 and 75 NuPODs with no AntiMBP and then with 1 μl and 5 μl of the stock AntiMBP (approximately 110 and 550 nM). c) Averaged radial profiles of 48×MBP NuPOD with AntiMBP addition. The shaded region indicates the standard deviation. Note a maximum in height is quickly reached when all their binding sites are filled (AntiMBP is approximately 150 kDa and of similar molecular weight to the importin-βEos which is 129 kDa). Scale bars in the AFM images are 200 nm and the colour bar represents 40 nm.

the $\sim$1 μM concentrations of importin-β used here are of the same order of magnitude as those measured *in vivo* (3-5 μM),[240] the total concentration of all NTRs combined is estimated at around 10 μM.[70]

On account of convolution effects from the AFM tip as it tracks over the pore scaffold and compression artefacts that may result from the imaging force,[153] it is non-trivial to equate the central channel height to a precise number of bound importin-β molecules.

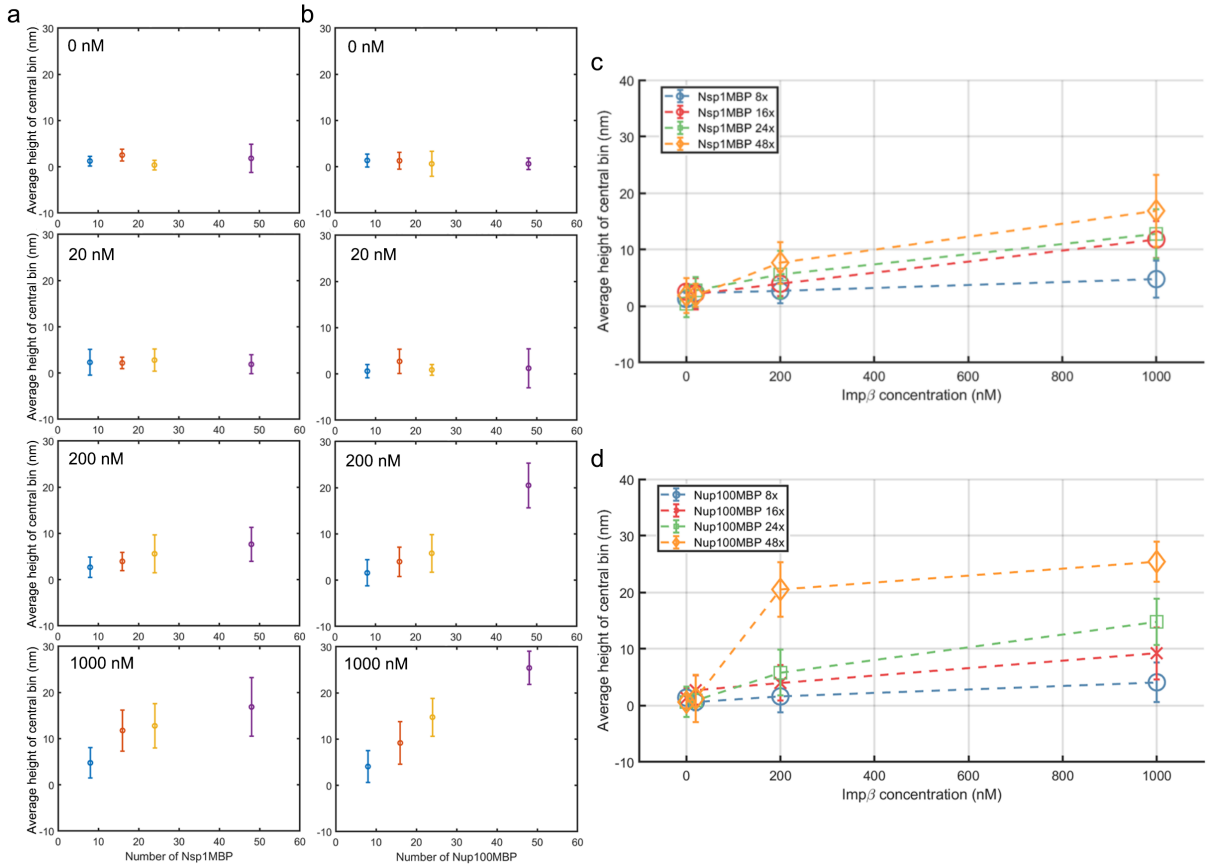


Figure 6.9: **Importin-βmEos2 addition to NuPODs containing different numbers of FxFG or GLFG repeats.** a) For NuPODs housing different numbers of MBPNsp1 molecules the height in the central 8 nm of the pore lumen is seen to increase with FG-nup copy number and importin-βmEos2 concentation. b) as a) but for MBPNup100 molecules. c) a plot of all data for MBPNsp1 d) as for c) but for MBPNup100. The data presented here is the mean height detected in the central lumen using AFM, across a large number of NuPODs in one or more images(n = 100-1600 NuPODs for each data point).

Moreover, the central mass is a heterogenous mixture of FG-nups along with transport receptors, which makes it even more challenging to estimate the volumes occupied by each of these species as their arrangement in the pores is unclear. At the most physiologically relevant solution concentration of 1 μM the average height of the central conduit can converted to a volume assuming an inner diameter of 32 (or 46 nm). Subtracted from this the combined volume of the FG-nups and MBPs (estimating $\sim$115 and 118 nm^3 per molecule for Nsp1MBP and Nup100MBP, respectively[46,151,152]) and approximating the importin-βmEos2 volume as $\sim$150 nm^3,[73,243] we find the number of importin-β molecules

to be of the order of ∼10 (or ∼100 for the larger diameter). This implies that ∼10% of the FG repeats are occupied, in line with previous results on FG-nup films, where only ∼20% of FG-motifs engaged in NTR binding.[73]

In these binding studies, select interactions i.e those between Nsp1 and Nup100 proteins from *S. cerevisiae* and vertebrate importin-β (from *Homo sapiens*)have been studied. Experiments adding the *S. cerevisiae* orthologue Kap95 (or scImportin-β) were also conducted to rule out any affect from the heterogenous origin of the proteins employed. In our AFM studies we were unable to detect any Kap95 binding, despite previous work that has shown the FxFG repeats of Nsp1 and GLFG repeats of Nup100 bind in a similar manner to both scImp-β and hsImp-β.[244] However, hsImportin-β from a number of different sources (see methods section 2.1.7) all bound strongly to the FG-nups housed within the NuPODs, (irrespective of labelling with fluorescent tags). It would be interesting to anchor human orthologues of Nsp1 and Nup100 (namely nup62 and nup98) to the DNA origami scaffold and see if the same behaviour was observed — owing to time constraints, such experiments are beyond the scope of this thesis.

6.2.3 Replicating transport - NTR binding reversibility

A somewhat puzzling aspect of the results so far is the observed irreversibility of hsImportin-β binding in our assays, which appears in contradiction with the notion that NTR•cargo complexes shuttle rapidly in and out of the NPC (see introductory Section 1.1.2). This may in part be explained by the absence — in this *in vitro* approach — of other cellular proteins that may influence NTR—FG-nup interactions *in vivo*.[55] Although, in other minimalist *in vitro* experiments, scImportin-β (Kap95) could be washed out of surface grafted Nsp1 (with similar density as in the NuPODs) by simple buffer exchange,[53,73] in other work washing with a denaturing buffer containing 8M Urea was required to regenerate a clean FG-nup film.[238] Neverless, despite many attempts bound hsImportin-β (and hsImportin-βmEos2) was not able to be removed by droplet dilution. This observation is consistent with AFM studies on native NPCs from *Xenopus laevis*[34] and supports the idea that at steady state a number of Imp-β molecules may occupy the central barrier.[62]

Taking inspiration from previous work I also attempted to release hsImportin-β by adding

cyclohexandiol, an alcohol known to disrupt hydrophobic interactions between FG-nups.[245] However, using AFM, no change of the central mass was detected that would indicate a release of bound hsImportin-β. Competitive binders namely BSA and bacterial cell lysate were also added in high concentration, since their presence has previously been shown to reduce FG-nup—NTR avidity.[55] Yet again, these agents did not induce any noticeable pore un-filling which would amount to a lowered NTR—FG-nup avidity

Since RanGTP (and its yeast orthologue Gsp1p) is thought to promote NTR release from FG-nups this was also aded to the system yet failed to show a clear reversibility of Imp-β binding. Equally, RanGTP did not increase the size of the central condensate. Some studies have suggested that unbinding by RanGTP addition is only promoted for the Imp-α—Imp-β complex.[131] Experiments were also conducted to detect unbinding of this pre-formed assembly, but again dissociation was not apparent. Interestingly Imp-α alone did not bind to the NuPODs, in line with previous observations that suggest it does not engage directly with FG-nups.[131]

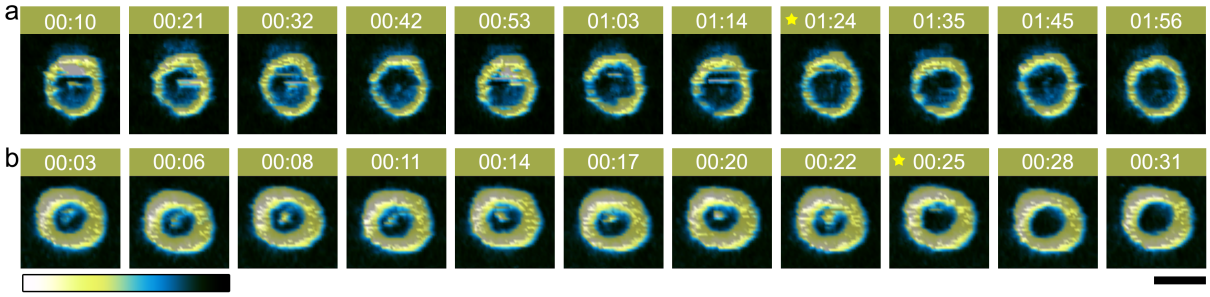


Figure 6.10: **Importin-βmEos2 forms mobile, fuzzy complexes with FG-nups** AFM images shown as a composite of the height and peak force error channels for a) Sequence of AFM images for 8×MBPNsp1 NuPODs in the presence of ∼200 nM hsImportin-βmEos2 and b)As a, for 48×MBPNup100 NuPODs in the presence of ∼20 nM hsImportin-βmEos2. Time stamps are shown above the images, stars indicate the points at which the lumens appear to empty. Colour scale represents 25 nm and the scale bar is 50 nm.

In some cases, for importin-β concentrations at which some of the NuPODs in the field of view showed weak signatures of bound importin-β molecules, the NuPOD lumens showed significant dynamics and repeated scanning over the pore appeared to dislodge bound NTRs. This is possibly due to the forces exerted by the AFM tip, causing the FG-nup NuPODs to change to an apparently empty configuration (see Figure 6.10). The observed

dynamics may — most cautiously — be thought consistent with NTRs and FG-nups forming a 'fuzzy' complex where the FG-nups retain their conformational flexability.[59] The multivalency of the interaction facilitating rapid re-binding. It is tempting to correlate the here observed importin-β/FG-nup dynamics with FG-nup dynamics (without NTRs) as described in in chapters 4 and 5, but this is complicated by the different surface functionalisations used in these respective experiments.

6.2.4 TIRF microscopy study

Since the AFM tip is only able to detect surface-bound molecules or sufficiently dense ensembles (see earlier discussion and Figure 6.2), transient interactions that may also occur between the FG-nups and Imp-β molecules cannot be recorded using this technique. Previous studies have suggested that there may be two different ways in which importin-β interacts with the FG-nup barrier,[56,57,131] proposing that high-affinity interactions localise a stable pool to the central barrier, cross-linked in the FG-meshwork, as well as a more weakly bound population. Once saturated, low-affinity interactions of importin-β would yield a 'fast-phase' able to rapidly translocate cargo molecules through the NPC. In other work, it was found that the binding affinity of additional NTRs decreased upon saturating FG-nup assemblies with NTRs.[45,73] Light based techniques such as total internal reflection fluorescence microscopy (TIRFM) lend themselves to detection of the binding modes of NTRs. Moreover, one can achieve chemical identification (with specific labelling), higher temporal resolution, and there is no requirement of any applied force. This method does, however, come with the caveat of a lower spatial resolution and data interpretation is often not as straightforward.

To facilitate studies using fluorescence based techniques, the NuPODs were labelled with Alexa Fluor 647 dye molecules. This allows the positions of the NuPODs to be identified so that the addition of fluorescent NTRs to these locations can then be monitored. For labelling, we added the fluorescent oligonucleotide-Alexa Fluor 647 complimentary to 8 ssDNA handles on the outside of the DNA scaffold, prior to purification, (in a 4×excess, see methods section 2.1.3). To measure how many fluorophores were anchored to each NuPOD, image stacks were recorded until all intensity spots had dropped to background levels. Exemplary photobleaching traces for NuPODs (containing 16×MBPNup100 pro-

teins) alone on PLL-*b*-PEG functionalised glass is shown in Figure 6.11.

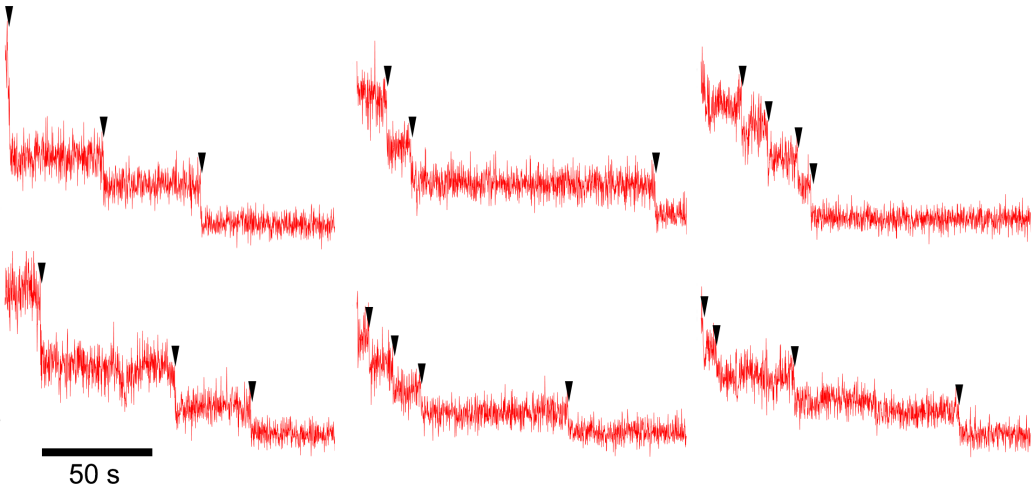


Figure 6.11: **Photobleaching traces of NuPODs labelled with Alexa Fluor 647** Recordings of intensity (in arbitrary units) against time for DNA rings containing 16 copies of MBPNup100 labelled with Alexa Fluor 647-oligonucleotides. Each ring had 8 ssDNA anchoring sites for dye attachment. Photobleaching traces were recorded with an exposure time of 100 ms.

Photobleaching of individual fluorophores anchored to the DNA origami scaffold resulted in a clear step-wise decrease in emitted intensity. A maximum of four steps were detected in our bleaching traces. There are however some discrepancies in the sizes of the steps. There are a number of possible explanations for this, firstly illumination across the entire field of view may be uneven leading to differences in the summed intensity in the region of interest (as plotted in Figure 6.11) which is a sum of the fluorescent molecules and the backgound. Secondly, although the pixel window was optimised include the whole Gaussian of the intensity signal, some may be cut off leading to small differences. Thirdly, two molecules may bleach at once (see top left), leading to larger steps. Although a comprehensive analysis was not performed, this indicates that each DNA ring had between 3-4 dye molecules attached. Several factors can bias the detection of photobleaching steps such as signal noise and the proximity of dyes. To improve these traces a different oxygen scavenging system could be tested or incubation with a larger excess of oligonucleotide-dyes during hybridisation. However, the emitted fluorescence was sufficient for NuPOD localisation.

Next the interaction between hsImportin-β-mEos2 and the FG-nups anchored on the in-

side of the DNA rings was explored. The mEos2 tag is photoconvertible protein, emitting strong green fluorescence (519 nm), this shifts to red (584 nm) following near-UV irradiation. For these experiments, the red-shifted form was used. Firstly the positions of the NuPODs were identified by exciting with a 640 nm laser. The sample was then illuminated with a constant source of low intensity 405 nm light in addition to 561 nm illumination to detect hsImp-βEos molecules (see Methods section 2.6). For TIRF microscopy fluorescent importin-β is used at a low nanomolar concentration, orders of magnitude lower than in the AFM experiments. Although the generation of an evanescent field causes only molecules within ∼100 nm of the surface to be detected, the presence of a large concentration of fluorophores in solution greatly increases the background noise. At the concentrations used, the efficacy of the surface passivation protocol using PLL_{10}-*b*-PEG_{113} is further validated on glass. As this is an optical-based single-molecule technique it is particularly sensitive to the detection of labelled molecules that have non-specifically adsorbed onto the surface.

Figure 6.12 shows overlaid localisation spots for 16 and 48×MBPNup100 NuPODs (in magenta) with 7 nM hsImportin-βmEos2 (in cyan). Colocalisation, i.e., binding is indicated by the appearance of yellow spots. By analysing a number of different areas on the sample, 75 ± 3 % of the 16×MBPNup100 NuPODs were found to colocalise with hsImp-βEos molecules. This increased to 96 ± 1 % of the 48×MBPNup100 NuPODs (n = 171 and 94 for 16× and 48×MBPNup100 NuPODs respectively). These observations agree well with AFM data, which shows increased binding for NuPODs containing more FG repeats, as expected. However, here hsImp-βEos is present at a very low concentration (∼7 nM), for which it was not possible to detect binding by AFM probing. Perhaps the importin-β molecules are binding more reversibly at these levels, or such a small amount is bound that it is not sufficient to induce FG-nup crosslinking to facilitate AFM detection. Although these concentrations are far lower that the micromolar concentrations *in vivo*, the cellular environment is far more crowded with other components which may act as competitors weakly occupying binding sites and lowering the avidity of these specific interactions.[55]

To identify whether these interactions are transient in nature, the intensity versus time traces for 6 pixel windows around each NuPOD were recorded, representative traces are shown in Figure 6.13 (for more detailed methods see section 2.6). The hsImp-βEos

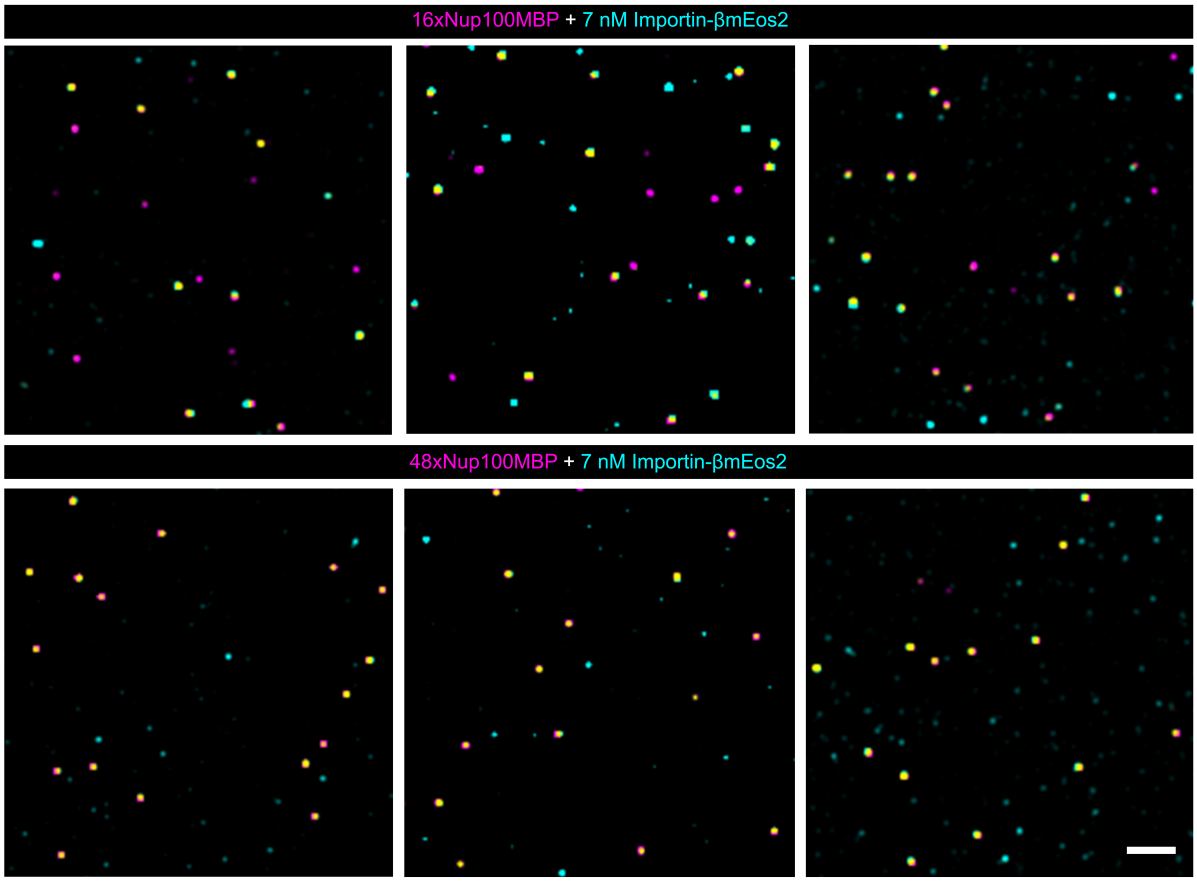


Figure 6.12: **Colocalisation of hsImportin-βmEos2 to NuPODs containing contain 16 or 48 MBPNup100 proteins** Image stacks collected during illumination with 640 or 561 nm light were processed using the ThunderSTORM plugin for ImageJ and visualised using the average shifted histograms method. The 640 nm stack corresponds to NuPOD positions and is shown in magenta. This is overlaid with the 561 nm stack coloured in cyan, corresponding to hsImp-βEos molecules. hsImp-βEos binding is determined by colocalisation and the appearance of a yellow spot (as opposed to magenta or cyan). The images have been offset a couple of pixels to account for misregistration of the colour channels (see Methods 2.6). The scale bar corresponds to 5 μm.

was equilibrated in solution before recording, therefore, mostly decays in the intensity as bound the mEos2 protein tags are photobleached are detected. Although for the 16×MBPNup100 NuPOD (Figure 6.13a), some molecules also appear to bind to the NuPODs later in the recorded traces. In contrast to the clear photobleaching steps observed for Alexa Fluor 647 dyes anchored to the ring (Figure 6.11), a stepwise decay is not as discernible in Figure 6.13b. This makes it difficult to correlate an intensity drop

to the photobleaching of a single fluorophore; a value that could be used to identify the number of hsImp-βEos molecules per NuPOD. Photobleaching traces of the fluorescent proteins only on glass were also recorded but again the traces appeared very heterogeneous and the average intensity and bleaching time for a single molecule could not be detected. Since mEos2 is a photoconvertible dye, the analysis is further complicated by fluorescence switching, the binding of hsImportin-β that is tagged with a single synthetic dye (Alexa Fluor 594) at a precise position along the molecule (at the 213^{rd} amino acid residue) was also studied.

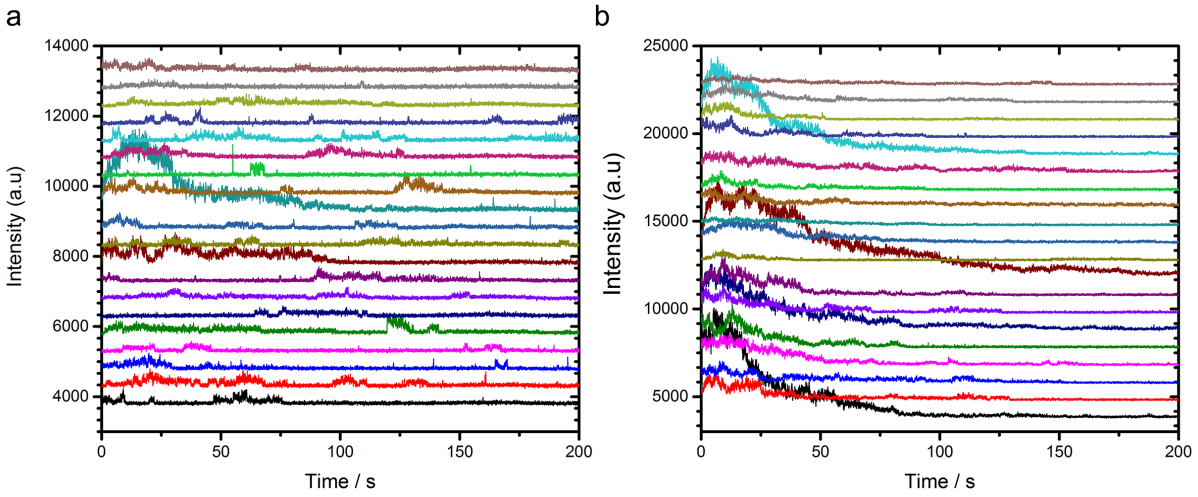


Figure 6.13: **Intensity vs. time traces for importin-βmEos2 molecules interacting with NuPODs containing 16 or 48 MBPNup100 proteins** 6 pixel windows were cropped around the positions of NuPODs and the intensity integrated in each window for each frame captured in the channel corresponding to importin-βmEos2 molecules. Exemplary traces shown have not been background subtracted and are offset for clarity. (a) for 16×MBPNup100 NuPODs (b) for 48×MBPNup100 NuPODs.

For a more contrasting density of FG-repeats, the binding of this synthetically labelled importin-β to NuPODs containing 8 or 48 copies of MBPNup100 was compared. A lower concentration of the NTR, ∼2 nM was also used (see Figure 6.14 for the co-localisation of fluorescence intensity spots). In this experiment, most NuPODs containing 8×MBPNup100 molecules did not bind the importin-β; only 14 ± 2% of the 221 NuPODs imaged were colocalised with the NTR. This increased to 63 ± 6% for NuPODs with 48 copies of the protein (n = 142 NuPODs).

Figure 6.15 shows the intensity vs. time traces for the hsImportin-β tagged with a single

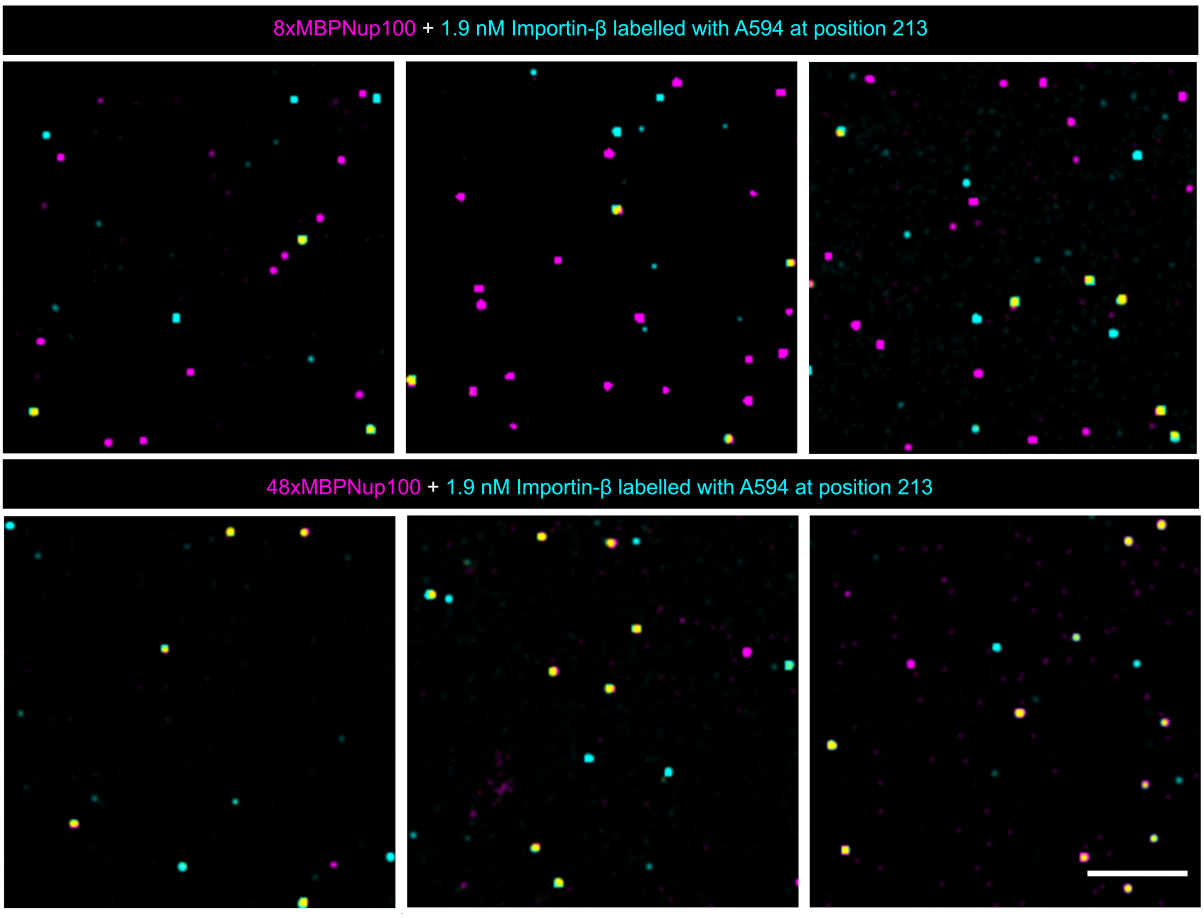


Figure 6.14: **Colocalisation of importin-βAlexa Fluor 594 to NuPODs containing 8 or 48 MBPNup100 repeats** Image stacks collected during illumination with 640 or 561 nm light were processed using the ThunderSTORM plugin for ImageJ and visualised using the average shifted histograms method. The 640 nm stack corresponds to NuPOD positions and is shown in magenta. This is overlaid with the 561 nm stack coloured in cyan, corresponding to hsImp-β molecules labelled with a single Alexa Fluor 594 dye. hsImp-β binding is determined by colocalisation and the appearance of a yellow spot (as opposed to magenta or cyan). The images have been offset a couple of pixels to account for misregistration of the colour channels (see Methods 2.6). The scale bar corresponds to 5 μm.

Alexa Fluor 594 dye. Again the NuPODs were pre-incubated with the NTR such that traces were recorded after equilibration. This means the analysis is not further complicated by the time it takes for a molecule to diffuse to the surface. In Figure 6.15a, i.e., the traces for windows around 8×MBPNup100 NuPODs, most intensity spikes corresponding to Imp-βAlexa Fluor 594 molecules on the surface occur after a some time, and are

very short lived. For the majority of the time, the traces remain mostly at the baseline, representative of a lack of binding. In contrast typical traces for 48×MBPNup100 NuPODs show a much increased intensity at the start of the recording. This indicates that a number of hsImp-β are bound to the higher density of FG-repeats at the beginning of recording. The drop in intensity most likely related to photobleaching as opposed to unbinding, owing to the long timescale and sloped decay, although again further information is needed to quantify these parameters. Bleaching experiments for the Imp-βAlexa Fluor 594 molecules only on glass were also conducted but any meaningful values from the data due to heterogeneity in the observed intensities could not be extracted.

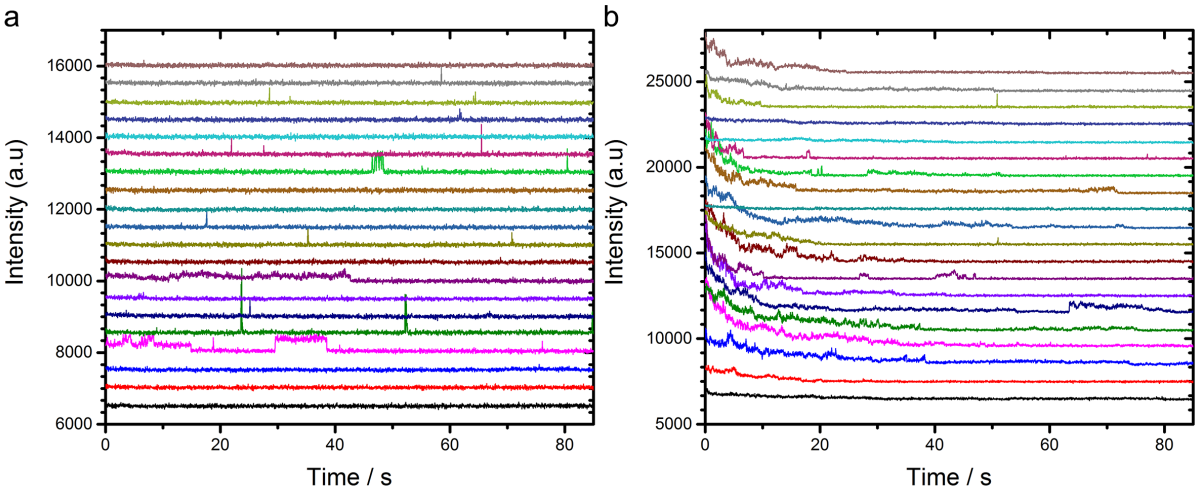


Figure 6.15: **Single molecule intensity traces of importin-βAlexa Fluor 594 interacting with NuPODs containing 8 or 48 MBPNup100 proteins** 6 pixel windows were cropped around the positions of NuPODs and the intensity integrated in each window for each frame captured in the channel corresponding to importin-βAlexa Fluor 594 molecules. Exemplary traces shown have not been background subtracted and are offset for clarity. (a) for 8×MBPNup100 NuPODs (b) for 48×MBPNup100 NuPODs.

Initial experiments suggest that TIRFM could be a powerful technique for observing interactions between FG-repeats and NTRs at the single molecule level, providing complementarity to AFM methods and offering chemical sensitivity. Since only fluorescent molecules are detected, one could also spike in additional, non-labelled components of the NPC transport system and see how they affect interactions between isolated components. However, these preliminary experiments also indicate that interpretation of such data may not be straightforward.

6.3 Discussion

These preliminary findings show that hsImportin-β molecules interact selectively with both FxFG and GLFG repeats from *S.cerevisae* that are anchored within a pore geometry. By systemically varying the concentration of FG-repeats housed within a DNA origami scaffold, the affect of density on NTR binding could be studied. AFM imaging allowed for direct visualisation of the FG-nup network before and after Imp-β addition. The central lumen became fully occluded with material as the concentration of Imp-β in solution was increased, these results are in line with previous experiments on *textitexvivo* NPCs.[34] Interestingly, the NuPODs appeared to fill sequentially, which suggests upon binding one importin-β molecule, the addition of further molecules is more favourable. This complementarity could be explained by a change in the conformation of FG-nups where binding induces a molecular compaction that increases the effective density of FG-motifs.

Although fast-scanning of the AFM tip across the pore indicated the NTR—FG-nup complexes were mobile and could be removed with relatively low imaging forces ($\sim$50 pN), the experimental conditions required for 'unbinding' could not be identified. In order to replicate conditions necessary for transport through the NPC channel one would hope to be able to detect a dissociation of NTRs. Attempts at removing hsImp-β from highly-concentrated FG-nups using alcohols (to disrupt hydrophobic interactions[245]), RanGTP (to recapitulate the mechanism thought to induce NTR removal *in vivo*[65]) along with competitive binders (such as BSA and cell lysate[55]) proved unsuccessful. This suggests that there is a strong attraction between FG-nups and the archetypal NTR, importin-β. Perhaps there is turnover of a 'stable pool' of importin-β in this system, but AFM is not sensitive enough to detect such movements, since they would presumably not occur whilst adhered on a surface and would therefore elude detection by the scanning tip.

To improve the temporal resolution and sensitivity for identifying individual importin-β molecules we employed a fluorescence based microscopy technique, namely TIRFM. NuPODs were labelled with up to 8 synthetic dyes via a 21 bp helix. Once the positions of the NuPODs were identified the intensity traces of fluorescently tagged importin-β molecules were monitored. Preliminary results show that importin-β molecules interact with FG-nups at much lower concentrations than first indicated by AFM results ($\sim$1 nM vs. $\sim$100 nM). However further experiments and analysis are required to confirm this.

Chapter 7

Conclusion

Entry to the nucleus is tightly regulated by the NPC, selectively transporting molecules as small as ∼4-5 nm in diameter,[22,23] whilst also facilitating the entry of cargos that encompass the entire inner diamter of the pore itself (∼40 nm).[246,247] For the regulation of many cellular processes, it is essential to control transport in both directions; each NPC transports around 100 MDa of chemically divergent molecules every second.[69] The transport barrier itself is formed by a network of disordered proteins comprising multiple FG-repeats. These proteins are anchored to the walls of the NPC, where they interact with a soluble pool of transport receptors that bind both cargo and FG-nups to promote passage through the channel. Despite much research, the biophysical characteristics of these barrier components remain unclear and many contradictory models have been proposed.[9,25,36,38,46,57,65,227,248] This thesis attempts to shed light on the biophysical nature of the nucleocytoplasmic transport barrier through the study of artificial, mimetic NPCs.

Synthetic NPCs were designed using a soft DNA origami scaffold, enabling the precise positioning of FG-nups to the pore's inner walls (assembled structures are referred to as NuPODs). Two FG-nups, Nsp1 and Nup100 from *S.cerevisae* were chosen since they comprise different FG-motifs and properties, yet are both important for barrier formation.[26,70] The disordered proteins were organised in different copy numbers within this scaffold and their behaviour probed using AFM. AFM facilitates imaging with high spatial and temporal resolution (∼1 nm and ∼100 ms) in solution, but the analyte of interest must be adhered to a surface. Therefore, first in Chapter 3 alternative strategies for

the adsorption of DNA to functionalised mica is presented. dsDNA could be imaged on cationic gel-phase supported lipid bilayers, as adopted for further study of FG-nup morphologies in the NuPOD system (in Chapters 4 and 5). Additionally a protocol for the facile preparation of polymer brushes that promote DNA adsorption while preventing the non-specific adsorption of proteins up to high concentration in solution is presented.[129] The brushes were formed from diblock polymers comprising surface-grafting (here poly-L-lysine) and surface-passivating (here polyethylene glycol) segments. PLL chains were electrostatically attracted to the negatively charged mica whilst the PEG chains extended into solution to form a dense polymer brush. dsDNA, with its highly negatively charged phosphate backbone stably adsorbed onto the underlying positively charged PLL layer in these films, whilst proteins added to the solution were repelled by the steric barrier formed by the PEG chains. Moreover, as a proof-of-principle example, streptavidin was shown to bind selectively to biotinylated ends of linear DNA, whilst background-binding was significantly reduced over traditional surface preparation protocols. This method could be further developed for the study of DNA-protein interactions as well as protein-protein interactions where one binding partner is attached to a DNA support structure. In the final Chapter 6, this method was used to study NTR binding to FG-nups housed within DNA origami pores.

The versatility of the NuPOD platform is discussed in Chapter 4. 0, 1, 8, 16, 24, 32 or 48 disordered nucleoporins can be anchored in a pore geometry whose inner diameter (∼46 nm) mimics that of the native NPC.[39] MD simulations corroborated findings from experimental approaches (namely TEM); both FG-nups tested appeared to occlude the central lumen when anchored in sufficient densities. Subtle differences were observed between the two nucleoporins examined. Being more charged and less cohesive than Nup100, Nsp1 appeared to extend further from the DNA origami scaffold in TEM images and MD simulations.

In Chapter 5 real-time AFM imaging of FG-nup morphologies in solution revealed clumps of protein that appeared to occlude the central lumen of the NuPODs. These clumps were often found to be mobile within the pore. Single-line kymographs were recorded where the height and position of FG-nup condensates in the pore was monitored with time. This allowed an increase in the temporal resolution (up to ∼50 ms) and enabled a more quantitative analysis by data averaging. Autocorrelation analysis revealed collective FG-

nup transitions that occured on a timescale on the order of seconds and that were located towards the scaffold walls as opposed to the very centre of the pore. The timescales of these dynamics appeared to shorten as the tip velocity was increased, perhaps due to increased invasiveness and energy transfer. Nevertheless, these observations support the notion that FG-nup cohesiveness is tuned such that stable FG-nup morphologies can transition at little energetic cost. This rigorous analysis also revealed a difference in transitioning speed between these two proteins: the more cohesive Nup100 persisting for longer than the less cohesive Nsp1.[130]

When such experiments were carried out on *ex vivo* NPCs from *Xenopus laevis*, no such fluctuations were detected. In this case, the presence of endogenous NTRs and cargo molecules is suspected to affect the mobility of the otherwise highly dynamic, intrinsically disordered FG-nucleoporins. This hypothesis was explored in Chapter 6 with the addition of NTRs to minimalist NuPODs. hsImportin-β was seen to bind to both scNup100 and scNsp1 comprising GLFG and FxFG repeats respectively. By systematically varying the density of FG-motifs, an increased filling of the central lumen was observed, this can be attributed to an increased number of Imp-β molecules binding. In AFM experiments on individual NuPODs, some NuPODs appeared to fill up completely whilst others remained empty, for given Imp-β concentrations. This is consistent with cooperative binding of the multivalent NTRs, i.e., once one receptor has bound it makes it more favourable for further molecules to bind. This may be expected as multiple FG-motifs are clustered by the NTR, increasing the local density of binding sites. As AFM is less sensitive to transiently binding molecules, TIRFM experiments were also conducted. Preliminary TIRFM results were broadly consistent with the AFM results. However NTR binding was detected for much lower NTR concentrations than for detection by AFM. More work is required to comprehensively characterise the nature of these interactions.

7.1 Future Work

Overall the NuPOD design is one that provides a versatile and well-defined platform for the 'bottom-up' study of bimolecular interactions. Combined with single molecule detection techniques, it is a powerful tool for probing the integral biophysics that underpins

the selectivity of nucleocytoplasmic transport. In this context although the interactions between FG-nups and select NTRs have been explored in this work much more needs to be done to understand the role of NTRs in cargo transport.

The NuPOD platform is also an interesting tool in the field of synthetic biology. One could invisage its incorporation into lipid membranes to build synthetic cells that allow for the entry of specific molecules.[249] Future applications may also be extended to biosensor devices; the surface modification of solid-state nanopores with FG-nups may be more suitable to design such devices.[99,250,251]

7.1.1 Understanding FG-nup-NTR interactions

The final chapter in this work presents preliminary data on NTR binding to FG-nups housed within DNA origami scaffolds. Such work is an important elementary step towards understanding how these interactions govern NPC selectively at the nanoscale. For high concentrations of FG-nups and high concentrations of importin-β, irreversible binding was observed, whereas when the concentrations were much lowered it was more challenging to detect any interactions at all. These experiments were conducted on a very minimalist system and therefore it is difficult to predict which concentrations best resemble the situation *in vivo* where many other proteins that may affect interaction strengths are present.[55] More work is needed to look at the affect of different NTRs of different origins (i.e., *S.cerevisae* in addition to *H. sapiens*) on the FG-nup meshwork within these minimalist NuPODs. Moreover it would be interesting to recapitulate more elements of the cellular environment, to look at the effect of different buffers and cargo-bound NTRs as opposed to isolated NTRs.

At lower concentrations of the NTRs and/or FG-nups, central condensates (attributed to FG-nups condensed by bound NTRs) could be removed by scanning of the AFM tip, as shown in Figure 6.10. More work is needed to understand the conditions and forces required to disrupt NTR binding. Although AFM is able to resolve structures with sub-nanometre resolution it is invasive, insensitive to the detection of molecules that are not surface-bound and its temporal resolution is limited to $\sim$50 ms. In addition to TIRFM, a label-free light-based technique that is gaining popularity for the study of

biomolecules is interferometric scattering microscopy (iSCAT).[252] Using this technique individual molecules can be detected binding to a glass surface, molecular masses can also be determined therefore one can clearly resolve any oligomerisation. Furthermore, frame rates approaching 1 MHz are also possible.[253]

Although techniques such as AFM, TIRFM and iSCAT offer single-molecule resolution as opposed to ensemble averaging, the specimen of interest must be surface-bound. Despite much work optimising the surface functionalisation to reduce non-specific interactions, it is possible that the surface has some influence on the behaviour of biomolecules. An alternative solution-based technique used to quantify biomolecular interations is microscale thermophoresis (MST).[254] The method is based upon the process of thermophoresis; the ordered movement of molecules when subjected to a temperature gradient. Since movement is highly dependent on a variety of molecular properties such as size and charge, small changes in molecular properties from binding are readily detected and association constants as low as 1 picomolar can be measured.[254] It would therefore be interesting to look at the affect of exogenous NTRs and cellular components on the movement of different NuPODs to obtain numerical binding constants. Binding anti-MBP to MBP-NuPODs would also provide a useful control for such experiments, since the association strength of the antibody binding would be expected to be much greater.

7.1.2 Measuring transport through NuPODs

Although some steps have been made to assemble DNA origami based NPC mimics into a transport-competent platform,[41] the presence of a large number of dynamic proteins within the pore lumen greatly increases the noise of the readout signal using classical current-voltage detection methods. Therefore it remains to be seen whether molecular translocations could be observed above this noise. Perhaps fluorescence-based tracking assays would be a more suitable detection method for this platform.[255,256] Figure 7.1a shows schematically how a NuPOD could be placed on top of a nanopipette, the design of the DNA origami presented in this work may need to be modified in incorporate a long ss-tail to direct docking.[41,109] In contrast to the labour-intensive fabrication of nanopores milled in insulating membranes,[99] nanopipettes are readily fabricated from laser-pulling of quartz capillaries.[257] In order to passivate the nanopipette surface against non-specific

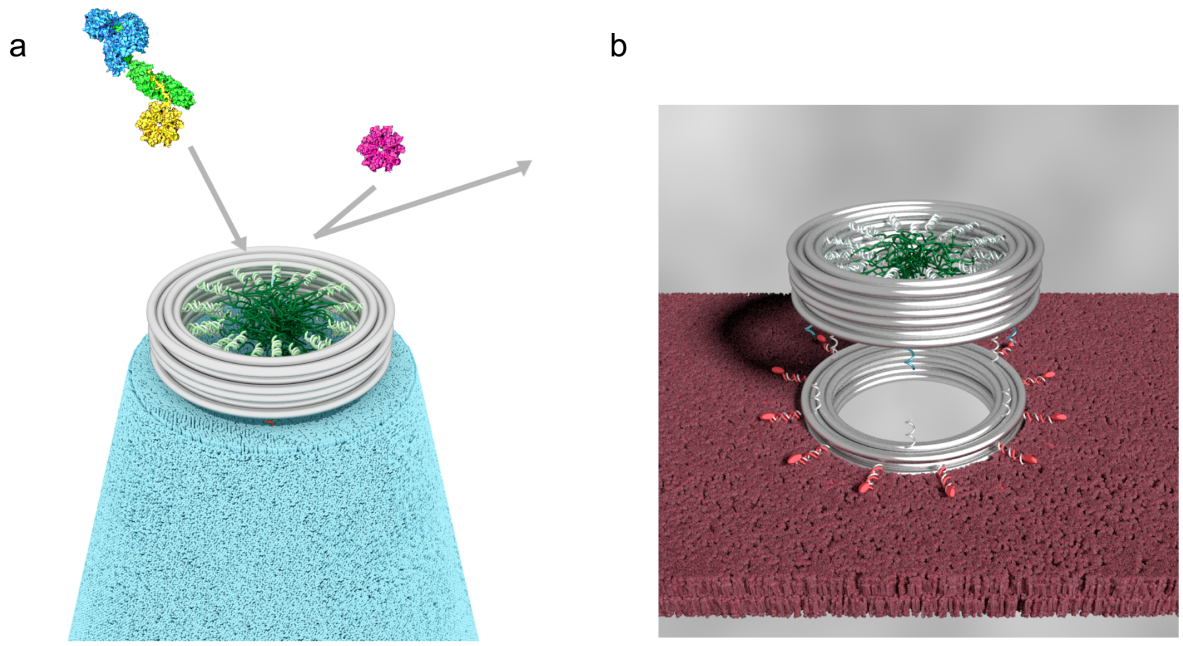


Figure 7.1: **Incorporating NuPODs into a transport competent platform** a) DNA origami NuPODs modified with a long ss-DNA tail could be docked into a passivated quartz nanopipette. If functional, complexes of cargo-importinα-importinβ would be able to pass (left) where as non-specific cargos which do not display an NLS would not be able to pass (right) b) DNA origami NuPODs could be modified to allow assembly into higher order structures for insertion into lipid bilayers. The first DNA origami ring could be decorated with hydrophobic groups on the outside (shown as red ovals) and inserted into a synthetic bilayer. ssDNA on the upper face, complementary to sequences on a second DNA origami ring would induce docking and the formation of a double-height ring where the second ring houses FG-nups on the inside (shown in green).

protein-binding, the functionalisation strategy used for AFM and TIRFM described in the Methods sections 2.2.4 and 2.6 could also be used to PEGylate the quartz.

An alternative strategy to facilitate transport through these NuPODs would be to span the DNA origami pore across a synthetic membrane.[124,126] Traditionally, decoration with hydrophobic moieties such as cholesterol[124,258] or tocopherol[126] has facilitated spontaneous insertion of DNA nanopores into lipid membranes, but it remains to be seen if structure with a large outer diameter of 62 nm (as here) could be stably inserted. Since hydrophobic modification may lead unfavourable interactions with the hydrophobic FG-nups and/or aggregation, I propose to design a secondary DNA-origami structure to dock into the

membrane, as shown schematically in Figure 7.1b. In this way the second structure could be highly decorated with hydrophobic groups, inserted into vesicles and then the NuPOD containing FG-nups could be docked onto the trans-membrane pore to build a higher-order structure.[116]

7.1.3 Solid-state nanopores

Biomimetic NPCs with selectivity for molecular transport have previously been demonstrated for solid-state nanopores directly modified with FG-nups.[40,101,102] In this prior work, a number of different chemistries were exploited to attach the FG-nups to various solid surfaces. Jovanovic-Talisman and co-workers coated polycarbonate membranes with gold upon which FG-nups, engineered with a single terminal cysteine residue spontaneously formed monolayers, as the thiol group forms a covalent bond with the gold

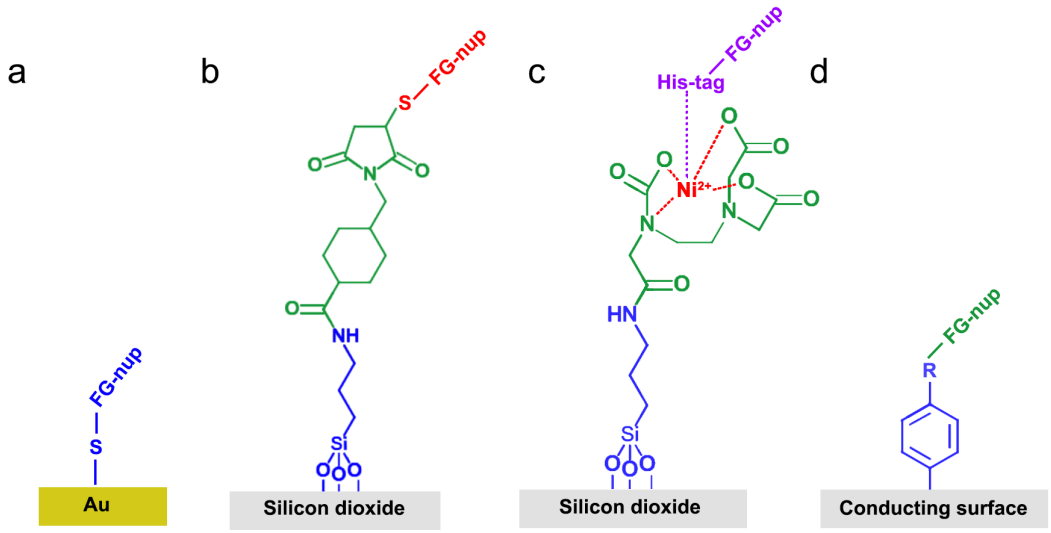


Figure 7.2: **Strategies for attaching FG-nups to surfaces and nanopores** a)FG-nups with a single thiol moiety form covalent bonds with gold surfaces.[101] b) Silicon-dioxide surfaces displaying OH groups can be modified using silanisation chemistry to display surface NH_2 groups. These can then be cross-coupled to FG-nups with a terminal thiol.[40,102] c) Reversible-attachment of FG-nups modified with terminal polyhistidines to silicon-dioxide surfaces displaying Ni^{2+}-EDTA groups.[261] d) Electrochemical deposition of diazonium cations onto conducting surfaces could offer an alternative strategy for directed attachment of FG-nups, where R = COO or NH.[262]

surface (see Figure 7.2a). Since sputter-coating the membranes yielded a ∼15 nm surface layer of gold, FG-nups coated only the upper entrance of the pore.[101] Work by Aizhan Bestembayeva sort to use this strategy to functionalise individual nanopores with a layer of embedded gold.[259,260] Although this architecture is more representative of the native NPC, problems with non-specific adsorption of molecules onto the exposed silicon dioxide were encountered when trying to prepare these devices.[259]

To covalently anchor FG-nups to nanopores milled in silison nitride/silicon dioxide membranes, the strategy employed by Ces Dekker's group was to first modify the surface with amines via silanisation with APTES (see Figure 7.2b). The second step uses a cross-linker with a terminal malemide group to which the thiol group of the cysteine-terminated FG-nup will then bind.[40,102] An alternative strategy for reversible-functionalisation of surfaces uses FG-nups terminated with polyhistidine groups as opposed to thiol-groups commonly employed, see Figure 7.2c.[261] Terminal amine groups introduced by silanisation are then reacted with EDTA ligands that can capture Ni^{2+} metal ions. The Ni^{2+}-EDTA complex selectively binds histidine tags, when the protein is modified with several histidines at one end the complex formed is relatively stable aginst buffer elution. The proteins can however be readily unbound by elution with imidazole which disrupts the interaction.[261]

An alternative strategy for surface-grafting of proteins is to use electrodeposition to deposit molecules. Diazonium salts are particularly useful surface modifiers as they readily form aryl films on conducting surfaces (see Figure 7.2d). By monitoring the current changes one can easily follow the reaction *in situ*.[263] Proteins have also been immobilised in this way using a one-step method, having linked the terminal end of the protein to a diazonium salt that can be directly deposited.[264]

I carried out some preliminary work to fabricate solid-state mimics using dual-barelled nanopipettes. The design of the platform is shown in Figure 7.3a. The idea was to deposit pyrolytic carbon into one-barrel to form an electrode that extended around the open end of the second barrel. In this way electrodeposition could be used to selectively deposit molecules soley around the edge of the open barrel. The nanopipettes were fabricated by pulling capillaries with two barrels using a laser-puller.[265] The large end of one barrel was then sealed whilst butane was flowed through the other. The nano-sized tip was inserted into an argon-filled capillary with a low flow and the end heated with a blow-torch to

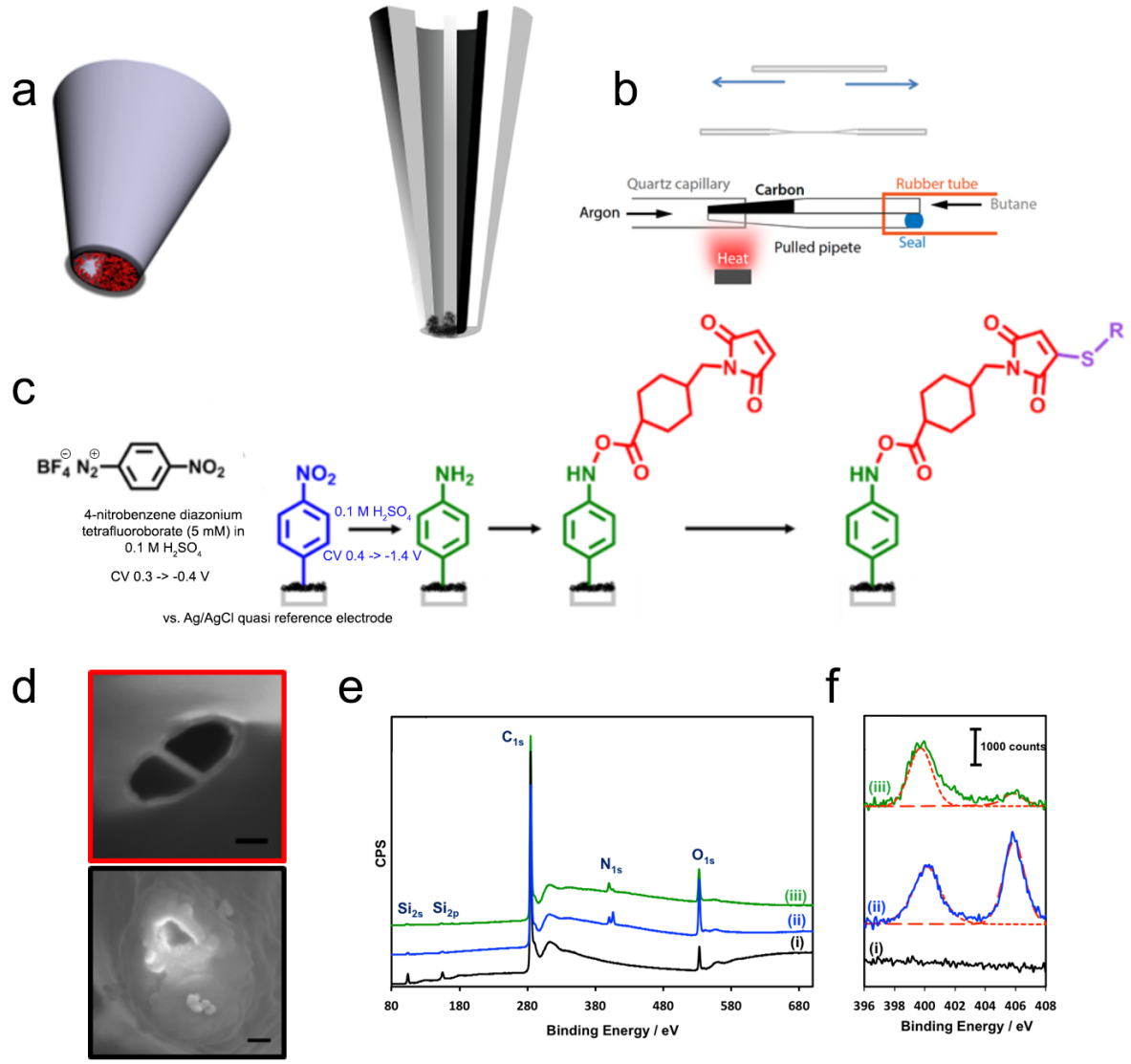


Figure 7.3: **Fabricating biomimetic NPCs from nanopipettes** a) Schematic of the design showing a dual barrel nanopipette where one barrel is filled with carbon that also circumferences the second barrel. This carbon can then be selectively functionalism. b) The nanopipettes are formed from laser-pulled capillaries (top). Pyrolytic carbon is then deposited into one barrel (bottom). c) Method for functionalising the carbon, firstly the diazonium salt of 4-nitobenzene is electrodeposited onto the surface, the solution is exchanged and the nitro-group reduced to an amine-group. Cross-coupling with Sulfo-SMCC could then introduce a terminal malemide onto which thiol-FG-nups would attach. d) SEM imaged of nanopipettes before and after the deposition of carbon. Scale bars are 100 nm. e) XPS acquired survey spectra b) N1s core level spectra of the bare (i) and diazonium-modified carbon surfaces before(ii) and after(iii) reduction of the nitro group to an amine.

induce the deposition of pyrolytic carbon into one-barrel and around the open end of the other (see Figure 7.3b).[265] Figure 7.3d shows SEM images acquired before and after carbon deposition with one barrel clearly filled with carbon.

The strategy for functionalisation of pyrolytic carbon in summarised in Figure 7.3c. This could be further optimised exploiting different chemistries to reduce the number of steps required. Nevertheless, I was able to show that nitro-groups could be electrochemically deposited onto pyrolytic carbon and then electrochemically reduced in hydrochloric acid to amine groups. The modification of the surface chemistry of quartz slides was confirmed using XPS, see Figure 7.3e.

Although this fabrication strategy showed some success I found a large variability in nanopore and electrode size between experiments - most likely due to differences in the way the pyrolytic carbon was being deposited. Such errors would ultimately make the platform not very suitable for the study of FG-nups, since the precise structure is ill-defined and poorly reproducible.

Bibliography

[1] B. Alberts, A. Johnson, J. Lewis, M. Raff, K. Roberts, and P. Walter, "The Compartmentalization of Cells," in *Molecular Biology of the Cell*, New York: Garland Science, 4th ed., 2002.

[2] G. G. Maul and L. Deaven, "Quantitative determination of nuclear pore complexes in cycling cells with differing DNA content," *The Journal of Cell Biology*, vol. 73, no. 3, pp. 748–760, 1977.

[3] D. Görlich and U. Kutay, "Transport between the cell nucleus and the cytoplasm.," *Annual Review of Cell and Developmental Biology*, vol. 15, pp. 607–660, 1999.

[4] M. P. Rout, J. D. Aitchison, A. Suprapto, K. Hjertaas, Y. Zhao, and B. T. Chait, "The Yeast Nuclear Pore Complex," *The Journal of Cell Biology*, vol. 148, no. 4, p. 635, 2000.

[5] F. Alber, S. Dokudovskaya, L. M. Veenhoff, W. Zhang, J. Kipper, D. Devos, A. Suprapto, O. Karni-Schmidt, R. Williams, B. T. Chait, M. P. Rout, and A. Sali, "Determining the architectures of macromolecular assemblies.," *Nature*, vol. 450, no. 7170, pp. 683–694, 2007.

[6] C. Strambio-De-Castillia, M. Niepel, and M. P. Rout, "The nuclear pore complex: bridging nuclear transport and gene regulation," *Nature Reviews Molecular Cell Biology*, vol. 11, p. 490, 2010.

[7] B. Cautain, R. Hill, N. de Pedro, and W. Link, "Components and regulation of nuclear transport processes.," *The FEBS journal*, vol. 282, no. 3, pp. 445–462, 2015.

[8] S. J. Kim, J. Fernandez-Martinez, I. Nudelman, Y. Shi, W. Zhang, B. Raveh, T. Herricks, B. D. Slaughter, J. A. Hogan, P. Upla, I. E. Chemmama, R. Pellarin, I. Echeverria, M. Shivaraju, A. S. Chaudhury, J. Wang, R. Williams, J. R. Unruh, C. H. Greenberg, E. Y. Jacobs, Z. Yu, M. J. de la Cruz, R. Mironska, D. L. Stokes, J. D. Aitchison, M. F. Jarrold, J. L. Gerton, S. J. Ludtke, C. W. Akey, B. T. Chait, A. Sali, and M. P. Rout, "Integrative structure and functional anatomy of a nuclear pore complex," *Nature*, vol. 555, p. 475, 2018.

[9] J. Yamada, J. L. Phillips, S. Patel, G. Goldfien, A. Calestagne-Morelli, H. Huang, R. Reza, J. Acheson, V. V. Krishnan, S. Newsam, A. Gopinathan, E. Y. Lau, M. E. Colvin, V. N. Uversky, and M. F. Rexach, "A Bimodal Distribution of Two Distinct Categories of Intrinsically Disordered Structures with Separate Functions in FG Nucleoporins," *Molecular & Cellular Proteomics*, vol. 9, no. 10, pp. 2205–2224, 2010.

[10] D. Stoffler, B. Fahrenkrog, and U. Aebi, "The nuclear pore complex: from molecular architecture to functional dynamics.," *Current Opinion in Cell Biology*, vol. 11, no. 3, pp. 391–401, 1999.

[11] F. Alber, S. Dokudovskaya, L. M. Veenhoff, W. Zhang, J. Kipper, D. Devos, A. Suprapto, O. Karni-Schmidt, R. Williams, B. T. Chait, A. Sali, and M. P. Rout, "The molecular architecture of the nuclear pore complex," *Nature*, vol. 450, pp. 695–701, 2007.

[12] A. Hoelz, E. W. Debler, and G. Blobel, "The Structure of the Nuclear Pore Complex," *Annual Review of Biochemistry*, vol. 80, no. 1, pp. 613–643, 2011.

[13] K. H. Bui, A. von Appen, A. L. DiGuilio, A. Ori, L. Sparks, M. T. Mackmull, T. Bock, W. Hagen, A. Andres-Pons, J. S. Glavy, and M. Beck, "Integrated structural analysis of the human nuclear pore complex scaffold," *Cell*, vol. 155, no. 6, pp. 1233–1243, 2013.

[14] A. Von Appen, J. Kosinski, L. Sparks, A. Ori, A. L. DiGuilio, B. Vollmer, M.-T. Mackmull, N. Banterle, L. Parca, P. Kastritis, K. Buczak, S. Mosalaganti, W. Hagen, A. Andres-Pons, E. A. Lemke, P. Bork, W. Antonin, J. S. Glavy, K. H. Bui, and M. Beck, "In situ structural analysis of the human nuclear pore complex," *Nature*, vol. 526, pp. 140–143, 2015.

[15] S. Mosalaganti, J. Kosinski, S. Albert, M. Schaffer, D. Strenkert, P. A. Salomé, S. S. Merchant, J. M. Plitzko, W. Baumeister, B. D. Engel, and M. Beck, "In situ architecture of the algal nuclear pore complex," *Nature Communications*, vol. 9, no. 1, p. 2361, 2018.

[16] D. Frenkiel-Krispin, B. Maco, U. Aebi, and O. Medalia, "Structural Analysis of a Metazoan Nuclear Pore Complex Reveals a Fused Concentric Ring Architecture," *Journal of Molecular Biology*, vol. 395, no. 3, pp. 578–586, 2010.

[17] Q. Yang, M. P. Rout, and C. W. Akey, "Three-Dimensional Architecture of the Isolated Yeast Nuclear Pore Complex: Functional and Evolutionary Implications," *Molecular Cell*, vol. 1, no. 2, pp. 223–234, 1998.

[18] C. W. Akey and M. Radermacher, "Architecture of the Xenopus Nuclear-Pore Complex Revealed By 3-Dimensional Cryoelectron Microscopy," *Journal of Cell Biology*, vol. 122, no. 1, pp. 1–19, 1993.

[19] H. G. Callan, J. T. Randall, and S. G. Tomlin, "An Electron Microscope Study of the Nuclear Membrane," *Nature*, vol. 163, no. 4138, p. 280, 1949.

[20] D. P. Denning, S. S. Patel, V. Uversky, A. L. Fink, and M. Rexach, "Disorder in the nuclear pore complex: The FG repeat regions of nucleoporins are natively unfolded," *Proceedings of the National Academy of Sciences*, vol. 100, no. 5, pp. 2450–2455, 2003.

[21] S. S. Patel, B. J. Belmont, J. M. Sante, and M. F. Rexach, "Natively Unfolded Nucleoporins Gate Protein Diffusion across the Nuclear Pore Complex," *Cell*, vol. 129, no. 1, pp. 83–96, 2007.

[22] B. L. Timney, B. Raveh, R. Mironska, J. M. Trivedi, S. J. Kim, D. Russel, S. R. Wente, A. Sali, and M. P. Rout, "Simple rules for passive diffusion through the nuclear pore complex," *The Journal of Cell Biology*, vol. 215, no. 1, pp. 57–76, 2016.

[23] H. B. Schmidt and D. Görlich, "Transport Selectivity of Nuclear Pores, Phase Separation, and Membraneless Organelles," *Trends in Biochemical Sciences*, vol. 41, no. 1, pp. 46–61, 2016.

[24] T. Jovanovic-Talisman and A. Zilman, "Protein Transport by the Nuclear Pore Complex: Simple Biophysics of a Complex Biomachine," *Biophysical Journal*, vol. 113, no. 1, pp. 6–14, 2017.

[25] G. J. Stanley, A. Fassati, and B. W. Hoogenboom, "Biomechanics of the transport barrier in the nuclear pore complex," in *Seminars in cell & developmental biology*, vol. 68, pp. 42–51, Elsevier, 2017.

[26] L. A. Strawn, T. Shen, N. Shulga, D. S. Goldfarb, and S. R. Wente, "Minimal nuclear pore complexes define FG repeat domains essential for transport," *Nature Cell Biology*, vol. 6, no. 3, pp. 197–206, 2004.

[27] A. Ghavami, L. M. Veenhoff, E. van der Giessen, and P. R. Onck, "Probing the Disordered Domain of the Nuclear Pore Complex through Coarse-Grained Molecular Dynamics Simulations," *Biophysical Journal*, vol. 107, no. 6, pp. 1393–1402, 2014.

[28] P. Popken, A. Ghavami, P. R. Onck, B. Poolman, and L. M. Veenhoff, "Size-dependent leak of soluble and membrane proteins through the yeast nuclear pore complex," *Molecular Biology of the Cell*, vol. 26, no. 7, pp. 1386–1394, 2015.

[29] J. Ma, A. Goryaynov, A. Sarma, and W. Yang, "Self-regulated viscous channel in the nuclear pore complex," *Proceedings of the National Academy of Sciences of the United States of America*, vol. 109, no. 19, pp. 7326–7331, 2012.

[30] C. E. Atkinson, A. L. Mattheyses, M. Kampmann, and S. M. Simon, "Conserved Spatial Organization of FG Domains in the Nuclear Pore Complex," *Biophysical Journal*, vol. 104, no. 1, pp. 37–50, 2013.

[31] G. Fu, L.-C. Tu, A. Zilman, and S. M. Musser, "Investigating Molecular Crowding within Nuclear Pores using Polarization PALM (p-PALM)," *Biophysical Journal*, vol. 110, no. 3, p. 15a, 2016.

[32] A. Bestembayeva, A. Kramer, A. A. Labokha, D. Osmanović, I. Liashkovich, E. V. Orlova, I. J. Ford, G. Charras, A. Fassati, and B. W. Hoogenboom, "Nanoscale stiffness topography reveals structure and mechanics of the transport barrier in intact nuclear pore complexes," *Nature Nanotechnology*, vol. 10, no. 1, pp. 60–64, 2015.

[33] Y. Sakiyama, A. Mazur, L. E. Kapinos, and R. Y. H. Lim, "Spatiotemporal dynamics of the nuclear pore complex transport barrier resolved by high-speed atomic force microscopy," *Nat Nano*, vol. 11, no. 8, pp. 719–723, 2016.

[34] G. J. Stanley, A. Fassati, and B. W. Hoogenboom, "Atomic force microscopy reveals structural variability amongst nuclear pore complexes," *Life Science Alliance*, vol. 1, no. 4, 2018.

[35] S. Frey, R. P. Richter, and D. Görlich, "FG-rich repeats of nuclear pore proteins form a three-dimensional meshwork with hydrogel-like properties," *Science*, vol. 314, no. 5800, pp. 815–817, 2006.

[36] S. Frey and D. Görlich, "A Saturated FG-Repeat Hydrogel Can Reproduce the Permeability Properties of Nuclear Pore Complexes," *Cell*, vol. 130, no. 3, pp. 512–523, 2007.

[37] D. Mohr, S. Frey, T. Fischer, T. Güttler, and D. Görlich, "Characterisation of the passive permeability barrier of nuclear pore complexes.," *The EMBO Journal*, vol. 28, no. 17, pp. 2541–2553, 2009.

[38] N. B. Eisele, A. A. Labokha, S. Frey, D. Görlich, and R. P. Richter, "Cohesiveness tunes assembly and morphology of FG nucleoporin domain meshworks - Implications for nuclear pore permeability," *Biophysical Journal*, vol. 105, no. 8, pp. 1860–1870, 2013.

[39] P. D. E. Fisher, Q. Shen, B. Akpinar, L. K. Davis, K. K. H. Chung, D. Baddeley, A. Šarić, T. J. Melia, B. W. Hoogenboom, C. Lin, and C. P. Lusk, "A Programmable DNA Origami Platform for Organizing Intrinsically Disordered Nucleoporins within Nanopore Confinement," *ACS Nano*, vol. 12, no. 2, pp. 1508–1518, 2018.

[40] A. N. Ananth, A. Mishra, S. Frey, A. Dwarkasing, R. Versloot, E. van der Giessen, D. Görlich, P. Onck, and C. Dekker, "Spatial structure of disordered proteins dictates conductance and selectivity in nuclear pore complex mimics," *eLife*, vol. 7, p. e31510, 2018.

[41] P. Ketterer, A. N. Ananth, D. S. Laman Trip, A. Mishra, E. Bertosin, M. Ganji, J. van der Torre, P. Onck, H. Dietz, and C. Dekker, "DNA origami scaffold for studying

intrinsically disordered proteins of the nuclear pore complex," *Nature Communications*, vol. 9, no. 1, p. 902, 2018.

[42] D. Osmanovic, J. Bailey, A. H. Harker, A. Fassati, B. W. Hoogenboom, and I. J. Ford, "Bistable collective behavior of polymers tethered in a nanopore," *Physical Review E*, vol. 85, no. 6, p. 061917, 2012.

[43] D. Osmanović, A. Fassati, I. J. Ford, and B. W. Hoogenboom, "Physical modelling of the nuclear pore complex," *Soft Matter*, vol. 9, no. 44, p. 10442, 2013.

[44] D. Osmanović, I. J. Ford, and B. W. Hoogenboom, "Model Inspired by Nuclear Pore Complex Suggests Possible Roles for Nuclear Transport Receptors in Determining Its Structure," *Biophysical Journal*, vol. 105, no. 12, pp. 2781–2789, 2013.

[45] A. Vovk, C. Gu, M. G. Opferman, L. E. Kapinos, R. Y. Lim, R. D. Coalson, D. Jasnow, and A. Zilman, "Simple biophysics underpins collective conformations of the intrinsically disordered proteins of the Nuclear Pore Complex," *eLife*, vol. 5, p. e10785, 2016.

[46] L. K. Davis, I. J. Ford, A. Šarić, and B. W. Hoogenboom, "Intrinsically disordered nuclear pore proteins show ideal-polymer morphologies and dynamics," *bioRxiv*, p. 571687, 2019.

[47] M. Kimura and N. Imamoto, "Biological Significance of the Importin-beta Family-Dependent Nucleocytoplasmic Transport Pathways," *Traffic*, vol. 15, no. 7, pp. 727–748, 2014.

[48] I. W. Mattaj and L. Englmeier, "Nucleocytoplasmic Transport: The Soluble Phase," *Annual Review of Biochemistry*, vol. 67, pp. 265–306, 1998.

[49] Y. Ogawa, Y. Miyamoto, M. Oka, and Y. Yoneda, "The Interaction Between Importin-α and Nup153 Promotes Importin-α/β-Mediated Nuclear Import," *Traffic*, vol. 13, no. 7, pp. 934–946, 2012.

[50] F. R. Bischoff and H. Ponstingl, "Mitotic regulator protein RCC1 is complexed with a nuclear ras-related polypeptide," *Proceedings of the National Academy of Sciences*, vol. 88, no. 23, pp. 10830 – 10834, 1991.

[51] I. Ben-Efraim and L. Gerace, "Gradient of Increasing Affinity of Importin beta for Nucleoporins along the Pathway of Nuclear Import," *The Journal of Cell Biology*, vol. 152, no. 2, pp. 411–417, 2001.

[52] B. Pyhtila and M. Rexach, "A gradient of affinity for the karyopherin Kap95p along the yeast nuclear pore complex.," *The Journal of biological chemistry*, vol. 278, no. 43, pp. 42699–42709, 2003.

[53] N. B. Eisele, S. Frey, J. Piehler, D. Görlich, and R. P. Richter, "Ultrathin nucleoporin phenylalanine-glycine repeat films and their interaction with nuclear transport receptors," *EMBO Reports*, vol. 11, no. 5, pp. 366–372, 2010.

[54] R. L. Schoch, L. E. Kapinos, and R. Y. H. Lim, "Nuclear transport receptor binding avidity triggers a self-healing collapse transition in FG-nucleoporin molecular brushes.," *Proceedings of the National Academy of Sciences of the United States of America*, vol. 109, no. 42, pp. 16911–16916, 2012.

[55] J. Tetenbaum-Novatt, L. E. Hough, R. Mironska, A. S. McKenney, and M. P. Rout, "Nucleocytoplasmic transport: a role for nonspecific competition in karyopherin-nucleoporin interactions," *Molecular & cellular proteomics : MCP*, vol. 11, no. 5, pp. 31–46, 2012.

[56] L. E. Kapinos, R. L. Schoch, R. S. Wagner, K. D. Schleicher, and R. Y. H. Lim, "Karyopherin-centric control of nuclear pores based on molecular occupancy and kinetic analysis of multivalent binding with FG nucleoporins," *Biophysical Journal*, vol. 106, no. 8, pp. 1751–1762, 2014.

[57] R. S. Wagner, L. E. Kapinos, N. J. Marshall, M. Stewart, and R. Y. H. Lim, "Promiscuous Binding of Karyopherin β Modulates FG Nucleoporin Barrier Function and Expedites NTF2 Transport Kinetics," *Biophysical Journal*, vol. 108, no. 4, pp. 918–927, 2015.

[58] L. E. Hough, K. Dutta, S. Sparks, D. B. Temel, A. Kamal, M. P. Rout, and D. Cowburn, "The molecular mechanism of nuclear transport revealed by atomic-scale measurements," *eLife*, vol. 4, p. e10027, 2015.

[59] S. Milles, D. Mercadante, I. V. Aramburu, M. R. Jensen, N. Banterle, C. Koehler, S. Tyagi, J. Clarke, S. L. Shammas, M. Blackledge, F. Gräter, and E. A. Lemke, "Plasticity of an Ultrafast Interaction between Nucleoporins and Nuclear Transport Receptors," *Cell*, vol. 163, no. 3, pp. 734–745, 2015.

[60] R. Hayama, S. Sparks, L. M. Hecht, K. Dutta, J. M. Karp, C. M. Cabana, M. P. Rout, and D. Cowburn, "Thermodynamic characterization of the multivalent interactions underlying rapid and selective translocation through the nuclear pore complex.," *Journal of Biological Chemistry*, vol. 293, no. 12, pp. 4555–4563, 2018.

[61] P. S. Tan, I. V. Aramburu, D. Mercadante, S. Tyagi, A. Chowdhury, D. Spitz, S. L. Shammas, F. Gräter, and E. A. Lemke, "Two Differential Binding Mechanisms of FG-Nucleoporins and Nuclear Transport Receptors," *Cell Reports*, vol. 22, no. 13, pp. 3660–3671, 2018.

[62] A. Paradise, M. K. Levin, G. Korza, and J. H. Carson, "Significant Proportions of Nuclear Transport Proteins with Reduced Intracellular Mobilities Resolved by Fluorescence Correlation Spectroscopy," *Journal of Molecular Biology*, vol. 365, no. 1, pp. 50–65, 2007.

[63] M. P. Rout and J. D. Aitchison, "The nuclear pore complex as a transport machine.," *The Journal of biological chemistry*, vol. 276, no. 20, pp. 16593–16596, 2001.

[64] A. Kramer, I. Liashkovich, Y. Ludwig, and V. Shahin, "Atomic force microscopy visualises a hydrophobic meshwork in the central channel of the nuclear pore," *Pflügers Archiv - European Journal of Physiology*, vol. 456, no. 1, pp. 155–162, 2008.

[65] A. R. Lowe, J. H. Tang, J. Yassif, M. Graf, W. Y. Huang, J. T. Groves, K. Weis, and J. T. Liphardt, "Importin-β modulates the permeability of the nuclear pore complex in a Ran-dependent manner," *eLife*, vol. 4, p. e04052, 2015.

[66] M. P. Rout, J. D. Aitchison, M. O. Magnasco, and B. T. Chait, "Virtual gating and nuclear transport: The hole picture," *Trends in Cell Biology*, vol. 13, no. 12, pp. 622–628, 2003.

[67] R. Y. H. Lim and B. Fahrenkrog, "The nuclear pore complex up close," *Current Opinion in Cell Biology*, vol. 18, no. 3, pp. 342–347, 2006.

[68] R. Peters, "Translocation Through the Nuclear Pore Complex: Selectivity and Speed by Reduction-of-Dimensionality," *Traffic*, vol. 6, no. 5, pp. 421–427, 2005.

[69] K. Ribbeck and D. Görlich, "Kinetic analysis of translocation through nuclear pore complexes," *The EMBO Journal*, vol. 20, no. 6, pp. 1320–1330, 2001.

[70] S. Frey and D. Görlich, "FG/FxFG as well as GLFG repeats form a selective permeability barrier with self-healing properties," *EMBO Journal*, vol. 28, no. 17, pp. 2554–2567, 2009.

[71] B. B. Hülsmann, A. A. Labokha, and D. Görlich, "The permeability of reconstituted nuclear pores provides direct evidence for the selective phase model," *Cell*, vol. 150, no. 4, pp. 738–751, 2012.

[72] A. A. Labokha, S. Gradmann, S. Frey, B. B. Hülsmann, H. Urlaub, M. Baldus, and D. Görlich, "Systematic analysis of barrier-forming FG hydrogels from Xenopus nuclear pore complexes," *The EMBO Journal*, vol. 32, no. 2, pp. 204–218, 2013.

[73] R. Zahn, D. Osmanović, S. Ehret, C. Araya Callis, S. Frey, M. Stewart, C. You, D. Görlich, B. W. Hoogenboom, and R. P. Richter, "A physical model describing the interaction of nuclear transport receptors with FG nucleoporin domain assemblies," *eLife*, vol. 5, p. e14119, 2016.

[74] N. Pante, R. Bastos, I. McMorrow, B. Burke, and U. Aebi, "Interactions and three-dimensional localization of a group of nuclear pore complex proteins," *Journal of Cell Biology*, vol. 126, no. 3, pp. 603–617, 1994.

[75] C. M. Feldherr and D. Akin, "The location of the transport gate in the nuclear pore complex," *Journal of Cell Science*, vol. 110, no. 24, pp. 3065–3070, 1997.

[76] B. Fahrenkrog, E. C. Hurt, U. Aebi, and N. Panté, "Molecular Architecture of the Yeast Nuclear Pore Complex: Localization of Nsp1p Subcomplexes," *Journal of Cell Biology*, vol. 143, no. 3, pp. 577–588, 1998.

[77] B. Fahrenkrog, J. P. Aris, E. C. Hurt, N. Panté, and U. Aebi, "Comparative Spatial Localization of Protein-A-Tagged and Authentic Yeast Nuclear Pore Complex Proteins by Immunogold Electron Microscopy," *Journal of Structural Biology*, vol. 129, pp. 295–305, 2000.

[78] S. Krull, J. Thyberg, B. Bjo, H.-r. Rackwitz, and V. C. Cordes, "Nucleoporins as Components of the Nuclear Pore Complex Core Structure and Tpr as the Architectural Element of the Nuclear Basket," *Molecular Biology of the Cell*, vol. 15, no. 9, pp. 4261–4277, 2004.

[79] N. Panté and B. Fahrenkrog, "Chapter 4 - Exploring Nuclear Pore Complex Molecular Architecture by Immuno-Electron Microscopy Using Xenopus Oocytes," in *Nuclear Pore Complexes and Nucleocytoplasmic Transport - Methods* (V. Doye, ed.), vol. 122, pp. 81–98, Elsevier Academic Press, 2014.

[80] A. R. Lowe, J. J. Siegel, P. Kalab, M. Siu, K. Weis, and J. T. Liphardt, "Selectivity mechanism of the nuclear pore complex characterized by single cargo tracking," *Nature*, vol. 467, no. 7315, pp. 600–603, 2010.

[81] J. Ma, A. Goryaynov, and W. Yang, "Super-resolution 3D tomography of interactions and competition in the nuclear pore complex," *Nature Structural & Molecular Biology*, vol. 23, no. 3, pp. 239–247, 2016.

[82] Y. F. Dufrêne, T. Ando, R. Garcia, D. Alsteens, D. Martinez-Martin, A. Engel, C. Gerber, and D. J. Müller, "Imaging modes of atomic force microscopy for application in molecular and cell biology," *Nature Nanotechnology*, vol. 12, no. 4, pp. 295–307, 2017.

[83] T. Ando, T. Uchihashi, and S. Scheuring, "Filming Biomolecular Processes by High-Speed Atomic Force Microscopy," *Chemical Reviews*, vol. 114, no. 6, pp. 3120–3188, 2014.

[84] H. Oberleithner, E. Brinckmann, A. Schwab, and G. Krohne, "Imaging nuclear pores of aldosterone-sensitive kidney cells by atomic force microscopy," *Proceedings of the National Academy of Sciences of the United States of America*, vol. 91, no. 21, pp. 9784–9788, 1994.

[85] J. O. Bustamante, A. Liepins, R. A. Prendergast, J. A. Hanover, and H. Oberleithner, "Membrane biology patch clamp and atomic force microscopy demonstrate TATA-binding protein (TBP) interactions with the nuclear pore complex," *The Journal of Membrane Biology*, vol. 272, pp. 263–272, 1995.

[86] S. Schneider, G. Folprecht, G. Krohne, and H. Oberleithner, "Immunolocalization of lamins and nuclear pore complex proteins by atomic force microscopy," *Pflügers Archiv European Journal of Physiology*, vol. 430, no. 5, pp. 795–801, 1995.

[87] T. Danker, M. Mazzanti, R. Tonini, A. A. Rakowska, and H. Oberleithner, "Using Atomic Force Microscopy to Investigate Patch-Clamped Nuclear Membrane," *Cell Biology International*, vol. 21, no. 11, pp. 747–757, 1997.

[88] A. Rakowska, T. Danker, S. W. Schneider, and H. Oberleithner, "ATP-induced shape change of nuclear pores visualized with the atomic force microscope," *Journal of Membrane Biology*, vol. 163, no. 2, pp. 129–136, 1998.

[89] H. Wang and D. E. Clapham, "Conformational Changes of the in Situ Nuclear Pore Complex," *Biophysical Journal*, vol. 77, no. 1, pp. 241–247, 1999.

[90] V. Shahin, T. Danker, K. Enss, R. Ossig, and H. Oberleithner, "Evidence for Ca2+ - and ATP-sensitive peripheral channels in nuclear pore complexes," *The FASEB Journal*, vol. 15, no. 11, pp. 1895–1901, 2001.

[91] R. D. Jäggi, A. Franco-Obregón, P. Mühlhäusser, F. Thomas, U. Kutay, and K. Ensslin, "Modulation of nuclear pore topology by transport modifiers," *Biophysical Journal*, vol. 84, no. 1, pp. 665–670, 2003.

[92] R. D. Jäggi, A. Franco-Obregón, and K. Ensslin, "Quantitative topographical analysis of nuclear pore complex function using scanning force microscopy.," *Biophysical Journal*, vol. 85, no. 6, pp. 4093–4098, 2003.

[93] A. Kramer, Y. Ludwig, V. Shahin, and H. Oberleithner, "A pathway separate from the central channel through the nuclear pore complex for inorganic ions and small macromolecules," *Journal of Biological Chemistry*, vol. 282, no. 43, pp. 31437–31443, 2007.

[94] A. Kramer, I. Liashkovich, H. Oberleithner, S. Ludwig, I. Mazur, and V. Shahin, "Apoptosis leads to a degradation of vital components of active nuclear transport and a dissociation of the nuclear lamina.," *Proceedings of the National Academy of Sciences of the United States of America*, vol. 105, no. 32, pp. 11236–11241, 2008.

[95] M. S. Mohamed, A. Kobayashi, A. Taoka, T. Watanabe-Nakayama, Y. Kikuchi, M. Hazawa, T. Minamoto, Y. Fukumori, N. Kodera, T. Uchihashi, T. Ando, and R. W. Wong, "High-Speed Atomic Force Microscopy Reveals Loss of Nuclear Pore Resilience as a Dying Code in Colorectal Cancer Cells," *ACS Nano*, vol. 11, no. 6, pp. 5567–5578, 2017.

[96] S. W. Kowalczyk, T. R. Blosser, and C. Dekker, "Biomimetic nanopores: learning from and about nature," *Trends in Biotechnology*, vol. 29, no. 12, pp. 607–614, 2011.

[97] T. Jovanovic-Talisman and A. Zilman, "Building a basic nanomachine," *Nature Nanotechnology*, vol. 6, no. 7, pp. 397–398, 2011.

[98] T. Jovanovic-Talisman, B. T. Chait, and M. P. Rout, "Chapter 17 - NPC Mimics: Probing the Mechanism of Nucleocytoplasmic Transport," in *Methods in Cell Biology* (V. Doye, ed.), vol. 122, pp. 379–393, Academic Press, 2014.

[99] B. N. Miles, A. P. Ivanov, K. A. Wilson, F. Doğan, D. Japrung, and J. B. Edel, "Single molecule sensing with solid-state nanopores: novel materials, methods, and applications," *Chemical Society Reviews*, vol. 42, no. 1, pp. 15–28, 2013.

[100] M. Wanunu and A. Meller, "Chemically Modified Solid-State Nanopores," *Nano Letters*, vol. 7, no. 6, pp. 1580–1585, 2007.

[101] T. Jovanovic-Talisman, J. Tetenbaum-Novatt, A. S. McKenney, A. Zilman, R. Peters, M. P. Rout, and B. T. Chait, "Artificial nanopores that mimic the transport selectivity of the nuclear pore complex," *Nature*, vol. 457, no. 7232, pp. 1023–1027, 2009.

[102] S. W. Kowalczyk, L. Kapinos, T. R. Blosser, T. Magalhães, P. van Nies, R. Y. H. Lim, and C. Dekker, "Single-molecule transport across an individual biomimetic nuclear pore complex," *Nature Nanotechnology*, vol. 6, no. 7, pp. 433–438, 2011.

[103] S. M. Bezrukov, "Ion Channels as Molecular Coulter Counters to Probe Metabolite Transport," *The Journal of Membrane Biology*, vol. 174, no. 1, pp. 1–13, 2000.

[104] H. Bayley and C. R. Martin, "Resistive-Pulse SensingFrom Microbes to Molecules," *Chemical Reviews*, vol. 100, no. 7, pp. 2575–2594, 2000.

[105] S. Howorka, L. Movileanu, O. Braha, and H. Bayley, "Kinetics of duplex formation for individual DNA strands within a single protein nanopore.," *Proceedings of the National Academy of Sciences of the United States of America*, vol. 98, no. 23, pp. 12996–13001, 2001.

[106] M. Rincon-Restrepo, E. Mikhailova, H. Bayley, and G. Maglia, "Controlled Translocation of Individual DNA Molecules through Protein Nanopores with Engineered Molecular Brakes," *Nano Letters*, vol. 11, no. 2, pp. 746–750, 2011.

[107] D. Wendell, P. Jing, J. Geng, V. Subramaniam, T. J. Lee, C. Montemagno, and P. Guo, "Translocation of double-stranded DNA through membrane-adapted phi29 motor protein nanopores," *Nature Nanotechnology*, vol. 4, pp. 765–772, 2009.

[108] L. Franceschini, M. Soskine, A. Biesemans, and G. Maglia, "A nanopore machine promotes the vectorial transport of DNA across membranes," *Nature Communications*, vol. 4, p. 2415, 2013.

[109] N. A. W. Bell and U. F. Keyser, "Nanopores formed by DNA origami: A review," *FEBS letters*, vol. 588, no. 19, pp. 3564–3570, 2014.

[110] N. C. Seeman, "Nucleic acid junctions and lattices," *Journal of Theoretical Biology*, vol. 99, no. 2, pp. 237–247, 1982.

[111] P. W. Rothemund, "Folding DNA to create nanoscale shapes and patterns," *Nature*, vol. 440, no. 7082, pp. 297–302, 2006.

[112] S. M. Douglas, H. Dietz, T. Liedl, B. Högberg, F. Graf, and W. M. Shih, "Self-assembly of DNA into nanoscale three-dimensional shapes," *Nature*, vol. 459, p. 414, 2009.

[113] A. N. Marchi, I. Saaem, B. N. Vogen, S. Brown, and T. H. LaBean, "Toward larger DNA origami.," *Nano letters*, vol. 14, no. 10, pp. 5740–5747, 2014.

[114] P. C. Nickels, Y. Ke, R. Jungmann, D. M. Smith, M. Leichsenring, W. M. Shih, T. Liedl, and B. Högberg, "DNA Origami Structures Directly Assembled from Intact Bacteriophages," *Small*, vol. 10, no. 9, pp. 1765–1769, 2014.

[115] L. L. Ong, N. Hanikel, O. K. Yaghi, C. Grun, M. T. Strauss, P. Bron, J. Lai-Kee-Him, F. Schueder, B. Wang, P. Wang, J. Y. Kishi, C. Myhrvold, A. Zhu, R. Jungmann,

G. Bellot, Y. Ke, and P. Yin, "Programmable self-assembly of three-dimensional nanostructures from 10,000 unique components," *Nature*, vol. 552, p. 72, 2017.

[116] K. F. Wagenbauer, C. Sigl, and H. Dietz, "Gigadalton-scale shape-programmable DNA assemblies," *Nature*, vol. 552, p. 78, 2017.

[117] F. Hong, F. Zhang, Y. Liu, and H. Yan, "DNA Origami: Scaffolds for Creating Higher Order Structures," *Chem Rev*, vol. 117, no. 20, pp. 12584–12640, 2017.

[118] G. P. Acuna, F. M. Möller, P. Holzmeister, S. Beater, B. Lalkens, and P. Tinnefeld, "Fluorescence Enhancement at Docking Sites of DNA-Directed Self-Assembled Nanoantennas," *Science*, vol. 338, no. 6106, pp. 506–510, 2012.

[119] K. Jahn, T. Tørring, N. V. Voigt, R. S. Sørensen, A. L. Bank Kodal, E. S. Andersen, K. V. Gothelf, and J. Kjems, "Functional Patterning of DNA Origami by Parallel Enzymatic Modification," *Bioconjugate Chemistry*, vol. 22, pp. 819–823, apr 2011.

[120] C. Lin, R. Jungmann, A. M. Leifer, C. Li, D. Levner, G. M. Church, W. M. Shih, and P. Yin, "Submicrometre geometrically encoded fluorescent barcodes self-assembled from DNA," *Nature chemistry*, vol. 4, no. 10, pp. 832–839, 2012.

[121] N. A. W. Bell, C. R. Engst, M. Ablay, G. Divitini, C. Ducati, T. Liedl, and U. F. Keyser, "DNA Origami Nanopores," *Nano Letters*, vol. 12, no. 1, pp. 512–517, 2012.

[122] S. Hernández-Ainsa, N. A. W. Bell, V. V. Thacker, K. Göpfrich, K. Misiunas, M. E. Fuentes-Perez, F. Moreno-Herrero, and U. F. Keyser, "DNA Origami Nanopores for Controlling DNA Translocation," *ACS Nano*, vol. 7, no. 7, pp. 6024–6030, 2013.

[123] C. Plesa, A. N. Ananth, V. Linko, C. Gülcher, A. J. Katan, H. Dietz, and C. Dekker, "Ionic Permeability and Mechanical Properties of DNA Origami Nanoplates on Solid-State Nanopores," *ACS Nano*, vol. 8, no. 1, pp. 35–43, 2014.

[124] M. Langecker, V. Arnaut, T. G. Martin, J. List, S. Renner, M. Mayer, H. Dietz, and F. C. Simmel, "Synthetic Lipid Membrane Channels Formed by Designed DNA Nanostructures," *Science*, vol. 338, no. 6109, pp. 932–936, 2012.

[125] J. R. Burns, E. Stulz, and S. Howorka, "Self-Assembled DNA Nanopores That Span Lipid Bilayers," *Nano Letters*, vol. 13, no. 6, pp. 2351–2356, 2013.

[126] S. Krishnan, D. Ziegler, V. Arnaut, T. G. Martin, K. Kapsner, K. Henneberg, A. R. Bausch, H. Dietz, and F. C. Simmel, "Molecular transport through large-diameter DNA nanopores," *Nature Communications*, vol. 7, p. 12787, 2016.

[127] J. R. Burns and S. Howorka, "Structural and Functional Stability of DNA Nanopores in Biological Media.," *Nanomaterials*, vol. 9, no. 4, p. E490, 2019.

[128] A. L. B. Pyne, *High Resolution Atomic Force Microscopy of Functional Biological Molecules*. PhD thesis, UCL, 2014.

[129] B. Akpinar, P. J. Haynes, N. A. W. Bell, K. Brunner, A. L. B. Pyne, and B. W. Hoogenboom, "PEGylated surfaces for the study of DNA-protein interactions by atomic force microscopy," *Nanoscale*, vol. 11, no. 42, pp. 20072–20080, 2019.

[130] G. J. Stanley, B. Akpinar, Q. Shen, P. D. E. Fisher, C. P. Lusk, C. Lin, and B. W. Hoogenboom, "Quantification of Biomolecular Dynamics Inside Real and Synthetic Nuclear Pore Complexes Using Time-Resolved Atomic Force Microscopy," *ACS Nano*, vol. 13, no. 7, pp. 7949–7956, 2019.

[131] L. E. Kapinos, B. Huang, C. Rencurel, and R. Y. H. Lim, "Karyopherins regulate nuclear pore complex barrier and transport function.," *Journal of Cell Biology*, vol. 216, no. 11, pp. 3609–3624, 2017.

[132] C. Lin, S. D. Perrault, M. Kwak, F. Graf, and W. M. Shih, "Purification of DNA-origami nanostructures by rate-zonal centrifugation," *Nucleic Acids Res*, vol. 41, no. 2, 2013.

[133] M. Howarth, D. J. F. Chinnapen, K. Gerrow, P. C. Dorrestein, M. R. Grandy, N. L. Kelleher, A. El-Husseini, and A. Y. Ting, "A monovalent streptavidin with a single femtomolar biotin binding site," *Nature methods*, vol. 3, no. 4, pp. 267–273, 2006.

[134] C. Leung, A. W. Hodel, A. J. Brennan, N. Lukoyanova, S. Tran, C. M. House, S. C. Kondos, J. C. Whisstock, M. A. Dunstone, and J. A. Trapani, "Real-time visualization of perforin nanopore assembly," *Nature nanotechnology*, vol. 12, no. 5, p. 467, 2017.

[135] J. R. Silvius, "Thermotropic phase transitions of pure lipids in model membranes and their modification by membrane proteins," in *Lipid Protein Interactions* (P. C. Jost and O. H. Griffith, eds.), vol. 2, pp. 239–281, John-Wiley & Sons, New York, 1982.

[136] E. Feitosa, R. D. Adati, P. Hansson, and M. Malmsten, "Thermal and Structural Behavior of Dioctadecyldimethylammonium Bromide Dispersions Studied by Differential Scanning Calorimetry and X-Ray Scattering," *PLOS ONE*, vol. 7, no. 9, p. e44702, 2012.

[137] M. Radmacher, R. W. Tillamnn, M. Fritz, and H. E. Gaub, "From molecules to cells: imaging soft samples with the atomic force microscope.," *Science (New York, N.Y.)*, vol. 257, pp. 1900–1905, sep 1992.

[138] B. W. Hoogenboom, "AFM in Liquids," in *Encyclopedia of Nanotechnology* (B. Bhushan, ed.), pp. 83–89, Dordrecht: Springer Verlag., 2nd ed., 2012.

[139] G. C. Radcliff, D. A. Erie, and R. Superfine, "Photothermal modulation for oscillating mode atomic force microscopy in solution," *Appl. Phys. Lett.*, vol. 72, pp. 1911–1913, 1998.

[140] I. Revenko and R. Proksch, "Magnetics and acoustic tapping mode microscopy of liquid phase phospholipid bilayers and {DNA} molecules," *J. Appl. Phys.*, vol. 87, pp. 526–533, 2000.

[141] T. E. Schäffer, J. P. Cleveland, F. Ohnesorge, D. A. Walters, and P. K. Hansma, "Studies of vibrating atomic force microscope cantilevers in liquid," *J. Appl. Phys.*, vol. 80, pp. 3622–3627, 1996.

[142] S. C. Minne, Y. Hu, S. Hu, B. Pittenger, and C. Su, "NanoScale Quantitative Mechanical Property Mapping Using Peak Force Tapping Atomic Force Microscopy," *Microscopy and Microanalysis*, vol. 16, no. S2, pp. 464–465, 2010.

[143] B. Pittenger, N. Erina, and C. Su, "Quantitative mechanical property mapping at the nanoscale with PeakForce QNM." jan 2010.

[144] M. Winey, J. B. Meehl, E. T. O'Toole, and T. H. Giddings Jr, "Conventional transmission electron microscopy," *Molecular biology of the cell*, vol. 25, pp. 319–323, feb 2014.

[145] M. C. Leake, "Making the invisible visible: part 2 – without visible light," in *Single-Molecule Cellular Biophysics* (M. C. Leake, ed.), pp. 102–120, Cambridge: Cambridge University Press, 2013.

[146] D. Axelrod, "Total internal reflection fluorescence microscopy in cell biology," *TRAFFIC*, vol. 2, pp. 764–774, nov 2001.

[147] M. C. Leake, "Making the invisible visible: part 1 – methods that use visible light," in *Single-Molecule Cellular Biophysics* (M. C. Leake, ed.), pp. 60–101, Cambridge: Cambridge University Press, 2013.

[148] S. Shashkova and M. Leake, "Single-molecule fluorescence microscopy review: shedding new light on old problems," *Bioscience Reports*, vol. 37, no. 4, 2017.

[149] S. A. McKinney, C. S. Murphy, K. L. Hazelwood, M. W. Davidson, and L. L. Looger, "A bright and photostable photoconvertible fluorescent protein," *Nature methods*, vol. 6, no. 2, pp. 131–133, 2009.

[150] M. Ovesný, P. Křížek, J. Borkovec, Z. Švindrych, and G. M. Hagen, "ThunderSTORM: a comprehensive ImageJ plug-in for PALM and STORM data analysis and super-resolution imaging," *Bioinformatics*, vol. 30, no. 16, pp. 2389–2390, 2014.

[151] A. J. Sharff, L. E. Rodseth, J. C. Spurlino, and F. A. Quiocho, "Crystallographic evidence of a large ligand-induced hinge-twist motion between the two domains of the maltodextrin binding protein involved in active transport and chemotaxis," *Biochemistry*, vol. 31, no. 44, pp. 10657–10663, 1992.

[152] N. R. Voss and M. Gerstein, "3V: cavity, channel and cleft volume calculator and extractor," *Nucleic acids research*, vol. 38, no. Web Server issue, pp. W555–W562, 2010.

[153] A. Pyne, R. Thompson, C. Leung, D. Roy, and B. W. Hoogenboom, "Single-Molecule Reconstruction of Oligonucleotide Secondary Structure by Atomic Force Microscopy," *Small*, vol. 10, no. 16, pp. 3257–3261, 2014.

[154] G. Binnig, C. F. Quate, and G. C, "Atomic force microscope.," *Physical review letters*, vol. 56, no. 9, pp. 930–933, 1986.

[155] D. Pastre, O. Pietrement, S. Fusil, F. Landousy, J. Jeusset, M.-O. David, L. Hamon, E. Le Cam, and A. Zozime, "Adsorption of DNA to mica mediated by divalent counterions: a theoretical and experimental study.," *Biophysical journal*, vol. 85, pp. 2507–2518, oct 2003.

[156] C. Leung, H. Kinns, B. W. Hoogenboom, S. Howorka, and P. Mesquida, "Imaging Surface Charges of Individual Biomolecules," *Nano Letters*, vol. 9, no. 7, pp. 2769–2773, 2009.

[157] M. Bezanilla, S. Manne, D. E. Laney, Y. L. Lyubchenko, and H. G. Hansma, "Adsorption of DNA to Mica, Silylated Mica, and Minerals: Characterization by Atomic Force Microscopy," *Langmuir*, vol. 11, no. 2, pp. 655–659, 1995.

[158] H. G. Hansma, D. E. Laney, M. Bezanilla, R. L. Sinsheimer, and P. K. Hansma, "Applications for atomic force microscopy of DNA," *Biophys. J.*, vol. 68, pp. 1672–1677, 1995.

[159] A. J. Lee, M. Szymonik, J. K. Hobbs, and C. Wälti, "Tuning the translational freedom of DNA for high speed AFM," *Nano Research*, vol. 8, no. 6, pp. 1811–1821, 2015.

[160] P. R. Heenan and T. T. Perkins, "Imaging DNA Equilibrated onto Mica in Liquid Using Biochemically Relevant Deposition Conditions," *ACS Nano*, vol. 13, no. 4, pp. 4220–4229, 2019.

[161] Y. L. Lyubchenko, L. S. Shlyakhtenko, and A. A. Gall, "Atomic Force Microscopy Imaging and Probing of DNA, Proteins, and Protein-DNA Complexes: Silatrane Surface Chemistry," in *Methods in molecular biology*, vol. 543, pp. 337–351, Springer Protocols, 2009.

[162] M. Shibata, H. Nishimasu, N. Kodera, S. Hirano, T. Ando, T. Uchihashi, and O. Nureki, "Real-space and real-time dynamics of CRISPR-Cas9 visualized by high-speed atomic force microscopy," *Nature Communications*, vol. 8, no. 1, p. 1430, 2017.

[163] J. Mou, D. M. Czajkowsky, Y. Zhang, and Z. Shao, "High-resolution atomic-force microscopy of DNA: the pitch of the double helix," *FEBS letters*, vol. 371, no. 3, pp. 279–282, 1995.

[164] M. Bussiek, N. Mücke, and J. Langowski, "Polylysine-coated mica can be used to observe systematic changes in the supercoiled DNA conformation by scanning force microscopy in solution," *Nucleic acids research*, vol. 31, no. 22, pp. e137–e137, 2003.

[165] T. Brouns, H. De Keersmaecker, S. F. Konrad, N. Kodera, T. Ando, J. Lipfert, S. De Feyter, and W. Vanderlinden, "Free Energy Landscape and Dynamics of Supercoiled

DNA by High-Speed Atomic Force Microscopy," *ACS Nano*, vol. 12, no. 12, pp. 11907–11916, 2018.

[166] R. P. Richter, R. Bérat, and A. R. Brisson, "Formation of Solid-Supported Lipid Bilayers An Integrated View," *Langmuir*, vol. 22, no. 8, pp. 3497–3505, 2006.

[167] M.-P. Mingeot-Leclercq, M. Deleu, R. Brasseur, and Y. F. Dufrêne, "Atomic force microscopy of supported lipid bilayers," *Nature Protocols*, vol. 3, p. 1654, 2008.

[168] R. N. A. H. Lewis and R. N. McElhaney, *The Structure of Biological Membranes*. CRC Press, 3rd ed., 2005.

[169] M. S. Malghani and J. Yang, "Stable Binding of DNA to Zwitterionic Lipid Bilayers in Aqueous Solutions," *The Journal of Physical Chemistry B*, vol. 102, no. 44, pp. 8930–8933, 1998.

[170] M. Langecker, V. Arnaut, J. List, and F. C. Simmel, "DNA Nanostructures Interacting with Lipid Bilayer Membranes," *Accounts of Chemical Research*, vol. 47, no. 6, pp. 1807–1815, 2014.

[171] Y. Suzuki, M. Endo, and H. Sugiyama, "Lipid-bilayer-assisted two-dimensional self-assembly of DNA origami nanostructures," *Nat Commun*, vol. 6, p. 8052, 2015.

[172] S. Kocabey, S. Kempter, J. List, Y. Xing, W. Bae, D. Schiffels, W. M. Shih, F. C. Simmel, and T. Liedl, "Membrane-Assisted Growth of DNA Origami Nanostructure Arrays," *ACS Nano*, vol. 9, no. 4, pp. 3530–3539, 2015.

[173] M. Heuberger, T. Drobek, and N. D. Spencer, "Interaction Forces and Morphology of a Protein-Resistant Poly(ethylene glycol) Layer," *Biophysical Journal*, vol. 88, no. 1, pp. 495–504, 2005.

[174] P. Kingshott, H. Thissen, and H. J. Griesser, "Effects of cloud-point grafting, chain length, and density of PEG layers on competitive adsorption of ocular proteins," *Biomaterials*, vol. 23, no. 9, pp. 2043–2056, 2002.

[175] G. L. Kenausis, J. Vörös, D. L. Elbert, N. Huang, R. Hofer, L. Ruiz-Taylor, M. Textor, J. A. Hubbell, and N. D. Spencer, "Poly(l-lysine)-g-Poly(ethylene glycol) Layers on Metal Oxide Surfaces Attachment Mechanism and Effects of Polymer Architecture

on Resistance to Protein Adsorption," *The Journal of Physical Chemistry B*, vol. 104, no. 14, pp. 3298–3309, 2000.

[176] N.-P. Huang, R. Michel, J. Voros, M. Textor, R. Hofer, A. Rossi, D. L. Elbert, J. A. Hubbell, and N. D. Spencer, "Poly(l-lysine)-g-poly(ethylene glycol) Layers on Metal Oxide Surfaces: Surface-Analytical Characterization and Resistance to Serum and Fibrinogen Adsorption," *Langmuir*, vol. 17, no. 2, pp. 489–498, 2001.

[177] S. Pasche, S. M. De Paul, J. Vörös, N. D. Spencer, and M. Textor, "Poly(l-lysine)-graft-poly(ethylene glycol) Assembled Monolayers on Niobium Oxide Surfaces: A Quantitative Study of the Influence of Polymer Interfacial Architecture on Resistance to Protein Adsorption by ToF-SIMS and in Situ OWLS," *Langmuir*, vol. 19, no. 22, pp. 9216–9225, 2003.

[178] S. VandeVondele, J. Vörös, and J. A. Hubbell, "RGD-grafted poly-l-lysine-graft-(polyethylene glycol) copolymers block non-specific protein adsorption while promoting cell adhesion," *Biotechnology and Bioengineering*, vol. 82, no. 7, pp. 784–790, 2003.

[179] S. Patel, R. G. Thakar, J. Wong, S. D. McLeod, and S. Li, "Control of cell adhesion on poly(methyl methacrylate)," *Biomaterials*, vol. 27, no. 14, pp. 2890–2897, 2006.

[180] L. A. Ruiz-Taylor, T. L. Martin, F. G. Zaugg, K. Witte, P. Indermuhle, S. Nock, and P. Wagner, "Monolayers of derivatized poly(l-lysine)-grafted poly(ethylene glycol) on metal oxides as a class of biomolecular interfaces," *Proceedings of the National Academy of Sciences of the United States of America*, vol. 98, no. 3, pp. 852–857, 2001.

[181] R. Schlapak, D. Armitage, N. Saucedo-Zeni, W. Chrzanowski, M. Hohage, D. Caruana, and S. Howorka, "Selective protein and DNA adsorption on PLL-PEG films modulated by ionic strength," *Soft Matter*, vol. 5, no. 3, pp. 613–621, 2009.

[182] E. Tkachenko, M. Sabouri-Ghomi, O. Pertz, C. Kim, E. Gutierrez, M. Machacek, A. Groisman, G. Danuser, and M. H. Ginsberg, "Protein kinase A governs a RhoA–RhoGDI protrusion–retraction pacemaker in migrating cells," *Nature Cell Biology*, vol. 13, no. 6, p. 660, 2011.

[183] C. Hennesthal and C. Steinem, "Pore-Spanning Lipid Bilayers Visualized by Scanning Force Microscopy," *Journal of the American Chemical Society*, vol. 122, no. 33, pp. 8085–8086, 2000.

[184] T. Isogai, S. Nakada, N. Yoshida, H. Sumi, R. Tero, S. Harada, T. Ujihara, and M. Tagawa, "Phase transition process in DDAB supported lipid bilayer," *Journal of Crystal Growth*, vol. 468, pp. 88–92, 2017.

[185] J. L. Slater and C. H. Huang, "Interdigitated bilayer membranes.," *Progress in lipid research*, vol. 27, no. 4, pp. 325–359, 1988.

[186] D. Jamróz, M. Kepczynski, and M. Nowakowska, "Molecular Structure of the Dioctadecyldimethylammonium Bromide (DODAB) Bilayer," *Langmuir*, vol. 26, no. 19, pp. 15076–15079, 2010.

[187] S. Connell and D. Smith, "The atomic force microscope as a tool for studying phase separation in lipid membranes (Review)," *Molecular membrane biology*, vol. 23, pp. 17–28, 2006.

[188] L. Baranello, D. Levens, A. Gupta, and F. Kouzine, "The importance of being supercoiled: how DNA mechanics regulate dynamic processes," *Biochimica et biophysica acta*, vol. 1819, pp. 632–638, jul 2012.

[189] J. M. Fogg, N. Kolmakova, I. Rees, S. Magonov, H. Hansma, J. J. Perona, and E. L. Zechiedrich, "Exploring writhe in supercoiled minicircle DNA," *Journal of Physics: Condensed Matter*, vol. 18, no. 14, pp. S145–S159, 2006.

[190] R. N. Irobalieva, J. M. Fogg, D. J. Catanese Jr, T. Sutthibutpong, M. Chen, A. K. Barker, S. J. Ludtke, S. A. Harris, M. F. Schmid, W. Chiu, and L. Zechiedrich, "Structural diversity of supercoiled DNA," *Nature Communications*, vol. 6, no. 8440, 2015.

[191] D. Y. Kwoh, C. C. Coffin, C. P. Lollo, J. Jovenal, M. G. Banaszczyk, P. Mullen, A. Phillips, A. Amini, J. Fabrycki, R. M. Bartholomew, S. W. Brostoff, and D. J. Carlo, "Stabilization of poly-l-lysine/DNA polyplexes for in vivo gene delivery to the liver," *Biochimica et Biophysica Acta (BBA) - Gene Structure and Expression*, vol. 1444, no. 2, pp. 171–190, 1999.

[192] N. M. Luscombe, S. E. Austin, H. M. Berman, and J. M. Thornton, "An overview of the structures of protein-DNA complexes," *Genome biology*, vol. 1, no. 1, 2000.

[193] M. Porus, P. Maroni, and M. Borkovec, "Structure of Adsorbed Polyelectrolyte Monolayers Investigated by Combining Optical Reflectometry and Piezoelectric Techniques," *Langmuir*, vol. 28, no. 13, pp. 5642–5651, 2012.

[194] X. Jin, L. Leclercq, N. Sisavath, and H. Cottet, "Investigating the Influence of Phosphate Ions on Poly(l-lysine) Conformations by Taylor Dispersion Analysis," *Macromolecules*, vol. 47, no. 15, pp. 5320–5327, 2014.

[195] T. Arai, K. Sato, A. Iida, and M. Tomitori, "Quasi-stabilized hydration layers on muscovite mica under a thin water film grown from humid air," *Scientific Reports*, vol. 7, no. 1, p. 4054, 2017.

[196] N. M. Green, "Avidin and streptavidin," *Methods Enzymol*, vol. 184, pp. 51–67, 1990.

[197] J. N. Israelachvili, "Steric (Polymer-Mediated) and Thermal Fluctuation Forces," in *Intermolecular and Surface Forces* (J. N. B. T. Israelachvili, ed.), pp. 381–413, Boston: Academic Press, 2011.

[198] N. Giamblanco, G. Marletta, A. Graillot, N. Bia, C. Loubat, and J.-F. Berret, "Serum Protein-Resistant Behavior of Multisite-Bound Poly(ethylene glycol) Chains on Iron Oxide Surfaces," *ACS Omega*, vol. 2, no. 4, pp. 1309–1320, 2017.

[199] G. V. Dubacheva, C. Araya-Callis, A. Geert Volbeda, M. Fairhead, J. Codée, M. Howarth, and R. P. Richter, "Controlling Multivalent Binding through Surface Chemistry: Model Study on Streptavidin," *Journal of the American Chemical Society*, vol. 139, no. 11, pp. 4157–4167, 2017.

[200] S. Amlacher, P. Sarges, D. Flemming, V. van Noort, R. Kunze, D. P. Devos, M. Arumugam, P. Bork, and E. Hurt, "Insight into structure and assembly of the nuclear pore complex by utilizing the genome of a eukaryotic thermophile.," *Cell*, vol. 146, no. 2, pp. 277–289, 2011.

[201] J. Fischer, R. Teimer, S. Amlacher, R. Kunze, and E. Hurt, "Linker Nups connect the nuclear pore complex inner ring with the outer ring and transport channel.," *Nature structural & molecular biology*, vol. 22, no. 10, pp. 774–781, 2015.

[202] L. Apelt, K. E. Knockenhauer, N. C. Leksa, N. Benlasfer, T. U. Schwartz, and U. Stelzl, "Systematic Protein–Protein Interaction Analysis Reveals Intersubcomplex Contacts

in the Nuclear Pore Complex," *Molecular & Cellular Proteomics*, vol. 15, no. 8, pp. 2594 – 2606, 2016.

[203] A. Ori, N. Banterle, M. Iskar, A. Andres-Pons, C. Escher, H. Khanh Bui, L. Sparks, V. Solis-Mezarino, O. Rinner, P. Bork, E. A. Lemke, and M. Beck, "Cell type-specific nuclear pores: a case in point for context-dependent stoichiometry of molecular machines.," *Molecular systems biology*, vol. 9, p. 648, 2013.

[204] O. Peleg, M. Tagliazucchi, M. Kröger, Y. Rabin, and I. Szleifer, "Morphology control of hairy nanopores," *ACS Nano*, vol. 5, no. 6, pp. 4737–4747, 2011.

[205] C. Ader, S. Frey, W. Maas, H. B. Schmidt, D. Görlich, and M. Baldus, "Amyloid-like interactions within nucleoporin FG hydrogels," *Proceedings of the National Academy of Sciences of the United States of America*, vol. 107, no. 14, pp. 6281–6285, 2010.

[206] W. Xu, B. Nathwani, C. Lin, J. Wang, E. Karatekin, F. Pincet, W. Shih, and J. E. Rothman, "A Programmable DNA Origami Platform to Organize SNAREs for Membrane Fusion.," *Journal of the American Chemical Society*, vol. 138, no. 13, pp. 4439–4447, 2016.

[207] N. D. Derr, B. S. Goodman, R. Jungmann, A. E. Leschziner, W. M. Shih, and S. L. Reck-Peterson, "Tug-of-War in Motor Protein Ensembles Revealed with a Programmable DNA Origami Scaffold," *Science*, vol. 338, no. 6107, pp. 662–665, 2012.

[208] R. F. Hariadi, R. F. Sommese, A. S. Adhikari, R. E. Taylor, S. Sutton, J. A. Spudich, and S. Sivaramakrishnan, "Mechanical coordination in motor ensembles revealed using engineered artificial myosin filaments," *Nature nanotechnology*, vol. 10, no. 8, pp. 696–700, 2015.

[209] J. Fu, M. Liu, Y. Liu, N. W. Woodbury, and H. Yan, "Interenzyme substrate diffusion for an enzyme cascade organized on spatially addressable DNA nanostructures.," *Journal of the American Chemical Society*, vol. 134, no. 12, pp. 5516–5519, 2012.

[210] A. Shaw, V. Lundin, E. Petrova, F. Fordos, E. Benson, A. Al-Amin, A. Herland, A. Blokzijl, B. Hogberg, and A. I. Teixeira, "Spatial control of membrane receptor function using ligand nanocalipers.," *Nature methods*, vol. 11, no. 8, pp. 841–846, 2014.

[211] N. C. Seeman, "The origin of structural DNA nanotechnology," in *Structural DNA Nanotechnology* (N. C. Seeman, ed.), pp. 1–10, Cambridge: Cambridge University Press, 2016.

[212] D. P. Denning and M. F. Rexach, "Rapid evolution exposes the boundaries of domain structure and function in natively unfolded FG nucleoporins.," *Molecular & cellular proteomics : MCP*, vol. 6, no. 2, pp. 272–282, 2007.

[213] J. Israelachvili, *Intermolecular and Surface Forces*. Elsevier, 3rd ed., 2011.

[214] D. Mohr, S. Frey, T. Fischer, T. Güttler, and D. Görlich, "Characterisation of the passive permeability barrier of nuclear pore complexes.," *The EMBO Journal*, vol. 28, no. 17, pp. 2541–2553, 2009.

[215] K. Hatch, C. Danilowicz, V. Coljee, and M. Prentiss, "Demonstration that the shear force required to separate short double-stranded DNA does not increase significantly with sequence length for sequences longer than 25 base pairs," *Phys. Rev. E*, vol. 78, p. 11920, jul 2008.

[216] M. Tagliazucchi, O. Peleg, M. Kroger, Y. Rabin, and I. Szleifer, "Effect of charge, hydrophobicity, and sequence of nucleoporins on the translocation of model particles through the nuclear pore complex.," *Proceedings of the National Academy of Sciences of the United States of America*, vol. 110, no. 9, pp. 3363–3368, 2013.

[217] M. B. Viani, L. I. Pietrasanta, J. B. Thompson, A. Chand, I. C. Gebeshuber, J. H. Kindt, M. Richter, H. G. Hansma, and P. K. Hansma, "Probing protein–protein interactions in real time," *Nature Structural Biology*, vol. 7, no. 8, pp. 644–647, 2000.

[218] G. R. Heath and S. Scheuring, "High-speed AFM height spectroscopy reveals μs-dynamics of unlabeled biomolecules," *Nature Communications*, vol. 9, no. 4983, 2018.

[219] G. R. Heath, B. Ramm, P. Schwille, and S. Scheuring, "High-Speed AFM Correlation Spectroscopy (HS-AMF-CS): μS Protein Dynamics without Labels," *Biophysical Journal*, vol. 114, no. 3, pp. 70a—71a, 2018.

[220] T. Ando, "High-speed atomic force microscopy and its future prospects," *Biophysical Reviews*, vol. 10, no. 2, pp. 285–292, 2018.

[221] N. Kodera, D. Yamamoto, R. Ishikawa, and T. Ando, "Video imaging of walking myosin V by high-speed atomic force microscopy," *Nature*, vol. 468, no. 7320, pp. 72–76, 2010.

[222] N. Chiaruttini, L. Redondo-Morata, A. Colom, F. Humbert, M. Lenz, S. Scheuring, and A. Roux, "Relaxation of Loaded ESCRT-III Spiral Springs Drives Membrane Deformation," *Cell*, vol. 163, no. 4, pp. 866–879, 2015.

[223] A. P. Nievergelt, N. Banterle, S. H. Andany, P. Gönczy, and G. E. Fantner, "High-speed photothermal off-resonance atomic force microscopy reveals assembly routes of centriolar scaffold protein SAS-6," *Nature Nanotechnology*, vol. 13, no. 8, pp. 696–701, 2018.

[224] A. Miyagi, Y. Tsunaka, T. Uchihashi, K. Mayanagi, S. Hirose, K. Morikawa, and T. Ando, "Visualization of Intrinsically Disordered Regions of Proteins by High-Speed Atomic Force Microscopy," *ChemPhysChem*, vol. 9, no. 13, pp. 1859–1866, 2008.

[225] Y. Sakiyama, R. Panatala, and R. Y. H. Lim, "Structural dynamics of the nuclear pore complex," *Seminars in Cell & Developmental Biology*, vol. 68, pp. 27–33, 2017.

[226] T. A. Isgro and K. Schulten, "Binding Dynamics of Isolated Nucleoporin Repeat Regions to Importin-β," *Structure*, vol. 13, no. 12, pp. 1869–1879, 2005.

[227] R. Y. H. Lim, B. Fahrenkrog, J. Köser, K. Schwarz-Herion, J. Deng, and U. Aebi, "Nanomechanical Basis of Selective Gating by the Nuclear Pore Complex," *Science*, vol. 318, no. 5850, pp. 640–643, 2007.

[228] W. Yang, J. Gelles, and S. M. Musser, "Imaging of single-molecule translocation through nuclear pore complexes.," *Proceedings of the National Academy of Sciences of the United States of America*, vol. 101, no. 35, pp. 12887–12892, 2004.

[229] H. J. Dyson and P. E. Wright, "Intrinsically unstructured proteins and their functions," *Nature Reviews Molecular Cell Biology*, vol. 6, no. 3, pp. 197–208, 2005.

[230] E. A. Lemke, "The Multiple Faces of Disordered Nucleoporins," *Journal of Molecular Biology*, vol. 428, no. 10, pp. 2011–2024, 2016.

[231] K. Kasahara, H. Terazawa, T. Takahashi, and J. Higo, "Studies on Molecular Dynamics of Intrinsically Disordered Proteins and Their Fuzzy Complexes: A Mini-Review," *Computational and structural biotechnology journal*, vol. 17, pp. 712–720, 2019.

[232] S. Sparks, D. B. Temel, M. P. Rout, and D. Cowburn, "Deciphering the "Fuzzy" Interaction of FG Nucleoporins and Transport Factors Using Small-Angle Neutron Scattering," *Structure*, vol. 26, no. 3, pp. 477–484, 2018.

[233] E. Conti, C. W. Müller, and M. Stewart, "Karyopherin flexibility in nucleocytoplasmic transport," *Current Opinion in Structural Biology*, vol. 16, no. 2, pp. 237–244, 2006.

[234] R. Bayliss, T. Littlewood, and M. Stewart, "Structural Basis for the Interaction between FxFG Nucleoporin Repeats and Importin-beta in Nuclear Trafficking," *Cell*, vol. 102, no. 1, pp. 99–108, 2000.

[235] T. L. Bullock, W. D. Clarkson, H. M. Kent, and M. Stewart, "The 1.6 ÅResolution Crystal Structure of Nuclear Transport Factor 2 (NTF2)," *Journal of Molecular Biology*, vol. 260, no. 3, pp. 422–431, 1996.

[236] I. V. Aramburu and E. A. Lemke, "Floppy but not sloppy: Interaction mechanism of FG-nucleoporins and nuclear transport receptors," *Seminars in Cell & Developmental Biology*, vol. 68, pp. 34–41, 2017.

[237] B. Raveh, J. M. Karp, S. Sparks, K. Dutta, M. P. Rout, A. Sali, and D. Cowburn, "Slide-and-exchange mechanism for rapid and selective transport through the nuclear pore complex.," *Proceedings of the National Academy of Sciences of the United States of America*, vol. 113, no. 18, pp. E2489–97, 2016.

[238] R. Hayama, M. Sorci, J. J. Keating, L. M. Hecht, J. L. Plawsky, G. Belfort, B. T. Chait, and M. P. Rout, "Interactions of nuclear transport factors and surface-conjugated FG nucleoporins: Insights and limitations," *PLOS ONE*, vol. 14, no. 6, p. e0217897, 2019.

[239] G. Riddick and I. G. Macara, "A systems analysis of importin-α - β mediated nuclear protein import," *The Journal of Cell Biology*, vol. 168, no. 7, pp. 1027–1038, 2005.

[240] K. Ribbeck, G. Lipowsky, H. M. Kent, M. Stewart, and D. Görlich, "NTF2 mediates nuclear import of Ran," *The EMBO Journal*, vol. 17, no. 22, pp. 6587–6598, 1998.

[241] U. Kutay, F. Bischoff, S. Kostka, R. Kraft, and D. Görlich, "Export of Importin α from the Nucleus Is Mediated by a Specific Nuclear Transport Factor," *Cell*, vol. 90, no. 6, pp. 1061–1071, 1997.

[242] R. Bayliss, T. Littlewood, and M. Stewart, "Structural basis for the interaction between FxFG nucleoporin repeats and importin-beta in nuclear trafficking.," *Cell*, vol. 102, no. 1, pp. 99–108, 2000.

[243] J. Wiedenmann, S. Ivanchenko, F. Oswald, F. Schmitt, C. Röcker, A. Salih, K.-D. Spindler, and G. U. Nienhaus, "EosFP, a fluorescent marker protein with UV-inducible green-to-red fluorescence conversion," *Proceedings of the National Academy of Sciences*, vol. 101, no. 45, pp. 15905–15910, 2004.

[244] R. Bayliss, T. Littlewood, L. A. Strawn, S. R. Wente, and M. Stewart, "GLFG and FxFG nucleoporins bind to overlapping sites on importin-beta.," *The Journal of biological chemistry*, vol. 277, no. 52, pp. 50597–50606, 2002.

[245] H. B. Schmidt and D. Görlich, "Nup98 FG domains from diverse species spontaneously phase-separate into particles with nuclear pore-like permselectivity.," *eLife*, vol. 4, p. e04251, 2015.

[246] N. Panté and M. Kann, "Nuclear Pore Complex Is Able to Transport Macromolecules with Diameters of ˜39 nm," *Molecular Biology of the Cell*, vol. 13, no. 2, pp. 425–434, 2002.

[247] B. Rabe, A. Vlachou, N. Panté, A. Helenius, and M. Kann, "Nuclear import of hepatitis B virus capsids and release of the viral genome.," *Proceedings of the National Academy of Sciences of the United States of America*, vol. 100, no. 17, pp. 9849–9854, 2003.

[248] R. Peters, "Translocation through the nuclear pore: Kaps pave the way," *BioEssays*, vol. 31, no. 4, pp. 466–477, 2009.

[249] Y. Elani, R. V. Law, and O. Ces, "Vesicle-based artificial cells as chemical microreactors with spatially segregated reaction pathways," *Nature Communications*, vol. 5, no. 1, p. 5305, 2014.

[250] E. C. Yusko, J. M. Johnson, S. Majd, P. Prangkio, R. C. Rollings, J. Li, J. Yang, and M. Mayer, "Controlling protein translocation through nanopores with bio-inspired fluid walls," *Nature nanotechnology*, vol. 6, p. 253, 2011.

[251] M. Pla-Roca, L. Isa, K. Kumar, and E. Reimhult, "Selective (Bio)Functionalization of Solid-State Nanopores," *ACS Applied Materials & Interfaces*, vol. 7, no. 11, pp. 6030–6035, 2015.

[252] G. Young and P. Kukura, "Interferometric Scattering Microscopy," *Annual Review of Physical Chemistry*, vol. 70, no. 1, pp. 301–322, 2019.

[253] S. Spindler, J. Ehrig, K. König, T. Nowak, M. Piliarik, H. E. Stein, R. W. Taylor, E. Garanger, S. Lecommandoux, I. D. Alves, and V. Sandoghdar, "Visualization of lipids and proteins at high spatial and temporal resolution via interferometric scattering ({iSCAT}) microscopy," *Journal of Physics D: Applied Physics*, vol. 49, p. 274002, jun 2016.

[254] M. Jerabek-Willemsen, T. André, R. Wanner, H. M. Roth, S. Duhr, P. Baaske, and D. Breitsprecher, "MicroScale Thermophoresis: Interaction analysis and beyond," *Journal of Molecular Structure*, vol. 1077, pp. 101–113, 2014.

[255] W. H. Pitchford, H.-J. Kim, A. P. Ivanov, H.-M. Kim, J.-S. Yu, R. J. Leatherbarrow, T. Albrecht, K.-B. Kim, and J. B. Edel, "Synchronized Optical and Electronic Detection of Biomolecules Using a Low Noise Nanopore Platform," *ACS Nano*, vol. 9, no. 2, pp. 1740–1748, 2015.

[256] S. Cai, J. Y. Y. Sze, A. P. Ivanov, and J. B. Edel, "Small molecule electro-optical binding assay using nanopores," *Nature Communications*, vol. 10, no. 1, p. 1797, 2019.

[257] X. Gong, A. V. Patil, A. P. Ivanov, Q. Kong, T. Gibb, F. Dogan, A. J. DeMello, and J. B. Edel, "Label-Free In-Flow Detection of Single DNA Molecules using Glass Nanopipettes," *Analytical Chemistry*, vol. 86, no. 1, pp. 835–841, 2014.

[258] T. Diederichs, G. Pugh, A. Dorey, Y. Xing, J. R. Burns, Q. Hung Nguyen, M. Tornow, R. Tampé, and S. Howorka, "Synthetic protein-conductive membrane nanopores built with DNA," *Nature Communications*, vol. 10, no. 1, p. 5018, 2019.

[259] A. Bestembayeva, "Biophysical properties of the transport barrier in the nuclear pore complex," *Thesis Dissertation*, pp. 1–186, 2016.

[260] A. Rutkowska, K. Freedman, J. Skalkowska, M. J. Kim, J. B. Edel, and T. Albrecht, "Electrodeposition and Bipolar Effects in Metallized Nanopores and Their Use in the Detection of Insulin," *Analytical Chemistry*, vol. 87, no. 4, pp. 2337–2344, 2015.

[261] A. Ananth, M. Genua, N. Aissaoui, L. Diaz, N. B. Eisele, S. Frey, C. Dekker, R. P. Richter, and D. Gorlich, "Reversible Immobilization of Proteins in Sensors and Solid-State Nanopores.," *Small (Weinheim an der Bergstrasse, Germany)*, vol. 14, p. e1703357, may 2018.

[262] S. Mahouche-Chergui, S. Gam-Derouich, C. Mangeney, and M. M. Chehimi, "Aryl diazonium salts: a new class of coupling agents for bonding polymers, biomacromolecules and nanoparticles to surfaces," *Chem. Soc. Rev.*, vol. 40, no. 7, pp. 4143–4166, 2011.

[263] W. Richard, D. Evrard, and P. Gros, "New insight into 4-nitrobenzene diazonium reduction process: Evidence for a grafting step distinct from NO2 electrochemical reactivity," *Journal of Electroanalytical Chemistry*, vol. 685, pp. 109–115, 2012.

[264] B. P. Corgier, C. A. Marquette, and L. J. Blum, "DiazoniumProtein Adducts for Graphite Electrode Microarrays Modification: Direct and Addressed Electrochemical Immobilization," *Journal of the American Chemical Society*, vol. 127, pp. 18328–18332, dec 2005.

[265] B. P. Nadappuram, K. McKelvey, R. Al Botros, A. W. Colburn, and P. R. Unwin, "Fabrication and Characterization of Dual Function Nanoscale pH-Scanning Ion Conductance Microscopy (SICM) Probes for High Resolution pH Mapping," *Analytical Chemistry*, vol. 85, pp. 8070–8074, sep 2013.

Appendix A

Copyright permissions

All material from P.D.E Fisher *et al.*,"A programmable DNA origami platform for organizing intrinsically disordered nucleoporins within nanopore confinement", *ACS Nano*, vol. 12, no. 2, pp 1508-1518, 2018 are reproduced and adapted with permission. Copyright 2018 American Chemical Society.

All material from G. J. Stanley *et al.* "Quantification of biomolecular dynamics inside real and synthetic nuclear pore complexes using time-resolved atomic force microscopy", *ACS Nano*, vol. 13, no 7, pp 7949-7956, 2019 have been published with an Creative Commons Attribution 4.0 International license (CC BY 4.0)

All material from B. Akpinar *et al.* "PEGylated surfaces for the study of DNA-protein interactions by atomic force microscopy", *Nanoscale*, vol. 11, pp 20072-20080, 2019 have been published with an Creative Commons Attribution 3.0 Unported license (CC BY 3.0)

Page No.	Fig No.	Source of work	Copyright holder	Permission note
20	Fig. 1.2	Bistable collective behavior of polymers tethered in a nanopore, Phys. Rev. E, 85, 6 (2012)	©2012 American Physical Society	Permission granted, 02.09.19
26	Fig. 1.4	Atomic force microscopy reveals structural variability amongst nuclear pore complexes, Life Sci. Alliance, 1, 4 (2017)	©Stanley *et al.*	Subject to a Creative Commons license (Attribution 4.0 International, CC BY 4.0)
26	Fig. 1.4	Nanoscale stiffness topography reveals structure and mechanics of the transport barrier in intact nuclear pore complexes, Nat. Nanotechnol., 10, 1 (2015)	©Springer Nature	Permission granted, 04.09.19
26	Fig. 1.4	Spatiotemporal dynamics of the nuclear pore complex transport barrier resolved by high-speed atomic force microscopy, 11, 8 (2016)	©Springer Nature	Permission granted, 04.09.19
28	Fig. 1.5	Artificial nanopores that mimic the transport selectivity of the nuclear pore complex, 457, 7232 (2008)	©Springer Nature	Permission granted, 04.09.19
28	Fig. 1.5	Single-molecule transport across an individual biomimetic nuclear pore complex, 6, 7 (2011)	©Springer Nature	Permission granted, 04.09.19
30	Fig. 1.6	Folding DNA to create nanoscale shapes and patterns, 440, 7082 (2006)	©Springer Nature	Permission granted, 04.09.19
30	Fig. 1.6	Self-assembly of DNA into nanoscale three-dimensional shapes, 459, 7245 (2009)	©Springer Nature	Permission granted, 04.09.19
31	Fig. 1.7	DNA origami nanopores, 12, 1 (2011)	©American Chemical Society	Permission granted, 23.01.20
31	Fig. 1.7	Synthetic lipid membrane channels formed by designed DNA nanostructures, 338, 6109 (2012)	©American Association for the Advancement of Science	Permission granted, 23.01.20
31	Fig. 1.7	DNA origami scaffold for studying intrinsically disordered proteins of the nuclear pore complex, 9, 902 (2018)	©Springer Nature	Subject to a Creative Commons license (Attribution 4.0 International, CC BY 4.0)

34	Full page graphic	The Douglas Lab Artwork, http://bionano.ucsf.edu/downloads		Subject to a Creative Commons license (Attribution-NonCommercial, CC BY-NC 3.0)
47	Fig. 2.4	AFM in Liquids, Encyclopedia of Nanotechnology, 2012 edition, ISBN:978-90-481-9750-7	©Springer Nature	Permission granted, 04.09.19

Copyright Clearance Center RightsLink®

Home Create Account Help LIVE CHAT

ACS Publications Most Trusted. Most Cited. Most Read.

Title: A Programmable DNA Origami Platform for Organizing Intrinsically Disordered Nucleoporins within Nanopore Confinement

Author: Patrick D. Ellis Fisher, Qi Shen, Bernice Akpinar, et al

Publication: ACS Nano

Publisher: American Chemical Society

Date: Feb 1, 2018

Copyright © 2018, American Chemical Society

LOGIN

If you're a copyright.com user, you can login to RightsLink using your copyright.com credentials.

Already **a RightsLink user** or want to learn more?

PERMISSION/LICENSE IS GRANTED FOR YOUR ORDER AT NO CHARGE

This type of permission/license, instead of the standard Terms & Conditions, is sent to you because no fee is being charged for your order. Please note the following:

- Permission is granted for your request in both print and electronic formats, and translations.
- If figures and/or tables were requested, they may be adapted or used in part.
- Please print this page for your records and send a copy of it to your publisher/graduate school.
- Appropriate credit for the requested material should be given as follows: "Reprinted (adapted) with permission from (COMPLETE REFERENCE CITATION). Copyright (YEAR) American Chemical Society." Insert appropriate information in place of the capitalized words.
- One-time permission is granted only for the use specified in your request. No additional uses are granted (such as derivative works or other editions). For any other uses, please submit a new request.

BACK CLOSE WINDOW

Copyright © 2019 Copyright Clearance Center, Inc. All Rights Reserved. Privacy statement. Terms and Conditions.
Comments? We would like to hear from you. E-mail us at customercare@copyright.com

American Physical Society
Reuse and Permissions License

02-Sep-2019

This license agreement between the American Physical Society ("APS") and Bernice Akpinar ("You") consists of your license details and the terms and conditions provided by the American Physical Society and SciPris.

Licensed Content Information

License Number:	**RNP/19/SEP/018354**
License date:	02-Sep-2019
DOI:	10.1103/PhysRevE.85.061917
Title:	Bistable collective behavior of polymers tethered in a nanopore
Author:	Dino Osmanovic et al.
Publication:	Physical Review E
Publisher:	American Physical Society
Cost:	USD $ 0.00

Request Details

Does your reuse require significant modifications: No

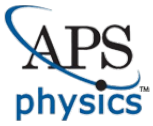
Specify intended distribution locations:	Worldwide
Reuse Category:	Reuse in a thesis/dissertation
Requestor Type:	Student
Items for Reuse:	Figures/Tables
Number of Figure/Tables:	1
Figure/Tables Details:	Figure 2, Snapshots taken from converged Monte Carlo simulations. Reuse with recolouring.
Format for Reuse:	Electronic

Information about New Publication:

University/Publisher:	Imperial College London
Title of dissertation/thesis:	The nanoscale behaviour of disordered polypeptides confined within biomimetic nuclear pore complexes
Author(s):	Bernice Akpinar
Expected completion date:	Oct. 2019

License Requestor Information

Name:	Bernice Akpinar
Affiliation:	Individual
Email Id:	b.akpinar15@ic.ac.uk
Country:	United Kingdom



American Physical Society
Reuse and Permissions License

TERMS AND CONDITIONS

The American Physical Society (APS) is pleased to grant the Requestor of this license a non-exclusive, non-transferable permission, limited to Electronic format, provided all criteria outlined below are followed.

1. You must also obtain permission from at least one of the lead authors for each separate work, if you haven't done so already. The author's name and affiliation can be found on the first page of the published Article.
2. For electronic format permissions, Requestor agrees to provide a hyperlink from the reprinted APS material using the source material's DOI on the web page where the work appears. The hyperlink should use the standard DOI resolution URL, http://dx.doi.org/{DOI}. The hyperlink may be embedded in the copyright credit line.
3. For print format permissions, Requestor agrees to print the required copyright credit line on the first page where the material appears: "Reprinted (abstract/excerpt/figure) with permission from [(FULL REFERENCE CITATION) as follows: Author's Names, APS Journal Title, Volume Number, Page Number and Year of Publication.] Copyright (YEAR) by the American Physical Society."
4. Permission granted in this license is for a one-time use and does not include permission for any future editions, updates, databases, formats or other matters. Permission must be sought for any additional use.
5. Use of the material does not and must not imply any endorsement by APS.
6. APS does not imply, purport or intend to grant permission to reuse materials to which it does not hold copyright. It is the requestor's sole responsibility to ensure the licensed material is original to APS and does not contain the copyright of another entity, and that the copyright notice of the figure, photograph, cover or table does not indicate it was reprinted by APS with permission from another source.
7. The permission granted herein is personal to the Requestor for the use specified and is not transferable or assignable without express written permission of APS. This license may not be amended except in writing by APS.
8. You may not alter, edit or modify the material in any manner.
9. You may translate the materials only when translation rights have been granted.
10. APS is not responsible for any errors or omissions due to translation.
11. You may not use the material for promotional, sales, advertising or marketing purposes.
12. The foregoing license shall not take effect unless and until APS or its agent, Aptara, receives payment in full in accordance with Aptara Billing and Payment Terms and Conditions, which are incorporated herein by reference.
13. Should the terms of this license be violated at any time, APS or Aptara may revoke the license with no refund to you and seek relief to the fullest extent of the laws of the USA. Official written notice will be made using the contact information provided with the permission request. Failure to receive such notice will not nullify revocation of the permission.
14. APS reserves all rights not specifically granted herein.
15. This document, including the Aptara Billing and Payment Terms and Conditions, shall be the entire agreement between the parties relating to the subject matter hereof.

SPRINGER NATURE LICENSE
TERMS AND CONDITIONS

Sep 04, 2019

This Agreement between Imperial College London -- Bernice Akpinar ("You") and Springer Nature ("Springer Nature") consists of your license details and the terms and conditions provided by Springer Nature and Copyright Clearance Center.

License Number	4661870935028
License date	Sep 04, 2019
Licensed Content Publisher	Springer Nature
Licensed Content Publication	Nature Nanotechnology
Licensed Content Title	Nanoscale stiffness topography reveals structure and mechanics of the transport barrier in intact nuclear pore complexes
Licensed Content Author	Aizhan Bestembayeva, Armin Kramer, Aksana A. Labokha, Dino Osmanović, Ivan Liashkovich et al.
Licensed Content Date	Nov 24, 2014
Licensed Content Volume	10
Licensed Content Issue	1
Type of Use	Thesis/Dissertation
Requestor type	academic/university or research institute
Format	print and electronic
Portion	figures/tables/illustrations
Number of figures/tables/illustrations	1
High-res required	no
Will you be translating?	no
Circulation/distribution	1 - 29
Author of this Springer Nature content	no
Title	The nanoscale behaviour of disordered polypeptides confined within biomimetic nuclear pore complexes
Institution name	Imperial College London
Expected presentation date	Dec 2019
Portions	Figure 1c, the rotationally symmetrized nanomechanical stiffness of a NPC
Requestor Location	Imperial College London Department of Materials, Imperial College London, South Kensington Campus London, - SW7 2AZ United Kingdom Attn: Imperial College London
Total	0.00 GBP
Terms and Conditions	

Springer Nature Customer Service Centre GmbH
Terms and Conditions

This agreement sets out the terms and conditions of the licence (the **Licence**) between you and **Springer Nature Customer Service Centre GmbH** (the **Licensor**). By clicking 'accept' and completing the transaction for the material (**Licensed Material**), you also confirm your acceptance of these terms and conditions.

1. Grant of License

1. 1. The Licensor grants you a personal, non-exclusive, non-transferable, world-wide licence to reproduce the Licensed Material for the purpose specified in your order only. Licences are granted for the specific use requested in the order and for no other use, subject to the conditions below.

1. 2. The Licensor warrants that it has, to the best of its knowledge, the rights to license reuse of the Licensed Material. However, you should ensure that the material you are requesting is original to the Licensor and does not carry the copyright of another entity (as credited in the published version).

1. 3. If the credit line on any part of the material you have requested indicates that it was reprinted or adapted with permission from another source, then you should also seek permission from that source to reuse the material.

2. Scope of Licence

2. 1. You may only use the Licensed Content in the manner and to the extent permitted by these Ts&Cs and any applicable laws.

2. 2. A separate licence may be required for any additional use of the Licensed Material, e.g. where a licence has been purchased for print only use, separate permission must be obtained for electronic re-use. Similarly, a licence is only valid in the language selected and does not apply for editions in other languages unless additional translation rights have been granted separately in the licence. Any content owned by third parties are expressly excluded from the licence.

2. 3. Similarly, rights for additional components such as custom editions and derivatives require additional permission and may be subject to an additional fee. Please apply to Journalpermissions@springernature.com/bookpermissions@springernature.com for these rights.

2. 4. Where permission has been granted **free of charge** for material in print, permission may also be granted for any electronic version of that work, provided that the material is incidental to your work as a whole and that the electronic version is essentially equivalent to, or substitutes for, the print version.

2. 5. An alternative scope of licence may apply to signatories of the STM Permissions Guidelines, as amended from time to time.

3. Duration of Licence

3. 1. A licence for is valid from the date of purchase ('Licence Date') at the end of the relevant period in the below table:

Scope of Licence	Duration of Licence
Post on a website	12 months
Presentations	12 months
Books and journals	Lifetime of the edition in the language purchased

4. Acknowledgement

4. 1. The Licensor's permission must be acknowledged next to the Licenced Material in print. In electronic form, this acknowledgement must be visible at the same time as the figures/tables/illustrations or abstract, and must be hyperlinked to the journal/book's homepage.

Our required acknowledgement format is in the Appendix below.

5. Restrictions on use

5. 1. Use of the Licensed Material may be permitted for incidental promotional use and minor editing privileges e.g. minor adaptations of single figures, changes of format, colour and/or style where the adaptation is credited as set out in Appendix 1 below. Any other changes including but not limited to, cropping, adapting, omitting material that affect the meaning, intention or moral rights of the author are strictly prohibited.

5. 2. You must not use any Licensed Material as part of any design or trademark.

5. 3. Licensed Material may be used in Open Access Publications (OAP) before publication by Springer Nature, but any Licensed Material must be removed from OAP sites prior to final publication.

6. Ownership of Rights

6. 1. Licensed Material remains the property of either Licensor or the relevant third party and any rights not explicitly granted herein are expressly reserved.

7. Warranty

IN NO EVENT SHALL LICENSOR BE LIABLE TO YOU OR ANY OTHER PARTY OR ANY OTHER PERSON OR FOR ANY SPECIAL, CONSEQUENTIAL, INCIDENTAL OR INDIRECT DAMAGES, HOWEVER CAUSED, ARISING OUT OF OR IN CONNECTION WITH THE DOWNLOADING, VIEWING OR USE OF THE MATERIALS REGARDLESS OF THE FORM OF ACTION, WHETHER FOR BREACH OF CONTRACT, BREACH OF WARRANTY, TORT, NEGLIGENCE, INFRINGEMENT OR OTHERWISE (INCLUDING, WITHOUT LIMITATION, DAMAGES BASED ON LOSS OF PROFITS, DATA, FILES, USE, BUSINESS OPPORTUNITY OR CLAIMS OF THIRD PARTIES), AND WHETHER OR NOT THE PARTY HAS BEEN ADVISED OF THE POSSIBILITY OF SUCH DAMAGES. THIS LIMITATION SHALL APPLY NOTWITHSTANDING ANY FAILURE OF ESSENTIAL PURPOSE OF ANY LIMITED REMEDY PROVIDED HEREIN.

8. Limitations

8. 1. ***BOOKS ONLY:***Where **'reuse in a dissertation/thesis'** has been selected the following terms apply: Print rights of the final author's accepted manuscript (for clarity, NOT the published version) for up to 100 copies, electronic rights for use only on a personal website or institutional repository as defined by the Sherpa guideline (www.sherpa.ac.uk/romeo/).

9. Termination and Cancellation

9. 1. Licences will expire after the period shown in Clause 3 (above).

9. 2. Licensee reserves the right to terminate the Licence in the event that payment is not received in full or if there has been a breach of this agreement by you.

Appendix 1 — Acknowledgements:

For Journal Content:
Reprinted by permission from [**the Licensor**]: [**Journal Publisher** (e.g.

Nature/Springer/Palgrave)] [**JOURNAL NAME**] [**REFERENCE CITATION** (Article name, Author(s) Name), [**COPYRIGHT**] (year of publication)

For **Advance Online Publication papers:**
Reprinted by permission from [**the Licensor**]: [**Journal Publisher** (e.g. Nature/Springer/Palgrave)] [**JOURNAL NAME**] [**REFERENCE CITATION** (Article name, Author(s) Name), [**COPYRIGHT**] (year of publication), advance online publication, day month year (doi: 10.1038/sj.[JOURNAL ACRONYM].)

For Adaptations/Translations:
Adapted/Translated by permission from [**the Licensor**]: [**Journal Publisher** (e.g. Nature/Springer/Palgrave)] [**JOURNAL NAME**] [**REFERENCE CITATION** (Article name, Author(s) Name), [**COPYRIGHT**] (year of publication)

Note: For any republication from the British Journal of Cancer, the following credit line style applies:

Reprinted/adapted/translated by permission from [**the Licensor**]: on behalf of Cancer Research UK: : [**Journal Publisher** (e.g. Nature/Springer/Palgrave)] [**JOURNAL NAME**] [**REFERENCE CITATION** (Article name, Author(s) Name), [**COPYRIGHT]** (year of publication)

For **Advance Online Publication** papers:
Reprinted by permission from The [**the Licensor**]: on behalf of Cancer Research UK: [**Journal Publisher** (e.g. Nature/Springer/Palgrave)] [**JOURNAL NAME**] [**REFERENCE CITATION** (Article name, Author(s) Name), [**COPYRIGHT**] (year of publication), advance online publication, day month year (doi: 10.1038/sj.[JOURNAL ACRONYM])

For Book content:
Reprinted/adapted by permission from [**the Licensor**]: [**Book Publisher** (e.g. Palgrave Macmillan, Springer etc) [**Book Title**] by [**Book author**(s)] [**COPYRIGHT**] (year of publication)

Other Conditions:

Version 1.2

Questions? customercare@copyright.com or +1-855-239-3415 (toll free in the US) or +1-978-646-2777.

SPRINGER NATURE LICENSE
TERMS AND CONDITIONS

Sep 04, 2019

This Agreement between Imperial College London -- Bernice Akpinar ("You") and Springer Nature ("Springer Nature") consists of your license details and the terms and conditions provided by Springer Nature and Copyright Clearance Center.

License Number	4661871474987
License date	Sep 04, 2019
Licensed Content Publisher	Springer Nature
Licensed Content Publication	Nature Nanotechnology
Licensed Content Title	Spatiotemporal dynamics of the nuclear pore complex transport barrier resolved by high-speed atomic force microscopy
Licensed Content Author	Yusuke Sakiyama, Adam Mazur, Larisa E. Kapinos, Roderick Y. H. Lim
Licensed Content Date	May 2, 2016
Licensed Content Volume	11
Licensed Content Issue	8
Type of Use	Thesis/Dissertation
Requestor type	academic/university or research institute
Format	print and electronic
Portion	figures/tables/illustrations
Number of figures/tables/illustrations	1
High-res required	no
Will you be translating?	no
Circulation/distribution	1 - 29
Author of this Springer Nature content	no
Title	The nanoscale behaviour of disordered polypeptides confined within biomimetic nuclear pore complexes
Institution name	Imperial College London
Expected presentation date	Dec 2019
Portions	Figure 2b, dynamic conformations of FG-nups
Requestor Location	Imperial College London Department of Materials, Imperial College London, South Kensington Campus London, - SW7 2AZ United Kingdom Attn: Imperial College London
Total	0.00 USD
Terms and Conditions	

Springer Nature Customer Service Centre GmbH
Terms and Conditions

This agreement sets out the terms and conditions of the licence (the **Licence**) between you and **Springer Nature Customer Service Centre GmbH** (the **Licensor**). By clicking

'accept' and completing the transaction for the material (**Licensed Material**), you also confirm your acceptance of these terms and conditions.

1. Grant of License

1. 1. The Licensor grants you a personal, non-exclusive, non-transferable, world-wide licence to reproduce the Licensed Material for the purpose specified in your order only. Licences are granted for the specific use requested in the order and for no other use, subject to the conditions below.

1. 2. The Licensor warrants that it has, to the best of its knowledge, the rights to license reuse of the Licensed Material. However, you should ensure that the material you are requesting is original to the Licensor and does not carry the copyright of another entity (as credited in the published version).

1. 3. If the credit line on any part of the material you have requested indicates that it was reprinted or adapted with permission from another source, then you should also seek permission from that source to reuse the material.

2. Scope of Licence

2. 1. You may only use the Licensed Content in the manner and to the extent permitted by these Ts&Cs and any applicable laws.

2. 2. A separate licence may be required for any additional use of the Licensed Material, e.g. where a licence has been purchased for print only use, separate permission must be obtained for electronic re-use. Similarly, a licence is only valid in the language selected and does not apply for editions in other languages unless additional translation rights have been granted separately in the licence. Any content owned by third parties are expressly excluded from the licence.

2. 3. Similarly, rights for additional components such as custom editions and derivatives require additional permission and may be subject to an additional fee. Please apply to Journalpermissions@springernature.com/bookpermissions@springernature.com for these rights.

2. 4. Where permission has been granted **free of charge** for material in print, permission may also be granted for any electronic version of that work, provided that the material is incidental to your work as a whole and that the electronic version is essentially equivalent to, or substitutes for, the print version.

2. 5. An alternative scope of licence may apply to signatories of the STM Permissions Guidelines, as amended from time to time.

3. Duration of Licence

3. 1. A licence for is valid from the date of purchase ('Licence Date') at the end of the relevant period in the below table:

Scope of Licence	Duration of Licence
Post on a website	12 months
Presentations	12 months
Books and journals	Lifetime of the edition in the language purchased

4. Acknowledgement

4. 1. The Licensor's permission must be acknowledged next to the Licenced Material in print. In electronic form, this acknowledgement must be visible at the same time as the figures/tables/illustrations or abstract, and must be hyperlinked to the journal/book's homepage. Our required acknowledgement format is in the Appendix below.

5. Restrictions on use

5. 1. Use of the Licensed Material may be permitted for incidental promotional use and minor editing privileges e.g. minor adaptations of single figures, changes of format, colour and/or style where the adaptation is credited as set out in Appendix 1 below. Any other changes including but not limited to, cropping, adapting, omitting material that affect the meaning, intention or moral rights of the author are strictly prohibited.

5. 2. You must not use any Licensed Material as part of any design or trademark.

5. 3. Licensed Material may be used in Open Access Publications (OAP) before publication by Springer Nature, but any Licensed Material must be removed from OAP sites prior to final publication.

6. Ownership of Rights

6. 1. Licensed Material remains the property of either Licensor or the relevant third party and any rights not explicitly granted herein are expressly reserved.

7. Warranty

IN NO EVENT SHALL LICENSOR BE LIABLE TO YOU OR ANY OTHER PARTY OR ANY OTHER PERSON OR FOR ANY SPECIAL, CONSEQUENTIAL, INCIDENTAL OR INDIRECT DAMAGES, HOWEVER CAUSED, ARISING OUT OF OR IN CONNECTION WITH THE DOWNLOADING, VIEWING OR USE OF THE MATERIALS REGARDLESS OF THE FORM OF ACTION, WHETHER FOR BREACH OF CONTRACT, BREACH OF WARRANTY, TORT, NEGLIGENCE, INFRINGEMENT OR OTHERWISE (INCLUDING, WITHOUT LIMITATION, DAMAGES BASED ON LOSS OF PROFITS, DATA, FILES, USE, BUSINESS OPPORTUNITY OR CLAIMS OF THIRD PARTIES), AND
WHETHER OR NOT THE PARTY HAS BEEN ADVISED OF THE POSSIBILITY OF SUCH DAMAGES. THIS LIMITATION SHALL APPLY NOTWITHSTANDING ANY FAILURE OF ESSENTIAL PURPOSE OF ANY LIMITED REMEDY PROVIDED HEREIN.

8. Limitations

8. 1. ***BOOKS ONLY:***Where **'reuse in a dissertation/thesis'** has been selected the following terms apply: Print rights of the final author's accepted manuscript (for clarity, NOT the published version) for up to 100 copies, electronic rights for use only on a personal website or institutional repository as defined by the Sherpa guideline (www.sherpa.ac.uk/romeo/).

9. Termination and Cancellation

9. 1. Licences will expire after the period shown in Clause 3 (above).

9. 2. Licensee reserves the right to terminate the Licence in the event that payment is not received in full or if there has been a breach of this agreement by you.

Appendix 1 — Acknowledgements:

For Journal Content:
Reprinted by permission from [**the Licensor**]: [**Journal Publisher** (e.g.

Nature/Springer/Palgrave)] [**JOURNAL NAME**] [**REFERENCE CITATION** (Article name, Author(s) Name), [**COPYRIGHT**] (year of publication)

For **Advance Online Publication papers:**
Reprinted by permission from [**the Licensor**]: [**Journal Publisher** (e.g. Nature/Springer/Palgrave)] [**JOURNAL NAME**] [**REFERENCE CITATION** (Article name, Author(s) Name), [**COPYRIGHT**] (year of publication), advance online publication, day month year (doi: 10.1038/sj.[JOURNAL ACRONYM].)

For Adaptations/Translations:
Adapted/Translated by permission from [**the Licensor**]: [**Journal Publisher** (e.g. Nature/Springer/Palgrave)] [**JOURNAL NAME**] [**REFERENCE CITATION** (Article name, Author(s) Name), [**COPYRIGHT**] (year of publication)

Note: For any republication from the British Journal of Cancer, the following credit line style applies:

Reprinted/adapted/translated by permission from [**the Licensor**]: on behalf of Cancer Research UK: : [**Journal Publisher** (e.g. Nature/Springer/Palgrave)] [**JOURNAL NAME**] [**REFERENCE CITATION** (Article name, Author(s) Name), [**COPYRIGHT]** (year of publication)

For **Advance Online Publication** papers:
Reprinted by permission from The [**the Licensor**]: on behalf of Cancer Research UK: [**Journal Publisher** (e.g. Nature/Springer/Palgrave)] [**JOURNAL NAME**] [**REFERENCE CITATION** (Article name, Author(s) Name), [**COPYRIGHT**] (year of publication), advance online publication, day month year (doi: 10.1038/sj.[JOURNAL ACRONYM])

For Book content:
Reprinted/adapted by permission from [**the Licensor**]: [**Book Publisher** (e.g. Palgrave Macmillan, Springer etc) [**Book Title**] by [**Book author**(s)] [**COPYRIGHT**] (year of publication)

Other Conditions:

Version 1.2

Questions? customercare@copyright.com or +1-855-239-3415 (toll free in the US) or +1-978-646-2777.

SPRINGER NATURE LICENSE
TERMS AND CONDITIONS

Sep 04, 2019

This Agreement between Imperial College London -- Bernice Akpinar ("You") and Springer Nature ("Springer Nature") consists of your license details and the terms and conditions provided by Springer Nature and Copyright Clearance Center.

License Number	4661910037285
License date	Sep 04, 2019
Licensed Content Publisher	Springer Nature
Licensed Content Publication	Nature
Licensed Content Title	Artificial nanopores that mimic the transport selectivity of the nuclear pore complex
Licensed Content Author	Tijana Jovanovic-Talisman, Jaclyn Tetenbaum-Novatt, Anna Sophia McKenney, Anton Zilman, Reiner Peters et al.
Licensed Content Date	Dec 21, 2008
Licensed Content Volume	457
Licensed Content Issue	7232
Type of Use	Thesis/Dissertation
Requestor type	academic/university or research institute
Format	print and electronic
Portion	figures/tables/illustrations
Number of figures/tables/illustrations	2
High-res required	no
Will you be translating?	no
Circulation/distribution	1 - 29
Author of this Springer Nature content	no
Title	The nanoscale behaviour of disordered polypeptides confined within biomimetic nuclear pore complexes
Institution name	Imperial College London
Expected presentation date	Dec 2019
Portions	Figure 2b, a graph to show the coated nanopores permit the entry of Kap molecules but exclude BSA molecules. Supplementary figure 2c, TEM image showing the coated nanopores, with accompanying schematic.
Requestor Location	Imperial College London Department of Materials, Imperial College London, South Kensington Campus London, - SW7 2AZ United Kingdom Attn: Imperial College London
Total	0.00 USD
Terms and Conditions	

Springer Nature Customer Service Centre GmbH
Terms and Conditions

This agreement sets out the terms and conditions of the licence (the **Licence**) between you and **Springer Nature Customer Service Centre GmbH** (the **Licensor**). By clicking 'accept' and completing the transaction for the material (**Licensed Material**), you also confirm your acceptance of these terms and conditions.

1. Grant of License

1. 1. The Licensor grants you a personal, non-exclusive, non-transferable, world-wide licence to reproduce the Licensed Material for the purpose specified in your order only. Licences are granted for the specific use requested in the order and for no other use, subject to the conditions below.

1. 2. The Licensor warrants that it has, to the best of its knowledge, the rights to license reuse of the Licensed Material. However, you should ensure that the material you are requesting is original to the Licensor and does not carry the copyright of another entity (as credited in the published version).

1. 3. If the credit line on any part of the material you have requested indicates that it was reprinted or adapted with permission from another source, then you should also seek permission from that source to reuse the material.

2. Scope of Licence

2. 1. You may only use the Licensed Content in the manner and to the extent permitted by these Ts&Cs and any applicable laws.

2. 2. A separate licence may be required for any additional use of the Licensed Material, e.g. where a licence has been purchased for print only use, separate permission must be obtained for electronic re-use. Similarly, a licence is only valid in the language selected and does not apply for editions in other languages unless additional translation rights have been granted separately in the licence. Any content owned by third parties are expressly excluded from the licence.

2. 3. Similarly, rights for additional components such as custom editions and derivatives require additional permission and may be subject to an additional fee. Please apply to Journalpermissions@springernature.com/bookpermissions@springernature.com for these rights.

2. 4. Where permission has been granted **free of charge** for material in print, permission may also be granted for any electronic version of that work, provided that the material is incidental to your work as a whole and that the electronic version is essentially equivalent to, or substitutes for, the print version.

2. 5. An alternative scope of licence may apply to signatories of the STM Permissions Guidelines, as amended from time to time.

3. Duration of Licence

3. 1. A licence for is valid from the date of purchase ('Licence Date') at the end of the relevant period in the below table:

Scope of Licence	Duration of Licence
Post on a website	12 months
Presentations	12 months
Books and journals	Lifetime of the edition in the language purchased

4. Acknowledgement

4. 1. The Licensor's permission must be acknowledged next to the Licenced Material in print. In electronic form, this acknowledgement must be visible at the same time as the figures/tables/illustrations or abstract, and must be hyperlinked to the journal/book's homepage. Our required acknowledgement format is in the Appendix below.

5. Restrictions on use

5. 1. Use of the Licensed Material may be permitted for incidental promotional use and minor editing privileges e.g. minor adaptations of single figures, changes of format, colour and/or style where the adaptation is credited as set out in Appendix 1 below. Any other changes including but not limited to, cropping, adapting, omitting material that affect the meaning, intention or moral rights of the author are strictly prohibited.

5. 2. You must not use any Licensed Material as part of any design or trademark.

5. 3. Licensed Material may be used in Open Access Publications (OAP) before publication by Springer Nature, but any Licensed Material must be removed from OAP sites prior to final publication.

6. Ownership of Rights

6. 1. Licensed Material remains the property of either Licensor or the relevant third party and any rights not explicitly granted herein are expressly reserved.

7. Warranty

IN NO EVENT SHALL LICENSOR BE LIABLE TO YOU OR ANY OTHER PARTY OR ANY OTHER PERSON OR FOR ANY SPECIAL, CONSEQUENTIAL, INCIDENTAL OR INDIRECT DAMAGES, HOWEVER CAUSED, ARISING OUT OF OR IN CONNECTION WITH THE DOWNLOADING, VIEWING OR USE OF THE MATERIALS REGARDLESS OF THE FORM OF ACTION, WHETHER FOR BREACH OF CONTRACT, BREACH OF WARRANTY, TORT, NEGLIGENCE, INFRINGEMENT OR OTHERWISE (INCLUDING, WITHOUT LIMITATION, DAMAGES BASED ON LOSS OF PROFITS, DATA, FILES, USE, BUSINESS OPPORTUNITY OR CLAIMS OF THIRD PARTIES), AND
WHETHER OR NOT THE PARTY HAS BEEN ADVISED OF THE POSSIBILITY OF SUCH DAMAGES. THIS LIMITATION SHALL APPLY NOTWITHSTANDING ANY FAILURE OF ESSENTIAL PURPOSE OF ANY LIMITED REMEDY PROVIDED HEREIN.

8. Limitations

8. 1. ***BOOKS ONLY:***Where **'reuse in a dissertation/thesis'** has been selected the following terms apply: Print rights of the final author's accepted manuscript (for clarity, NOT the published version) for up to 100 copies, electronic rights for use only on a personal website or institutional repository as defined by the Sherpa guideline (www.sherpa.ac.uk/romeo/).

9. Termination and Cancellation

9. 1. Licences will expire after the period shown in Clause 3 (above).

9. 2. Licensee reserves the right to terminate the Licence in the event that payment is not received in full or if there has been a breach of this agreement by you.

Appendix 1 — Acknowledgements:

For Journal Content:
Reprinted by permission from [**the Licensor**]: [**Journal Publisher** (e.g. Nature/Springer/Palgrave)] [**JOURNAL NAME**] [**REFERENCE CITATION** (Article name, Author(s) Name), [**COPYRIGHT**] (year of publication)

For **Advance Online Publication papers:**
Reprinted by permission from [**the Licensor**]: [**Journal Publisher** (e.g. Nature/Springer/Palgrave)] [**JOURNAL NAME**] [**REFERENCE CITATION** (Article name, Author(s) Name), [**COPYRIGHT**] (year of publication), advance online publication, day month year (doi: 10.1038/sj.[JOURNAL ACRONYM].)

For Adaptations/Translations:
Adapted/Translated by permission from [**the Licensor**]: [**Journal Publisher** (e.g. Nature/Springer/Palgrave)] [**JOURNAL NAME**] [**REFERENCE CITATION** (Article name, Author(s) Name), [**COPYRIGHT**] (year of publication)

Note: For any republication from the British Journal of Cancer, the following credit line style applies:

Reprinted/adapted/translated by permission from [**the Licensor**]: on behalf of Cancer Research UK: : [**Journal Publisher** (e.g. Nature/Springer/Palgrave)] [**JOURNAL NAME**] [**REFERENCE CITATION** (Article name, Author(s) Name), [**COPYRIGHT]** (year of publication)

For **Advance Online Publication** papers:
Reprinted by permission from The [**the Licensor**]: on behalf of Cancer Research UK: [**Journal Publisher** (e.g. Nature/Springer/Palgrave)] [**JOURNAL NAME**] [**REFERENCE CITATION** (Article name, Author(s) Name), [**COPYRIGHT**] (year of publication), advance online publication, day month year (doi: 10.1038/sj.[JOURNAL ACRONYM])

For Book content:
Reprinted/adapted by permission from [**the Licensor**]: [**Book Publisher** (e.g. Palgrave Macmillan, Springer etc) [**Book Title**] by [**Book author**(s)] [**COPYRIGHT**] (year of publication)

Other Conditions:

Version 1.2

Questions? customercare@copyright.com or +1-855-239-3415 (toll free in the US) or +1-978-646-2777.

SPRINGER NATURE LICENSE
TERMS AND CONDITIONS

Sep 04, 2019

This Agreement between Imperial College London -- Bernice Akpinar ("You") and Springer Nature ("Springer Nature") consists of your license details and the terms and conditions provided by Springer Nature and Copyright Clearance Center.

License Number	4661910749567
License date	Sep 04, 2019
Licensed Content Publisher	Springer Nature
Licensed Content Publication	Nature Nanotechnology
Licensed Content Title	Single-molecule transport across an individual biomimetic nuclear pore complex
Licensed Content Author	Stefan W. Kowalczyk, Larisa Kapinos, Timothy R. Blosser, Tomás Magalhães, Pauline van Nies et al.
Licensed Content Date	Jun 19, 2011
Licensed Content Volume	6
Licensed Content Issue	7
Type of Use	Thesis/Dissertation
Requestor type	academic/university or research institute
Format	print and electronic
Portion	figures/tables/illustrations
Number of figures/tables/illustrations	2
High-res required	no
Will you be translating?	no
Circulation/distribution	1 - 29
Author of this Springer Nature content	no
Title	The nanoscale behaviour of disordered polypeptides confined within biomimetic nuclear pore complexes
Institution name	Imperial College London
Expected presentation date	Dec 2019
Portions	Figure 1b and c, Sketch to show the experimental setup of the biomimetic NPC along with TEM images showing uncoated and coated nanopores. Figure 4, graphs showing the coated nanopores are effective at replicating NPC selectivity.
Requestor Location	Imperial College London Department of Materials, Imperial College London, South Kensington Campus London, - SW7 2AZ United Kingdom Attn: Imperial College London
Total	0.00 USD
Terms and Conditions	

Springer Nature Customer Service Centre GmbH
Terms and Conditions

This agreement sets out the terms and conditions of the licence (the **Licence**) between you and **Springer Nature Customer Service Centre GmbH** (the **Licensor**). By clicking 'accept' and completing the transaction for the material (**Licensed Material**), you also confirm your acceptance of these terms and conditions.

1. Grant of License

1. 1. The Licensor grants you a personal, non-exclusive, non-transferable, world-wide licence to reproduce the Licensed Material for the purpose specified in your order only. Licences are granted for the specific use requested in the order and for no other use, subject to the conditions below.

1. 2. The Licensor warrants that it has, to the best of its knowledge, the rights to license reuse of the Licensed Material. However, you should ensure that the material you are requesting is original to the Licensor and does not carry the copyright of another entity (as credited in the published version).

1. 3. If the credit line on any part of the material you have requested indicates that it was reprinted or adapted with permission from another source, then you should also seek permission from that source to reuse the material.

2. Scope of Licence

2. 1. You may only use the Licensed Content in the manner and to the extent permitted by these Ts&Cs and any applicable laws.

2. 2. A separate licence may be required for any additional use of the Licensed Material, e.g. where a licence has been purchased for print only use, separate permission must be obtained for electronic re-use. Similarly, a licence is only valid in the language selected and does not apply for editions in other languages unless additional translation rights have been granted separately in the licence. Any content owned by third parties are expressly excluded from the licence.

2. 3. Similarly, rights for additional components such as custom editions and derivatives require additional permission and may be subject to an additional fee. Please apply to Journalpermissions@springernature.com/bookpermissions@springernature.com for these rights.

2. 4. Where permission has been granted **free of charge** for material in print, permission may also be granted for any electronic version of that work, provided that the material is incidental to your work as a whole and that the electronic version is essentially equivalent to, or substitutes for, the print version.

2. 5. An alternative scope of licence may apply to signatories of the STM Permissions Guidelines, as amended from time to time.

3. Duration of Licence

3. 1. A licence for is valid from the date of purchase ('Licence Date') at the end of the relevant period in the below table:

Scope of Licence	Duration of Licence
Post on a website	12 months
Presentations	12 months
Books and journals	Lifetime of the edition in the language purchased

4. Acknowledgement

4. 1. The Licensor's permission must be acknowledged next to the Licenced Material in print. In electronic form, this acknowledgement must be visible at the same time as the figures/tables/illustrations or abstract, and must be hyperlinked to the journal/book's homepage. Our required acknowledgement format is in the Appendix below.

5. Restrictions on use

5. 1. Use of the Licensed Material may be permitted for incidental promotional use and minor editing privileges e.g. minor adaptations of single figures, changes of format, colour and/or style where the adaptation is credited as set out in Appendix 1 below. Any other changes including but not limited to, cropping, adapting, omitting material that affect the meaning, intention or moral rights of the author are strictly prohibited.

5. 2. You must not use any Licensed Material as part of any design or trademark.

5. 3. Licensed Material may be used in Open Access Publications (OAP) before publication by Springer Nature, but any Licensed Material must be removed from OAP sites prior to final publication.

6. Ownership of Rights

6. 1. Licensed Material remains the property of either Licensor or the relevant third party and any rights not explicitly granted herein are expressly reserved.

7. Warranty

IN NO EVENT SHALL LICENSOR BE LIABLE TO YOU OR ANY OTHER PARTY OR ANY OTHER PERSON OR FOR ANY SPECIAL, CONSEQUENTIAL, INCIDENTAL OR INDIRECT DAMAGES, HOWEVER CAUSED, ARISING OUT OF OR IN CONNECTION WITH THE DOWNLOADING, VIEWING OR USE OF THE MATERIALS REGARDLESS OF THE FORM OF ACTION, WHETHER FOR BREACH OF CONTRACT, BREACH OF WARRANTY, TORT, NEGLIGENCE, INFRINGEMENT OR OTHERWISE (INCLUDING, WITHOUT LIMITATION, DAMAGES BASED ON LOSS OF PROFITS, DATA, FILES, USE, BUSINESS OPPORTUNITY OR CLAIMS OF THIRD PARTIES), AND WHETHER OR NOT THE PARTY HAS BEEN ADVISED OF THE POSSIBILITY OF SUCH DAMAGES. THIS LIMITATION SHALL APPLY NOTWITHSTANDING ANY FAILURE OF ESSENTIAL PURPOSE OF ANY LIMITED REMEDY PROVIDED HEREIN.

8. Limitations

8. 1. ***BOOKS ONLY:***Where **'reuse in a dissertation/thesis'** has been selected the following terms apply: Print rights of the final author's accepted manuscript (for clarity, NOT the published version) for up to 100 copies, electronic rights for use only on a personal website or institutional repository as defined by the Sherpa guideline (www.sherpa.ac.uk/romeo/).

9. Termination and Cancellation

9. 1. Licences will expire after the period shown in Clause 3 (above).

9. 2. Licensee reserves the right to terminate the Licence in the event that payment is not received in full or if there has been a breach of this agreement by you.

Appendix 1 — Acknowledgements:

For Journal Content:
Reprinted by permission from [**the Licensor**]: [**Journal Publisher** (e.g. Nature/Springer/Palgrave)] [**JOURNAL NAME**] [**REFERENCE CITATION** (Article name, Author(s) Name), [**COPYRIGHT**] (year of publication)

For **Advance Online Publication papers:**
Reprinted by permission from [**the Licensor**]: [**Journal Publisher** (e.g. Nature/Springer/Palgrave)] [**JOURNAL NAME**] [**REFERENCE CITATION** (Article name, Author(s) Name), [**COPYRIGHT**] (year of publication), advance online publication, day month year (doi: 10.1038/sj.[JOURNAL ACRONYM].)

For Adaptations/Translations:
Adapted/Translated by permission from [**the Licensor**]: [**Journal Publisher** (e.g. Nature/Springer/Palgrave)] [**JOURNAL NAME**] [**REFERENCE CITATION** (Article name, Author(s) Name), [**COPYRIGHT**] (year of publication)

Note: For any republication from the British Journal of Cancer, the following credit line style applies:

Reprinted/adapted/translated by permission from [**the Licensor**]: on behalf of Cancer Research UK: : [**Journal Publisher** (e.g. Nature/Springer/Palgrave)] [**JOURNAL NAME**] [**REFERENCE CITATION** (Article name, Author(s) Name), [**COPYRIGHT**] (year of publication)

For **Advance Online Publication** papers:
Reprinted by permission from The [**the Licensor**]: on behalf of Cancer Research UK: [**Journal Publisher** (e.g. Nature/Springer/Palgrave)] [**JOURNAL NAME**] [**REFERENCE CITATION** (Article name, Author(s) Name), [**COPYRIGHT**] (year of publication), advance online publication, day month year (doi: 10.1038/sj.[JOURNAL ACRONYM])

For Book content:
Reprinted/adapted by permission from [**the Licensor**]: [**Book Publisher** (e.g. Palgrave Macmillan, Springer etc) [**Book Title**] by [**Book author**(s)] [**COPYRIGHT**] (year of publication)

Other Conditions:

Version 1.2

Questions? customercare@copyright.com or +1-855-239-3415 (toll free in the US) or +1-978-646-2777.

SPRINGER NATURE LICENSE
TERMS AND CONDITIONS

Sep 04, 2019

This Agreement between Imperial College London -- Bernice Akpinar ("You") and Springer Nature ("Springer Nature") consists of your license details and the terms and conditions provided by Springer Nature and Copyright Clearance Center.

License Number	4661911173929
License date	Sep 04, 2019
Licensed Content Publisher	Springer Nature
Licensed Content Publication	Nature
Licensed Content Title	Folding DNA to create nanoscale shapes and patterns
Licensed Content Author	Paul W. K. Rothemund
Licensed Content Date	Mar 16, 2006
Type of Use	Thesis/Dissertation
Requestor type	academic/university or research institute
Format	print and electronic
Portion	figures/tables/illustrations
Number of figures/tables/illustrations	2
High-res required	no
Will you be translating?	no
Circulation/distribution	1 - 29
Author of this Springer Nature content	no
Title	The nanoscale behaviour of disordered polypeptides confined within biomimetic nuclear pore complexes
Institution name	Imperial College London
Expected presentation date	Dec 2019
Portions	Figure 1e - schematic showing the design of DNA origami Figure 2d - Folding path and AFM image of the DNA origami smiley face
Requestor Location	Imperial College London Department of Materials, Imperial College London, South Kensington Campus London, - SW7 2AZ United Kingdom Attn: Imperial College London
Total	0.00 USD
Terms and Conditions	

Springer Nature Customer Service Centre GmbH
Terms and Conditions

This agreement sets out the terms and conditions of the licence (the **Licence**) between you and **Springer Nature Customer Service Centre GmbH** (the **Licensor**). By clicking

'accept' and completing the transaction for the material (**Licensed Material**), you also confirm your acceptance of these terms and conditions.

1. Grant of License

1. 1. The Licensor grants you a personal, non-exclusive, non-transferable, world-wide licence to reproduce the Licensed Material for the purpose specified in your order only. Licences are granted for the specific use requested in the order and for no other use, subject to the conditions below.

1. 2. The Licensor warrants that it has, to the best of its knowledge, the rights to license reuse of the Licensed Material. However, you should ensure that the material you are requesting is original to the Licensor and does not carry the copyright of another entity (as credited in the published version).

1. 3. If the credit line on any part of the material you have requested indicates that it was reprinted or adapted with permission from another source, then you should also seek permission from that source to reuse the material.

2. Scope of Licence

2. 1. You may only use the Licensed Content in the manner and to the extent permitted by these Ts&Cs and any applicable laws.

2. 2. A separate licence may be required for any additional use of the Licensed Material, e.g. where a licence has been purchased for print only use, separate permission must be obtained for electronic re-use. Similarly, a licence is only valid in the language selected and does not apply for editions in other languages unless additional translation rights have been granted separately in the licence. Any content owned by third parties are expressly excluded from the licence.

2. 3. Similarly, rights for additional components such as custom editions and derivatives require additional permission and may be subject to an additional fee. Please apply to Journalpermissions@springernature.com/bookpermissions@springernature.com for these rights.

2. 4. Where permission has been granted **free of charge** for material in print, permission may also be granted for any electronic version of that work, provided that the material is incidental to your work as a whole and that the electronic version is essentially equivalent to, or substitutes for, the print version.

2. 5. An alternative scope of licence may apply to signatories of the STM Permissions Guidelines, as amended from time to time.

3. Duration of Licence

3. 1. A licence for is valid from the date of purchase ('Licence Date') at the end of the relevant period in the below table:

Scope of Licence	Duration of Licence
Post on a website	12 months
Presentations	12 months
Books and journals	Lifetime of the edition in the language purchased

4. Acknowledgement

4. 1. The Licensor's permission must be acknowledged next to the Licenced Material in print. In electronic form, this acknowledgement must be visible at the same time as the figures/tables/illustrations or abstract, and must be hyperlinked to the journal/book's homepage. Our required acknowledgement format is in the Appendix below.

5. Restrictions on use

5. 1. Use of the Licensed Material may be permitted for incidental promotional use and minor editing privileges e.g. minor adaptations of single figures, changes of format, colour and/or style where the adaptation is credited as set out in Appendix 1 below. Any other changes including but not limited to, cropping, adapting, omitting material that affect the meaning, intention or moral rights of the author are strictly prohibited.

5. 2. You must not use any Licensed Material as part of any design or trademark.

5. 3. Licensed Material may be used in Open Access Publications (OAP) before publication by Springer Nature, but any Licensed Material must be removed from OAP sites prior to final publication.

6. Ownership of Rights

6. 1. Licensed Material remains the property of either Licensor or the relevant third party and any rights not explicitly granted herein are expressly reserved.

7. Warranty

IN NO EVENT SHALL LICENSOR BE LIABLE TO YOU OR ANY OTHER PARTY OR ANY OTHER PERSON OR FOR ANY SPECIAL, CONSEQUENTIAL, INCIDENTAL OR INDIRECT DAMAGES, HOWEVER CAUSED, ARISING OUT OF OR IN CONNECTION WITH THE DOWNLOADING, VIEWING OR USE OF THE MATERIALS REGARDLESS OF THE FORM OF ACTION, WHETHER FOR BREACH OF CONTRACT, BREACH OF WARRANTY, TORT, NEGLIGENCE, INFRINGEMENT OR OTHERWISE (INCLUDING, WITHOUT LIMITATION, DAMAGES BASED ON LOSS OF PROFITS, DATA, FILES, USE, BUSINESS OPPORTUNITY OR CLAIMS OF THIRD PARTIES), AND
WHETHER OR NOT THE PARTY HAS BEEN ADVISED OF THE POSSIBILITY OF SUCH DAMAGES. THIS LIMITATION SHALL APPLY NOTWITHSTANDING ANY FAILURE OF ESSENTIAL PURPOSE OF ANY LIMITED REMEDY PROVIDED HEREIN.

8. Limitations

8. 1. ***BOOKS ONLY:***Where **'reuse in a dissertation/thesis'** has been selected the following terms apply: Print rights of the final author's accepted manuscript (for clarity, NOT the published version) for up to 100 copies, electronic rights for use only on a personal website or institutional repository as defined by the Sherpa guideline (www.sherpa.ac.uk/romeo/).

9. Termination and Cancellation

9. 1. Licences will expire after the period shown in Clause 3 (above).

9. 2. Licensee reserves the right to terminate the Licence in the event that payment is not received in full or if there has been a breach of this agreement by you.

Appendix 1 — Acknowledgements:

For Journal Content:
Reprinted by permission from [**the Licensor**]: [**Journal Publisher** (e.g.

Nature/Springer/Palgrave)] [**JOURNAL NAME**] [**REFERENCE CITATION** (Article name, Author(s) Name), [**COPYRIGHT**] (year of publication)

For **Advance Online Publication papers:**
Reprinted by permission from [**the Licensor**]: [**Journal Publisher** (e.g. Nature/Springer/Palgrave)] [**JOURNAL NAME**] [**REFERENCE CITATION** (Article name, Author(s) Name), [**COPYRIGHT**] (year of publication), advance online publication, day month year (doi: 10.1038/sj.[JOURNAL ACRONYM].)

For Adaptations/Translations:
Adapted/Translated by permission from [**the Licensor**]: [**Journal Publisher** (e.g. Nature/Springer/Palgrave)] [**JOURNAL NAME**] [**REFERENCE CITATION** (Article name, Author(s) Name), [**COPYRIGHT**] (year of publication)

Note: For any republication from the British Journal of Cancer, the following credit line style applies:

Reprinted/adapted/translated by permission from [**the Licensor**]: on behalf of Cancer Research UK: : [**Journal Publisher** (e.g. Nature/Springer/Palgrave)] [**JOURNAL NAME**] [**REFERENCE CITATION** (Article name, Author(s) Name), [**COPYRIGHT]** (year of publication)

For **Advance Online Publication** papers:
Reprinted by permission from The [**the Licensor**]: on behalf of Cancer Research UK: [**Journal Publisher** (e.g. Nature/Springer/Palgrave)] [**JOURNAL NAME**] [**REFERENCE CITATION** (Article name, Author(s) Name), [**COPYRIGHT**] (year of publication), advance online publication, day month year (doi: 10.1038/sj.[JOURNAL ACRONYM])

For Book content:
Reprinted/adapted by permission from [**the Licensor**]: [**Book Publisher** (e.g. Palgrave Macmillan, Springer etc) [**Book Title**] by [**Book author**(s)] [**COPYRIGHT**] (year of publication)

Other Conditions:

Version 1.2

Questions? customercare@copyright.com or +1-855-239-3415 (toll free in the US) or +1-978-646-2777.

SPRINGER NATURE LICENSE
TERMS AND CONDITIONS

Sep 04, 2019

This Agreement between Imperial College London -- Bernice Akpinar ("You") and Springer Nature ("Springer Nature") consists of your license details and the terms and conditions provided by Springer Nature and Copyright Clearance Center.

License Number	4661920113961
License date	Sep 04, 2019
Licensed Content Publisher	Springer Nature
Licensed Content Publication	Nature
Licensed Content Title	Self-assembly of DNA into nanoscale three-dimensional shapes
Licensed Content Author	Shawn M. Douglas, Hendrik Dietz, Tim Liedl, Björn Högberg, Franziska Graf et al.
Licensed Content Date	May 21, 2009
Licensed Content Volume	459
Licensed Content Issue	7245
Type of Use	Thesis/Dissertation
Requestor type	academic/university or research institute
Format	print and electronic
Portion	figures/tables/illustrations
Number of figures/tables/illustrations	2
High-res required	no
Will you be translating?	no
Circulation/distribution	1 - 29
Author of this Springer Nature content	no
Title	The nanoscale behaviour of disordered polypeptides confined within biomimetic nuclear pore complexes
Institution name	Imperial College London
Expected presentation date	Dec 2019
Portions	Figure 1 - The design of three-dimensional DNA origami Figure 2a - Projection and TEM image of a 3D DNA origami structure
Requestor Location	Imperial College London Department of Materials, Imperial College London, South Kensington Campus London, - SW7 2AZ United Kingdom Attn: Imperial College London
Total	0.00 USD
Terms and Conditions	

Springer Nature Customer Service Centre GmbH
Terms and Conditions

This agreement sets out the terms and conditions of the licence (the **Licence**) between you and **Springer Nature Customer Service Centre GmbH** (the **Licensor**). By clicking

'accept' and completing the transaction for the material (**Licensed Material**), you also confirm your acceptance of these terms and conditions.

1. Grant of License

1. 1. The Licensor grants you a personal, non-exclusive, non-transferable, world-wide licence to reproduce the Licensed Material for the purpose specified in your order only. Licences are granted for the specific use requested in the order and for no other use, subject to the conditions below.

1. 2. The Licensor warrants that it has, to the best of its knowledge, the rights to license reuse of the Licensed Material. However, you should ensure that the material you are requesting is original to the Licensor and does not carry the copyright of another entity (as credited in the published version).

1. 3. If the credit line on any part of the material you have requested indicates that it was reprinted or adapted with permission from another source, then you should also seek permission from that source to reuse the material.

2. Scope of Licence

2. 1. You may only use the Licensed Content in the manner and to the extent permitted by these Ts&Cs and any applicable laws.

2. 2. A separate licence may be required for any additional use of the Licensed Material, e.g. where a licence has been purchased for print only use, separate permission must be obtained for electronic re-use. Similarly, a licence is only valid in the language selected and does not apply for editions in other languages unless additional translation rights have been granted separately in the licence. Any content owned by third parties are expressly excluded from the licence.

2. 3. Similarly, rights for additional components such as custom editions and derivatives require additional permission and may be subject to an additional fee. Please apply to Journalpermissions@springernature.com/bookpermissions@springernature.com for these rights.

2. 4. Where permission has been granted **free of charge** for material in print, permission may also be granted for any electronic version of that work, provided that the material is incidental to your work as a whole and that the electronic version is essentially equivalent to, or substitutes for, the print version.

2. 5. An alternative scope of licence may apply to signatories of the STM Permissions Guidelines, as amended from time to time.

3. Duration of Licence

3. 1. A licence for is valid from the date of purchase ('Licence Date') at the end of the relevant period in the below table:

Scope of Licence	Duration of Licence
Post on a website	12 months
Presentations	12 months
Books and journals	Lifetime of the edition in the language purchased

4. Acknowledgement

4. 1. The Licensor's permission must be acknowledged next to the Licenced Material in print. In electronic form, this acknowledgement must be visible at the same time as the figures/tables/illustrations or abstract, and must be hyperlinked to the journal/book's homepage. Our required acknowledgement format is in the Appendix below.

5. Restrictions on use

5. 1. Use of the Licensed Material may be permitted for incidental promotional use and minor editing privileges e.g. minor adaptations of single figures, changes of format, colour and/or style where the adaptation is credited as set out in Appendix 1 below. Any other changes including but not limited to, cropping, adapting, omitting material that affect the meaning, intention or moral rights of the author are strictly prohibited.

5. 2. You must not use any Licensed Material as part of any design or trademark.

5. 3. Licensed Material may be used in Open Access Publications (OAP) before publication by Springer Nature, but any Licensed Material must be removed from OAP sites prior to final publication.

6. Ownership of Rights

6. 1. Licensed Material remains the property of either Licensor or the relevant third party and any rights not explicitly granted herein are expressly reserved.

7. Warranty

IN NO EVENT SHALL LICENSOR BE LIABLE TO YOU OR ANY OTHER PARTY OR ANY OTHER PERSON OR FOR ANY SPECIAL, CONSEQUENTIAL, INCIDENTAL OR INDIRECT DAMAGES, HOWEVER CAUSED, ARISING OUT OF OR IN CONNECTION WITH THE DOWNLOADING, VIEWING OR USE OF THE MATERIALS REGARDLESS OF THE FORM OF ACTION, WHETHER FOR BREACH OF CONTRACT, BREACH OF WARRANTY, TORT, NEGLIGENCE, INFRINGEMENT OR OTHERWISE (INCLUDING, WITHOUT LIMITATION, DAMAGES BASED ON LOSS OF PROFITS, DATA, FILES, USE, BUSINESS OPPORTUNITY OR CLAIMS OF THIRD PARTIES), AND
WHETHER OR NOT THE PARTY HAS BEEN ADVISED OF THE POSSIBILITY OF SUCH DAMAGES. THIS LIMITATION SHALL APPLY NOTWITHSTANDING ANY FAILURE OF ESSENTIAL PURPOSE OF ANY LIMITED REMEDY PROVIDED HEREIN.

8. Limitations

8. 1. ***BOOKS ONLY:***Where **'reuse in a dissertation/thesis'** has been selected the following terms apply: Print rights of the final author's accepted manuscript (for clarity, NOT the published version) for up to 100 copies, electronic rights for use only on a personal website or institutional repository as defined by the Sherpa guideline (www.sherpa.ac.uk/romeo/).

9. Termination and Cancellation

9. 1. Licences will expire after the period shown in Clause 3 (above).

9. 2. Licensee reserves the right to terminate the Licence in the event that payment is not received in full or if there has been a breach of this agreement by you.

Appendix 1 — Acknowledgements:

For Journal Content:
Reprinted by permission from [**the Licensor**]: [**Journal Publisher** (e.g.

Nature/Springer/Palgrave)] [**JOURNAL NAME**] [**REFERENCE CITATION** (Article name, Author(s) Name), [**COPYRIGHT**] (year of publication)

For **Advance Online Publication papers:**
Reprinted by permission from [**the Licensor**]: [**Journal Publisher** (e.g. Nature/Springer/Palgrave)] [**JOURNAL NAME**] [**REFERENCE CITATION** (Article name, Author(s) Name), [**COPYRIGHT**] (year of publication), advance online publication, day month year (doi: 10.1038/sj.[JOURNAL ACRONYM].)

For Adaptations/Translations:
Adapted/Translated by permission from [**the Licensor**]: [**Journal Publisher** (e.g. Nature/Springer/Palgrave)] [**JOURNAL NAME**] [**REFERENCE CITATION** (Article name, Author(s) Name), [**COPYRIGHT**] (year of publication)

Note: For any republication from the British Journal of Cancer, the following credit line style applies:

Reprinted/adapted/translated by permission from [**the Licensor**]: on behalf of Cancer Research UK: : [**Journal Publisher** (e.g. Nature/Springer/Palgrave)] [**JOURNAL NAME**] [**REFERENCE CITATION** (Article name, Author(s) Name), [**COPYRIGHT]** (year of publication)

For **Advance Online Publication** papers:
Reprinted by permission from The [**the Licensor**]: on behalf of Cancer Research UK: [**Journal Publisher** (e.g. Nature/Springer/Palgrave)] [**JOURNAL NAME**] [**REFERENCE CITATION** (Article name, Author(s) Name), [**COPYRIGHT**] (year of publication), advance online publication, day month year (doi: 10.1038/sj.[JOURNAL ACRONYM])

For Book content:
Reprinted/adapted by permission from [**the Licensor**]: [**Book Publisher** (e.g. Palgrave Macmillan, Springer etc) [**Book Title**] by [**Book author**(s)] [**COPYRIGHT**] (year of publication)

Other Conditions:

Version 1.2

Questions? customercare@copyright.com or +1-855-239-3415 (toll free in the US) or +1-978-646-2777.

Copyright Clearance Center RightsLink®

Home | Help | Email Support | Bernice Akpinar

DNA Origami Nanopores

Author: Nicholas A. W. Bell, Christian. R. Engst, Marc Ablay, et al
Publication: Nano Letters
Publisher: American Chemical Society
Date: Jan 1, 2012

Copyright © 2012, American Chemical Society

PERMISSION/LICENSE IS GRANTED FOR YOUR ORDER AT NO CHARGE

This type of permission/license, instead of the standard Terms & Conditions, is sent to you because no fee is being charged for your order. Please note the following:

- Permission is granted for your request in both print and electronic formats, and translations.
- If figures and/or tables were requested, they may be adapted or used in part.
- Please print this page for your records and send a copy of it to your publisher/graduate school.
- Appropriate credit for the requested material should be given as follows: "Reprinted (adapted) with permission from (COMPLETE REFERENCE CITATION). Copyright (YEAR) American Chemical Society." Insert appropriate information in place of the capitalized words.
- One-time permission is granted only for the use specified in your request. No additional uses are granted (such as derivative works or other editions). For any other uses, please submit a new request.

If credit is given to another source for the material you requested, permission must be obtained from that source.

BACK CLOSE WINDOW

© 2020 Copyright - All Rights Reserved | Copyright Clearance Center, Inc. | Privacy statement | Terms and Conditions
Comments? We would like to hear from you. E-mail us at customercare@copyright.com

THE AMERICAN ASSOCIATION FOR THE ADVANCEMENT OF SCIENCE LICENSE TERMS AND CONDITIONS

Jan 23, 2020

This Agreement between Imperial College London -- Bernice Akpinar ("You") and The American Association for the Advancement of Science ("The American Association for the Advancement of Science") consists of your license details and the terms and conditions provided by The American Association for the Advancement of Science and Copyright Clearance Center.

License Number	4754710736317
License date	Jan 23, 2020
Licensed Content Publisher	The American Association for the Advancement of Science
Licensed Content Publication	Science
Licensed Content Title	Synthetic Lipid Membrane Channels Formed by Designed DNA Nanostructures
Licensed Content Author	Martin Langecker,Vera Arnaut,Thomas G. Martin,Jonathan List,Stephan Renner,Michael Mayer,Hendrik Dietz,Friedrich C. Simmel
Licensed Content Date	Nov 16, 2012
Licensed Content Volume	338
Licensed Content Issue	6109
Volume number	338
Issue number	6109

Type of Use	Thesis / Dissertation
Requestor type	Scientist/individual at a research institution
Format	Print and electronic
Portion	Figure
Number of figures/tables	1
Order reference number	
Title of your thesis / dissertation	The nanoscale behaviour of disordered polypeptides confined within biomimetic nuclear pore complexes
Expected completion date	Dec 2019
Estimated size(pages)	1
Requestor Location	Imperial College London Department of Materials, Imperial College London, South Kensington Campus London, - SW7 2AZ United Kingdom Attn: Imperial College London
Total	0.00 GBP

Terms and Conditions

American Association for the Advancement of Science TERMS AND CONDITIONS

Regarding your request, we are pleased to grant you non-exclusive, non-transferable permission, to republish the AAAS material identified above in your work identified above, subject to the terms and conditions herein. We must be contacted for permission for any uses other than those specifically identified in your request above.

The following credit line must be printed along with the AAAS material: "From [Full Reference Citation]. Reprinted with permission from AAAS."

All required credit lines and notices must be visible any time a user accesses any part of the AAAS material and must appear on any printed copies and authorized user might make.

This permission does not apply to figures / photos / artwork or any other content or materials included in your work that are credited to non-AAAS sources. If the requested material is sourced to or references non-AAAS sources, you must obtain authorization from that source as well before using that material. You agree to hold harmless and indemnify AAAS against any claims arising from your use of any content in your work that is credited to non-AAAS sources.

If the AAAS material covered by this permission was published in Science during the years 1974 - 1994, you must also obtain permission from the author, who may grant or withhold permission, and who may or may not charge a fee if permission is granted. See original article for author's address. This condition does not apply to news articles.

The AAAS material may not be modified or altered except that figures and tables may be modified with permission from the author. Author permission for any such changes must be secured prior to your use.

Whenever possible, we ask that electronic uses of the AAAS material permitted herein include a hyperlink to the original work on AAAS's website (hyperlink may be embedded in the reference citation).

AAAS material reproduced in your work identified herein must not account for more than 30% of the total contents of that work.

AAAS must publish the full paper prior to use of any text.

AAAS material must not imply any endorsement by the American Association for the Advancement of Science.

This permission is not valid for the use of the AAAS and/or Science logos.

AAAS makes no representations or warranties as to the accuracy of any information contained in the AAAS material covered by this permission, including any warranties of

merchantability or fitness for a particular purpose.

If permission fees for this use are waived, please note that AAAS reserves the right to charge for reproduction of this material in the future.

Permission is not valid unless payment is received within sixty (60) days of the issuance of this permission. If payment is not received within this time period then all rights granted herein shall be revoked and this permission will be considered null and void.

In the event of breach of any of the terms and conditions herein or any of CCC's Billing and Payment terms and conditions, all rights granted herein shall be revoked and this permission will be considered null and void.

AAAS reserves the right to terminate this permission and all rights granted herein at its discretion, for any purpose, at any time. In the event that AAAS elects to terminate this permission, you will have no further right to publish, publicly perform, publicly display, distribute or otherwise use any matter in which the AAAS content had been included, and all fees paid hereunder shall be fully refunded to you. Notification of termination will be sent to the contact information as supplied by you during the request process and termination shall be immediate upon sending the notice. Neither AAAS nor CCC shall be liable for any costs, expenses, or damages you may incur as a result of the termination of this permission, beyond the refund noted above.

This Permission may not be amended except by written document signed by both parties.

The terms above are applicable to all permissions granted for the use of AAAS material. Below you will find additional conditions that apply to your particular type of use.

FOR A THESIS OR DISSERTATION
If you are using figure(s)/table(s), permission is granted for use in print and electronic versions of your dissertation or thesis. A full text article may be used in print versions only of a dissertation or thesis.

Permission covers the distribution of your dissertation or thesis on demand by ProQuest / UMI, provided the AAAS material covered by this permission remains in situ.

If you are an Original Author on the AAAS article being reproduced, please refer to your License to Publish for rules on reproducing your paper in a dissertation or thesis.

FOR JOURNALS:
Permission covers both print and electronic versions of your journal article, however the AAAS material may not be used in any manner other than within the context of your article.

FOR BOOKS/TEXTBOOKS:
If this license is to reuse figures/tables, then permission is granted for non-exclusive world rights in all languages in both print and electronic formats (electronic formats are defined below).

If this license is to reuse a text excerpt or a full text article, then permission is granted for non-exclusive world rights in English only. You have the option of securing either print or electronic rights or both, but electronic rights are not automatically granted and do garner additional fees. Permission for translations of text excerpts or full text articles into other languages must be obtained separately.

Licenses granted for use of AAAS material in electronic format books/textbooks are valid only in cases where the electronic version is equivalent to or substitutes for the print version of the book/textbook. The AAAS material reproduced as permitted herein must remain in situ and must not be exploited separately (for example, if permission covers the use of a full text article, the article may not be offered for access or for purchase as a stand-alone unit), except in the case of permitted textbook companions as noted below.

You must include the following notice in any electronic versions, either adjacent to the reprinted AAAS material or in the terms and conditions for use of your electronic products: "Readers may view, browse, and/or download material for temporary copying purposes only, provided these uses are for noncommercial personal purposes. Except as provided by law, this material may not be further reproduced, distributed, transmitted, modified, adapted, performed, displayed, published, or sold in whole or in part, without prior written permission from the publisher."

If your book is an academic textbook, permission covers the following companions to your textbook, provided such companions are distributed only in conjunction with your textbook at no additional cost to the user:

- Password-protected website
- Instructor's image CD/DVD and/or PowerPoint resource
- Student CD/DVD

All companions must contain instructions to users that the AAAS material may be used for non-commercial, classroom purposes only. Any other uses require the prior written permission from AAAS.

If your license is for the use of AAAS Figures/Tables, then the electronic rights granted herein permit use of the Licensed Material in any Custom Databases that you distribute the electronic versions of your textbook through, so long as the Licensed Material remains within the context of a chapter of the title identified in your request and cannot be downloaded by a user as an independent image file.

Rights also extend to copies/files of your Work (as described above) that you are required to provide for use by the visually and/or print disabled in compliance with state and federal laws.

This permission only covers a single edition of your work as identified in your request.

FOR NEWSLETTERS:
Permission covers print and/or electronic versions, provided the AAAS material reproduced as permitted herein remains in situ and is not exploited separately (for example, if permission covers the use of a full text article, the article may not be offered for access or for purchase as a stand-alone unit)

FOR ANNUAL REPORTS:
Permission covers print and electronic versions provided the AAAS material reproduced as permitted herein remains in situ and is not exploited separately (for example, if permission covers the use of a full text article, the article may not be offered for access or for purchase as a stand-alone unit)

FOR PROMOTIONAL/MARKETING USES:
Permission covers the use of AAAS material in promotional or marketing pieces such as information packets, media kits, product slide kits, brochures, or flyers limited to a single print run. The AAAS Material may not be used in any manner which implies endorsement or promotion by the American Association for the Advancement of Science (AAAS) or Science of any product or service. AAAS does not permit the reproduction of its name, logo or text on promotional literature.

If permission to use a full text article is permitted, The Science article covered by this permission must not be altered in any way. No additional printing may be set onto an article copy other than the copyright credit line required above. Any alterations must be approved in advance and in writing by AAAS. This includes, but is not limited to, the placement of sponsorship identifiers, trademarks, logos, rubber stamping or self-adhesive stickers onto the article copies.

Additionally, article copies must be a freestanding part of any information package (i.e. media kit) into which they are inserted. They may not be physically attached to anything, such as an advertising insert, or have anything attached to them, such as a sample product. Article copies must be easily removable from any kits or informational packages in which they are used. The only exception is that article copies may be inserted into three-ring binders.

FOR CORPORATE INTERNAL USE:
The AAAS material covered by this permission may not be altered in any way. No additional printing may be set onto an article copy other than the required credit line. Any alterations must be approved in advance and in writing by AAAS. This includes, but is not limited to the placement of sponsorship identifiers, trademarks, logos, rubber stamping or self-adhesive stickers onto article copies.

If you are making article copies, copies are restricted to the number indicated in your request and must be distributed only to internal employees for internal use.

If you are using AAAS Material in Presentation Slides, the required credit line must be visible on the slide where the AAAS material will be reprinted

If you are using AAAS Material on a CD, DVD, Flash Drive, or the World Wide Web, you must include the following notice in any electronic versions, either adjacent to the reprinted AAAS material or in the terms and conditions for use of your electronic products: "Readers may view, browse, and/or download material for temporary copying purposes only, provided these uses are for noncommercial personal purposes. Except as provided by law, this material may not be further reproduced, distributed, transmitted, modified, adapted, performed, displayed, published, or sold in whole or in part, without prior written permission from the publisher." Access to any such CD, DVD, Flash Drive or Web page must be restricted to your organization's employees only.

FOR CME COURSE and SCIENTIFIC SOCIETY MEETINGS:
Permission is restricted to the particular Course, Seminar, Conference, or Meeting indicated in your request. If this license covers a text excerpt or a Full Text Article, access to the reprinted AAAS material must be restricted to attendees of your event only (if you have been granted electronic rights for use of a full text article on your website, your website must be password protected, or access restricted so that only attendees can access the content on your site).

If you are using AAAS Material on a CD, DVD, Flash Drive, or the World Wide Web, you must include the following notice in any electronic versions, either adjacent to the reprinted AAAS material or in the terms and conditions for use of your electronic products: "Readers may view, browse, and/or download material for temporary copying purposes only, provided these uses are for noncommercial personal purposes. Except as provided by law, this material may not be further reproduced, distributed, transmitted, modified, adapted, performed, displayed, published, or sold in whole or in part, without prior written permission from the publisher."

FOR POLICY REPORTS:
These rights are granted only to non-profit organizations and/or government agencies. Permission covers print and electronic versions of a report, provided the required credit line appears in both versions and provided the AAAS material reproduced as permitted herein remains in situ and is not exploited separately.

FOR CLASSROOM PHOTOCOPIES:
Permission covers distribution in print copy format only. Article copies must be freestanding and not part of a course pack. They may not be physically attached to anything or have anything attached to them.

FOR COURSEPACKS OR COURSE WEBSITES:
These rights cover use of the AAAS material in one class at one institution. Permission is valid only for a single semester after which the AAAS material must be removed from the Electronic Course website, unless new permission is obtained for an additional semester. If the material is to be distributed online, access must be restricted to students and instructors enrolled in that particular course by some means of password or access control.

FOR WEBSITES:
You must include the following notice in any electronic versions, either adjacent to the reprinted AAAS material or in the terms and conditions for use of your electronic products: "Readers may view, browse, and/or download material for temporary copying purposes only, provided these uses are for noncommercial personal purposes. Except as provided by law, this material may not be further reproduced, distributed, transmitted, modified, adapted, performed, displayed, published, or sold in whole or in part, without prior written permission from the publisher."

Permissions for the use of Full Text articles on third party websites are granted on a case by case basis and only in cases where access to the AAAS Material is restricted by some means of password or access control. Alternately, an E-Print may be purchased through our reprints department (brocheleau@rockwaterinc.com).

REGARDING FULL TEXT ARTICLE USE ON THE WORLD WIDE WEB IF YOU ARE AN 'ORIGINAL AUTHOR' OF A SCIENCE PAPER

If you chose "Original Author" as the Requestor Type, you are warranting that you are one of authors listed on the License Agreement as a "Licensed content author" or that you are acting on that author's behalf to use the Licensed content in a new work that one of the authors listed on the License Agreement as a "Licensed content author" has written.

Original Authors may post the 'Accepted Version' of their full text article on their personal or on their University website and not on any other website. The 'Accepted Version' is the version of the paper accepted for publication by AAAS including changes resulting from peer review but prior to AAAS's copy editing and production (in other words not the AAAS published version).

FOR MOVIES / FILM / TELEVISION:
Permission is granted to use, record, film, photograph, and/or tape the AAAS material in connection with your program/film and in any medium your program/film may be shown or heard, including but not limited to broadcast and cable television, radio, print, world wide web, and videocassette.

The required credit line should run in the program/film's end credits.

FOR MUSEUM EXHIBITIONS:
Permission is granted to use the AAAS material as part of a single exhibition for the duration of that exhibit. Permission for use of the material in promotional materials for the exhibit must be cleared separately with AAAS (please contact us at permissions@aaas.org).

FOR TRANSLATIONS:
Translation rights apply only to the language identified in your request summary above.

The following disclaimer must appear with your translation, on the first page of the article, after the credit line: "This translation is not an official translation by AAAS staff, nor is it endorsed by AAAS as accurate. In crucial matters, please refer to the official English-language version originally published by AAAS."

FOR USE ON A COVER:
Permission is granted to use the AAAS material on the cover of a journal issue, newsletter issue, book, textbook, or annual report in print and electronic formats provided the AAAS material reproduced as permitted herein remains in situ and is not exploited separately

By using the AAAS Material identified in your request, you agree to abide by all the terms and conditions herein.

Questions about these terms can be directed to the AAAS Permissions department permissions@aaas.org.

Other Terms and Conditions:

v 2

Questions? customercare@copyright.com or +1-855-239-3415 (toll free in the US) or +1-978-646-2777.

SPRINGER NATURE LICENSE
TERMS AND CONDITIONS

Sep 04, 2019

This Agreement between Imperial College London -- Bernice Akpinar ("You") and Springer Nature ("Springer Nature") consists of your license details and the terms and conditions provided by Springer Nature and Copyright Clearance Center.

License Number	4661920532645
License date	Sep 04, 2019
Licensed Content Publisher	Springer Nature
Licensed Content Publication	Springer eBook
Licensed Content Title	AFM in Liquids
Licensed Content Author	Bart W. Hoogenboom
Licensed Content Date	Jan 1, 2012
Type of Use	Thesis/Dissertation
Requestor type	academic/university or research institute
Format	print and electronic
Portion	figures/tables/illustrations
Number of figures/tables/illustrations	1
Will you be translating?	no
Circulation/distribution	1 - 29
Author of this Springer Nature content	no
Title	The nanoscale behaviour of disordered polypeptides confined within biomimetic nuclear pore complexes
Institution name	Imperial College London
Expected presentation date	Dec 2019
Portions	AFM in liquids Fig.1 - A schematic representation of AFM in liquid.
Requestor Location	Imperial College London Department of Materials, Imperial College London, South Kensington Campus London, - SW7 2AZ United Kingdom Attn: Imperial College London
Total	0.00 USD
Terms and Conditions	

Springer Nature Customer Service Centre GmbH
Terms and Conditions

This agreement sets out the terms and conditions of the licence (the **Licence**) between you and **Springer Nature Customer Service Centre GmbH** (the **Licensor**). By clicking 'accept' and completing the transaction for the material (**Licensed Material**), you also confirm your acceptance of these terms and conditions.

1. Grant of License

1. 1. The Licensor grants you a personal, non-exclusive, non-transferable, world-wide licence to reproduce the Licensed Material for the purpose specified in your order only. Licences are granted for the specific use requested in the order and for no other use,

subject to the conditions below.

1. 2. The Licensor warrants that it has, to the best of its knowledge, the rights to license reuse of the Licensed Material. However, you should ensure that the material you are requesting is original to the Licensor and does not carry the copyright of another entity (as credited in the published version).

1. 3. If the credit line on any part of the material you have requested indicates that it was reprinted or adapted with permission from another source, then you should also seek permission from that source to reuse the material.

2. Scope of Licence

2. 1. You may only use the Licensed Content in the manner and to the extent permitted by these Ts&Cs and any applicable laws.

2. 2. A separate licence may be required for any additional use of the Licensed Material, e.g. where a licence has been purchased for print only use, separate permission must be obtained for electronic re-use. Similarly, a licence is only valid in the language selected and does not apply for editions in other languages unless additional translation rights have been granted separately in the licence. Any content owned by third parties are expressly excluded from the licence.

2. 3. Similarly, rights for additional components such as custom editions and derivatives require additional permission and may be subject to an additional fee. Please apply to Journalpermissions@springernature.com/bookpermissions@springernature.com for these rights.

2. 4. Where permission has been granted **free of charge** for material in print, permission may also be granted for any electronic version of that work, provided that the material is incidental to your work as a whole and that the electronic version is essentially equivalent to, or substitutes for, the print version.

2. 5. An alternative scope of licence may apply to signatories of the STM Permissions Guidelines, as amended from time to time.

3. Duration of Licence

3. 1. A licence for is valid from the date of purchase ('Licence Date') at the end of the relevant period in the below table:

Scope of Licence	Duration of Licence
Post on a website	12 months
Presentations	12 months
Books and journals	Lifetime of the edition in the language purchased

4. Acknowledgement

4. 1. The Licensor's permission must be acknowledged next to the Licenced Material in print. In electronic form, this acknowledgement must be visible at the same time as the figures/tables/illustrations or abstract, and must be hyperlinked to the journal/book's homepage. Our required acknowledgement format is in the Appendix below.

5. Restrictions on use

5. 1. Use of the Licensed Material may be permitted for incidental promotional use and minor editing privileges e.g. minor adaptations of single figures, changes of format, colour and/or style where the adaptation is credited as set out in Appendix 1 below. Any other changes including but not limited to, cropping, adapting, omitting material that affect the meaning,

intention or moral rights of the author are strictly prohibited.

5. 2. You must not use any Licensed Material as part of any design or trademark.

5. 3. Licensed Material may be used in Open Access Publications (OAP) before publication by Springer Nature, but any Licensed Material must be removed from OAP sites prior to final publication.

6. Ownership of Rights

6. 1. Licensed Material remains the property of either Licensor or the relevant third party and any rights not explicitly granted herein are expressly reserved.

7. Warranty

IN NO EVENT SHALL LICENSOR BE LIABLE TO YOU OR ANY OTHER PARTY OR ANY OTHER PERSON OR FOR ANY SPECIAL, CONSEQUENTIAL, INCIDENTAL OR INDIRECT DAMAGES, HOWEVER CAUSED, ARISING OUT OF OR IN CONNECTION WITH THE DOWNLOADING, VIEWING OR USE OF THE MATERIALS REGARDLESS OF THE FORM OF ACTION, WHETHER FOR BREACH OF CONTRACT, BREACH OF WARRANTY, TORT, NEGLIGENCE, INFRINGEMENT OR OTHERWISE (INCLUDING, WITHOUT LIMITATION, DAMAGES BASED ON LOSS OF PROFITS, DATA, FILES, USE, BUSINESS OPPORTUNITY OR CLAIMS OF THIRD PARTIES), AND
WHETHER OR NOT THE PARTY HAS BEEN ADVISED OF THE POSSIBILITY OF SUCH DAMAGES. THIS LIMITATION SHALL APPLY NOTWITHSTANDING ANY FAILURE OF ESSENTIAL PURPOSE OF ANY LIMITED REMEDY PROVIDED HEREIN.

8. Limitations

8. 1. ***BOOKS ONLY:*** Where **'reuse in a dissertation/thesis'** has been selected the following terms apply: Print rights of the final author's accepted manuscript (for clarity, NOT the published version) for up to 100 copies, electronic rights for use only on a personal website or institutional repository as defined by the Sherpa guideline (www.sherpa.ac.uk/romeo/).

9. Termination and Cancellation

9. 1. Licences will expire after the period shown in Clause 3 (above).

9. 2. Licensee reserves the right to terminate the Licence in the event that payment is not received in full or if there has been a breach of this agreement by you.

Appendix 1 — Acknowledgements:

For Journal Content:
Reprinted by permission from [**the Licensor**]: [**Journal Publisher** (e.g. Nature/Springer/Palgrave)] [**JOURNAL NAME**] [**REFERENCE CITATION** (Article name, Author(s) Name), [**COPYRIGHT**] (year of publication)

For **Advance Online Publication papers:**
Reprinted by permission from [**the Licensor**]: [**Journal Publisher** (e.g. Nature/Springer/Palgrave)] [**JOURNAL NAME**] [**REFERENCE CITATION**

(Article name, Author(s) Name), [**COPYRIGHT**] (year of publication), advance online publication, day month year (doi: 10.1038/sj.[JOURNAL ACRONYM].)

For Adaptations/Translations:
Adapted/Translated by permission from [**the Licensor**]: [**Journal Publisher** (e.g. Nature/Springer/Palgrave)] [**JOURNAL NAME**] [**REFERENCE CITATION** (Article name, Author(s) Name), [**COPYRIGHT**] (year of publication)

Note: For any republication from the British Journal of Cancer, the following credit line style applies:

Reprinted/adapted/translated by permission from [**the Licensor**]: on behalf of Cancer Research UK: : [**Journal Publisher** (e.g. Nature/Springer/Palgrave)] [**JOURNAL NAME**] [**REFERENCE CITATION** (Article name, Author(s) Name), [**COPYRIGHT]** (year of publication)

For **Advance Online Publication** papers:
Reprinted by permission from The [**the Licensor**]: on behalf of Cancer Research UK: [**Journal Publisher** (e.g. Nature/Springer/Palgrave)] [**JOURNAL NAME**] [**REFERENCE CITATION** (Article name, Author(s) Name), [**COPYRIGHT**] (year of publication), advance online publication, day month year (doi: 10.1038/sj.[JOURNAL ACRONYM])

For Book content:
Reprinted/adapted by permission from [**the Licensor**]: [**Book Publisher** (e.g. Palgrave Macmillan, Springer etc) [**Book Title**] by [**Book author**(s)] [**COPYRIGHT**] (year of publication)

Other Conditions:

Version 1.2

Questions? customercare@copyright.com or +1-855-239-3415 (toll free in the US) or +1-978-646-2777.